

Architected Cellular Ferroelectric Metamaterials

Jiahao Shi

Department of Bioresource Engineering
McGill University, Montreal

August 2022

A thesis submitted to McGill University in partial fulfillment of
the requirements of the degree of Doctor of Philosophy

©Jiahao Shi, 2022

Abstract

Materials have shaped human civilizations from the Stone Age to the present. Apart from modifying the chemical constituents, in the past decades, cellular materials have provided a promising material design method to achieve lightweight high-performance advanced materials. By tailoring their typically periodic microarchitectures, metamaterials deliver many exotic properties beyond those found in natural materials or chemically synthesized substances. In the current study, we present a rationale strategy to design smart ferroelectric metamaterials responsive to ambient mechanical, electrical, and thermal stimuli and explore the influence of relative density and cell topology on the effective multiphysical properties. In specific, alternative cell topologies, including 2D extruded cells, 3D truss lattices, hierarchical architectures, and spinodoids, are investigated. Multiscale asymptotic homogenization is first developed to obtain the effective thermo-electro-mechanical properties of the unit cells. Both detailed finite element simulations and closed-form equations are presented to further explain the multiphysical behavior of architected cellular ferroelectrics. Experimental studies are also conducted on additively manufactured cellular ferroelectric ceramics. Due to the complex microstructural features, a high-resolution 3D printing technology based on digital light processing (DLP) is developed. A modified multiphysical homogenization for 3D printed ferroelectric metamaterials is proposed, whose results are then used for machine learning-assisted optimization. To adapt the properties of metamaterials to constantly changing requirements for real-life applications, a reconfigurable

multistable metamaterial with a distinct stable configuration is designed and 3D printed in the form of perforated shellular metamaterials. The design can be extended to smart materials to develop multifunctional metamaterials with adjustable properties.

Architected cellular ferroelectric metamaterials exhibit promising potential for developing smart materials with enhanced piezoelectric and pyroelectric properties. In 2D extruded cellular ferroelectric metamaterials, if an appropriate pore topology is chosen, the ferroelectric figures of merit can be significantly improved, leading to an extension of the material selection charts of ferroelectric materials for applications in sensing, actuation, and energy harvesting. Our findings show that we can further enhance the multifunctional properties by decreasing the relative density. The effect of hierarchical order and hierarchical microarchitectural topology on the effective ferroelectric properties is explored for hierarchical ferroelectric metamaterials. While the 1st-order ferroelectric metamaterials remarkably improve the figures of merit compared to the fully-solid ferroelectrics, increasing hierarchical order magnifies these improvements. Hybrid hierarchical ferroelectric metamaterials also show further improvement in ferroelectric properties that are not necessarily achievable by fractal-like metamaterials. With the machine learning-assisted optimization, we find that some spinodoid ferroelectric metamaterials reveal relatively constant piezoelectric charge coefficients while their relative density is decreased; ultrahigh piezoelectric figures of merit are also achievable due to their ultralow dielectric constant. Both homogenization and experimental tests confirm the high performance of the developed optimized spinodoid. Furthermore, by adopting an n -layer staggered perforation on the surface of a shell-like metamaterial, the so-called shellular, we have achieved a three-directional multistable shellular with a maximum 2^{n-1} stable states within one shellular motif; this shell-like metamaterial can be exploited to develop reconfigurable intelligent structures and devices.

In general, this research offers a promising method to develop high-performance lightweight ferroelectric metamaterials in tandem with reconfigurable multistable mechanical metamaterials. Rationally designed cellular ferroelectric metamaterials can replace the conventionally fabricated random porous structures or bulk materials in many applications, including pressure sensing, ultrasonic sensing, and actuation. Future research can shed more light on exploring more distinct types of cell topologies to fill the gaps in material selection charts for realizing smart materials/structures.

Résumé

Les matériaux ont façonné les civilisations humaines de l'âge de pierre jusqu'à aujourd'hui. Outre la modification des constituants chimiques, les matériaux cellulaires ont fourni, au cours des dernières décennies, une méthode prometteuse pour obtenir des matériaux légers et performants. En adaptant leurs microarchitectures périodiquement répétées, les métamatériaux offrent de nombreuses propriétés exotiques au-delà de celles trouvées dans les matériaux naturels ou les substances synthétisées chimiquement. Dans cette étude, nous présentons une méthode simple pour concevoir des métamatériaux ferroélectriques intelligents répondant à des stimuli mécaniques, électriques et thermiques ambiants. Dans cette méthode, l'influence de la densité relative et de la topologie structurelle sur les propriétés multiphysiques effectives est explorée. En particulier, différentes topologies, y compris les cellules extrudées en 2D, les treillis en 3D, les architectures hiérarchiques et les spinodoïdes, sont considérées. Une méthode d'homogénéisation asymptotique multi-échelles est d'abord développée pour obtenir les propriétés thermo-électro-mécaniques effectives des cellules unitaires ci-dessus. Des simulations détaillées par éléments finis et des équations à forme fermée sont présentées pour fournir des explications supplémentaires. Des études expérimentales sont menées sur des céramiques ferroélectriques cellulaires fabriquées de

manière additive. En raison des caractéristiques structurelles complexes, une technologie d'impression 3D haute résolution est développée. Une homogénéisation multiphysique modifiée pour les métamatériaux ferroélectriques imprimés en 3D est proposée, dont les résultats sont ensuite utilisés pour l'optimisation assistée par apprentissage machine. En outre, l'ajout de perforations dans les matériaux coquilliers permet de créer des métamatériaux multistables reconfigurables, qui possèdent différentes configurations stables, même sans charge externe, et qui s'adaptent aux exigences en constante évolution des applications réelles.

Les métamatériaux ferroélectriques cellulaires architecturés présentent un potentiel intéressant pour améliorer les propriétés piézoélectriques et pyroélectriques. Pour les matériaux cellulaires extrudés en 2D, si une topologie de pore appropriée est sélectionnée, les figures de mérite ferroélectriques peuvent être améliorées de manière significative, ce qui élargit considérablement les tableaux de sélection des matériaux pour les applications dans les capteurs, les actionneurs et les collecteurs d'énergie. Il est intéressant de noter que nos résultats montrent également que nous pouvons encore améliorer ces propriétés multifonctionnelles en diminuant la densité relative. L'effet de l'ordre hiérarchique, de la topologie structurelle et de la densité relative sur les propriétés ferroélectriques effectives est exploré pour les architectures hiérarchiques. Bien que les métamatériaux ferroélectriques de 1er ordre améliorent remarquablement les facteurs de mérite par rapport aux ferroélectriques entièrement solides; l'augmentation de l'ordre hiérarchique peut amplifier ces améliorations. De plus, les métamatériaux ferroélectriques hiérarchiques hybrides présentent une amélioration supplémentaire des propriétés ferroélectriques, qui ne peut être obtenue avec des métamatériaux de type fractal. Grâce à l'optimisation assistée par l'apprentissage automatique, nous constatons que certains métamatériaux spinodoïdes peuvent atteindre des constantes de charge piézoélectrique constantes avec une densité relative décroissante. Les figures

de mérite piézoélectriques très élevées sont également obtenues en raison de la constante diélectrique très faible. L'homogénéisation et l'expérience prouvent la haute performance du spinodoïde optimisé. De plus, en adoptant une perforation échelonnée à n couches sur la surface de la coquille, nous avons obtenu des coquille multi-stables tridirectionnelles avec un maximum de 2^{n-1} états stables dans un motif de coquille pendant le chargement et le déchargement.

En général, cette recherche offre une méthode prometteuse pour développer des métamatériaux ferroélectriques légers et performants ainsi que des métamatériaux multistables reconfigurables. Par conséquent, les métamatériaux ferroélectriques cellulaires conçus rationnellement peuvent remplacer les structures cellulaires poreuses aléatoires fabriquées de manière conventionnelle ou les matériaux en vrac dans de nombreuses applications telles que la détection de la pression, la détection des ultrasons et l'actionnement. Les recherches futures peuvent apporter un éclairage supplémentaire sur l'exploration de différents types de topologies cellulaires, ce qui peut combler les lacunes dans les tableaux de sélection des matériaux.

Contribution and Claims of Originality

In this section, a list of journal articles and conference proceedings prepared by the author during his Ph.D. studies is presented in chronological order.

• Peer-reviewed journal articles

Published/Submitted journal articles:

1. **J. Shi**, A.H. Akbarzadeh, “Architected Cellular Piezoelectric Metamaterials: Thermo-Electro-Mechanical Properties”, *Acta Materialia* 163 (2018) 91-121.

Contributions: This article reports the first and second phases of the present dissertation on the multiphysical homogenization of cellular metamaterials. J. Shi conceived the idea, derived the equations, wrote the numerical code for multiphysical homogenization, conducted the finite element analysis, developed the outline of the article, analyzed the results, and wrote and revised the manuscript.

2. **J. Shi**, A.H. Akbarzadeh, “3D Hierarchical lattice ferroelectric metamaterials”, *International Journal of Engineering Science* 149 (2020) 103247.

Contributions: This article reports the first and third phases of the present dissertation, involving the ferroelectric properties of hierarchical lattice metamaterials. J. Shi conceived the idea, derived the equations, wrote the numerical code for multiphysical homogenization, conducted the finite element analysis, developed the outline of the article, analyzed the results, and wrote and revised the manuscript.

3. **J. Shi**, A.H. Akbarzadeh, “Hierarchical cellular ferroelectric metamaterials: A design motif to enhance multifunctional figures of merit”, *Composite Structures* 250 (2020) 112395.

Contributions: This article reports the fourth phase of the present dissertation, considering different families of hierarchical cellular materials. J. Shi conceived the idea, derived the equations, wrote the code for multiphysical homogenization, conducted the FE analysis, developed the outline, analyzed the results, and drafted the manuscript.

4. C. Gao, W. Wu, **J. Shi**, Z. Xiao, A.H. Akbarzadeh, “Simultaneous enhancement of strength, ductility, and hardness of TiN/AlSi10Mg nanocomposites via selective laser melting”, *Additive Manufacturing* 34 (2020) 101378.

Contributions: J. Shi contributed to modelling and experimentation of 3D nanocomposites with rationally–designed architectures and revising the manuscript.

5. **J. Shi**, H. Mofatteh, A. Mirabolghasemi, G. Desharnais, A.H. Akbarzadeh, “Programmable Multistable Perforated Shellular”, *Advanced Materials* 33 (2021) 2102423.

Contributions: This article deals with the last phase of the present dissertation. J. Shi, H. Mofatteh, and A. Mirabolghasemi contributed equally to this work. J. Shi, H. Mofatteh, and A. Mirabolghasemi designed the multistable perforated shellular. J. Shi and H.

Mofatteh conducted the simulations and experimental tests on 3D printed samples. J. Shi wrote and revised the manuscript in collaboration with H. Mofatteh, and A. Mirabolghasemi.

6. E. Estakhrianhaghghi, A. Mirabolghasemi, **J. Shi**, L. Lessard, A.H. Akbarzadeh, “Architected Cellular Fiber-Reinforced Composite”, *Composites Part B: Engineering* 238 (2022) 109894.

Contributions: J. Shi helped in writing the code for generating the random fiber composite structures and revising the manuscript.

7. R. Tao, **J. Shi**, M. Rafiee, A.H. Akbarzadeh, D. Therriault, “FFF 3D printing of PVDF for piezoelectric sensors and energy harvesters”, *Materials Advances* (2022), <https://doi.org/10.1039/d2ma00072e>.

Contributions: J. Shi helped in enhancing the piezoelectric properties of PVDF, conducting the experiments, and revising the manuscript.

8. R. Tao, **J. Shi**, F. Granier, M. Moeini, A.H. Akbarzadeh, D. Therriault, “Multi-material fused filament fabrication of flexible 3D piezoelectric composite lattices for pressure sensing and energy harvesting applications”, *Applied Materials Today* 29 (2022) 101596.

Contributions: J. Shi helped in designing the structures, conducting the simulations and experiments, and revising the manuscript.

9. K. Ju, C. Duan, Y. Sun, **J. Shi**, A.H. Akbarzadeh, “Prediction of machining deformation induced by residual stress in thin circular parts using Ritz method”, *Journal of Materials Processing Technology* 307 (2022) 117664.

Contributions: J. Shi helped in conducting the simulations, and revising the manuscript.

In-Preparation journal articles:

1. **J. Shi**, A. Mirabolghasemi, S. Akhtar, A. Sasmito, A.H. Akbarzadeh, “3D Spinodoid Piezoelectric Metamaterials”, *Energy and Environmental Science* (In-Preparation for submission).

Contributions: This article reports the fifth phase of the present dissertation. J. Shi conceived the idea, modelled the structures, conducted the numerical simulation, contributed to the machine learning analysis, conducted the 3D printing and experiments, and wrote and revised the manuscript.

2. J. Cai, Y. Li, **J. Shi**, A.H. Akbarzadeh, “Mechanical Properties of Three-dimensional Nano-architected Metallic Metamaterial”, *NPJ computational materials* (In-Preparation for submission).

Contributions: J. Shi helped in designing the structures, conducting the mechanical homogenization, and revising the manuscript.

• **Patents and disclosures**

1. A.H. Akbarzadeh, **J. Shi**, H. Mofatteh, A. Mirabolghasemi, “Shell-based material” United States Provisional Patent Application No. 63/312,176, February 2022.

• **Peer-reviewed conference proceedings**

1. **J. Shi**, A.H. Akbarzadeh. Mechanical properties of 3D printed primitive shellular materials with metasurfaces. *Proceedings of the Joint Canadian Society for Mechanical Engineering and CFD Society of Canada International Congress*. June 2-5, 2019, London, On, Canada.

2. **J. Shi**, A.H. Akbarzadeh. Multiscale Analysis of Ferroelectric Cellular Metamaterials. *Proceedings of the Joint Canadian Society for Mechanical Engineering and CFD Society of Canada International Congress*. June 2-5, 2019, London, On, Canada.
3. **J. Shi**, A.H. Akbarzadeh. Proceedings of the Canadian Society for Mechanical Engineering International Congress 2020. June 21-24, 2020, Charlottetown, PE, Canada.
4. **J. Shi**, Y. Li, H. Niknam, A. Mirabolghasemi, et al. Resilient 3D Printed Shellular Metamaterials. *Progress in Canadian Mechanical Engineering* 2021. <https://doi.org/10.32393/csme.2021.113>.
5. **J. Shi**, A.H. Akbarzadeh. Hierarchical Cellular Ferroelectric Metamaterials. *Progress in Canadian Mechanical Engineering* 2021. <https://doi.org/10.32393/csme.2021.81>.
6. A.H. Akbarzadeh, **J. Shi**, A. Mirabolghasemi, H. Mofatteh, G. Desharnais, 3D Printed shellular metamaterials, Proceedings of *2021 Holistic Innovation in Additive Manufacturing (HI-AM) Conference*, Montreal, QC, Canada, June 25 – 26, 2021 (Online)
7. A.H. Akbarzadeh, **J. Shi**, H. Mofatteh, A. Mirabolghasemi, B. Shahryari, G. Desharnais, Reconfigurable Shellular Metamaterials, *European Mechanics Society – EUROMECH Colloquium on Architected Materials*, Nancy, France, May 2 – 6, 2022 (Invited Talk)
8. **J. Shi**, H. Mofatteh, A. Mirabolghasemi, B. Shahryari, G. Desharnais, A.H. Akbarzadeh, 3D Printed multistable perforated P-shellular, *2022 Holistic Innovation in Additive Manufacturing (HI-AM) Conference*, Montreal, QC, Canada, June 21 – 22, 2022
9. **J. Shi**, H. Mofatteh, A. Mirabolghasemi, B. Shahryari, G. Desharnais, A.H. Akbarzadeh, Programmable multistable 3D printed perforated shellular, *Canadian Society for Mechanical Engineering International Congress CSME 2022*, Edmonton, AB, Canada, June 5 – 8, 2022

• **Poster**

1. **J. Shi**, A.H.Akbarzadeh, Architected Piezoelectric Metamaterials, *13th Colloque Annuel CREPEC*, Montreal, QC, Canada, May 6, 2018
2. **J. Shi**, A. Mirabolghasemi, S. Akhtar, A. Sasmito, A.H. Akbarzadeh, 3D spinodoid piezoelectric metamaterials, *33th Canadian Materials Science Conference CMSC 2022*, Toronto, ON, Canada, June 22-24, 2022

Acknowledgements

I am very grateful to my supervisor, Prof. Hamid Akbarzadeh, who provided support, encouragement, and great ideas for this research. As a patient supervisor, he has been involved in all steps of my research, from conceiving the idea and conducting experiments to writing the manuscript. I also appreciate the guidance and all the discussions we had that helped me finish my Ph.D. studies.

I would like to acknowledge the financial support provided by the China Scholarship Council (CSC) for my five-year stay at McGill University. I am also grateful for McGill Graduate Excellence Award and Fonds de recherche du Québec - Nature et technologies (FRQNT) - Bourses de doctorat (B2X). Funding from these institutions has given me the freedom to pursue my Ph.D. research in Canada.

Furthermore, I would like to express my appreciation to all my friends and colleagues in Advanced Multifunctional and Multiphysics Metamaterials Lab (AM³L): Jun Cai, Youjian Li, Haoyu Chen, Bin Yang, Hossein Mofatteh, Armin Mirabolghasemi, Hamed Niknam, Alireza Seyedkanani, Shahin Eskandari, Ehsan Estakhrian, Jin Wang, Rui Tao, Liang He, and Minghan Xu.

Finally, I would like to thank my family, including my parents and sisters, for encouraging me to pursue my doctoral study, without which I would not have completed this thesis. I also want to address my deep and sincere gratitude to my wife, Kang Ju, who has given me constant love and faith during the four years of separation.

Table of Contents

Abstract	II
Résumé	V
Contribution and Claims of Originality	VIII
Acknowledgements	XIV
List of Figures	XIX
List of Tables	XXVII
CHAPTER 1 Introduction	1
1.1 Problem.....	2
1.2 Literature Review.....	5
1.2.1 Ferroelectric materials	5
1.2.2 Cellular ferroelectric materials	9
1.2.3 3D printing of cellular ferroelectric materials	15
1.2.4 Multistable structure.....	20
1.3 Research objectives.....	24
CHAPTER 2 Homogenization of cellular ferroelectric materials	28
2.1 Constitutive and governing equations of ferroelectric materials	28
2.2 Asymptotic homogenization (AH).....	34
2.3 Multiscale asymptotic homogenization (MAH)	41
CHAPTER 3 2D extruded cellular ferroelectric metamaterials	51
3.1 Pore topology of cellular ferroelectric metamaterials.....	51
3.2 Porous ferroelectric metamaterials with single material.....	55
3.2.1 Influence of shape parameters and polarization direction on effective piezoelectric properties for Type I/II metamaterials.....	55
3.2.2 Influence of shape parameters and polarization direction on effective thermal and pyroelectric properties for Type I/II metamaterials.....	60
3.2.3 Relation between effective thermo-electro-mechanical properties and solid volume fraction.....	62
3.2.4 Comparison between type I/II metamaterials and conventional honeycomb ferroelectric material	66
3.3 Porous ferroelectric metamaterials with bi-phase materials	67

3.3.1 Influence of inclusion and pore volume fraction on effective piezoelectric properties of type III/IV metamaterials.....	67
3.3.2 Influence of inclusion and pore volume fraction on effective thermal and pyroelectric properties of type III/IV metamaterials	70
3.3.3 Relation between effective thermo-electro-mechanical properties of type III/IV metamaterials and inclusion volume fraction	72
3.4 Comparison between type I/II/III/IV metamaterials.....	74
3.5 Concluding remarks on 2D extruded cellular ferroelectric metamaterials	78
CHAPTER 4 3D Hierarchical lattice ferroelectric metamaterials.....	80
4.1 3D hierarchical lattices	80
4.2 1 st -order lattice ferroelectric metamaterials	85
4.3 High-order hierarchical lattice ferroelectric metamaterials	89
4.3.1 Influence of order of hierarchy on the improvement of figures of merit	89
4.3.2 Influence of lattice architecture on the improvement of figures of merit of 2 nd -order hierarchical ferroelectric metamaterials	91
4.3.3 Influence of relative density	92
4.4 Comprehensive 2 nd -order figures of merit	94
4.5 Discussion on the scaling relationship of ferroelectric properties	99
4.6 Concluding remarks on 3D hierarchical lattice ferroelectric metamaterials	106
CHAPTER 5 Hierarchical cubic cellular ferroelectric metamaterials	109
5.1 Hierarchical cubic cellular metamaterials.....	109
5.2 1 st -order cellular ferroelectric metamaterials	113
5.3 2 nd -order hierarchical cellular ferroelectric metamaterials	122
5.4 High order hierarchical cellular ferroelectric metamaterials	127
5.5 Discussion on the electric field distribution and stress concentration	133
5.5.1 Electric field distribution during poling	133
5.5.2 Stress concentration factor.....	137
5.6 Conclusion remarks on hierarchical cubic cellular ferroelectric metamaterials.....	141
CHAPTER 6 Machine learning-assisted design of ferroelectric spinodoids.....	144
6.1 Parametric spinodoid metamaterials.....	144
6.2 Finite element homogenization.....	148
6.3 Machine learning implementation	151
6.3.1 Multilayer perceptron (MLP)	151

6.3.2 Dataset generation	154
6.3.3 Model performance assessment.....	154
6.4 Ferroelectric properties of spinodoid metamaterials.....	155
6.4.1 MLP model parameters	155
6.4.2 Performance of MLP model	157
6.4.3 Prediction of ferroelectric properties of spinodoid ferroelectric metamaterials using MLP model	160
6.5 Experiment.....	164
6.5.1 DLP 3D printing of ferroelectric ceramic.....	164
6.5.2 Ferroelectric properties of printed spinodoid metamaterials	169
6.6 Conclusion remarks on spinodoid ferroelectric metamaterials.....	172
CHAPTER 7 Programmable Multistable Perforated Shellular	174
7.1 Bistable shellular with elliptical holes	174
7.2 Multistable shellular with multilayer staggered perforations	179
7.3 Conclusion remarks on multistable perforated shellular	183
CHAPTER 8 General Conclusions.....	185
8.1 Future directions	188
8.1.1 Ferroelectric ceramic aspect	189
8.1.2 Ferroelectric composite aspect	189
Bibliography	190

List of Figures

Figure 1.1. Architected cellular materials in the core of (a) Bird beaks, (b) Cancellous and cortical bones, and (c) Scots pine softwood. Two types of cellular materials: (d) Foams with irregular microarchitectures, and (e) 2D extruded honeycomb and (f) 3D octet truss lattices with periodic microarchitectures.....3

Figure 1.2. Properties of ferroelectric materials: (a) Piezoelectric effect, (b) Pyroelectric effect, (c) Relationship between piezoelectric, pyroelectric, and ferroelectric materials.....4

Figure 1.3. (a) Tunable acoustic metamaterials. (b) Reconfigurable photonic metamaterials.....5

Figure 1.4. (a) The lower-temperature tetragonal phase of BaTiO₃; the Ti⁴⁺ ion is off-center. (b) β -PVDF polymer chain structure. (c) Polarization of ferroelectric ceramic.....7

Figure 1.5. Ten types of two-phase composite. The white and grey colors represent different phases.....9

Figure 1.6. Four types of cellular ferroelectric materials based on the interconnection of the pores. (a) 0-3, (b) 1-3, (c) 2-3, (d) 3-3.....10

Figure 1.7. Microstructures of porous ferroelectric fabricated by: (a) Coral replamine, (b) BURPS, (c) Polymeric sponge, and (d) Freeze casting.....15

Figure 1.8. 3D printing technologies for the manufacturing of ferroelectric materials: (a) FDM, (b) DW, (c) DLP, and (d) SLS.....16

Figure 1.9. (a) Contact poling; (b) Corona poling.....19

Figure 1.10. (a) Potential energy and force versus displacement curves in bistable materials and structures. (b) Bistable beams with two stable states. (c) Bistable shallow dome.....21

Figure 1.11. (a) Open and closed states of Venus flytrap. (b) Tristable spherical shell. (c) Schwarz P TPMS.....23

Figure 2.1. Partly coupled stationary thermo-piezoelectric fields.....30

Figure 2.2. Schematic figure of (a) homogenization process and (b) periodic boundary conditions.....35

Figure 2.3. Comparison between present results and those provided in [189-191]: (a) effective Young’s modulus of octet truss made of polymer and (b) effective ferroelectric charge constant, d_{33} , of a smart composite material.....41

Figure 2.4. Schematic figure of multiscale homogenization process of hierarchical lattice ferroelectric metamaterials.42

Figure 3.1. Four types of 1-3 cellular, 2D extruded, ferroelectric metamaterials: (a) Type I (single material with longitudinal polarization); (b) Type II (single material with transverse polarization), (c) Type III (bi-material with longitudinal polarization), and (d) Type IV (bi-material with transverse polarization).....52

Figure 3.2. Cross section of 1-3 cellular, 2D extruded, ferroelectric metamaterials: (a) Single material with $\alpha = 4, \beta = 8, \omega_r = 0$ and $s = 1$, (b) Single material with $\alpha = 4, \beta = 8, \omega_r = 45^\circ$ and $s = 1$, (c) Single material with $\alpha = 3, \beta = 6, \omega_r = 0$ and $s = 1$, and (d) Bi-material with $f_{vm} = 0.6, f_{vi} = 0.3, \alpha = 4, \beta = 8, \omega_r = 0$ and $s = 1$53

Figure 3.3. Variation of ferroelectric properties and figures of merit of type I and type II cellular metamaterial with solid volume fraction $f_v = 0.7$ and shape coefficient $c_2 = -0.2$60

Figure 3.4. Variation of the thermal-related properties and associated figure of merits of type I and type II cellular metamaterials with a solid volume fraction $f_v = 0.7$ and shape coefficient $c_2 = -0.2$62

Figure 3.5. Property and figures of merit design charts for type I and type II cellular ferroelectric metamaterials with solid volume fraction f_v varying from 0.3 to 1.....	64
Figure 3.6. Normalized maximum figures of merit of Type I and Type II ferroelectric cellular metamaterials.....	66
Figure 3.7. Influence of inclusion and pore volume fraction on ferroelectric properties of type III and type IV cellular ferroelectric metamaterials with pore volume fractions $f_{\text{pore}} = 0.1$ and 0.3 , $\alpha = 4$, $\beta = 8$, $c_1 = 0$ and $c_2 = 0$ (blue line), and $c_1 = -0.4$ and $c_2 = 0$ (red line).....	69
Figure 3.8. Influence of inclusion and pore volume fraction on the thermal-related properties of type III and type IV cellular metamaterials with pore volume fractions $f_{\text{pore}} = 0.1$ and 0.3 , $\alpha = 4$, $\beta = 8$, $c_1 = 0$ and $c_2 = 0$ (blue line), $c_1 = -0.4$ and $c_2 = 0$ (red line).....	71
Figure 3.9. Design charts for thermo-electro-mechanical properties and figures of merit of type III and type IV cellular ferroelectric metamaterials for a wide range of inclusion solid volume fraction f_{vi} from 0.2 to 0.6.....	74
Figure 3.10. Comparison between piezoelectric and pyroelectric application of four types of metamaterials.....	77
Figure 4.1. Topology of eight lattice architectures considered in this research: (a) Lattice architectures with three different aspect ratios and (b) Cubic and octahedron families with an aspect ratio as 1.....	81
Figure 4.2. (a) Coordinate transformation. Power law relationship along different directions for (b) SC, (c) FDC, (d) FCC, (e) BCC, (f) Octahedron, (g) Octet truss, (h) Cuboctahedron and (i) Tetrakaidecahedron.....	83
Figure 4.3. Relationship between relative density and architectural parameters for ferroelectric lattice metamaterials.....	83
Figure 4.4. Hierarchical configurations: (a) Pattern mechanism, (b) Cubic family, (c) Octahedron family, and (d) Hybrid family.....	85
Figure 4.5. Normalized piezoelectric and pyroelectric figures of merit of 1 st -order lattice ferroelectric metamaterials with different aspect ratios and relative densities.....	89

Figure 4.6. (a) Influence of hierarchical order on the improvement of figures of merit. The overall relative densities for these hierarchical lattice metamaterials are kept at 0.05. More specifically, when $n = 2$, the relative densities for 1st-order and 2nd-order are 0.1 and 0.5, respectively; when $n = 3$, the relative densities for the 1st-order, 2nd-order, and 3rd-order are 0.2, 0.5, and 0.5, respectively; when $n = 4$, the relative densities for 1st-order, 2nd-order, 3rd-order, and 4th-order are 0.4, 0.5, 0.5 and 0.5, respectively; (b) Normalized D_3 of solid material, 1st-order octet-truss, and 1st-order BCC; (c) Influence of hierarchical order on the output voltage of ferroelectric unimorph cantilever beam.....91

Figure 4.7. Influence of lattice topology on figures of merit. The overall relative densities for these hierarchical lattice metamaterials are 0.05. More specifically, the relative densities for the 1st-order and the 2nd-order are 0.1 and 0.5, respectively.....92

Figure 4.8. Influence of the 1st-order relative density of the 2nd-order H-Octet truss ferroelectric metamaterials with an overall relative density at 0.05 on the improvement of figures of merit.....93

Figure 4.9. Maximum improvement and normalized figures of merit for the 2nd-order hierarchical lattice ferroelectric metamaterials with an aspect ratio of 1.....97

Figure 4.10. Normalized properties of 1st-order octet truss and tetrakaidecahedron with AR = 1 and ρ ranging from 0.001 to 1.....102

Figure 4.11. Comparison between the predicted results of developed scaling relationships and MAH of the 2nd-order H-Octet truss.....104

Figure 5.1. Six types of 3D cubic cellular ferroelectric metamaterials.....110

Figure 5.2. Successive hierarchical orders in 3D hierarchical cubic cellular ferroelectric metamaterials.....111

Figure 5.3. 36 types of 2nd-order hierarchical cubic cellular ferroelectric metamaterials.....112

Figure 5.4. Ashby charts where the normalized ferroelectric properties versus relative density for six types of 1st-order cellular ferroelectric metamaterials are plotted.....115

Figure 5.5. Loading conditions and effective volumes used to obtain the effective (a) κ_{33} , (b) p_3^ϵ , (c) d_{31} , and (d) d_{33} ; the corresponding electric displacement along direction 3 for (e) κ_{33} , (f) p_3^ϵ , (g) d_{31} , and (h) d_{33} ; (i) comparison of effective pyroelectric properties obtained by MAH and proposed analytical method, solid line: analytical results, dashed line with markers: MAH results.....117

Figure 5.6. Piezoelectric and pyroelectric figures of merit of 1st-order cellular ferroelectric metamaterials. The error bar shows the difference between the figures of merit of 1st-order 3-0 cellular metamaterial obtained by MAH and scaling relationship.....121

Figure 5.7. Ferroelectric figures of merit of 36 types of 2nd-order hierarchical cellular metamaterials with overall relative densities varying from 0.05 to 0.95. The relative density within each subsection increases linearly in a counterclockwise direction; the color shown in the inner circle denotes the 1st-order unit cell, and the color shown in the outer circle indicates the 2nd-order unit cell; the solid black and dashed black lines show the figures of merit of 1st-order unit cell and 2nd-order unit cell, respectively.....123

Figure 5.8. Six different trends for effective properties of the 2nd-order hierarchical cellular ferroelectric metamaterials with varying ρ_1 . The overall relative density of these 2nd-order hierarchical metamaterials is 0.05.....127

Figure 5.9. Influence of hierarchical order on the improvement of figures of merit. The overall relative density is 0.05. In specific, $\rho_1 = 0.1, \rho_2 = 0.5$ for 2nd-order; $\rho_1 = 0.2, \rho_2 = 0.5, \rho_3 = 0.5$ for 3rd-order; $\rho_1 = 0.4, \rho_2 = 0.5, \rho_3 = 0.5, \rho_4 = 0.5$ for 4th-order.....130

Figure 5.10. Maximum improvement of figures of merit of 3rd-order hierarchical metamaterials compared with that of 3rd-order unit cell with $\rho = 0.05$. 1st-order and 2nd-order share the same unit cell.....131

Figure 5.11. Piezoelectric cymbal transducer (PCT) with hierarchical cellular ferroelectric metamaterials: (a) Geometric information of PCT, (b) Generated voltage in a piezoelectric disc, (c) Effect of hierarchical orders on the output voltage of PCT with 1st-order 3-0 and 3-3 ($\rho_1 = 0.05$), 2nd-order 3-0/3-0 and 3-3/3-3 ($\rho_1 = 0.1, \rho_2 = 0.5$), 3rd-order 3-0/3-0/3-0 and 3-3/3-3/3-3 ($\rho_1 = 0.2, \rho_2 = 0.5, \rho_3 = 0.5$), 4th-order 3-0/3-0/3-0/3-0 and 3-3/3-3/3-3/3-3 ($\rho_1 = 0.4, \rho_2 = 0.5, \rho_3 = 0.5, \rho_4 = 0.5$).....132

Figure 5.12. Electric field distribution at each level of 3rd-order hierarchical cubic ferroelectric metamaterials with $\rho_3 = 0.4$, $\rho_2 = 0.5$, and $\rho_1 = 0.6$ during polarization. The left large contour figures indicate the normalized electric field; the right small contour presents the poled regions (red color) and unpoled regions (green color). The normalized electric field versus fraction curve indicates the distribution of electric field over the population of ferroelectric material elements.137

Figure 5.13. Stress distribution and concentration at each level of 3rd-order hierarchical cubic ferroelectric metamaterials with $\rho_3 = 0.4$, $\rho_2 = 0.5$, and $\rho_1 = 0.6$. Colors indicate the normalized von Miss stress. The normalized von Mises stress versus fraction curve indicates the distribution of stress over the population of elements.....141

Figure 6.1. (a) The phase separation process to generate porous spinodal material (black: solid, white: air). (b) Electrochemical dealloying of Ag₉₃Au₇ master alloy (yellow) in 0.01M H₂SO₄ aqueous electrolyte (white) leading to a hierarchical spinodal nanoscale.....145

Figure 6.2. (a) Schematic of the design parameters: θ_1 , θ_2 , θ_3 . (b) Discretization/voxelization of the spinodoid (elements in green refer air, and elements in brown present the solid material). (c) lamellar, (d) Columnar, and (e) Cubic spinodoids.....147

Figure 6.3. (a) Poling simulation. (b) Six boundary surfaces.....148

Figure 6.4. Comparison of the effective stiffness (C_{33}) (a) and dielectric constant (κ_{33}) (b) of ferroelectric octet truss metamaterials calculated by AH method and finite element homogenization.....151

Figure 6.5. Feedforward MLP network structure. The blue circles mean the input, purple circles mean the output, and the orange ones mean hidden layer neurons.....153

Figure 6.6. Influence of number of (a) epoch and (b) batch size on the convergence of RMSE...156

Figure 6.7. Comparison between the true and predicted effective mechanical properties of spinodoid ferroelectric metamaterials.....158

Figure 6.8. Comparison between the true and predicted effective piezoelectric properties of spinodoid ferroelectric metamaterials.....159

Figure 6.9. Comparison between the true and predicted effective dielectric constants of spinodoid ferroelectric metamaterials.....160

Figure 6.10. The predicted piezoelectric properties of spinodoid ferroelectric metamaterials based on the trained MLP model: (a) d_{33} , (b) κ_{33} , (c) g_{33} , and (d) FOM_{33} . Three representative structures are marked in these figures, where ‘*’, ‘□’, and ‘○’ stand for spinodoid structure types A, B, and C with geometrical parameters as $(0^\circ, 0^\circ, 30^\circ)$, $(30^\circ, 30^\circ, 0^\circ)$, and $(60^\circ, 60^\circ, 60^\circ)$, respectively....163

Figure 6.11. Schematic of DLP 3D printing process.....165

Figure 6.12. The relationship between the viscosity of the ceramic slurry and dispersant concentration at a 50 s^{-1} shear rate.....166

Figure 6.13. TGA curves for the thermal decomposition of the PEGDA in the printed green body.....167

Figure 6.14. (a) Debinding and (b) sintering temperature profiles of the 3D printed green bodies.....168

Figure 6.15. 3D printed along with the 3D models of (a) Type A, (b) Type B, and (c) Type C samples.....169

Figure 6.16. Comparison of the effective (a) d_{33} , (b) κ_{33} , (c) g_{33} , and (d) FOM_{33} of the three types of ferroelectric spinodoids determined through finite element homogenization, MLP, and experiment.....172

Figure 7.1. Overview of bistable P shellulars motif. (a) The designed half-cell of perforated P shellular metamaterial can exhibit two stable states when four sides (marked by red color) are fixed, and the pressure is applied on the top surface (highlighted by orange color). (b, c) Force displacement curve of a half-cell of intact P shellular with $f = 0$ shows snap-through behavior while the perforated counterpart can present mechanical bistability, indicated by the sign of their reaction force F . (d) Geometrical parameters of the designed perforated P shellular unit cells. Three samples with different level set constants f and thickness t are 3D printed by SLS. (e) Effect of level set f and shell thickness t/S on the bistability of perforated and intact shellulars, investigated by FE simulation.....177

Figure 7.2. Programmability of bistable perforated P shellulars. (a, b) Experimental (blue and pink area) and FE simulation (solid black line) stress-strain curves of samples I and III. (c) Experimental results of 3D printed graded perforated shellulars with the same thickness.....179

Figure 7.3. Multistable behavior of staggered perforated P shellulars. (a) Schematic view showing the staggered perforated P shellular. (b) Representative deformation pattern and stress-strain curve of the designed multistable metamaterial during the loading and unloading. (c) Four stable states of 3D printed sample II during loading and unloading.....181

Figure 7.4. Analysis of geometrical parameters' effect on the snapping behavior of the designed multidirectional multistable perforated shellular metamaterials. (a) Five 3D printed motifs. Red numbers in parenthesis indicate the number of stable states, including the initial configuration. (b) Contour associated with the number of stable states (left blue color), maximum snap-back induced energy dissipation (middle green color), and total snap-back induced energy dissipation during a cyclic load (right red color) with respect to the circumferential angle α and flexible beam height t' , determined by FE simulation. (c) 3D deployment of multidirectional multistable unit cell.....183

List of Tables

Table 3.1. Piezoelectric properties of material constituents of ferroelectric cellular metamaterials: \mathbf{C} ($\times 10^9$) in Pa, \mathbf{e} ($\times 10^{-2}$) in C/m ² , and $\boldsymbol{\kappa}$ ($\times 10^{-11}$) in C/(Vm ²) from Reference [192,198].....	55
Table 3.2. Thermal properties of material constituents of ferroelectric cellular metamaterials: ρ in g/cm ³ , Δ ($\times 10^{-6}$ K ⁻¹) in Pa, γ in Vm ⁻¹ K ⁻¹ , \mathbf{K} in Wm ⁻¹ K ⁻¹ , C_p in J/(gK) from References [192,199].....	55
Table 3.3. Comparison of properties of four types of cellular ferroelectric metamaterials with the solid volume fraction of 0.3. The considered type I and type II metamaterials are: regular honeycomb (left), $c_1 = 0$ and $c_2 = 0$ (middle) and $c_1 = -0.4$ and $c_2 = 0$ (right). From left to right, type III and type IV metamaterials include: $c_1 = 0$, $c_2 = 0$ and $f_{\text{pore}} = 0$ (first one), $c_1 = 0$, $c_2 = 0$ and $f_{\text{pore}} = 0.1$ (second one), $c_1 = 0$, $c_2 = 0$ and $f_{\text{pore}} = 0.3$ (third one), $c_1 = -0.4$, $c_2 = 0$ and $f_{\text{pore}} = 0.1$ (fourth one) and $c_1 = 0$, $c_2 = 0$ and $f_{\text{pore}} = 0.3$ (fifth one).....	76
Table 4.1. Maximum improvement of figures of merit for the 2 nd -order hierarchical lattice ferroelectric metamaterials with an overall relative density of 0.05 and aspect ratios of 4 and 0.25. The bold number highlights the maximum normalized figures of merit.....	99
Table 5.1. Proportionality and scaling constants of six 1 st -order cellular ferroelectric metamaterials.....	116

Table 6.1. Boundary conditions (displacement/electric potential) and equations to calculate the effective properties of spinodoid unit cell. $i = 1, 2, 3$ and $j = 1, 2, 3, 4, 5, 6$150

Table 6.2. Influence of hidden layer dimension on the RMSE, MAE, and R^2 157

CHAPTER 1

Introduction

This chapter begins by addressing the rationality for studying the problem of interest, following a comprehensive review of architected smart metamaterials. The challenges in the field of architected smart metamaterials with tunable properties, including both ferroelectric and multistable properties, are stated, and the proposed approaches to overcome those obstacles are explained. The literature survey section is divided into four major subsections. Firstly, ferroelectric materials and their composites for achieving high-performance mechanical and ferroelectric properties are discussed by reviewing previous studies. Cellular ferroelectric materials are then classified and discussed. Specifically, theoretical methods to predict their effective multiphysical properties along with the traditional fabrication techniques for porous ferroelectrics are introduced. The third part of the literature review offers an overview of the current three-dimensional (3D) printing technologies of ferroelectric materials. In addition, recent studies on the multistable metamaterials or metastructures are discussed, laying the groundwork for exploring multistable perforated shellulars as a type of reconfigurable mechanical metamaterials that can be used, in future studies, for developing smart deployable and programmable structures. Later, the employed methodology is identified, and the objectives of the thesis are articulated.

1.1 Problem

The emergence of new high-performance multifunctional materials accelerates the development of human civilization leading to its evolution from the Stone Age and Bronze Age to the Steel/Aluminum/Plastic Age and beyond. Challenged by the limited selection of constituent materials with poor intrinsic properties and extreme environmental conditions, natural materials have evolved a unique combination of strength or toughness in a lightweight fashion, stemming from their complex cellular microarchitectures, such as the beaks of birds [1,2] (Figure 1.1a), bones [1,3] (Figure 1.1b), and plants' stem [4,5] (Figure 1.1c). Inspired by natural materials, through deliberate tailoring of their microarchitectures, manmade cellular materials, or cellular metamaterials, are being developed to deliver many unprecedented multifunctional properties beyond those found in natural materials or chemically synthesized substances, which enable us to obtain unparalleled mechanical, thermal, electrical, and magnetic properties (e.g., negative refractive index [6,7], negative effective density [8,9], negative incremental stiffness [10,11], negative Poisson's ratio [12], shape reconfigurability [13], ultra-low density [14,15], and negative thermal conductivity [16,17]). Instead of a limited number of unit cells, these special properties are due to the tessellated arrangement of a larger number of rationally designed structural elements. For example, by tailoring the microarchitecture of the unit cell, it is possible to tune or even reverse the direction of heat flux to achieve negative conductivity [16,17]. A Cellular Material is commonly defined as "an interconnected network of solid struts or plates that form the edges and faces of cells" [18]. As shown in Figure 1.1d-f, cellular materials, consisting of solid and air, include foams with irregular nano/microarchitectures [19] and lattices with regular nano/microarchitectures (e.g., 2D extruded honeycomb [20], 3D octet-truss [2]), and have attracted increasing attention due to their potential for expanding the range of available material properties.

If these cellular materials are reconfigurable or made of smart materials (e.g., piezoelectric, piezomagnetic, magnetostrictive materials, and electroactive) in the form of optimized architectures, they can open a new venue for designing lightweight advanced multifunctional materials responsive/sensitive to ambient multiphysical stimuli.

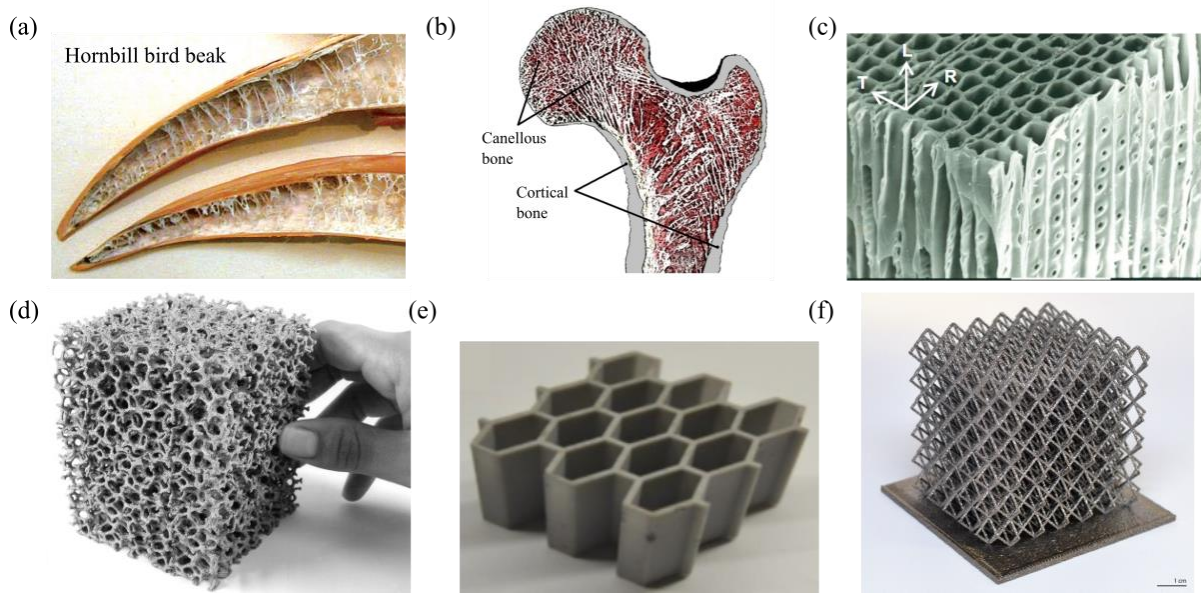


Figure 1.1. Architected cellular materials in the core of (a) Bird beaks, (b) Cancellous and cortical bones, and (c) Scots pine softwood. Two types of cellular materials: (d) Foams with irregular microarchitectures and (e) 2D extruded honeycomb, and (f) 3D octet truss lattices with periodic microarchitectures. (Figure 1.1a and f adapted from ref [2] under the terms of the CCC license; Figure 1.1b reprinted with permission from ref [21], copyright 2009 Springer nature; Figure 1.1c reprinted with permission from ref [4], copyright 2015 Elsevier; Figure 1.1d reprinted with permission from ref [19], copyright 2010 Elsevier; Figure 1.1e reprinted with permission from ref [20], copyright 2019 Elsevier)

The ferroelectric material is one of the widely used smart materials, which possesses both piezoelectric and pyroelectric properties. As shown in Figure 1.2a, the piezoelectric effect causes the generation of electric power from mechanical oscillations [22], while the pyroelectric effect converts temperature fluctuations into electricity [23]. Both effects can be found in ferroelectric materials, e.g., lead zirconate titanate (PZT), barium titanate (BaTiO_3), and polyvinylidene fluoride

(PVDF), with a wide range of applications in pressure sensing [24,25], ultrasonic sensing [26,27], actuation, [28,29] and energy harvesting [30,31]. In general, all ferroelectrics are both pyroelectric and piezoelectric, and all pyroelectric are piezoelectric but not vice versa, implying that not all piezoelectric materials exhibit pyroelectric properties; an example for that is such as quartz (Figure 1.2c) [32]. Both templating [33,34] and freeze casting [35,36] techniques have been used to produce piezoelectric foams, which have experimentally and theoretically showcased potentials for reduced mass density and improved hydrostatic figures of merit in piezoelectric materials. However, due to the limitation of traditional fabrication methods [37–39], complex and optimized architected ferroelectric materials is difficult to be manufactured, which impedes the exploration of rational designed architected cellular ferroelectric materials and the development of high-performance ferroelectric devices with unprecedented multifunctional properties.

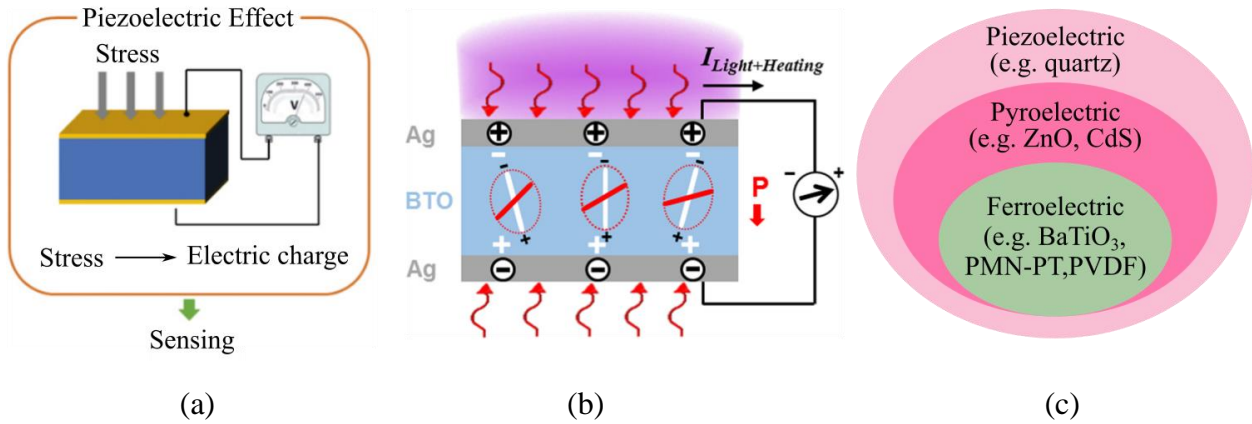


Figure 1.2 Properties of ferroelectric materials: (a) Piezoelectric effect, (b) Pyroelectric effect, (c) Relationship between piezoelectric, pyroelectric, and ferroelectric materials. (Figure 1.2a reprinted with permission from ref [22], copyright 2018 Springer nature; Figure 1.2b reprinted with permission from ref [23], copyright 2017 Elsevier; Figure 1.2c adapted from ref [32] under the terms of the CCC license)

Apart from designing architected cellular materials made of smart materials, reconfigurable cellular materials that render programmable properties are also in high demand for developing

smart advanced materials adaptable to the constantly changing requirements in their real-life applications [40–43]. One of the promising strategies is to adopt structural bistability by triggering elastic instability and retaining different stable configurations. For example, by achieving different stable states, tunable acoustic [40,41] (Figure 1.3a) and photonic [42,43] (Figure 1.3b) bandgaps can be realized in multifunctional cellular materials. However, most of the current bistable elements are based on constrained inclined [44] or curved [45] beams and shallow domes [46]; exploiting new motifs with an arbitrary number of stable configurations facilitates the realization of the deployable metastructures with multiple configurations and soft robots with a plethora of controllable displacement degrees of freedom. In the following literature review, the efficacy of ferroelectric cellular metamaterials and multistable cellular metamaterials are reported.

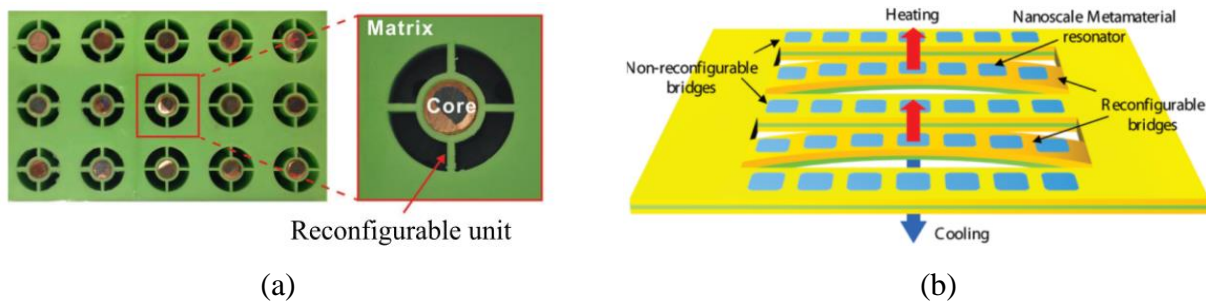


Figure 1.3 (a) Tunable acoustic metamaterials. (b) Reconfigurable photonic metamaterials. (Figure 1.3a reprinted with permission from ref [41], copyright 2014 American Physical Society; Figure 1.3b reprinted with permission from ref [43], copyright 2011 American Chemical Society)

1.2 Literature Review

1.2.1 Ferroelectric materials

Prefixes “piezo” and “pyro” are derived from Greek words with the meanings of “press” and “fire”, respectively [47]. In 1824, David Brewster observed the opposite polarities at the two ends of several heated crystals and gave it the name “pyroelectricity” [48,49]; In 1880, Pierre and Jacques

Curies firstly discovered the piezoelectric properties of quartz, in which positive and negative charges are generated on the surface under compression in a certain direction [47,50]. Both effects arise from the spontaneous polarization of ferroelectric materials, which show polarization even in the absence of an applied electric field [51]. Under applied stress or temperature fluctuations, the presence of spontaneous polarization in ferroelectric materials results in the presence of a charge on each surface of ferroelectric materials. For ionic bonded materials, this polarization is a consequence of the crystal structure [52,53]. For example, as shown in Figure 1.4a, below Curie temperature, the tetragonal phase of BaTiO_3 crystal has a net dipole since the center of the positive charge (Ti^{4+}) does not coincide with the center of the negative charge (O^{2-}) within the structure [54]. Generally, the piezoelectric effect can exist in crystals with non-centrosymmetric crystallographic symmetry classes. Among the 32 crystallographic classes, only 21 are non-centrosymmetric. Furthermore, in crystals with the cubic non-centrosymmetric class, the piezoelectric coefficients are all zero due to symmetry. Therefore, a total of 20 “piezo” crystallographic classes may exhibit non-zero piezoelectric coefficients [55]. For crystalline polymers with aligned molecular chains, it can be due to the alignment of polarized covalent bonds [56,57]. For example, the β -PVDF polymer exhibits piezoelectric properties, and its dipole moment arises from the C-F bond. However, the dipole moments are randomly scattered within the materials, and their orientations are in different directions. The overall materials thus do not have piezoelectric and pyroelectric properties. Poling process, which applies high electric fields at elevated temperature on the ferroelectric materials, is needed to align these dipoles along the poling electric field direction [47] (Figure 1.4c).

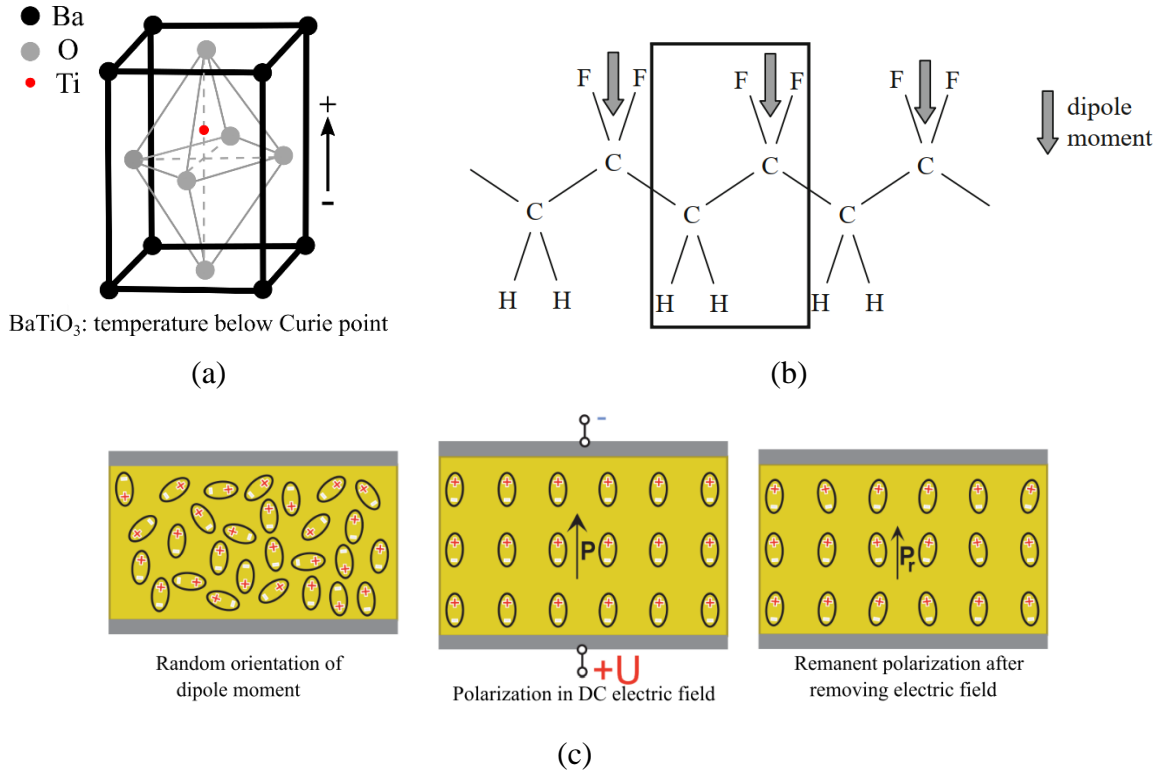


Figure 1.4 (a) The lower-temperature tetragonal phase of BaTiO₃; the Ti⁴⁺ ion is off-center. (b) β-PVDF polymer chain structure. (c) Polarization of ferroelectric ceramic.

After the observation of piezoelectricity in quartz, various ferroelectric materials have been developed, such as perovskite crystals [58,59], ceramics [60], and polymers [56,57]. Featuring high ferroelectric coefficients, brittle ceramics are the most commonly used ferroelectric materials, e.g., PZT ceramic has $d_{33} > 300$ pC/N [61]. Ferroelectric polymers, such as P(VDF-TrFE), on the other hand, offer unique capabilities for applications that require mechanical flexibility and biocompatibility, but at the cost of much smaller ferroelectric properties ($d_{33} \approx 20$ to 34 pC/N) [62]. Ferroelectric composites, encapsulating brittle ferroelectric ceramics by soft polymers, provide a promising method to possess an excellent combination of mechanical flexibility and ferroelectric properties.

As shown in Figure 1.5, based on the phase connectivity, there are ten types of two-phase ferroelectric composites, i.e., 0-0, 1-0, 2-0, 3-0, 1-1, 2-1, 3-1, 2-2, 2-3, and 3-3 [63], where the two

values denote the number of connected directions of the matrix and filler, respectively. However, the type of the connectivity pattern is not enough to describe the effective properties of the composite ferroelectrics. Tailoring the microarchitecture of the composites is also of great importance in determining the overall properties. For polymer-based ferroelectric composites, a ferroelectric matrix (such as Polyvinylidene fluoride (PVDF) [64–66]) showed better figures of merit and piezoelectric properties than a non-piezoelectric matrix (such as epoxy [67–74]). The ceramic-based ferroelectric composites (such as PZT-7A/BaTiO₃ [64]) were explored to modify the electro-mechanical properties of ferroelectric composites. Regarding the dimension of inclusion connectivity, 0-3, 1-3, and 2-2 types of piezocomposites with different inclusion shapes and unit cell position arrangements were modeled in reference [65]. The 0-3 ferroelectric composites with short ferroelectric cylindrical fibers [66] and particulate spherical inclusion [67] have exhibited similar properties for different volume fractions of inclusion. Due to their extensive use in biomedical and naval applications, 1-3 ferroelectric composites attracted more attention than the other three types of ferroelectric composites. One method to modify the properties of 1-3 ferroelectric composites is to engineer the inclusion topology (prismatic (octagon and square) and non-prismatic (circle and ellipse) inclusions [65]) and unit cell positional arrangement (hexagonal and square positional arrangement [68]), especially for transversely polarized 1-3 ferroelectric composite (with polarization perpendicular to the inclusion). Other categories of 1-3 ferroelectric composites, such as four-step braided cylindrical inclusions [69], randomly distributed cylindrical inclusions [70], and parallelogram periodic cells [71], have also been investigated to seek the possibility of improving electromechanical properties; it was found that only changing the positional arrangement of unit cells had an obvious influence on the effective electro-mechanical properties. In addition, functionally graded ferroelectric composites have been introduced by

tailoring polarization direction and material gradation within the smart composites [72]. Compared to 1-3 ferroelectric composites with cylindrical inclusions, one advantage of 2-2 ferroelectric composites was their simple processing method and avoiding direct connection between electrodes and piezoelectric phase [73]. One noticeable 2-2 piezocomposite was a Macro Fiber Composite (MFC) with interdigitated electrodes, which has been used as actuators and sensors by a company named *Smart Material Corporation*. In general, 1-3 ferroelectric composites showed better figures of merit for energy harvesting (higher piezoelectric charge coefficients and coupling constants), while 0-3 ferroelectric composites revealed the lowest acoustic impedance for biomedical imaging devices. However, the separation of the interface between inclusion and matrix might deteriorate piezocomposites [74].

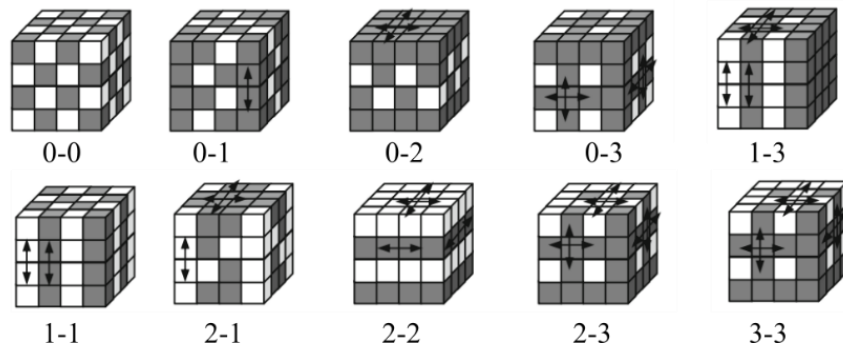


Figure 1.5 Ten types of two-phase composites. The white and grey colors represent different phases. (reprinted with permission from ref [63], copyright 1978 Elsevier)

1.2.2 Cellular ferroelectric materials

1.2.2.1 Multiphysical properties of cellular ferroelectric materials

Typically, apart from adding a second phase (ferroelectric composites), introducing pores (cellular ferroelectric materials) is also a commonly used method to modify the properties of ferroelectric materials. Introducing pores makes ferroelectric materials less stiff; however, cellular ferroelectric metamaterials can show remarkable improvement in figures of merit, especially for hydrophone applications. Cellular ferroelectric metamaterials can be considered as ferroelectric composites

with empty inclusions periodically distributed in a piezoelectric matrix [75]. Similar to Figure 1.5, there are four types of commonly considered cellular ferroelectric materials (Figure 1.6): (1) 0-3 type (pore phase is enclosed by the matrix phase), (2) 1-3 type (pore phase is connected in one direction and matrix is connected in all three directions), (3) 2-3 type (both pore and matrix phases exhibit connectivity in two dimensions), and (4) 3-3 type (both pore and matrix exhibit connectivity in all three directions).

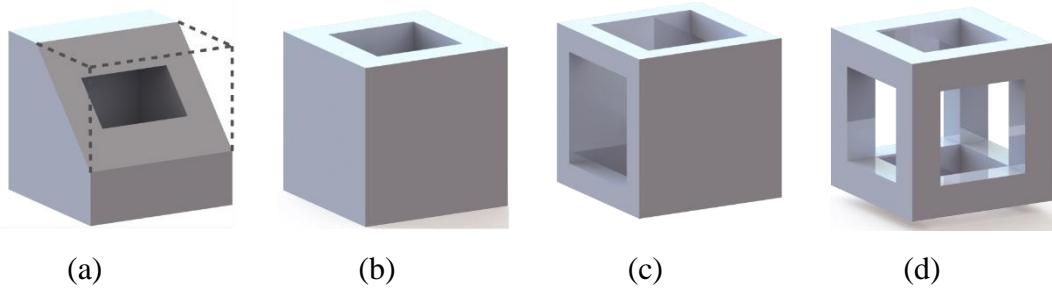


Figure 1.6 Four types of cellular ferroelectric materials based on the interconnection of the pores. (a) 0-3, (b) 1-3, (c) 2-3, (d) 3-3.

In general, there are three aspects of improvement for piezoelectric and pyroelectric properties of cellular ferroelectric materials. (1) Due to the porosity, the increased transverse piezoelectric charge constant, d_{31} (negative value), and almost constant longitudinal piezoelectric charge constant, d_{33} (positive value), result in the enhanced hydrostatic strain constant, $d_h = d_{33} + 2 d_{31}$, indicating a better sensitivity to hydrostatic pressure [76]. (2) The dielectric permittivity at constant stress, κ_{33}^σ , decreases by increasing porosity. As a result, the reduction of κ_{33}^σ leads to a high hydrostatic voltage coefficient, $g_h = d_h/\kappa_{33}^\sigma$ (generated voltage by a hydrostatic pressure) [76], pyroelectric voltage responsivity, $F_V = p_3/(c_E \kappa_{33}^\sigma)$ (generated voltage by a given thermal input) [77], piezoelectric energy harvesting figure of merit, $FOM_{33} = d_{33}^2/\kappa_{33}^\sigma$ (electric energy density caused by applied mechanical stress) [78], and pyroelectric energy harvesting figure of merit, $F_E = p_3^2/(c_E^2 \cdot \kappa_{33}^\sigma)$ (generated electrical energy density due to unit temperature fluctuation) [77],

where c_E is heat capacity and p_3 is pyroelectric constant. (3) The acoustic impedance, $Z = (\rho \cdot C_{33}^D)^{0.5}$ (ρ is material density and C_{33}^D is Young's modulus under constant charge density), is reduced by the increase of porosity, which improves matching the ferroelectric material and the surrounding aquatic medium for applications such as in sonar, hydrophone, and medical ultrasonography [75]. It is noted that for random porous materials, due to the significant difference between the dielectric constant of air and ferroelectric materials, these porous ferroelectric materials cannot be fully polarized, contributing to low ferroelectric properties [79–83].

Although cellular ferroelectric materials exhibit obvious improvement in ferroelectric properties compared to their solid counterpart, the deliberate engineering of the pore topology can further enhance the ferroelectric properties. A few studies have recently been conducted to optimize electro-mechanical properties of cellular ferroelectric materials by tailoring their microarchitectures [84,85,94,95,86–93]. For 0-3 cellular ferroelectric metamaterials, alternative pores, e.g., flat-cuboidal, spherical, and short-cylindrical pores, showed different effective electromechanical properties; flat cuboidal pores resulted in a better hydrostatic charge and hydrostatic voltage constants [84]. Similar to ferroelectric composite, electromechanical properties of 1-3 cellular ferroelectric materials can be improved by optimizing alternative parameters, e.g., pore shape [75], pore aspect ratio [85], and polarization direction [85–87]. For longitudinally polarized porous ferroelectric materials, electromechanical properties were shown to be insensitive to pore shapes and aspect ratio; an opposite behavior has been found for transversely-polarized porous ferroelectric materials [75,86–90]. In addition, acoustic impedance and hydrostatic charge constant can be modified by tailoring pore position arrangement [86,87]. As for prismatic pores, auxetic [88], honeycomb [88–90], tetragonal [89,90], and triangular microarchitectures [91,92] have shown different deformation modes and electromechanical properties. It was found that along

the polarization direction, the bending dominant deformation mode enhanced the piezoelectric figures of merit. Compared to 1-3 cellular ferroelectric materials, 3-3 cellular ferroelectric materials have shown great improvement in the piezoelectric figures of merit at the cost of deteriorating mechanical performance [91,93–97]. Apart from the piezoelectric effect, some pyroelectric figures of merit with cellular microarchitectures also showed obvious improvement compared to that of dense materials [97,98].

Although a series of research works have been done on the area of cellular ferroelectric metamaterials, most of them concentrated on simple 2D, e.g., honeycomb, or simple 3D, e.g., cubic architecture. The architected cellular ferroelectric metamaterials made of complex 3D lattice unit cells, e.g., octet truss, are yet to be explored, let alone shell-like (shellular) and hierarchical metamaterials. Further research on shellular, hierarchical lattice and shape-reconfigurable ferroelectric metamaterials will shed light on the potential of cellular ferroelectric metamaterials for applications as high-performance intelligent materials.

1.2.2.2 Theoretical analysis

In order to obtain the effective properties of architected cellular materials with periodic microarchitectures, both analytical and numerical methods have been proposed. Based on a pioneering work conducted by Eshelby [99], several analytical mean field methods [100–102], e.g., dilute, self-consistent, and Mori–Tanaka, were proposed to predict the effective electromechanical properties of piezocomposite with alternative inclusion topologies. However, the local fluctuations of the field quantities were not taken into account in these analytical micromechanical models. This restriction can be solved by the combination of analytical models with numerical methods, e.g., the finite element method. Although the finite element method is straightforward to understand, detailed numerical simulation of structures made of many cells of ferroelectric

microarchitectures is a cumbersome task since it is a computationally expensive process. One of the most efficient approaches for predicting the overall multiphysical properties of heterogeneous advanced architected materials with engineered microstructures is to analyze their representative volume elements (RVE) and obtain a macroscopic homogenous medium equivalent to the original heterogeneous microstructure using homogenization techniques [84–90,103–105]. Two widely adopted homogenization techniques are: *standard method* (SM) [83], [84], [87]–[91] or so-called finite element method and *asymptotic homogenization* (AH) [102]–[104]. In this thesis, AH is used to predict the effective thermo-electromechanical properties of the architected cellular ferroelectric metamaterials and is described in **Chapter 2**. In contrast to SM homogenization, AH has a robust mathematical basis, which provides closed-form expressions for accurate theoretical predictions of effective multiphysical properties of advanced materials with periodic microstructures.

1.2.2.3 Fabrication of cellular ferroelectrics

Coral replamine. The coral is combined with wax under vacuum and then dissolved away using acid, thus forming the wax negative. Ferroelectric slip, such as PZT-slip, are filled into the wax mode. After drying and sintering, the wax is removed, and the ferroelectric ceramic is sintered, sharing the shape of the original coral [63,106,107]. The resulting structures have large pores, leading to 3-3 connectivity (Figure 1.7a). As an initial method, this technology is simple and used to realize the ferroelectric porous materials. However, this method is difficult to scale up.

Burned out polymer spheres (BURPS). The pore-forming agent is first added to the ceramic powder and then pressed. During the sintering process, these agents will be burned out, and pores are formed. Since BURPS can be used for tape casting, scale-up manufacturing based on this method is feasible [108–110]. By controlling the additive size, the pore structure and size can also

be tuned. However, due to the aggressive burn-off associated with the volatile additive, fracture of the ceramic occurs, leading to decreased mechanical and ferroelectric properties. Therefore, a 60-70% porosity is obtainable (Figure 1.7b) [110].

Polymeric sponge. As a sacrificial template method, the sponge is combined with ceramic slip and then removed by sintering, contributing to a densified ceramic foam structure (Figure 1.7c) [111,112]. By stretching and clamping the ceramic-soaked sponge during sintering, the relative density of the foam can be tailored. Although this method is simple, incomplete sintering can result in the fracture of ceramic struts and reduce the structural integrity.

Freeze casting. The ceramic powders are first dissolved in a solvent with a dispersant to ensure uniform distribution. The solution is then cooled from one end to stimulate directional freezing of the solvent. During this process, the generated dendrites form the pore channels of the porous materials, consisting of the solidified ceramic particulates. The freezing solvent is then removed at low pressure to keep the shape of the unsintered ceramic [97,113–115]. The 3-1 and 2-2 cellular materials can be generated using this method (Figure 1.7d). In addition, the porosity and pore shapes can be controlled by altering the freezing agent, degree of undercooling, and ceramic particle size. Compared to BURPS, the porous ferroelectric ceramics fabricated by the freeze casting show a higher ferroelectric constant and permittivity.

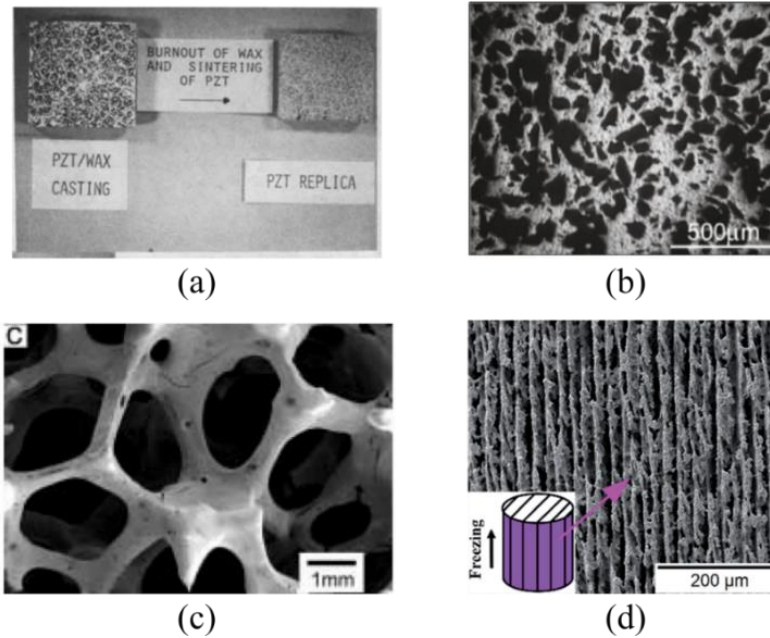


Figure 1.7 Microstructures of porous ferroelectric fabricated by: (a) Coral replamine, (b) BURPS, (c) Polymeric sponge, and (d) Freeze casting. (Figure 1.7a reprinted with permission from ref [107], copyright 2011 Taylor & Francis; Figure 1.7b reprinted with permission from ref [110], copyright 2003 IEEE; Figure 1.7c reprinted with permission from ref [112], copyright 1994 Taylor & Francis; Figure 1.7d adapted from ref [97] under the terms of CC BY-NC 3.0)

1.2.3 3D printing of cellular ferroelectric materials

Up to now, only simple 0-3, 1-3, 2-2, and 3-3 cellular ferroelectric metamaterials have been investigated and successfully manufactured by traditional fabrication methods mentioned in Chapter 1.2.2. However, ferroelectric metamaterials with complex lattice topologies, such as the mechanically-efficient octet truss, have not been explored; their fabrication is also impeded by the aforementioned traditional manufacturing methods.

Additive manufacturing, or so-called 3D printing, has recently been introduced as an efficient manufacturing method since the layer-by-layer printing method offers the manufacturing of samples, out of ceramics, polymers, and metals, without the limitation of the complexity of their topology [116]. Based on the printing mechanism, 3D printing technology can be classified as

fused deposition modeling (FDM) [117,118], stereolithography (SLA) [119,120], digital light processing (DLP) [121,122], direct writing (DW) [123,124], selective laser sintering (SLS) [125,126], and selective laser melting (SLM) [127,128] among the others. For ferroelectric materials, the polarization that exposes these ferroelectric materials to a high electric field is needed after/during the 3D printing process to align the spontaneous electrons along the polarization direction [129]. Figure 1.8 shows the most commonly used technologies for 3D printing of ferroelectric materials.

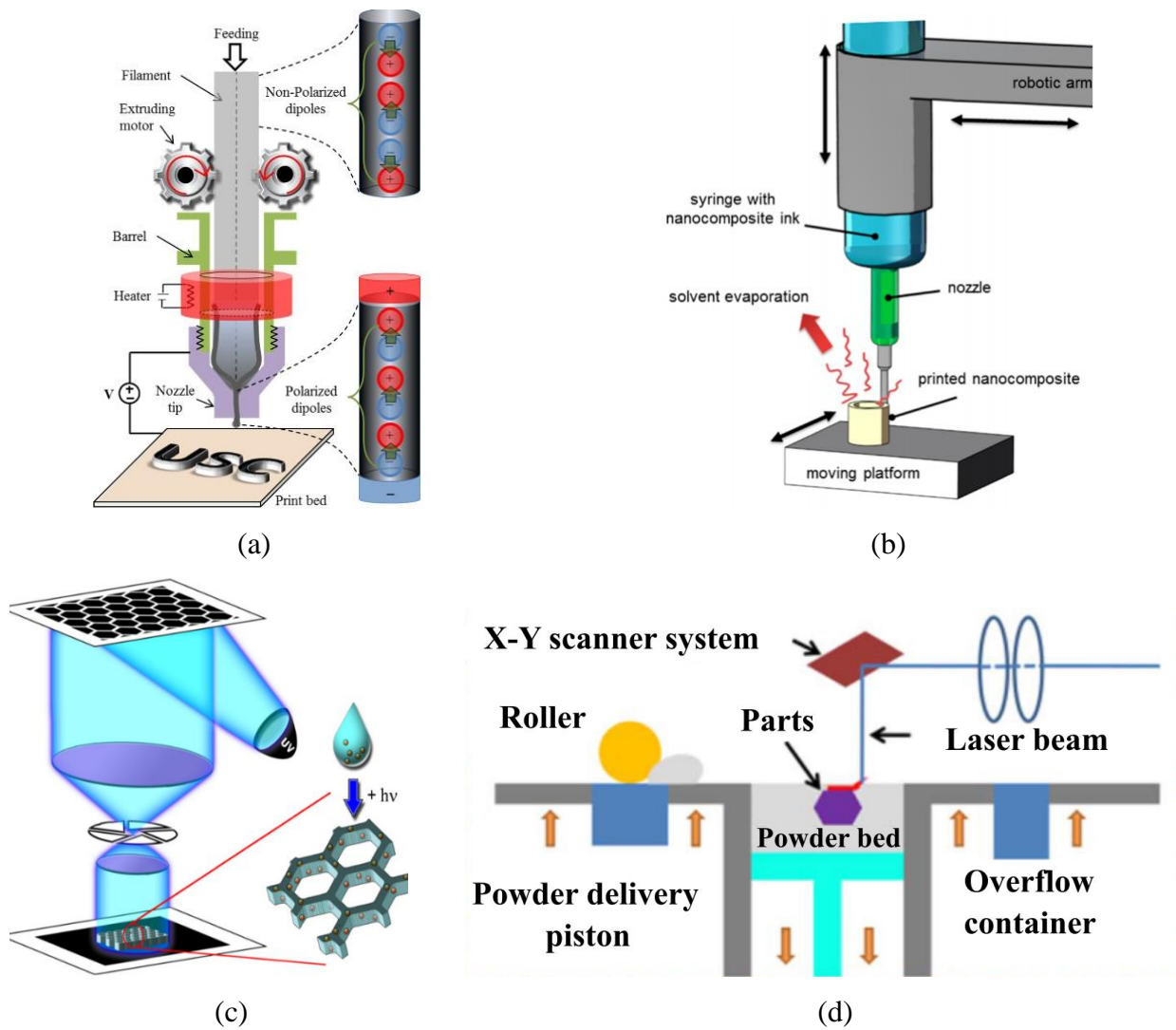


Figure 1.8. 3D printing technologies for the manufacturing of ferroelectric materials: (a) FDM, (b) DW, (c) DLP, and (d) SLS. (Figure 1.8a adapted from ref [130] under the terms of CC BY NC ND)

license; Figure 1.8b reprinted with permission from ref [131], copyright 2017 American Chemical Society; Figure 1.8c reprinted with permission from ref [132], copyright 2014 American Chemical Society; Figure 1.8d reprinted with permission from ref [133], copyright 2017 Elsevier)

Fused deposition modeling (FDM). Figure 1.8a shows the FDM-based Electric Poling assisted Additive Manufacturing (EPAM) or Integrated 3D Printing and Corona poling (IPC) method [130,134,135]. The ferroelectric PVDF polymer is produced in the form of 3D printing filaments with a diameter of 3 mm and then 3D printed by IPC technology. In the EPAM or IPC technology, a high electric field between the nozzle tip and printing bed is applied to polarize the PVDF filament during 3D printing. More specifically, the extruder and bed temperatures are around 230°C and 100°C, respectively. The extruder feed is 200mm/min, and the electric field is 3.0 MV/m. It should be mentioned that the stress induced by the movement of the leading nozzle further enhances the piezoelectric effect and could generate d_{31} of 4.8×10^{-2} pC/N [135]. However, the FDM printed samples suffer from low resolution [136] and nozzle clogging for some composite filaments [137].

Direct writing (DW). As shown in Figure 1.8b, the prepared printed liquid is poured into a syringe, and a pneumatically operating dispensing system is used to apply precise pressures for 3D printing ferroelectric PVDF nanocomposite structures [131,138–141]. The syringe is mounted on a robotic arm, and its movement can be controlled, leading to a similar 3D printing mechanism as FDM. In reference [131], the printed ferroelectric materials consisted of PVDF and barium titanate nanoparticles and were mixed with a solvent system of acetone (BDH) and dimethylformamide (DMF). Therefore, when the liquid was extruded from the nozzle, evaporation of the solvents provided the required rigidity to retain the designed architecture. It was reported that the 3D printed ferroelectric material possessed a ferroelectric coefficient d_{31} , of 18 pC/N.

Although the material preparation is simple, printing complex 3D truss-like lattice is difficult due to the failure of overhangs.

Digital light processing (DLP). DLP builds 3D structures by exposing a photolabile liquid to light and uses a digital projector screen to flash a single image of each layer across the entire platform at once (Figure 1.8c) [132,142–144]. Since ferroelectric materials are not photolabile, they are normally mixed with 3D printable photolabile resin. In reference [141], BaTiO₃ nanoparticles were embedded in a polyethylene glycol diacrylate (PEGDA) matrix. To enhance the stress transfer efficiency from matrix to BaTiO₃, some linker molecules, e.g., 3-trimethoxysilylpropyl methacrylate (TMSPM), are also added. It is found that the printing of 2D and 3D patterns can reach a resolution limit of around 5 μm with curved, adjoining, straight, and/or void regions, and the piezoelectric coefficients d_{33} can approach 40 pC/N. It is noted that there is a tradeoff between high-performance ferroelectric properties and printability, where high volume nanoparticles lead to high viscosity and lower curable depth.

Selective laser sintering (SLS). As shown in Figure 1.8d, a layer of ceramic powder or their composites is first deposited on the printing bed, and then a laser moves along the designed profile to form the sliced patterns. After completing the current layer, the bed moves down, and a roller distributes the powder uniformly among the bed surface. This process is repeated until the whole process is finished [133,145–147]. Through increasing the BaTiO₃ nanoparticles loading in the BT/PA11 composite system, the highest d_{33} is 4.7 pC/N achieved with 80 wt% [133]. One drawback of SLS is the low printing resolution and high cost.

Apart from the 3D printing process, poling process is an essential set for ferroelectric materials to obtain the piezoelectric and pyroelectric properties, which orientates the microscopic molecular dipoles along the field direction by applying an external electric field. Based on the contact of

poling electrode/needle and sample, there are two kinds of poling methods, i.e., contacting poling and corona poling [129]. As shown in Figure 1.9a, the contacting poling needs the physical contact of the electrode and the sample, which can generate a large electric field. Corona poling (Figure 1.9b), on the other hand, separates the poling needle and sample and the charges are generated around the sharp end point of the top electrode. Due to the electric field, these generated charges move to the surface of ceramics, and an electric field is created between the two surfaces of the samples. In this thesis, simple contact poling is used to pole the printed ceramics, which can provide high voltage for architected cellular materials.

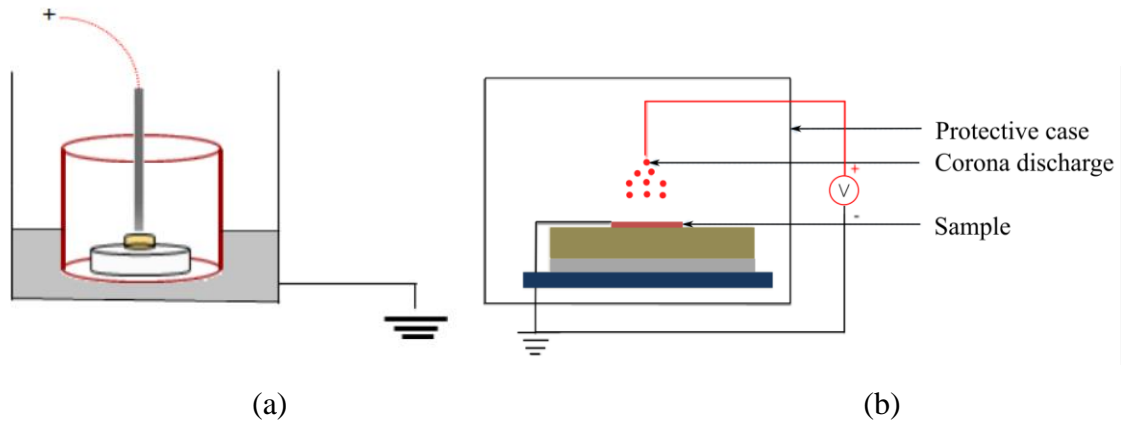


Figure 1.9 (a) Contact poling; (b) Corona poling. (Adapted from ref [129] under the terms of the CC BY 3.0 license.)

The engineering of cell topologies of cellular ferroelectric metamaterials may enhance their piezoelectric and pyroelectric properties. Further investigations on the relationship between pore topologies and ferroelectric properties can pave the way for obtaining unprecedented multifunctional multiphysical properties in smart lightweight materials. Therefore, this thesis focuses on the design, analysis, and manufacturing of architected cellular ferroelectric metamaterials aiming at improving their performance for applications as sensors, actuators, and mechanical/thermal energy harvesters. The microarchitectural design of the cellular ferroelectric

metamaterials may vary from simple two-dimensional (2D) pores to complex three-dimensional (3D) hierarchical lattices and shellulars; the analysis also spans different length scales. Finally, DLP 3D printing is used to fabricate high-performance lightweight multifunctional ferroelectric materials as a proof of concept for the new category of smart metamaterials. These developed cellular ferroelectric metamaterials can be used to develop sustainable energy harvesters collecting power from human body motion, building and bridge oscillations, vehicle vibrations, daily and industrial wasted heat, etc.

1.2.4 Multistable structure

Although ferroelectric materials are capable of multifunctionality through piezoelectric and pyroelectric effects, their properties cannot be changed after fabrication. Multistable ferroelectric materials provide a promising approach for developing reconfigurable intelligent structures and devices. Featuring two structurally stable states, bistable mechanical metamaterials are marked by their unique local minima of the elastic potential energy and exhibit snap-through/back behaviors with negative incremental stiffness (Figure 1.10a). Apart from the original state, bistable structures can rest in the second stable equilibrium state in the absence of an external load. This unique property makes them promising candidates for developing programmable structures [40–43] and enables their various applications in actuators [148], robotic arms [149], microelectromechanical systems (MEMS) [150], and energy harvesters [151]. At present, most of these rationally-designed materials are comprised of two pivotal elements, i.e., constrained inclined [44] or curved [45] (Figure 1.10b) beams and 3D shallow domes [46,152] (Figure 1.10c).

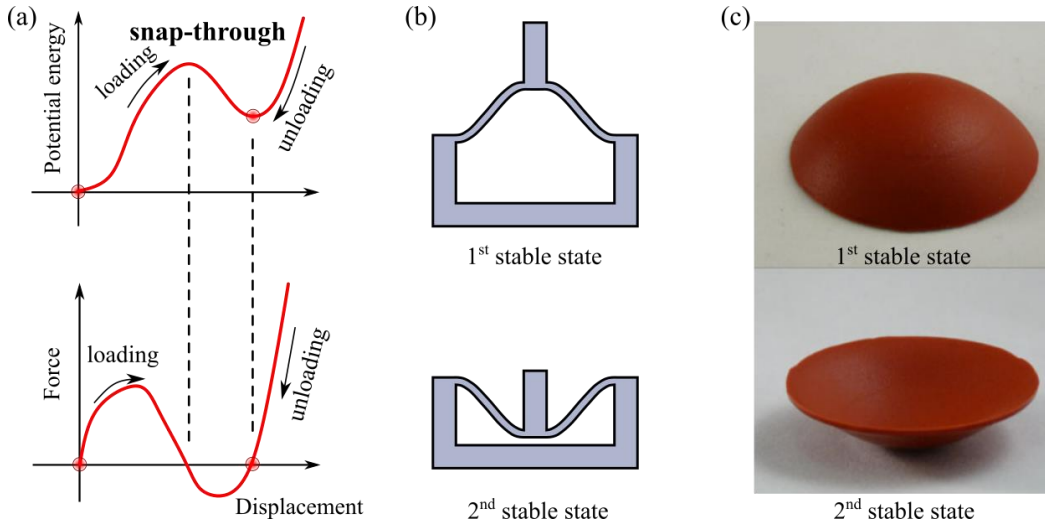


Figure 1.10 (a) Potential energy and force versus displacement curves in bistable materials and structures. (b) Bistable beams with two stable states. (c) Bistable shallow dome. (Adapted from ref [152] under the terms of the CC BY 4.0 license.)

Structural multistability can be simply realized by assembling these bistable elements in a form of 1D chains [153], 2D planar/cylindrical sheets [44,153,154], or 3D lattices [44,153,155]. By tailoring the topology of their underlying architectures, a series of multiphysical properties (e.g., elastic waves band gaps [156], strain energy entrapment [153], thermal expansion coefficient, and Poisson's ratio [154]) of the bi/multistable metamaterials can be tuned. Rapid shape changing triggered by external stimuli (e.g., water or solvent content [157] and temperature change [158]) is also viably realized in mechanical metamaterials fabricated by passive constitutive solids. Several design strategies for structural bi/multistability, including but not limited to creased cones [159], foldable origamis [160], waved sleeves [161], compliant hinges [160,162], multiple magnetic systems [163], and integrated granular particles and compliant stretchable components [164], have also been proposed for developing deployable structures with improved stiffness and durability. The motif or building blocks of these metamaterials (i.e., the fundamental region of the cell, which has more than one stable state, and from which the whole architecture can be built using various transformations) switch only between two stable configurations, and multistability

is achieved by utilizing an assembly of these bistable blocks. Exploiting 3D motifs with arbitrary stable configurations facilitates the realization of the deployable structures with multiple configurations.

Due to their highly nonlinear deformation behavior caused by their intriguing structural instability, elastic shells can be invoked to design multistable unit cells for mechanical metamaterials that can adapt themselves to loading conditions [165]. Conventional bistable (Figure 1.11a) or tristable shells (Figure 1.11b), e.g., half tennis ball [166] and Venus flytrap [167], display buckling [168] and snapping [152] configurations, determined by their curvature, prestress, and residual stress [165]. In addition, surface patterning, like corrugation [169] or varied thickness surfaces [152], can impose structural multistability in elastic shells. Although shells may serve as a promising design platform for discovering new structural elements, their complex nonlinear deformation modes and challenges associated with their tessellation to form mechanical metamaterials have impeded their applications in advanced multistable material design. Based on polyhedron templates and high degrees of freedom of soft hinges, assembled prismatic metamaterials can exhibit multistable behavior along multiple directions [170]; nevertheless, to the best of author's knowledge, none of the existing polyhedron-based multidirectional multistable cells can achieve simultaneous stable states along different directions, as their multidirectional stable states are not independent of each other, and the realization of a new stable state in one direction can break the multistability in other directions.

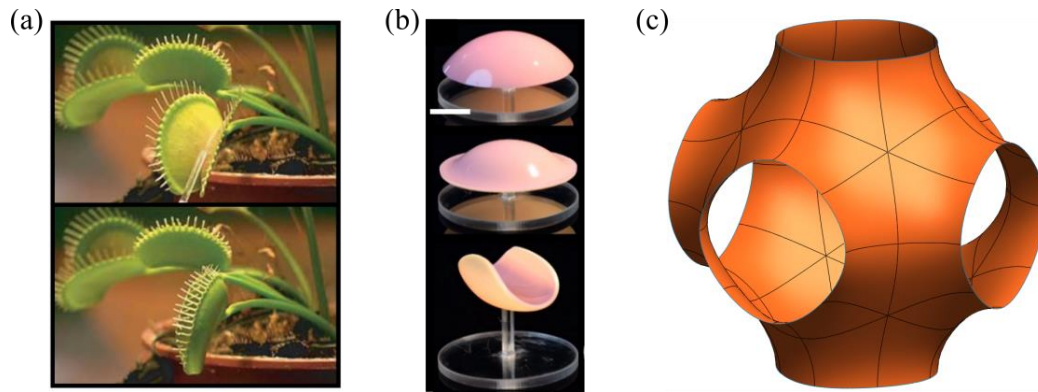


Figure 1.11 (a) Open and closed states of Venus flytrap. (b) Tristable spherical shell. (c) Schwarz P TPMS. (Figure 1.11a reprinted with permission from ref [167], Copyright © 2005, Macmillan Magazines Ltd; Figure 1.11b reprinted with permission from ref [165], Copyright 2018 American Physical Society)

As a new type of architected materials, shell-based cellular solids or *shellulars* (as a portmanteau word blending *shell* and *cellular*) are composed of periodic 3D unit cells of continuously smooth and curved thin shells [171] (Figure 1.11c). With less sensitivity to stress concentration and architectural defects than truss and plate-based cellular solids, shell-like metamaterials have shown promising potentials for achieving enhanced stiffness and strength [171–173], and extreme resilience [174] at ultralow relative density. While shellular metamaterials can be formed by any non-self-intersecting shell surface, they are commonly developed based on triply periodic minimal surfaces (TPMS), e.g., Schwarz P (Primitive), Schwarz D (Diamond), and Gyroid, in which *triply periodic* refers to periodicity in three directions, and *minimal surfaces* represents a locally minimum surface area for a given boundary [175]. TPMSs are intersection-free smooth surfaces with zero mean curvature at any point and they partition the space into two independent but intertwined continuous sub-volumes [175]. The geometric features of TPMSs hold great promise for creating shellular materials with unrivaled multifunctional properties, such as minimal stress concentration, high fluid permeability, and enhanced heat transfer, for a wide range of applications in bionic scaffolds [176,177], catalytic converters [178], heat exchanger

[179], ultrafiltration [180], and microbatteries [181]. Although the rapid snapping and fast closure of Venus flytrap [182] in the nature exemplifies the bistability of shell-like architectures, structural bi/multistability of shellulars with complex architectures are yet to be discovered; for Schwarz P shellular metamaterials, this thesis has introduced a novel perforation strategy to impart multistability. The realization of programmable and previously inaccessible deployable multistable shellulars can offer a new paradigm for advanced reconfigurable materials in the form of programmable shell-based multistable mechanical metamaterials for potential applications as soft robotic grippers/muscles, actuators, reusable energy absorbers, adaptive structures, and even sensors/actuators made of ferroelectric materials.

1.3 Research objectives

The general framework of the present study is to propose new kinds of smart cellular metamaterials and involves design, theoretical and computational analysis, and fabrication of both ferroelectric cellular materials and multistable shellulars. Theoretical methods to predict the effective multiphysical properties of ferroelectric cellular materials are first developed. Different cellular topologies, from simple 2D pores to complex 3D lattices along with their hierarchical counterparts, are investigated step by step to explore the potential of tailoring microarchitectures for achieving high-performance ferroelectric materials. With the assistance of machine learning, efficient analysis of a family of spinodoid ferroelectric structures is conducted to avoid computationally expensive massive homogenization cases; a strategy to select ferroelectric spinodoid metamaterials with desired properties is also developed based on machine learning. In addition, a 3D printing technology is adopted to fabricate the designed cellular ferroelectric materials, which is used to prove the effectiveness of the designed ferroelectric metamaterials. A novel strategy to design multistable mechanical metamaterials by introducing perforations on the shellular surface

is presented. A brief overview of the next chapters of this thesis is presented below to outline a comprehensive perspective of the conducted research.

Chapter 2 mainly focuses on the development of the homogenization method for predicting the multiphysical properties of cellular materials. The constitutive and governing equations of ferroelectric materials are first introduced, and then the basis of the asymptotic homogenization (AH) method for evaluating the multiphysical properties is derived. In addition, a multiscale asymptotic homogenization (MAH) method is proposed to calculate the effective properties of hierarchical cellular ferroelectric materials. The developed theoretical method here is the basis for the analysis in the following chapters.

In **Chapter 3**, a Fourier series expansion-based pore topology is used to construct 2D extruded cellular ferroelectric metamaterials. Their effective thermo-electro-mechanical properties are obtained by the AH method. It is demonstrated that piezoelectric and pyroelectric figures of merit of cellular ferroelectric metamaterials can be significantly improved by scaling and rotating the pore topologies and changing the polarization direction. Different design charts for ferroelectric properties are also developed to provide a broad view of feasible ferroelectric materials through tailoring their microarchitectures.

The ferroelectric properties of 3D hierarchical lattice ferroelectric metamaterials are analyzed in **Chapter 4**. Three families, including cubic, octahedron, and hybrid, of 3D hierarchical lattice ferroelectric metamaterials are considered. Based on the previously proposed multiscale asymptotic homogenization (MAH), the relationship between architecture and effective thermo-electro-mechanical properties is determined. The effect of hierarchical order, lattice topology, and relative density on piezoelectric and pyroelectric figures of merit assessing the performance of ferroelectric metamaterials as sensors and energy harvesters, is then explored. In addition, scaling

relationships for predicting the multiphysical behavior of ferroelectric metamaterials, covering the whole range of relative densities, are proposed.

A design motif to enhance multifunctional figures of merit of hierarchical cellular ferroelectric metamaterials is presented in **Chapter 5**. Six commonly used primitive cubic unit cells are investigated and both multiscale asymptotic homogenization and scaling relationships are proposed to predict the effective ferroelectric properties of hierarchical cellular metamaterials. A theoretical model that reveals the relationship between cellular ferroelectric materials and their multiphysical properties is created, consistent with the fitted scaling relationship. Based on the prediction methods, a comprehensive analysis of the influence of design parameters, e.g., hierarchical order, cell topologies, and relative density, on the effective ferroelectric figures of merit is conducted.

Machine learning-assisted design of ferroelectric spinodoid metamaterials is described in **Chapter 6**. Due to the tunable mechanical property space of spinodoid metamaterials, the spinodoid ferroelectric metamaterials are introduced in this chapter. Finite element homogenization is used to obtain the multiphysical properties of hundreds of randomly generated spinodoid structures. A machine learning technique, i.e., Multi-layer perceptron (MLP), is trained with these spinodoid metamaterials. Optimally selected spinodoid metamaterials are then selected through massive predicted results from the well-trained MLP. A 3D printing based on digital light processing is developed to fabricate and corroborate the high-performance of machine learning-assisted designed spinodoid ferroelectric metamaterials.

In **Chapter 7**, a new 3D multistable shellular metamaterial is designed by introducing delicate perforations on the surface of Schwarz's Primitive shellular. An elliptical perforation is first used to obtain mechanical bistability from the Primitive shellular. Multilayer staggered perforations are

then introduced to achieve multistable perforation shellular. The snap-through, snap-back behaviors, and self-contact of this multistable perforated shellular are further explored.

The last chapter is dedicated to summarizing the main conclusions and highlighting the outcomes of this thesis. The contributions to the knowledge of architected ferroelectrics and programmable multistable metamaterials are discussed, and a comprehensive discussion on the perspective and the future direction of the field of smart cellular materials is presented.

CHAPTER 2

Homogenization of cellular ferroelectric metamaterials

This chapter covers the numerical methods used throughout this dissertation for evaluating the multiphysical properties of cellular ferroelectric materials. The details related to the derivation of equations associated with the homogenization of cellular ferroelectric materials with hierarchical architectures are provided. The chapter is divided into three main sections, including constitutive and governing equations of ferroelectric materials, asymptotic homogenization, and multiscale asymptotic homogenization.

2.1 Constitutive and governing equations of ferroelectric materials

The constitutive equations of ferroelectric materials are derived by applying the principle of free energy. The Helmholtz free energy, F , can be written as follows [183,184]

$$F(\varepsilon_{ij}, E_i, \theta) = \frac{1}{2} C_{ijkl} \varepsilon_{kl} - e_{ijk} E_i \varepsilon_{jk} - \frac{1}{2} \kappa_{ij} E_i E_j - \lambda_{ij} \theta \varepsilon_{ij} + p_i E_i \theta - \frac{1}{2} c_T \theta^2 \quad (2.1)$$

where ε_{ij} , E_i and θ ($i, j, k, l=1,2,3$) are strain tensor, electric field vector, and temperature difference changing from reference temperature, respectively; C_{ijkl} , e_{kij} , κ_{ij} , λ_{ij} and p_i are, respectively, elastic, piezoelectric, dielectric, thermal-stress and primary pyroelectric coefficient

vectors; c_T is volume specific heat capacity and defined as c_E/θ_0 , where c_E is heat capacity and θ_0 is initial temperature.

Ferroelectric material with linear constitutive relation is considered in the present work. This implies constant material constants, and the constitutive relations can be written as

$$\sigma_{ij} = \frac{\partial F}{\partial \varepsilon_{ij}} = C_{ijkl} \varepsilon_{ij} - e_{ijk} E_k - \lambda_{ij} \theta \quad (2.2a)$$

$$D_i = -\frac{\partial F}{\partial E_i} = e_{ijk} \varepsilon_{jk} + \kappa_{ij} E_j - p_i \theta \quad (2.2b)$$

$$S = -\frac{\partial F}{\partial \theta} = \lambda_{ij} \varepsilon_{ij} + p_i E_i + c_T \theta \quad (2.2c)$$

where σ_{ij} , D_i and S ($i, j = 1, 2, 3$) are stress tensor, electric displacement vector, and entropy, respectively. For a reversible process, S can be derived from the second law of thermodynamics, namely

$$dS = dQ/\theta \quad (2.3)$$

where Q is the system absorbed heat.

Assuming no body force and volume charges, governing equations for the thermo-piezoelectric problems are [185–187]

$$\sigma_{ij,j} = \rho \ddot{u}_i \quad (2.4a)$$

$$D_{i,i} = 0 \quad (2.4b)$$

$$\rho(\theta \dot{S} - R) + q_{i,i} = 0 \quad (2.4c)$$

where ρ is density, u_i is displacement vector, and R is the heat produced per unit time and unit mass, and q_i is heat flux per unit area and per unit time; \dot{S} is the derivative of entropy with respect to time. Combining Eq. (2.4c) and Fourier's law for heat conduction, the relationship between temperature and entropy is

$$\rho(\theta \dot{S} - R) + (K_{ij} \theta_{,j})_{,j} = 0 \quad (2.5)$$

where K_{ij} is thermal conductivity.

Based on Eq. (2.5), for stationary linear thermo-electro-mechanical fields, $\dot{S} = 0$ and entropy have no influence on the temperature field, while the temperature can indirectly affect entropy by heat flux q_i (Eq. (2.4c)). The multiphysical relationship among these partly coupled stationary thermo-electro-mechanical fields is further described in Figure 2.1.

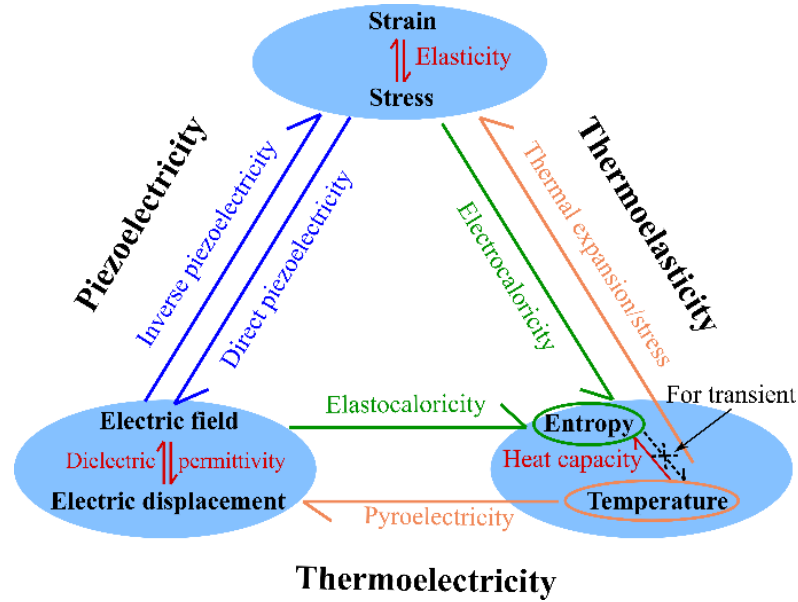


Figure 2.1 Partly coupled stationary thermo-piezoelectric fields. (Reprinted with permission from ref [188], copyright 2019 Elsevier)

As shown in Figure 2.1, electric/mechanical fields are fully coupled by piezoelectric/inverse piezoelectric effect; temperature affects electric field/displacement and strain/stress by pyroelectric effect and thermal expansion/stress, respectively. In addition, electric field and electric displacement have a mutual influence on each other, and it is also the same for strain and stress. Although temperature can affect the electric field, and mechanical field and both electric field and mechanical field have an influence on entropy, the variation of entropy has no influence on temperature. Therefore, for the stationary linear thermo-piezoelectric field, it is reasonable to keep the temperature field uncoupled from the mechanical/electrical fields, where Eqs. (2.2c) and

(2.4c) are neglected. Herein, effective thermo-piezoelectric properties are obtained on a stationary linear thermo-electro-mechanical field. Therefore, we assume mechanical and electric fields are coupled while the temperature field is not affected by the mechanical and electric fields; such analysis is so-called uncoupled thermo-piezoelectricity [185–187].

In linear piezoelectricity, strain tensor and electric field vector are related to mechanical displacement u_k and electric potential ϕ as:

$$\varepsilon_{kl} = \frac{1}{2} \left(\frac{\partial u_k}{\partial x_l} + \frac{\partial u_l}{\partial x_k} \right), \quad E_k = -\frac{\partial \phi}{\partial x_k} \quad (2.6)$$

The thermo-piezoelectric constants mentioned in Eq. (2.2) are defined as:

$\mathbf{C} = (\partial \boldsymbol{\sigma} / \partial \boldsymbol{\varepsilon})_{\mathbf{E}, \theta}$: Elastic tensor measured at constant electric field and temperature

$\mathbf{e} = (\partial \mathbf{D} / \partial \boldsymbol{\varepsilon})_{\mathbf{E}, \theta} = (-\partial \boldsymbol{\sigma} / \partial \mathbf{E})_{\boldsymbol{\varepsilon}, \theta}^T$: Piezoelectric tensor measured at constant electric field and temperature or at constant strain and temperature

$\boldsymbol{\kappa} = (\partial \mathbf{D} / \partial \mathbf{E})_{\boldsymbol{\varepsilon}, \theta}$: Dielectric permittivity tensor measured at constant strain and temperature

$\boldsymbol{\lambda} = (\partial \boldsymbol{\sigma} / \partial \theta)_{\boldsymbol{\varepsilon}, \mathbf{E}}$: Thermal stress tensor measured at constant strain and electric fields

$\mathbf{p} = (\partial \mathbf{D} / \partial \theta)_{\boldsymbol{\varepsilon}, \mathbf{E}}$: Pyroelectric tensor measured at constant strain and electric fields

In this section, bold symbols are used for tensors or matrices, bold italic symbols stand for vectors, superscript T denotes transposition, and the subscripts following the partial derivatives indicate the fields are constant during the measurement of the thermo-piezoelectric moduli.

The aforementioned fourth-ranked elastic tensor and third-ranked piezoelectric tensor can be simplified with Voigt notation, which uses the following mapping of adjacent indices: 11→1, 22→2, 33→3, 23→4, 13→5, 12→6. Correspondingly, Eq. (2.2) can be rewritten in a compact form as:

$$\boldsymbol{\Sigma} = \mathbf{E}\mathbf{Z} - \boldsymbol{\Pi}\theta \quad (2.7)$$

where $\boldsymbol{\Sigma} = (\sigma_1 \sigma_2 \sigma_3 \sigma_4 \sigma_5 \sigma_6 D_1 D_2 D_3)^T$, $\mathbf{Z} = (\varepsilon_1 \varepsilon_2 \varepsilon_3 \varepsilon_4 \varepsilon_5 \varepsilon_6 E_1 E_2 E_3)^T$, $\boldsymbol{\Pi} = (\lambda_1 \lambda_2 \lambda_3 \lambda_4 \lambda_5 \lambda_6 p_1 p_2 p_3)^T$ and

$$\mathbf{E} = \begin{bmatrix} C_{11} & C_{12} & C_{13} & C_{14} & C_{15} & C_{16} & e_{11} & e_{12} & e_{13} \\ \cdot & C_{22} & C_{23} & C_{24} & C_{25} & C_{26} & e_{21} & e_{22} & e_{23} \\ \cdot & \cdot & C_{33} & C_{34} & C_{35} & C_{36} & e_{31} & e_{32} & e_{33} \\ \cdot & \cdot & \cdot & C_{44} & C_{45} & C_{46} & e_{41} & e_{42} & e_{43} \\ \cdot & \cdot & \cdot & \cdot & C_{55} & C_{56} & e_{51} & e_{52} & e_{53} \\ \cdot & \cdot & \cdot & \cdot & \cdot & C_{66} & e_{61} & e_{62} & e_{63} \\ e_{11} & e_{21} & e_{31} & e_{41} & e_{51} & e_{61} & -\kappa_{11} & -\kappa_{21} & -\kappa_{31} \\ e_{21} & e_{22} & e_{23} & e_{24} & e_{25} & e_{26} & \cdot & -\kappa_{22} & -\kappa_{23} \\ e_{31} & e_{32} & e_{33} & e_{34} & e_{35} & e_{36} & \cdot & \cdot & -\kappa_{33} \end{bmatrix} \quad (2.8)$$

In Eq. (2.8), (\cdot) represents symmetric elastic, piezoelectric, and dielectric coefficients about the main diagonal of \mathbf{E} matrix. Therefore, 54 material constants (21 elastic, 18 piezoelectric, 6 permittivity, 6 thermal stress and 3 primary pyroelectric constants) are needed to describe the properties of the thermo-piezoelectric materials. In order to give more thermal-related properties, for the analysis below, the common alternative form of thermal-related coefficients, i.e., thermal expansion coefficients Δ_{ij} and total pyroelectric coefficients γ_i , are also used, which are calculated by [51]:

$$\boldsymbol{\Lambda} = \mathbf{E}^{-1} \boldsymbol{\Pi} \quad (2.9)$$

where $\boldsymbol{\Lambda} = (\Delta_{11} \Delta_{22} \Delta_{33} \Delta_{23} \Delta_{13} \Delta_{12} \gamma_1 \gamma_2 \gamma_3)^T$.

The governing equations of the thermo-piezoelectric materials are defined as [55]:

$$\nabla \cdot \boldsymbol{\sigma} + \mathbf{b} = 0 \quad (2.10a)$$

$$\nabla \cdot \mathbf{D} - q = 0 \quad (2.10b)$$

$$\nabla \cdot \mathbf{q} - R = 0 \quad (2.10c)$$

where \mathbf{b} is body force, q is free charge, \mathbf{q} is heat flux vector.

In order to assess the performance of devices made from piezoelectric materials, four figures of merit for piezoelectric applications (i.e., piezoelectric coupling constant (k_t), acoustic impedance (Z), piezoelectric charge coefficient (d_h), and hydrostatic figure of merit ($d_h \times g_h$)) and three figures of merit for pyroelectric applications, (i.e., current responsivity (F_I), voltage responsivity (F_V) and pyroelectric energy harvesting figure of merit (F_E')) are discussed [38, 56].

Piezoelectric coupling constant: The piezoelectric coupling constant, $k_t = (1 - C_{33}/C_{33}^D)^{0.5}$, describes the efficiency of energy conversion between the electrical domain and mechanical domain. For energy harvesting and biomedical imaging applications, higher k_t is desirable.

Acoustic impedance: The acoustic impedance, $Z = (\rho^* C_{33}^D)^{0.5}$, represents the overall acoustic load at the interface between a device (e.g., hydrophone) and its surrounding aqueous environment, where ρ^* is effective density and $C_{33}^D = C_{33} + (e_{33})^2/\kappa_{33}$. For underwater acoustic transducers or hydrophones, lower Z means better performance.

Hydrostatic charge coefficient: The hydrostatic (or piezoelectric) charge coefficient, $d_h = d_{33} + d_{31} + d_{32}$, assesses the conversion of mechanical loads (under hydrostatic loading) to electrical signals. Therefore, higher d_h will enhance hydrophone device sensitivity to detect sound. It should be mentioned that the piezoelectric strain coefficient (d_{nkl}) is related to the piezoelectric coefficient (e_{nij}) as: $e_{nij} = d_{nkl} \cdot C_{klij}$.

Hydrostatic figure of merit: The hydrostatic figure of merit, $d_h \times g_h$, defines the ability of a hydrophone device to identify and distinguish a signal from the ambient background noise. Here, the hydrostatic voltage coefficient, g_h , is given by d_h/κ_{33}^σ , where $\kappa^\sigma = \kappa + \mathbf{e}^T \mathbf{C}^{-1} \mathbf{e}$, and larger $d_h \times g_h$ means higher signal-to-noise ratio.

Voltage responsivity and *Current responsivity*: For heat and infrared (IR) detection, which is based on the generation of maximum current or voltage for given thermal energy input, higher voltage responsivity (F_I) and current responsivity (F_V) improve the device sensitivity:

$$F_I = \frac{P_3}{c_E} = \frac{P_3}{\rho \cdot c_p}, \quad F_V = \frac{P_3}{c_E \cdot \kappa_{33}^\sigma} = \frac{P_3}{\rho \cdot c_p \cdot \kappa_{33}^\sigma} \quad (2.11)$$

where c_p is specific heat capacity.

Pyroelectric energy harvesting figure of merit: The pyroelectric energy harvesting figure of merit, F_E' , indicates the thermal energy density generated by a given thermal input and can be seen as the product of F_I and F_V , namely:

$$F_E' = \frac{P_3^2}{c_E^2 \cdot \kappa_{33}^\sigma} \quad (2.12)$$

2.2 Asymptotic homogenization (AH)

Cellular ferroelectric metamaterials are considered advanced periodic structural elements with optimized multifunctional properties commonly used for application in meso and macro scales. However, detailed numerical simulation of structures made of many cells of ferroelectric metamaterials is a cumbersome task since it is very expensive computationally. One of the most efficient approaches for predicting the overall multiphysical properties of heterogeneous advanced architected materials with engineered microstructures is to analyze their representative volume elements (RVE) (see Figure 2.2a) and obtain a macroscopic homogenous medium equivalent to the original heterogeneous microstructure using homogenization techniques [103,104]. Two widely adopted homogenization techniques are: asymptotic homogenization (AH) and standard method (SM) or the so-called finite element method. In this thesis, AH is used to predict the effective thermo-electro-mechanical properties of the architected cellular ferroelectric metamaterials. In contrast to SM homogenization, AH has a well-developed mathematical

foundation that enables to extend this multiscale homogenization technique to other coupled multiphysical fields.

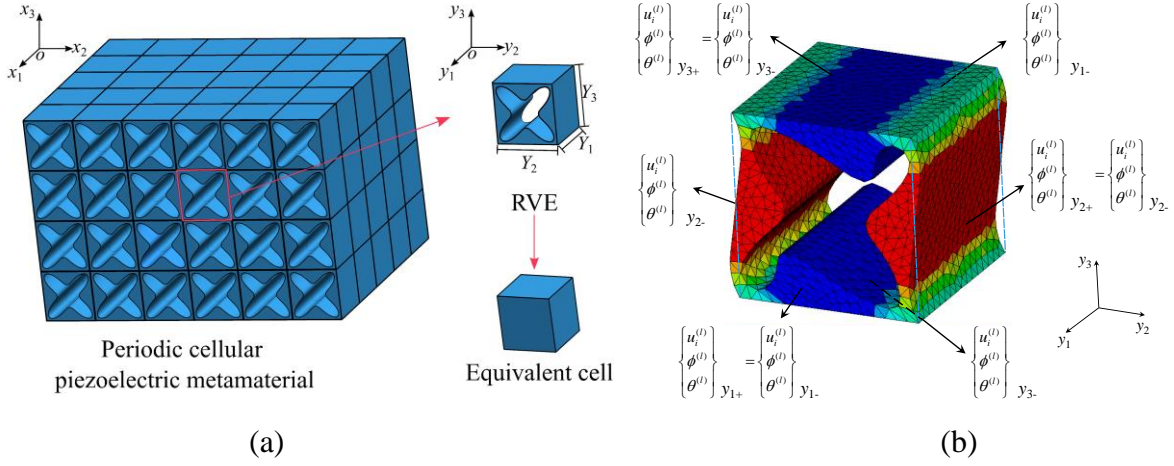


Figure 2.2 Schematic figure of (a) homogenization process and (b) periodic boundary conditions. (Reprinted with permission from ref [188], copyright 2019 Elsevier)

As shown in Figure 2.2a, there are two distinct scales in this periodic structure. The first one is the macroscopic scale with a coordinate of $\{O, x_1, x_2, x_3\}$ and the other one is the microscopic scale with a coordinate of $\{O, y_1, y_2, y_3\}$; $\eta (\ll 1)$ is a magnification factor and $y_i = x_i/\eta$. In microscopic coordinate, RVE is \mathbf{Y} -periodic with $\mathbf{Y} = (Y_1, Y_2, Y_3)$. Based on asymptotic expansion in powers of macroscopic scale x and microscopic scale y , thermo-electro-mechanical fields can be determined by:

$$\begin{aligned}
 u_i^* &= u_i \left(\mathbf{x}, \mathbf{y} = \frac{\mathbf{x}}{\eta} \right) = \sum_{l=0}^{+\infty} \eta^l u_i^{(l)}(\mathbf{x}, \mathbf{y}) = u_i^{(0)}(\mathbf{x}, \mathbf{y}) + \eta u_i^{(1)}(\mathbf{x}, \mathbf{y}) + O(\eta^2) \\
 \phi^* &= \phi \left(\mathbf{x}, \mathbf{y} = \frac{\mathbf{x}}{\eta} \right) = \sum_{l=0}^{+\infty} \eta^l \phi^{(l)}(\mathbf{x}, \mathbf{y}) = \phi^{(0)}(\mathbf{x}, \mathbf{y}) + \eta \phi^{(1)}(\mathbf{x}, \mathbf{y}) + O(\eta^2) \\
 \theta^* &= \theta \left(\mathbf{x}, \mathbf{y} = \frac{\mathbf{x}}{\eta} \right) = \sum_{l=0}^{+\infty} \eta^l \theta^{(l)}(\mathbf{x}, \mathbf{y}) = \theta^{(0)}(\mathbf{x}, \mathbf{y}) + \eta \theta^{(1)}(\mathbf{x}, \mathbf{y}) + O(\eta^2)
 \end{aligned} \tag{2.13}$$

where superscript ‘*’ represents dependency on the size of the RVE of inhomogeneity; $u_i^{(l)}$, $\phi^{(l)}$, $\theta^{(l)}$ are \mathbf{Y} -periodic with respect to the microscopic coordinate. Therefore, in Figure 2.2b, the

displacement, voltage, and temperature in two opposite faces are the same. In addition, within the same material, the stiffness tensor \mathbf{C}^* , piezoelectric tensor \mathbf{e}^* , dielectric permittivity tensor $\boldsymbol{\kappa}^*$, thermal stress tensor $\boldsymbol{\lambda}^*$ and pyroelectric tensor \mathbf{p}^* are also \mathbf{Y} -periodic but independent of macroscopic scale, namely $\mathbf{C}^*(\mathbf{x}, \mathbf{y}) = \mathbf{C}(\mathbf{y})$, $\mathbf{e}^*(\mathbf{x}, \mathbf{y}) = \mathbf{e}(\mathbf{y})$, $\boldsymbol{\kappa}^*(\mathbf{x}, \mathbf{y}) = \boldsymbol{\kappa}(\mathbf{y})$, $\boldsymbol{\lambda}^*(\mathbf{x}, \mathbf{y}) = \boldsymbol{\lambda}(\mathbf{y})$ and $\mathbf{p}^*(\mathbf{x}, \mathbf{y}) = \mathbf{p}(\mathbf{y})$. Based on the chain rule and the relationship between macroscopic and microscopic scales, we can write:

$$\frac{\partial}{\partial x_i} \rightarrow \frac{\partial}{\partial x_i} + \frac{1}{\eta} \frac{\partial}{\partial y_i} = \frac{\partial}{\partial x_i} + \frac{1}{\eta} (\cdot)_{,i} \quad (2.14)$$

Due to the arbitrary value of η , after substituting Eqs. (2.14) and (2.13) into Eq. (2.10a), the governing differential equation of the mechanical field can be expanded and rearranged with the same order of η as:

$$\eta^{-2} : \left(\mathbf{C}_{ijkl}^* \mathbf{u}_{k,l}^{(0)} \right)_j + \left(\mathbf{e}_{ijk}^* \phi_{,k}^{(0)} \right)_j = 0 \quad (2.15a)$$

$$\eta^{-1} : \left[\mathbf{C}_{ijkl}^* \left(\frac{\partial \mathbf{u}_k^{(0)}}{\partial x_l} + \mathbf{u}_{k,l}^{(1)} \right) \right]_{,j} + \frac{\partial}{\partial x_j} \left(\mathbf{C}_{ijkl}^* \mathbf{u}_{k,l}^{(0)} \right) + \left[\mathbf{e}_{ijk}^* \left(\frac{\partial \phi^{(0)}}{\partial x_k} + \phi_{,k}^{(1)} \right) \right]_{,j} + \frac{\partial}{\partial x_j} \left(\mathbf{e}_{ijk}^* \phi_{,k}^{(0)} \right) - \left(\lambda_{ij} \theta^{(0)} \right)_{,j} = 0 \quad (2.15b)$$

$$\eta^0 : \left[\mathbf{C}_{ijkl}^* \left(\frac{\partial \mathbf{u}_k^{(1)}}{\partial x_l} + \mathbf{u}_{k,l}^{(2)} \right) \right]_{,j} + \frac{\partial}{\partial x_j} \left[\mathbf{C}_{ijkl}^* \left(\frac{\partial \mathbf{u}_k^{(0)}}{\partial x_l} + \mathbf{u}_{k,l}^{(1)} \right) \right] + \left[\mathbf{e}_{ijk}^* \left(\frac{\partial \phi^{(1)}}{\partial x_k} + \phi_{,k}^{(2)} \right) \right]_{,j} + \frac{\partial}{\partial x_j} \left[\mathbf{e}_{ijk}^* \left(\frac{\partial \phi^{(0)}}{\partial x_k} + \phi_{,k}^{(1)} \right) \right] - \lambda_{ij} \frac{\partial \theta^{(0)}}{\partial x_j} - \left(\lambda_{ij} \theta^{(1)} \right)_{,j} + b_i = 0 \quad (2.15c)$$

Analogously, the following three equations can be extracted from Eq. (2.10b):

$$\eta^{-2} : \left(\mathbf{e}_{ikl}^* \mathbf{u}_{k,l}^{(0)} \right)_i - \left(\boldsymbol{\kappa}_{ij}^* \phi_{,j}^{(0)} \right)_i = 0 \quad (2.16a)$$

$$\eta^{-1} : \left[e_{ikl}^* \left(\frac{\partial u_k^{(0)}}{\partial x_l} + u_{k,l}^{(1)} \right) \right]_{,i} + \frac{\partial}{\partial x_i} \left(e_{ikl}^* u_{k,l}^{(0)} \right) - \left[\kappa_{il}^* \left(\frac{\partial \phi^{(0)}}{\partial x_l} + \phi_{,l}^{(1)} \right) \right]_{,i} - \frac{\partial}{\partial x_i} \left(\kappa_{il}^* \phi_{,l}^{(0)} \right) - (p_i \theta^{(0)})_{,i} = 0 \quad (2.16b)$$

$$\begin{aligned} \eta^0 : & \left[e_{ikl}^* \left(\frac{\partial u_k^{(1)}}{\partial x_l} + u_{k,l}^{(2)} \right) \right]_{,i} + \frac{\partial}{\partial x_i} \left[e_{ikl}^* \left(\frac{\partial u_k^{(0)}}{\partial x_l} + u_{k,l}^{(1)} \right) \right] - \left[\kappa_{il}^* \left(\frac{\partial \phi^{(1)}}{\partial x_l} + \phi_{,l}^{(2)} \right) \right]_{,i} \\ & - \frac{\partial}{\partial x_i} \left[\kappa_{il}^* \left(\frac{\partial \phi^{(0)}}{\partial x_l} + \phi_{,l}^{(1)} \right) \right] - p_i \frac{\partial \theta^{(0)}}{\partial x_i} - (p_i \theta^{(1)})_{,i} - q = 0 \end{aligned} \quad (2.16c)$$

In Eqs. (2.15a) and (2.16a), only mechanical and electric fields are involved. Referring to the governing equations of coupled fields in the thermo-piezoelectric medium (Eq. (2.10)), $u_i^{(0)}$ and $\phi^{(0)}$ are displacement and electric potentials of the coupled electro-mechanical fields within RVE without any applied force and electric field. Therefore, $u_i^{(0)}$ and $\phi^{(0)}$ remain constant in the microscopic scale and only depends on the macroscopic scale:

$$u_i^{(0)}(\mathbf{x}, \mathbf{y}) = U_i(\mathbf{x}) \text{ and } \phi^{(0)}(\mathbf{x}, \mathbf{y}) = \Phi(\mathbf{x}) \quad (2.17)$$

Similarly, in the temperature field, $\theta^{(0)}$ is also the macroscopic temperature and

$$\theta^{(0)}(\mathbf{x}, \mathbf{y}) = \Theta(\mathbf{x}) \quad (2.18)$$

Based on Eqs. (2.17) and (2.18), Eqs. (2.15b) and (2.16b) can be rewritten at the order of η^{-1} :

$$\begin{aligned} & \left(C_{ijkl}^* u_{k,l}^{(1)} \right)_{,j} + C_{ijkl}^* \frac{\partial U_k}{\partial x_l} + \left(e_{kij}^* \phi_{,k}^{(1)} \right)_{,j} + e_{ijk}^* \frac{\partial \Phi}{\partial x_k} - (\lambda_{ij} \theta^{(0)})_{,j} = 0 \\ & \left(e_{ikl}^* u_{k,l}^{(1)} \right)_{,i} + e_{ikl}^* \frac{\partial U_k}{\partial x_l} - \left(\kappa_{il}^* \phi_{,l}^{(1)} \right)_{,i} - \kappa_{il}^* \frac{\partial \Phi}{\partial x_l} - (p_i \theta^{(0)})_{,i} = 0 \end{aligned} \quad (2.19)$$

In Eq. (2.19), the first-order terms $u_i^{(1)}$, and $\phi^{(1)}$ represent the microscale fluctuations in mechanical displacement and electric potential and are related to macroscopic temperature change Θ , mechanical displacement U_i , and electric potential Φ as:

$$\begin{aligned}
u_k^{(1)}(\mathbf{x}, \mathbf{y}) &= MU_k^{mn}(\mathbf{y}) \frac{\partial U_m(\mathbf{x})}{\partial x_n} + M\Phi_k^n(\mathbf{y}) \frac{\partial \Phi(\mathbf{x})}{\partial x_n} + M\Theta_k(\mathbf{y}) \Theta(\mathbf{x}) \\
\phi^{(1)}(\mathbf{x}, \mathbf{y}) &= NU^{mn}(\mathbf{y}) \frac{\partial U_m(\mathbf{x})}{\partial x_n} + N\Phi^n(\mathbf{y}) \frac{\partial \Phi(\mathbf{x})}{\partial x_n} + N\Theta(\mathbf{y}) \Theta(\mathbf{x})
\end{aligned} \tag{2.20}$$

where $m, n = 1, 2, 3$ and these six kinds of functions MU_k^{mn} , $M\Phi_k^n$, $M\Theta_k$, NU^{mn} , $N\Phi^n$, and $M\Theta$ only depend on the microscopic scale. It should be mentioned that since $u_k^{(1)}(\mathbf{x}, \mathbf{y})$ and $\phi^{(1)}(\mathbf{x}, \mathbf{y})$ are \mathbf{Y} -periodic functions, MU_k^{mn} , $M\Phi_k^n$, $M\Theta_k$, NU^{mn} , $N\Phi^n$, and $M\Theta$ are also periodic. For the AH method, an important step is to obtain these six kinds of functions to express microscale fluctuation terms ($u_k^{(1)}(\mathbf{x}, \mathbf{y})$ and $\phi^{(1)}(\mathbf{x}, \mathbf{y})$) by the macroscopic field (U_i , Φ and Θ). Inserting Eq. (2.20) into Eq. (2.19) and rearranging these terms based on the derivation of the macroscopic field, three kinds of differential equation sets can be obtained. Since these three kinds of differential equations are only related to RVE, they are also called local problems, and the aforementioned six unknown functions are the solutions to these local problems. In particular, MU_k^{mn} and NU^{mn} are the solutions to the following local mechanical problem:

$$\begin{cases}
C_{ijkl}^* MU_{k,l}^{mn} + e_{kij}^* NU_{,k}^{mn} + C_{ijmn}^* = 0 \\
e_{ikl}^* MU_{k,l}^{mn} - \kappa_{il}^* NU_{,l}^{mn} + e_{mni}^* = 0 \\
\|MU_k^{mn}\| = 0 \quad \text{on } S \\
\|NU^{mn}\| = 0 \quad \text{on } S
\end{cases} \tag{2.21}$$

where double bar notation $\|f\|$ denotes the difference of function f between two opposite faces S , i.e., $\|f\| = f_{y_{i+}} - f_{y_{i-}}$, which guarantees the periodicity of the solution. In addition, for bi-material RVE, S includes the interface between the two different materials.

Similarly, $M\Phi_k^n$ and $N\Phi^n$ are determined by the following local electrical problem:

$$\begin{cases} C_{ijkl}^* M \Phi_{k,l}^n + e_{kij}^* N \Phi_{,k}^n + e_{ijn}^* = 0 \\ e_{ikl}^* M \Phi_{k,l}^n - \kappa_{il}^* N \Phi_{,l}^n - \kappa_{in}^* = 0 \\ \|M \Phi_k^n\| = 0 \quad \text{on S} \\ \|N \Phi^n\| = 0 \quad \text{on S} \end{cases} \quad (2.22)$$

and $M \Theta_k$ and $N \Theta$ are defined by the following local thermal problem:

$$\begin{cases} C_{ijkl}^* M \Theta_{k,l} + e_{kij}^* N \Theta_{,k} - \lambda_{ij} = 0 \\ e_{ikl}^* M \Theta_{k,l} - \kappa_{il}^* N \Theta_{,l} - p_i = 0 \\ \|M \Theta\| = 0 \quad \text{on S} \\ \|N \Theta\| = 0 \quad \text{on S} \end{cases} \quad (2.23)$$

In the order of η^0 , substituting Eq. (2.20) into Eqs. (2.15c) and (2.16c) and integrating it over the RVE, considering the Y-periodicity of $u_k^{(2)}$ and $\phi^{(2)}$, the following macroscopic constitutive equations are obtained:

$$\begin{aligned} & \left\langle C_{ijmn}^* + C_{ijkl}^* M U_{k,l}^{mn} + e_{ijl}^* N U_{,l}^{mn} \right\rangle \frac{\partial^2 U_m}{\partial x_j \partial x_n} + \left\langle e_{ijn}^* + C_{ijkl}^* M \Phi_{k,l}^n + e_{ijl}^* N \Phi_{,l}^n \right\rangle \frac{\partial^2 \Phi}{\partial x_j \partial x_n} - \\ & \left\langle \lambda_{ij}^* - C_{ijkl}^* M \Theta_{k,l} - e_{ijl}^* N \Theta_{,l} \right\rangle \frac{\partial \Theta}{\partial x_j} + b_i = 0 \end{aligned} \quad (2.24a)$$

$$\begin{aligned} & \left\langle e_{imn}^* + e_{ikl}^* M U_{k,l}^{mn} - \kappa_{il}^* N U_{,l}^{mn} \right\rangle \frac{\partial^2 U_m}{\partial x_i \partial x_n} - \left\langle \kappa_{in}^* - e_{ikl}^* M \Phi_{k,l}^n + \kappa_{il}^* N \Phi_{,l}^n \right\rangle \frac{\partial^2 \Phi}{\partial x_i \partial x_n} - \\ & \left\langle p_i^* - e_{ikl}^* M \Theta_{k,l} + \kappa_{il}^* N \Theta_{,l} \right\rangle \frac{\partial \Theta}{\partial x_i} - q = 0 \end{aligned} \quad (2.24b)$$

where $\langle (\cdot) \rangle = \frac{1}{V_\Omega} \int_\Omega (\cdot) dV$ and V_Ω is the volume of RVE. The corresponding effective stiffness tensor $\bar{\mathbf{C}}$, piezoelectric tensor $\bar{\mathbf{e}}$, dielectric permittivity tensor $\bar{\mathbf{\kappa}}$, thermal stress tensor $\bar{\boldsymbol{\lambda}}$ and pyroelectric $\bar{\mathbf{p}}$ are:

$$\begin{aligned}
\overline{C_{ijmn}} &= \langle C_{ijmn}^* + C_{ijkl}^* M U_{k,l}^{mn} + e_{ijl}^* N U_{,l}^{mn} \rangle \\
\overline{e_{ijn}} &= \langle e_{ijn}^* + C_{ijkl}^* M \Phi_{k,l}^n + e_{ijl}^* N \Phi_{,l}^n \rangle \\
\overline{\kappa_{in}} &= \langle \kappa_{in}^* - e_{ikl}^* M \Phi_{k,l}^n + \kappa_{il}^* N \Phi_{,l}^n \rangle \\
\overline{\lambda_{ij}} &= \langle \lambda_{ij}^* - C_{ijkl}^* M \Theta_{k,l} - e_{ijl}^* N \Theta_{,l} \rangle \\
\overline{p_i} &= \langle p_i^* - e_{ikl}^* M \Theta_{k,l} + \kappa_{il}^* N \Theta_{,l} \rangle
\end{aligned} \tag{2.25}$$

Using the expression provided in Eq. (2.7), the effective properties can be rewritten as

$$\overline{\mathbf{E}} = \langle \mathbf{E} + \mathbf{E}\mathbf{M} \rangle, \quad \overline{\mathbf{I}\mathbf{T}} = \langle \mathbf{I}\mathbf{T} - \mathbf{E}\mathbf{N} \rangle \tag{2.26}$$

where $\mathbf{M} = [\mathbf{M}\mathbf{u}, \mathbf{M}\boldsymbol{\phi}; \mathbf{N}\mathbf{u}, \mathbf{N}\boldsymbol{\phi}]$ and $\mathbf{N} = [\mathbf{M}\boldsymbol{\theta}; \mathbf{N}\boldsymbol{\theta}]$ with $M u_{klmn} = M U_{k,l}^{mn}$, $M \phi_{kln} = M \Phi_{k,l}^n$, $N u_{mnl} = N U_{,l}^{mn}$, $N \phi_{ln} = N \Phi_{,l}^n$, $M \theta_{kl} = M \Theta_{k,l}$ and $N \theta_{l} = N \Theta_{,l}$. It can be found from Eq. (2.26) that the effective properties for both coupled thermo-electro-mechanical field and single mechanical field share similar expressions based on the AH method [97].

The accuracy of the developed methodology is verified in Figure 2.3, where the calculated results are compared with those provided in the references [189–191]. In reference [190], different 3D lattice structures, e.g., octet truss, are considered, and their mechanical properties are analyzed both experimentally and theoretically. Reference [191] presented the experimental results of a 1-3 piezocomposite, while Reference [189] conducted the theoretical analysis for the same model. Figure 2.3 shows the comparison between the present results and those reported in the references. It can be seen that there is no difference between our results and theoretical results in reference [189,190]; all the theoretical results are also in excellent agreement with the experimental data [191].

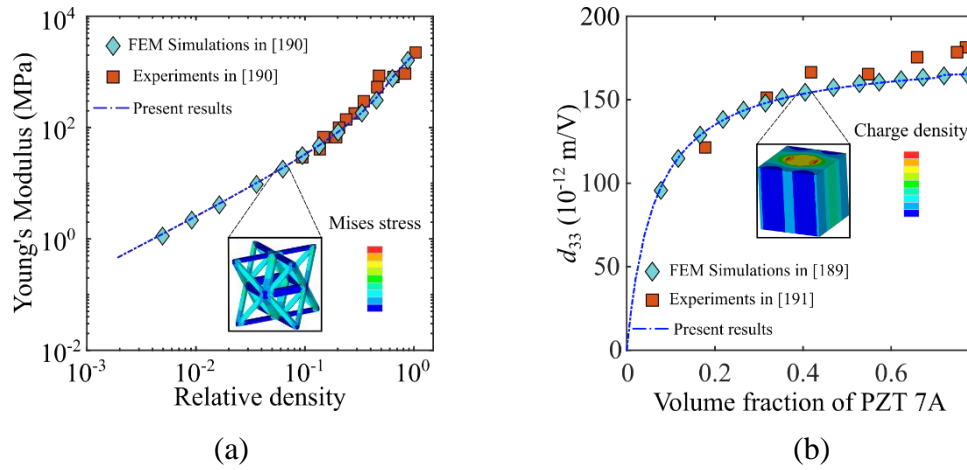


Figure 2.3 Comparison between present results and those provided in [189–191]: (a) Effective Young’s modulus of octet truss made of polymer and (b) Effective piezoelectric charge constant, d_{33} , of a smart composite material. (Reprinted with permission from ref [188], copyright 2019 Elsevier)

2.3 Multiscale asymptotic homogenization (MAH)

Hierarchical cellular ferroelectric metamaterials can be considered as ultralight periodic smart structural elements with optimized multifunctional properties consisting of different orders of hierarchy with distinct length scales. In this thesis, it is assumed that each hierarchical order of metamaterials remains a continuum. However, a detailed numerical approach, which involves the individual modelling of unit cells of lattices, could be impossible since it is computationally expensive. One viable strategy is to resort to a homogenization approach, in particular, asymptotic homogenization (AH) with a well-developed mathematical foundation, to analyze the representative volume elements (RVE) of ferroelectric lattice metamaterials (see Figure 2.4) in order to obtain their effective properties.

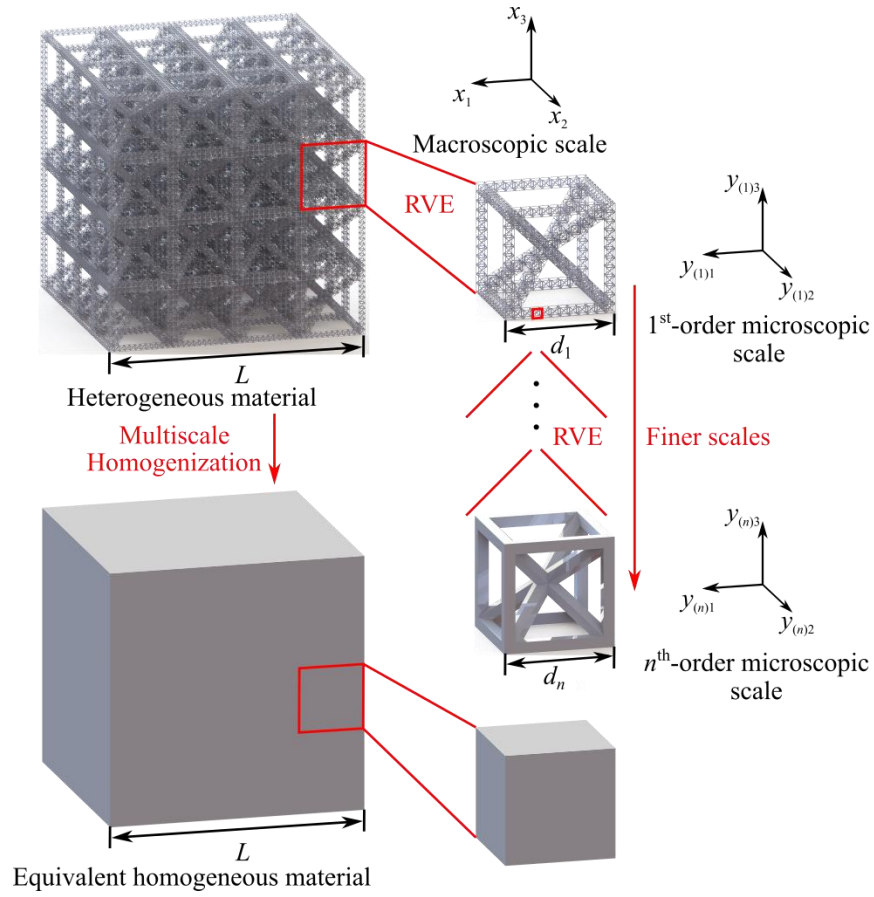


Figure 2.4 Schematic figure for multiscale homogenization process of hierarchical lattice ferroelectric metamaterials. (Reprinted with permission from ref [192], copyright 2020 Elsevier)

As shown in Figure 2.4, there are $n+1$ scales (including macroscopic scale) in the periodic hierarchical architecture. The first one is the macroscopic scale of the periodically repeated n^{th} -order hierarchical lattice ferroelectric metamaterials with a coordinate of $\{O, x_1, x_2, x_3\}$; for the other n orders of hierarchy, the order of their microscopic scales is the opposite of their hierarchical orders, which are defined from larger scales to smaller scales. For example, for n^{th} -order hierarchical lattice ferroelectric metamaterials, the microscopic coordinate of the k^{th} -order hierarchy is $\{O, y_{(n-k+1)1}, y_{(n-k+1)2}, y_{(n-k+1)3}\}$ ($k = 1, 2, \dots, n$); d_1, d_2, \dots, d_n , and L characterize the different scale sizes and it is assumed that they are well-separated as:

$$\eta_1 = \frac{d_1}{L} \leq 1, \quad \eta_2 = \frac{d_2}{L} \leq \eta_1, \quad \dots, \quad \eta_n = \frac{d_n}{L} \leq \eta_{n-1} \quad (2.27)$$

Using Eq. (2.27), the relationships between n independent microscopic coordinates and the macroscopic coordinate are:

$$\mathbf{y}_{(1)} = \frac{\mathbf{x}}{\eta_1}, \quad \mathbf{y}_{(2)} = \frac{\mathbf{x}}{\eta_2}, \quad \dots, \quad \mathbf{y}_{(n)} = \frac{\mathbf{x}}{\eta_n} \quad (2.28)$$

Based on the chain rule and the relationship between macroscopic and microscopic scales, we can write:

$$\frac{\partial}{\partial x_i} \rightarrow \frac{\partial}{\partial x_i} + \sum_{k=1}^n \frac{1}{\eta_k} \frac{\partial}{\partial y_{(k)i}} = (\cdot)_{,i} + \sum_{k=1}^n \frac{1}{\eta_k} (\cdot)_{,(k)i} \quad (2.29)$$

The thermo-electro-mechanical field can be expressed by asymptotic expansion in powers of macroscopic scale \mathbf{x} and microscopic scale $\mathbf{y}_{(k)}$ as:

$$\begin{aligned} u_i &= u_i(\mathbf{x}, \mathbf{y}_{(1)}, \dots, \mathbf{y}_{(n)}) = u_i^{(0)}(\mathbf{x}, \mathbf{y}_{(1)}, \dots, \mathbf{y}_{(n)}) + \sum_{k=1}^n \sum_{l=1}^{+\infty} \eta_{(k)}^l u_{(k)i}^{(l)}(\mathbf{x}, \mathbf{y}_{(1)}, \dots, \mathbf{y}_{(n)}) \\ \phi &= \phi(\mathbf{x}, \mathbf{y}_{(1)}, \dots, \mathbf{y}_{(n)}) = \phi^{(0)}(\mathbf{x}, \mathbf{y}_{(1)}, \dots, \mathbf{y}_{(n)}) + \sum_{k=1}^n \sum_{l=1}^{+\infty} \eta_{(k)}^l \phi_{(k)}^{(l)}(\mathbf{x}, \mathbf{y}_{(1)}, \dots, \mathbf{y}_{(n)}) \\ \theta &= \theta(\mathbf{x}, \mathbf{y}_{(1)}, \dots, \mathbf{y}_{(n)}) = \theta^{(0)}(\mathbf{x}, \mathbf{y}_{(1)}, \dots, \mathbf{y}_{(n)}) + \sum_{k=1}^n \sum_{l=1}^{+\infty} \eta_{(k)}^l \theta_{(k)}^{(l)}(\mathbf{x}, \mathbf{y}_{(1)}, \dots, \mathbf{y}_{(n)}) \end{aligned} \quad (2.30)$$

where k changes from 1 to number of scales n ; l represents the order of asymptotic series, changing from 1 to infinity; $u_{(k)i}^{(l)}$, $\phi_{(k)}^{(l)}$ and $\theta_{(k)}^{(l)}$ are d_k - periodic with respect to the k^{th} -order microscopic coordinate. Therefore, the displacement, voltage, and temperature in two opposite faces are the same. In addition, the stiffness tensor \mathbf{C} , piezoelectric tensor \mathbf{e} , dielectric permittivity tensor $\boldsymbol{\kappa}$, thermal stress tensor $\boldsymbol{\lambda}$, and pyroelectric tensor \mathbf{p} are also periodic in microscopic scales but independent of the macroscopic scale, namely $\mathbf{C}(\mathbf{x}, \mathbf{y}_{(1)}, \dots, \mathbf{y}_{(n)}) = \mathbf{C}(\mathbf{y}_{(1)}, \dots, \mathbf{y}_{(n)})$, $\mathbf{e}(\mathbf{x}, \mathbf{y}_{(1)}, \dots, \mathbf{y}_{(n)}) = \mathbf{e}(\mathbf{y}_{(1)}, \dots, \mathbf{y}_{(n)})$, $\boldsymbol{\kappa}(\mathbf{x}, \mathbf{y}_{(1)}, \dots, \mathbf{y}_{(n)}) = \boldsymbol{\kappa}(\mathbf{y}_{(1)}, \dots, \mathbf{y}_{(n)})$, $\boldsymbol{\lambda}(\mathbf{x}, \mathbf{y}_{(1)}, \dots, \mathbf{y}_{(n)}) = \boldsymbol{\lambda}(\mathbf{y}_{(1)}, \dots, \mathbf{y}_{(n)})$, and $\mathbf{p}(\mathbf{x}, \mathbf{y}_{(1)}, \dots, \mathbf{y}_{(n)}) = \mathbf{p}(\mathbf{y}_{(1)}, \dots, \mathbf{y}_{(n)})$.

nth-order microscopic scale problem

For simplification, in the following derivation, Eq. (2.30) is rewritten as

$$\begin{aligned}
 u_i &= u_{(n-1)i}(\mathbf{Y}_{(n-1)}, \mathbf{y}_{(n)}) + \sum_{l=1}^{+\infty} \eta_{(n)}^l u_{(n)i}^{(l)}(\mathbf{Y}_{(n-1)}, \mathbf{y}_{(n)}) \\
 \phi &= \phi_{(n-1)}(\mathbf{Y}_{(n-1)}, \mathbf{y}_{(n)}) + \sum_{l=1}^{+\infty} \eta_{(n)}^l \phi_{(n)}^{(l)}(\mathbf{Y}_{(n-1)}, \mathbf{y}_{(n)}) \\
 \theta &= \theta_{(n-1)}(\mathbf{Y}_{(n-1)}, \mathbf{y}_{(n)}) + \sum_{l=1}^{+\infty} \eta_{(n)}^l \theta_{(n)}^{(l)}(\mathbf{Y}_{(n-1)}, \mathbf{y}_{(n)})
 \end{aligned} \tag{2.31}$$

where $u_{(n-1)i}$, $\phi_{(n-1)}$, $\theta_{(n-1)}$, and $\mathbf{Y}_{(n-1)}$ are defined as

$$\begin{aligned}
 u_{(n-1)i}(\mathbf{Y}_{(n-1)}, \mathbf{y}_{(n)}) &= u_i^{(0)}(\mathbf{Y}_{(n-1)}, \mathbf{y}_{(n)}) + \sum_{k=1}^{n-1} \sum_{l=1}^{+\infty} \eta_{(k)}^l u_{(k)i}^{(l)}(\mathbf{Y}_{(n-1)}, \mathbf{y}_{(n)}) \\
 \phi_{(n-1)}(\mathbf{Y}_{(n-1)}, \mathbf{y}_{(n)}) &= \phi^{(0)}(\mathbf{Y}_{(n-1)}, \mathbf{y}_{(n)}) + \sum_{k=1}^{n-1} \sum_{l=1}^{+\infty} \eta_{(k)}^l \phi_{(k)}^{(l)}(\mathbf{Y}_{(n-1)}, \mathbf{y}_{(n)}) \\
 \theta_{(n-1)}(\mathbf{Y}_{(n-1)}, \mathbf{y}_{(n)}) &= \theta^{(0)}(\mathbf{Y}_{(n-1)}, \mathbf{y}_{(n)}) + \sum_{k=1}^{n-1} \sum_{l=1}^{+\infty} \eta_{(k)}^l \theta_{(k)}^{(l)}(\mathbf{Y}_{(n-1)}, \mathbf{y}_{(n)}) \\
 \mathbf{Y}_{(n-1)} &= [\mathbf{x}, \mathbf{y}_{(1)}, \dots, \mathbf{y}_{(n-1)}]
 \end{aligned} \tag{2.32}$$

After substituting Eq. (2.31) into Eq. (2.10), the governing differential equations of the thermo-electro-mechanical fields can be expanded and rearranged with the same order of $\eta_{(n)}^{-2}$ as:

$$\begin{aligned}
 (C_{ijst} u_{(n-1)s,(n)t})_{,(n)j} + (e_{ijt} \phi_{(n-1),(n)t})_{,(n)j} &= 0 \\
 (e_{ist} u_{(n-1)s,(n)t})_{,(n)i} - (\kappa_{it} \phi_{(n-1),(n)t})_{,(n)i} &= 0 \\
 (K_{it} \theta_{(n-1),(n)t})_{,(n)i} &= 0
 \end{aligned} \tag{2.33}$$

Since the right side of Eq. (2.33) is zero, the solvability condition is satisfied ([188,193]). Then, it is deduced that,

$$\left\{ \begin{array}{l} \mathbf{u}_{(n-1)} = \mathbf{U}_{(n-1)}(\mathbf{Y}_{(n-1)}) \\ \phi_{(n-1)} = \Phi_{(n-1)}(\mathbf{Y}_{(n-1)}) \\ \theta_{(n-1)} = \Theta_{(n-1)}(\mathbf{Y}_{(n-1)}) \end{array} \right\} \Leftrightarrow \left\{ \begin{array}{l} u_i^{(0)} = u_i^{(0)}(\mathbf{Y}_{(n-1)}) \\ \phi^{(0)} = \phi^{(0)}(\mathbf{Y}_{(n-1)}) \\ \theta^{(0)} = \theta^{(0)}(\mathbf{Y}_{(n-1)}) \end{array} \right\} \text{ and } \left\{ \begin{array}{l} \mathbf{u}_{(k)}^{(l)} = \mathbf{u}_{(k)}^{(l)}(\mathbf{Y}_{(n-1)}) \\ \phi_{(k)}^{(l)} = \phi_{(k)}^{(l)}(\mathbf{Y}_{(n-1)}), k = 1, 2, \dots, n-1; l = 1, 2, \dots \\ \theta_{(k)}^{(l)} = \theta_{(k)}^{(l)}(\mathbf{Y}_{(n-1)}) \end{array} \right.$$

(2.34)

which means that the solution of Eq. (2.33) does not depend on the n^{th} -order microscopic scale $\mathbf{y}_{(n)}$.

Similarly, by substituting Eq. (2.31) into Eq. (2.10) at the order of η_n^{-1} , one can obtain

$$\left[C_{ijst} \frac{\partial U_{(n-1)s}}{\partial Y_{(n-1)t}} + C_{ijst} u_{(n)s,(n)t}^{(1)} \right]_{,(n)j} + \left[e_{ijt} \frac{\partial \Phi_{(n-1)}}{\partial Y_{(n-1)t}} + e_{ijt} \phi_{(n),(n)t}^{(1)} \right]_{,(n)j} - (\lambda_{ij} \Theta_{(n-1)})_{,(n)j} = 0$$

$$\left[e_{sti} \frac{\partial U_{(n-1)s}}{\partial Y_{(n-1)t}} + e_{sti} u_{(n)s,(n)t}^{(1)} \right]_{,(n)i} - \left[\kappa_{ij} \frac{\partial \Phi_{(n-1)}}{\partial Y_{(n-1)t}} + \kappa_{ij} \phi_{(n),(n)t}^{(1)} \right]_{,(n)i} - (p_i \Theta_{(n-1)})_{,(n)i} = 0 \quad (2.35)$$

$$\left[K_{it} \frac{\partial \Theta_{(n-1)}}{\partial Y_{(n-1)t}} + K_{it} \theta_{(n),(n)t}^{(1)} \right]_{,(n)i} = 0$$

where the partial differentiation with respect to $\mathbf{Y}_{(n-1)t}$ is defined as

$$\frac{\partial}{\partial \mathbf{Y}_{(n-1)t}} \rightarrow (\cdot)_{,t} + \sum_{k=1}^{n-1} \frac{1}{\eta_k} (\cdot)_{,(k)t} \quad (2.36)$$

In particular, since Eq. (2.35) is linear, $\mathbf{u}_{(n)}^{(1)}$, $\phi_{(n)}^{(1)}$, and $\theta_{(n)}^{(1)}$ which respectively represent the mechanical displacement, electric potential, and temperature fluctuations in the n^{th} -order microscopic scale, can be written as

$$\left\{ \begin{array}{l} u_{(n)s}^{(1)}(\mathbf{Y}_{(n-1)}, \mathbf{y}_{(n)}) = M U_{(n)s}^{\alpha\beta}(\mathbf{y}_{(n)}) \frac{\partial U_{(n-1)\alpha}}{\partial Y_{(n-1)\beta}} + M \Phi_{(n)s}^{\beta}(\mathbf{y}_{(n)}) \frac{\partial \Phi_{(n-1)}}{\partial Y_{(n-1)\beta}} + M \Theta_{(n)s}(\mathbf{y}_{(n)}) \Theta \\ \phi_{(n)}^{(1)}(\mathbf{Y}_{(n-1)}, \mathbf{y}_{(n)}) = N U_{(n)}^{\alpha\beta}(\mathbf{y}_{(n)}) \frac{\partial U_{(n-1)\alpha}}{\partial Y_{(n-1)\beta}} + N \Phi_{(n)}^{\beta}(\mathbf{y}_{(n)}) \frac{\partial \Phi_{(n-1)}}{\partial Y_{(n-1)\beta}} + N \Theta_{(n)}(\mathbf{y}_{(n)}) \Theta \\ \theta_{(n)}^{(1)}(\mathbf{Y}_{(n-1)}, \mathbf{y}_{(n)}) = T \Theta_{(n)}^{\beta}(\mathbf{y}_{(n)}) \frac{\partial \Theta_{(n-1)}}{\partial Y_{(n-1)\beta}} \end{array} \right. \quad (2.37)$$

where $\alpha, \beta = 1, 2, 3$; seven kinds of functions $MU_{(n)s}^{\alpha\beta}$, $M\Phi_{(n)s}^{\beta}$, $M\Theta_{(n)s}$, $NU_{(n)}^{\alpha\beta}$, $N\Phi_{(n)}^{\beta}$, $N\Theta_{(n)}$, and $T\Theta_{(n)}^{\beta}$ only depend on the n^{th} -order microscopic scale and are also d_n - periodic functions.

Similar to two-scale asymptotic homogenization method, an important step is to use these seven kinds of functions to express $\mathbf{u}_{(n)}^{(1)}$, $\phi_{(n)}^{(1)}$, and $\theta_{(n)}^{(1)}$ by Eq. (2.37) and these functions can be obtained by solving three types of local problems, i.e., local mechanical problem, local electric problem, and local thermal problem, under periodic thermo-electro-mechanical boundary conditions. Details of the solution procedure can be found in ([188,193]).

Finally, the governing equation (Eq. (2.10)) can be rewritten in the same order of η_n^0 as:

$$\begin{aligned}
& \frac{\partial}{\partial \mathbf{Y}_{(n-1)j}} \left(C_{ijst} \frac{\partial U_{(n-1)s}}{\partial \mathbf{Y}_{(n-1)t}} + C_{ijst} u_{(n)s,(n)t}^{(1)} \right) + \left(C_{ijst} u_{(n)s,(n)t}^{(2)} + C_{ijst} u_{(n)s,t}^{(1)} \right)_{,(n)j} + \frac{\partial}{\partial \mathbf{Y}_{(n-1)j}} \left(e_{ijt} \frac{\partial \Phi_{(n-1)}}{\partial \mathbf{Y}_{(n-1)t}} + e_{ijt} \phi_{(n),(n)t}^{(1)} \right) \\
& + \left(e_{ijt} \phi_{(n),(n)t}^{(2)} + e_{ijt} \phi_{(n),t}^{(1)} \right)_{,(n)j} - \frac{\partial (\lambda_{it} \Theta_{(n-1)})}{\partial \mathbf{Y}_{(n-1)t}} - (\lambda_{it} \theta_{(n)}^{(1)})_{,(n)t} + b_i = 0 \\
& \frac{\partial}{\partial \mathbf{Y}_{(n-1)i}} \left(e_{sti} \frac{\partial U_{(n-1)s}}{\partial \mathbf{Y}_{(n-1)t}} + e_{sti} u_{(n)s,(n)t}^{(1)} \right) + \left(e_{sti} u_{(n)s,(n)t}^{(2)} + e_{sti} u_{(n)s,t}^{(1)} \right)_{,(n)i} - \frac{\partial}{\partial \mathbf{Y}_{(n-1)i}} \left(\kappa_{it} \frac{\partial \Phi_{(n-1)}}{\partial \mathbf{Y}_{(n-1)t}} + \kappa_{it} \phi_{(n),(n)t}^{(1)} \right) \\
& - \left(\kappa_{it} \phi_{(n),(n)t}^{(2)} + \kappa_{it} \phi_{(n),t}^{(1)} \right)_{,(n)i} - \frac{\partial (p_i \Theta_{(n-1)})}{\partial \mathbf{Y}_{(n-1)i}} - (p_i \theta_{(n)}^{(1)})_{,(n)i} - q = 0 \\
& \frac{\partial}{\partial \mathbf{Y}_{(n-1)i}} \left(K_{it} \frac{\partial \Theta_{(n-1)}}{\partial \mathbf{Y}_{(n-1)t}} + K_{it} \theta_{(n),(n)t}^{(1)} \right) + \left(K_{it} \theta_{(n),(n)t}^{(2)} + K_{it} \theta_{(n),t}^{(1)} \right)_{,(n)i} - R = 0
\end{aligned} \tag{2.38}$$

Substituting Eq. (2.37) into Eq. (2.38) and integrating it over the n^{th} -order microscopic representative volume element (RVE), considering the d_n -periodicity of $\mathbf{u}_{(n)}^{(2)}$, $\phi_{(n)}^{(1)}$ and $\theta_{(n)}^{(2)}$, the following $(n-1)^{\text{th}}$ -order microscopic constitutive equations are obtained:

$$\left\{ \begin{aligned}
& \left\langle C_{ij\alpha\beta} + C_{ijst} M U_{(n)s,(n)t}^{\alpha\beta} + e_{ijt} N U_{(n),(n)t}^{\alpha\beta} \right\rangle_{(n)} \frac{\partial^2 \mathbf{U}_{(n-1)\alpha}}{\partial \mathbf{Y}_{(n-1)j} \partial \mathbf{Y}_{(n-1)\beta}} + \left\langle e_{ij\beta} + C_{ijst} M \Phi_{(n)s,(n)t}^{\beta} + e_{ijt} N \Phi_{(n),(n)t}^{\beta} \right\rangle_{(n)} \frac{\partial^2 \Phi_{(n-1)}}{\partial \mathbf{Y}_{(n-1)j} \partial \mathbf{Y}_{(n-1)\beta}} \\
& - \left\langle \lambda_{ij} - C_{ijst} M \Theta_{(n)s,(n)t} - e_{ijt} N \Theta_{(n),(n)t} \right\rangle_{(n)} \frac{\partial \Theta_{(n-1)}}{\partial \mathbf{Y}_{(n-1)j}} + b_i = 0 \\
& \left\langle e_{\alpha\beta i} + e_{sti} M U_{(n)s,(n)t}^{\alpha\beta} - \kappa_{it} N U_{(n),(n)t}^{\alpha\beta} \right\rangle_{(n)} \frac{\partial^2 \mathbf{U}_{(n-1)\alpha}}{\partial \mathbf{Y}_{(n-1)i} \partial \mathbf{Y}_{(n-1)\beta}} - \left\langle \kappa_{i\beta} - e_{sti} M \Phi_{(n)s,(n)t}^{\beta} + \kappa_{it} N \Phi_{(n),(n)t}^{\beta} \right\rangle_{(n)} \frac{\partial^2 \Phi_{(n-1)}}{\partial \mathbf{Y}_{(n-1)i} \partial \mathbf{Y}_{(n-1)\beta}} \\
& - \left\langle p_i - e_{sti} M \Theta_{(n)s,(n)t} + \kappa_{it} N \Theta_{(n),(n)t} \right\rangle_{(n)} \frac{\partial \Theta_{(n-1)}}{\partial \mathbf{Y}_{(n-1)i}} - q = 0 \\
& \left\langle K_{i\beta} + K_{it} T \Theta_{(n),(n)t}^{\beta} \right\rangle_{(n)} \frac{\partial^2 \Theta_{(n-1)}}{\partial \mathbf{Y}_{(n-1)i} \partial \mathbf{Y}_{(n-1)\beta}} - R = 0
\end{aligned} \right. \quad (2.39)$$

where $\langle (\cdot) \rangle_{(n)} = \frac{1}{V_{(n)}} \int_{(n)} (\cdot) dV$ and this integration is over n^{th} -order microscopic scale representative volume element (RVE) with $V_{(n)}$ as its volume. The corresponding effective stiffness tensor $\bar{\mathbf{C}}_{(n)}$, piezoelectric tensor $\bar{\mathbf{e}}_{(n)}$, dielectric permittivity tensor $\bar{\mathbf{\kappa}}_{(n)}$, thermal stress tensor $\bar{\mathbf{\lambda}}_{(n)}$, and pyroelectric $\bar{\mathbf{p}}_{(n)}$ are:

$$\left\{ \begin{aligned}
\bar{C}_{ij\alpha\beta (n)} &= \left\langle C_{ij\alpha\beta} + C_{ijst} M U_{(n)s,(n)t}^{\alpha\beta} + e_{ijt} N U_{(n),(n)t}^{\alpha\beta} \right\rangle_{(n)} \\
\bar{e}_{ij\beta (n)} &= \left\langle e_{ij\beta} + C_{ijst} M \Phi_{(n)s,(n)t}^{\beta} + e_{ijt} N \Phi_{(n),(n)t}^{\beta} \right\rangle_{(n)} \\
\bar{\kappa}_{i\beta (n)} &= \left\langle \kappa_{i\beta} - e_{sti} M \Phi_{(n)s,(n)t}^{\beta} + \kappa_{it} N \Phi_{(n),(n)t}^{\beta} \right\rangle_{(n)} \\
\bar{\lambda}_{ij (n)} &= \left\langle \lambda_{ij} - C_{ijst} M \Theta_{(n)s,(n)t} - e_{ijt} N \Theta_{(n),(n)t} \right\rangle_{(n)} \\
\bar{p}_i (n) &= \left\langle p_i - e_{sti} M \Theta_{(n)s,(n)t} + \kappa_{it} N \Theta_{(n),(n)t} \right\rangle_{(n)} \\
\bar{K}_{i\beta (n)} &= \left\langle K_{i\beta} + K_{it} T \Theta_{(n),(n)t}^{\beta} \right\rangle_{(n)}
\end{aligned} \right. \quad (2.40)$$

We remark that Eq. (2.40) gives the effective properties of the hierarchical lattices at n^{th} -order microscopic scale or first-order hierarchy, which is called as ***n^{th} -order microscopic scale problem***. The solution to ***n^{th} -order microscopic scale problem*** will become the input values for finding the overall effective properties of the hierarchical lattice ferroelectric metamaterials.

(n-1)th-order microscopic scale problem

The solution procedure of ***(n-1)th-order microscopic scale problem*** is similar to that of ***nth-order microscopic scale problem***. Firstly, we can expand and rearrange the governing differential equations with the order of $\eta_{(n-1)}^{-2}$, $\eta_{(n-1)}^{-1}$, and $\eta_{(n-1)}^0$. Based on Eq. (2.39) and Eq. (2.40), the governing differential equations can be rewritten as

$$\begin{cases} \overline{C}_{ij\alpha\beta}^{(n)} \frac{\partial^2 \mathbf{U}_{(n-1)\alpha}}{\partial \mathbf{Y}_{(n-1)j} \partial \mathbf{Y}_{(n-1)\beta}} + \overline{e}_{ij\beta}^{(n)} \frac{\partial^2 \Phi_{(n-1)}}{\partial \mathbf{Y}_{(n-1)j} \partial \mathbf{Y}_{(n-1)\beta}} - \overline{\lambda}_{ij}^{(n)} \frac{\partial \Theta_{(n-1)}}{\partial \mathbf{Y}_{(n-1)j}} + b_i = 0 \\ \overline{e}_{\alpha\beta i}^{(n)} \frac{\partial^2 \mathbf{U}_{(n-1)\alpha}}{\partial \mathbf{Y}_{(n-1)i} \partial \mathbf{Y}_{(n-1)\beta}} - \overline{\kappa}_{i\beta}^{(n)} \frac{\partial^2 \Phi_{(n-1)}}{\partial \mathbf{Y}_{(n-1)i} \partial \mathbf{Y}_{(n-1)\beta}} - \overline{p}_{i}^{(n)} \frac{\partial \Theta_{(n-1)}}{\partial \mathbf{Y}_{(n-1)i}} - q = 0 \\ \overline{K}_{i\beta}^{(n)} \frac{\partial^2 \Theta_{(n-1)}}{\partial \mathbf{Y}_{(n-1)i} \partial \mathbf{Y}_{(n-1)\beta}} - R = 0 \end{cases} \quad (2.41)$$

For simplification, we can define $U_{(n-2)i}$, $\Phi_{(n-2)}$, $\Theta_{(n-2)}$, and $\mathbf{Y}_{(n-2)}$ as

$$\begin{aligned} U_{(n-2)i}(\mathbf{Y}_{(n-2)}, \mathbf{y}_{(n-1)}) &= u_i^{(0)}(\mathbf{Y}_{(n-2)}, \mathbf{y}_{(n-1)}) + \sum_{k=1}^{n-2} \sum_{l=1}^{+\infty} \eta_{(k)}^l u_{(k)i}^{(l)}(\mathbf{Y}_{(n-2)}, \mathbf{y}_{(n-1)}) \\ \Phi_{(n-2)}(\mathbf{Y}_{(n-2)}, \mathbf{y}_{(n-1)}) &= \phi^{(0)}(\mathbf{Y}_{(n-2)}, \mathbf{y}_{(n-1)}) + \sum_{k=1}^{n-2} \sum_{l=1}^{+\infty} \eta_{(k)}^l \phi_{(k)}^{(l)}(\mathbf{Y}_{(n-2)}, \mathbf{y}_{(n-1)}) \\ \Theta_{(n-2)}(\mathbf{Y}_{(n-2)}, \mathbf{y}_{(n-1)}) &= \theta^{(0)}(\mathbf{Y}_{(n-2)}, \mathbf{y}_{(n-1)}) + \sum_{k=1}^{n-2} \sum_{l=1}^{+\infty} \eta_{(k)}^l \theta_{(k)}^{(l)}(\mathbf{Y}_{(n-2)}, \mathbf{y}_{(n-1)}) \\ \mathbf{Y}_{(n-2)} &= [\mathbf{x}, \mathbf{y}_{(1)}, \dots, \mathbf{y}_{(n-2)}] \end{aligned} \quad (2.42)$$

Comparing with ***nth-order microscopic scale problem***, we can find the following counterpart variables and microscopic scale coordinates

$$\begin{aligned} \mathbf{u}_{(n-1)}^{(l)}(\phi_{(n-1)}^{(l)} \text{ or } \theta_{(n-1)}^{(l)}) &\Leftrightarrow \mathbf{u}_{(n)}^{(l)}(\phi_{(n)}^{(l)} \text{ or } \theta_{(n)}^{(l)}) \\ \mathbf{U}_{(n-2)}(\Phi_{(n-2)} \text{ or } \Theta_{(n-2)}) &\Leftrightarrow \mathbf{U}_{(n-1)}(\Phi_{(n-1)} \text{ or } \Theta_{(n-1)}) \\ \mathbf{Y}_{(n-2)}(\mathbf{y}_{(n-1)}) &\Leftrightarrow \mathbf{Y}_{(n-1)}(\mathbf{y}_{(n)}) \end{aligned} \quad (2.43)$$

Replacing the counterpart variables and coordinates in Eqs. (2.33) - (2.40) with the left ones in Eq. (2.43) and repeating the solution procedure of ***nth-order microscopic scale problem***, we can obtain the effective thermo-piezoelectric properties in $(n-1)^{\text{th}}$ -order microscopic scale, i.e.,

$$\left\{ \begin{array}{l} \overline{C}_{ij\alpha\beta}^{(n-1)} = \left\langle \overline{C}_{ij\alpha\beta}^{(n)} + \overline{C}_{ijst}^{(n)} MU_{(n-1)s,(n-1)t}^{\alpha\beta} + \overline{e}_{ijt}^{(n)} NU_{(n-1),(n-1)t}^{\alpha\beta} \right\rangle_{(n-1)} \\ \overline{e}_{ij\beta}^{(n-1)} = \left\langle \overline{e}_{ij\beta}^{(n)} + \overline{C}_{ijst}^{(n)} M\Phi_{(n-1)s,(n-1)t}^{\beta} + \overline{e}_{ijt}^{(n)} N\Phi_{(n-1),(n-1)t}^{\beta} \right\rangle_{(n-1)} \\ \overline{\kappa}_{i\beta}^{(n-1)} = \left\langle \overline{\kappa}_{i\beta}^{(n)} - \overline{e}_{sti}^{(n)} M\Phi_{(n-1)s,(n-1)t}^{\beta} + \overline{\kappa}_{it}^{(n)} N\Phi_{(n-1),(n-1)t}^{\beta} \right\rangle_{(n-1)} \\ \overline{\lambda}_{ij}^{(n-1)} = \left\langle \overline{\lambda}_{ij}^{(n)} - \overline{C}_{ijst}^{(n)} M\Theta_{(n-1)s,(n-1)t} - \overline{e}_{ijt}^{(n)} N\Theta_{(n-1),(n-1)t} \right\rangle_{(n-1)} \\ \overline{p}_{i(n-1)} = \left\langle \overline{p}_{i(n)} - \overline{e}_{sti}^{(n)} M\Theta_{(n-1)s,(n-1)t} + \overline{\kappa}_{it}^{(n)} N\Theta_{(n-1),(n-1)t} \right\rangle_{(n-1)} \\ \overline{K}_{i\beta}^{(n-1)} = \left\langle \overline{K}_{i\beta}^{(n)} + \overline{K}_{it}^{(n)} T\Theta_{(n-1),(n-1)t}^{\beta} \right\rangle_{(n-1)} \end{array} \right. \quad (2.44)$$

where $\langle (\cdot) \rangle_{(n-1)} = \frac{1}{V_{(n-1)}} \int_{(n-1)} (\cdot) dV$ and this integration is over $(n-1)^{\text{th}}$ -order microscopic scale representative volume element (RVE) with $V_{(n-1)}$ as its volume; $MU_{(n-1)s}^{\alpha\beta}$, $M\Phi_{(n-1)s}^{\beta}$, $M\Theta_{(n-1)s}$, $NU_{(n-1)}^{\alpha\beta}$, $N\Phi_{(n-1)}^{\beta}$, $N\Theta_{(n-1)}$, and $T\Theta_{(n-1)}^{\beta}$ only depend on the $(n-1)^{\text{th}}$ -order microscopic scale and can be obtained by solving the local problems in the $(n-1)^{\text{th}}$ -order microscopic scale.

kth-order microscopic scale problem

The first two microscopic scale problems provide a recursive method to obtain the effective properties at an arbitrary k^{th} -order microscopic scale, where the effective properties of representative volume element (RVE) in a finer scale are firstly calculated and then are used as the inputs to solve the homogenization problem at larger scales. Similar to Eqs. (2.40) and (2.44), we can determine the effective thermo-piezoelectric properties at k^{th} -order:

$$\left\{ \begin{aligned}
\overline{C_{ij\alpha\beta}}_{(k)} &= \left\langle \overline{C_{ij\alpha\beta}}_{(k+1)} + \overline{C_{ijst}}_{(k+1)} M U_{(k)s,(k)t}^{\alpha\beta} + \overline{e_{ijt}}_{(k+1)} N U_{(k),(k)t}^{\alpha\beta} \right\rangle_{(k)} \\
\overline{e_{ij\beta}}_{(k)} &= \left\langle \overline{e_{ij\beta}}_{(k+1)} + \overline{C_{ijst}}_{(k+1)} M \Phi_{(k)s,(k)t}^{\beta} + \overline{e_{ijt}}_{(k+1)} N \Phi_{(k),(k)t}^{\beta} \right\rangle_{(k)} \\
\overline{\kappa_{i\beta}}_{(k)} &= \left\langle \overline{\kappa_{i\beta}}_{(k+1)} - \overline{e_{sti}}_{(k+1)} M \Phi_{(k)s,(k)t}^{\beta} + \overline{\kappa_{it}}_{(k+1)} N \Phi_{(k),(k)t}^{\beta} \right\rangle_{(k)} \\
\overline{\lambda_{ij}}_{(k)} &= \left\langle \overline{\lambda_{ij}}_{(k+1)} - \overline{C_{ijst}}_{(k+1)} M \Theta_{(k)s,(k)t} - \overline{e_{ijt}}_{(k+1)} N \Theta_{(k),(k)t} \right\rangle_{(k)} \\
\overline{p_i}_{(k)} &= \left\langle \overline{p_i}_{(k+1)} - \overline{e_{sti}}_{(k+1)} M \Theta_{(k)s,(k)t} + \overline{\kappa_{it}}_{(k+1)} N \Theta_{(k),(k)t} \right\rangle_{(k)} \\
\overline{K_{i\beta}}_{(k)} &= \left\langle \overline{K_{i\beta}}_{(k+1)} + \overline{K_{it}}_{(k+1)} T \Theta_{(k),(k)t}^{\beta} \right\rangle_{(k)}
\end{aligned} \right. \quad (2.45)$$

where $\overline{\mathbf{C}}_{(k+1)}$, $\overline{\mathbf{e}}_{(k+1)}$, $\overline{\mathbf{\kappa}}_{(k+1)}$, $\overline{\mathbf{\lambda}}_{(k+1)}$, and $\overline{\mathbf{p}}_{(k+1)}$ have been obtained from the $(k+1)^{th}$ -order microscopic scale problem. In particular, when $k = 1$, we finally get the effective thermo-piezoelectric properties of the topmost order of hierarchical lattice ferroelectric metamaterials. During this solution procedure, since we need to iteratively insert the effective properties from the larger microscopic scale into a lower one, this multiscale homogenization can be called an *iterative homogenization method* [194]. The abovementioned formulations introduced in this section for theoretical multiscale homogenization can be considered as a mathematical framework for the computational iterative homogenization method.

CHAPTER 3

2D extruded cellular ferroelectric metamaterials

This chapter includes the effective ferroelectric properties of 2D extruded cellular metamaterials. The effect of pore microarchitecture (relative density and cell topology) and polarization direction on elastic, dielectric, piezoelectric, pyroelectric, and thermal conductive properties of periodic cellular ferroelectric metamaterials are explored. The chapter is divided into four main sections, including the pore topology of cellular ferroelectric metamaterials, porous ferroelectric metamaterials made of a single material, and porous ferroelectric metamaterials made of bi-phase materials, and the comparison of their properties.

3.1 Pore topology of cellular ferroelectric metamaterials

As shown in Figure 3.1a and b, according to the polarization direction (axis 3) of constitutive ferroelectric materials, 1-3 ferroelectric cellular metamaterials can be further classified as longitudinally polarized (i.e., polarized along the pore axis) and transversely polarized (i.e., polarized orthogonal to the pore axis) cellular ferroelectric metamaterials. Figure 3.1c and d show a similar metamaterial made of two different materials, whose interface between two materials is

assumed to be perfectly bonded. In particular, four types of cellular ferroelectric metamaterials are analyzed in this section: (1) Longitudinally polarized single material (type I), (2) Transversely polarized single material (type II), (3) Longitudinally polarized bi-material (type III) and (4) Transversely polarized bi-material (type IV).

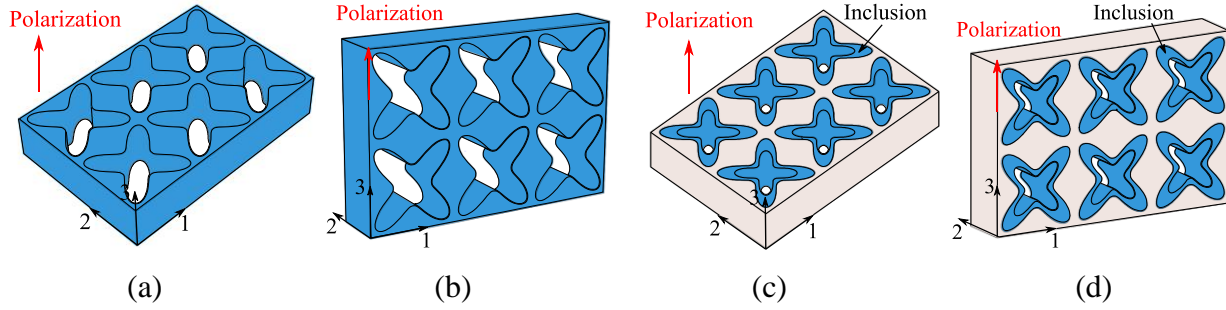


Figure 3.1 Four types of 1-3 cellular, 2D extruded, ferroelectric metamaterials: (a) Type I (single material with longitudinal polarization); (b) Type II (single material with transverse polarization), (c) Type III (bi-material with longitudinal polarization), and (d) Type IV (bi-material with transverse polarization). (Reprinted with permission from ref [188], copyright 2019 Elsevier)

To better understand the role of microarchitectural features of cellular ferroelectric metamaterials on their effective thermo-electro-mechanical properties, the following Fourier series expansion is used to generate pores of a general two-dimensional (2D) topology [195]: $x = r(\omega)\cos\omega$, $y = r(\omega)\sin\omega$, where

$$r(\omega) = r_0[1 + c_1\cos(\alpha\omega) + c_2\cos(\beta\omega)] \text{ and } (\alpha, \beta = 1, 2, \dots) \quad (3.1)$$

In Eq. (3.1), α and β control the symmetry of the pore topology. For example, when $\alpha = 2$ and $\beta = 4$, the pore is two-fold ω symmetry and when $\alpha = 3$ and $\beta = 6$, the pore is three-fold symmetry. In addition, c_1 and c_2 determine specific pore shapes. Assuming that the representative volume element (RVE) of the cell is a unit-length square, the solid volume fraction of cellular ferroelectric metamaterials made of a single material is expressed by:

$$f_v = 1 - \frac{\pi(2 + c_1^2 + c_2^2)}{2} r_0^2 \quad (3.2)$$

where f_v is solid volume fraction. Similarly, for bi-material cellular ferroelectric metamaterials, matrix (f_{vm}) and inclusion (f_{vi}) volume fraction are expressed by:

$$f_{vm} = 1 - \frac{\pi(2 + c_1^2 + c_2^2)}{2} r_{0m}^2, \quad f_{vi} = \frac{\pi(2 + c_1^2 + c_2^2)}{2} (r_{0m}^2 - r_{0i}^2) \quad (3.3)$$

where r_{0m} and r_{0i} determine the size of matrix and inclusion, respectively. By rotating (ω_r as rotation angle) and scaling (s as scaling factor or aspect ratio) pores, a wider range of pore microarchitecture can be achieved to further optimize thermo-electro-mechanical properties of cellular ferroelectric metamaterials. The topology of rotated or scaled pores can be determined by the following equations:

$$\begin{aligned} \text{Rotating: } \quad x &= r(\omega) \cos(\omega + \omega_r), & y &= r(\omega) \sin(\omega + \omega_r) \\ & \text{where } r(\omega) = r_0 [1 + c_1 \cos(\alpha\omega) + c_2 \cos(\beta\omega)] & \alpha, \beta &= 1, 2, \dots \end{aligned} \quad (3.4)$$

$$\begin{aligned} \text{Scaling: } \quad x &= r(\omega) \cos \omega, & y &= r(\omega) \sin \omega \cdot s \\ & \text{where } r(\omega) = r_0 [1 + c_1 \cos(\alpha\omega) + c_2 \cos(\beta\omega)] / s & \alpha, \beta &= 1, 2, \dots \end{aligned}$$

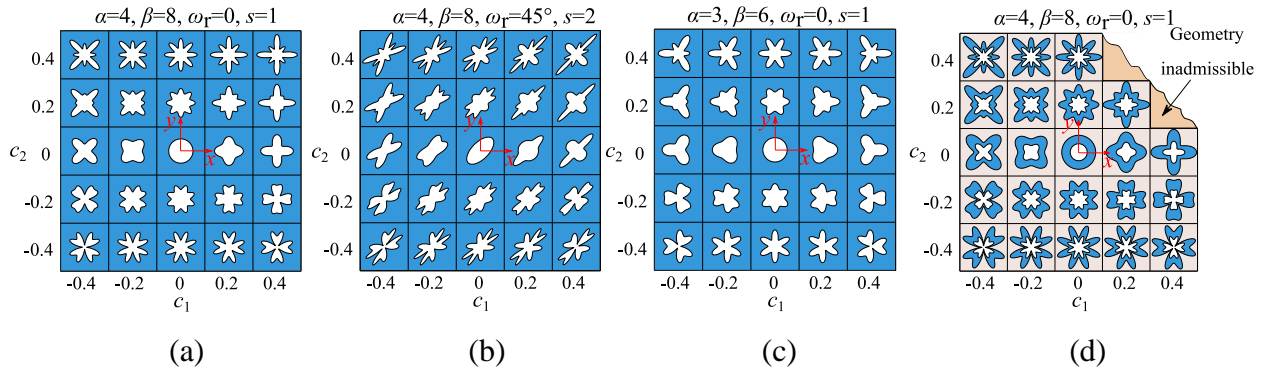


Figure 3.2 Cross section of 1-3 cellular, 2D extruded, ferroelectric metamaterials : (a) Single material with $\alpha = 4, \beta = 8, \omega_r = 0$ and $s = 1$, (b) Single material with $\alpha = 4, \beta = 8, \omega_r = 45^\circ$ and $s = 1$, (c) Single material with $\alpha = 3, \beta = 6, \omega_r = 0$ and $s = 1$, and (d) Bi-material with $f_{vm} = 0.6, f_{vi} = 0.3, \alpha = 4, \beta = 8, \omega_r = 0$ and $s = 1$. (Reprinted with permission from ref [188], copyright 2019 Elsevier)

Figure 3.2a presents 25 different shapes of four-fold symmetrical pores with $\alpha = 4$, $\beta = 8$, $\omega_r = 0$, $s = 1$ and $f_v = 0.8$, while c_1 and c_2 vary between -0.4 and 0.4 to show their effect on pore topology. Figure 3.2b scales down ($s = 2$) and rotates ($\omega_r = 45^\circ$ counterclockwise) pores presented in Figure 3.2a. Figure 3.2(c) shows three-fold symmetrical pores with $\alpha = 3$, $\beta = 6$, $s = 1$, $\omega_r = 0$ and $f_v = 0.8$ to reveal how shape parameters α and β tune the pore microarchitecture in cellular metamaterials. In Figure 3.2b, it can be seen that although neither x axis nor y axis is the symmetry axis of these pores, these pores still have four-fold symmetry. The bi-material cellular microarchitectures are shown in Figure 3.2d for matrix and inclusion volume fractions of $f_{vm} = 0.6$ and $f_{vi} = 0.3$; both ferroelectric inclusions (blue area) and pores share the same topology. It should be mentioned that when the ferroelectric inclusion boundary touches the unit cell or RVE boundary (e.g., for $c_1 = c_2 = 0.4$ in Figure 3.2d), we call this topology an *inadmissible geometry* since it makes the matrix unconnected. To showcase the unprecedented thermo-electro-mechanical properties of architected cellular ferroelectric metamaterials, we compare their effective properties with conventional 2D extruded ferroelectric honeycombs or ferroelectric composites with solid circle inclusion.

In the following sections, we use the previously developed asymptotic homogenization (AH) to theoretically predict the effect of pore topology, polarization direction, and material composition on the thermo-electro-mechanical properties of cellular ferroelectric metamaterials. In addition, 2062 different pores (1482 for type I and II and 580 for type III and IV) are analyzed, and their properties are compared to commonly used regular honeycomb ferroelectric cellular materials and ferroelectric composites with embedded cylindrical inclusions. An ecofriendly and biocompatible material, BaTiO₃, which can be used for 3D printing and has both piezoelectric and pyroelectric effects, is selected as ferroelectric material, and a non-ferroelectric epoxy is used as the matrix for

type III and IV cellular ferroelectric metamaterials. The piezoelectric properties of the constituent materials are given in Table 3.1, and their associated thermal properties are given in Table 3.2 [189,196,197].

Table 3.1 Piezoelectric properties of material constituents of ferroelectric cellular metamaterials: C ($\times 10^9$) Pa, e ($\times 10^{-2}$) C/m², κ ($\times 10^{-11}$) C/(Vm²) from Reference [189,196].

	C_{11}	C_{12}	C_{13}	C_{33}	C_{44}	e_{31}	e_{33}	e_{15}	κ_{11}	κ_{33}
Epoxy	8	4.4	4.4	8	1.8	0	0	0	3.7	3.7
BaTiO ₃	150	66	66	146	4.4	-4.3	17.5	11.4	987.2	111.6

Table 3.2 Thermal properties of material constituents of ferroelectric cellular metamaterials ρ in g/cm³, Δ ($\times 10^{-6}$ K⁻¹) Pa, γ Vm⁻¹K⁻¹, K Wm⁻¹K⁻¹, C_p J/(gK) from References [189,197].

	P	Δ_{11}	Δ_{33}	p_3	K	C_p
Epoxy	1.15	60	60	0	0.7	1.10
BaTiO ₃	5.70	8.53	1.99	13300	2.9	0.43

3.2 Porous ferroelectric metamaterials with a single material

A comprehensive study on type I and type II ferroelectric cellular metamaterials are conducted here, including the influence of shape parameters and polarization direction on effective properties and the relationship between effective properties and solid volume fraction.

3.2.1 Influence of shape parameters and polarization direction on effective piezoelectric properties for Type I/II metamaterials

In examining the effects of shape parameters, e.g., α , β and s , and polarization direction on effective ferroelectric properties of type I and type II metamaterials, Figure 3.3 presents the variation of seven ferroelectric constants and four ferroelectric figures of merit with several selected pore shapes. More specifically, f_v and c_2 are set as 0.7 and -0.2, respectively; c_1 varies as -0.4, -0.2, 0, 0.2 and 0.4; s is 0.5 and 1; two groups of α and β are considered, i.e., $\alpha = 4$, $\beta = 8$ and $\alpha = 3$, $\beta = 6$, whose pore shapes are sensitive to c_1 , c_2 and s , and still reasonable. Generally,

compared with type I metamaterials, type II metamaterials are more sensitive to shape parameters, and their piezoelectric figures of merit are also improved. The following observations are made:

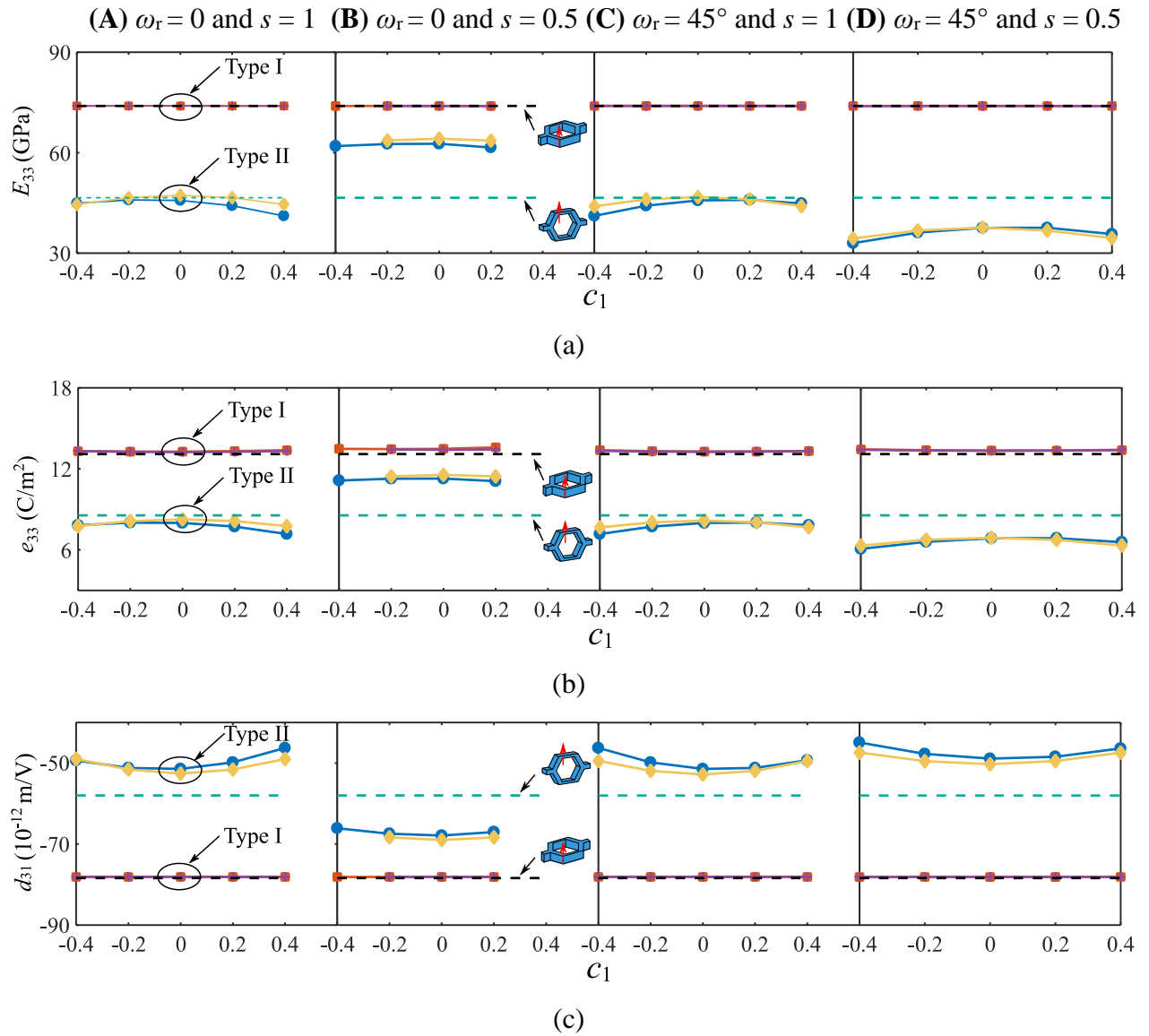
(i) With the exception of k_t (Figure 3.3j), other piezoelectric properties of type I metamaterials are insensitive to pore shapes and share the same value with type I honeycomb.

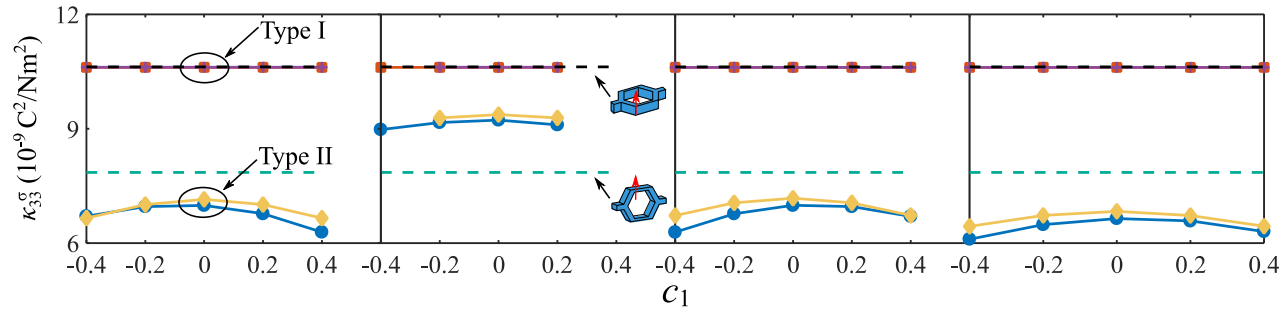
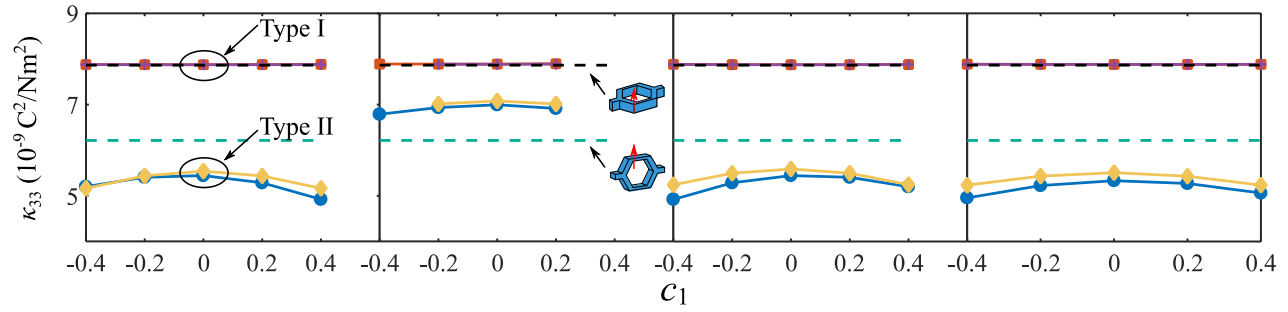
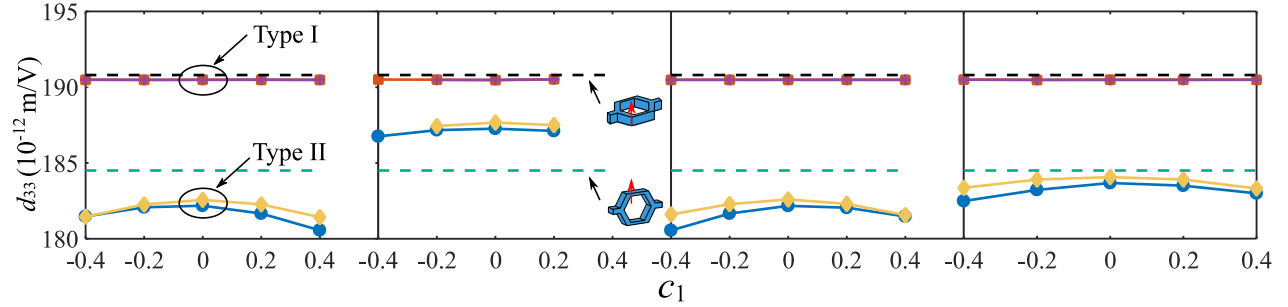
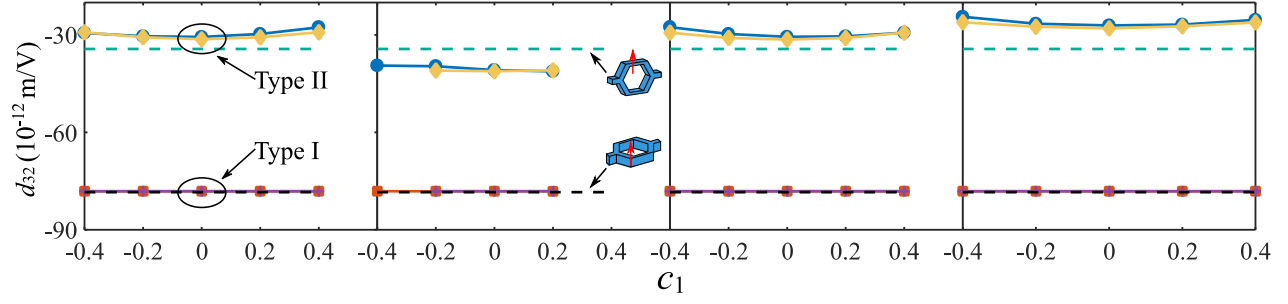
(ii) Type II metamaterials exhibit pronounced sensitivity to pore shapes. For example, by changing shape parameters, E_{33} changes from 32.99 GPa to 64.21 GPa, and Z varies between 13.69 Mrayls and 19.12 Mrayls, which provides more piezoelectric property selections. In addition, five fundamental piezoelectric properties along polarization direction, i.e., E_{33} , e_{33} , d_{33} , κ_{33} and κ_{33}^{σ} , share similar patterns, which means the same influence of pore shapes on these properties.

(iii) Original pore shapes (A category: $\omega_r = 0$ and $s = 1$), rotated pore shapes (C category: $\omega_r = 45^\circ$, $s = 1$) and scaled – rotated pore shapes (D category: $\omega_r = 45^\circ$, $s = 0.5$) have similar influence on type II metamaterials. For example, E_{33} varies between 41.15 GPa and 47.29 GPa, 41.15 GPa and 46.75 GPa, 32.99 GPa and 37.64 GPa for A category, C category, and D category, respectively, while varies between 61.96 GPa and 64.20 GPa for B category. Furthermore, apart from d_{31} , d_{32} , d_h and $d_h \times g_h$, other seven piezoelectric properties of type II metamaterials with C category pore shapes are higher than those with A category, C category and D category pore shapes. For example, for type II metamaterials with $\alpha = 3$, $\beta = 6$, $c_1 = 0$, $\omega_r = 0$ and $s = 0.5$, E_{33} , e_{33} , d_{33} , κ_{33} and κ_{33}^{σ} are 64.25 GPa, 11.55 C/m², 0.19×10^{-12} m/V, 7.08×10^{-9} C²/N/m² and 9.37 C²/N/m², respectively, which are 37.96%, 35.09%, 3.0%, 14% and 19.66% higher than that of type II honeycombs. It should be mentioned α and β just have marginal influence on type II metamaterials.

(vi) With transverse polarization, type II metamaterials have a significant improvement on d_h and $d_h \times g_h$. Since d_{33} is positive, while d_{31} and d_{32} are negative, the reason for the improvement of d_h is that transverse polarization decreases the absolute value of d_{31} and d_{32} . For example, for type

II metamaterials with $\alpha = 4$, $\beta = 8$, $c_1 = 0$, $\omega_r = 0$ and $s = 1$, d_{31} , d_{32} and d_h are 34.31%, 60.96% and 195.28% higher than that of type I honeycomb, which is more suitable for hydrophone devices. In addition, the decrease of κ_{33}^σ for type II metamaterials further improve $d_h \times g_h$. Since κ_{33} and κ_{33}^σ share the same variation trend and $\boldsymbol{\kappa}^\sigma = \boldsymbol{\kappa} + \mathbf{e}^T \mathbf{C}^{-1} \mathbf{e}$, the variation of κ_{33}^σ only depends on κ_{33} and only κ_{33} is analyzed in the following analysis. However, with longitudinal polarization, type I metamaterials show higher k_t and Z .





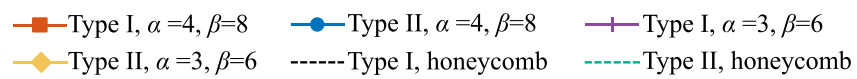
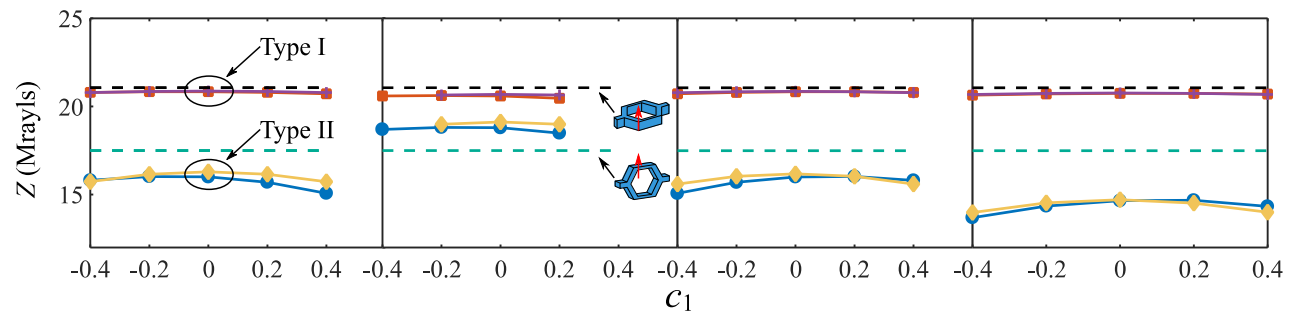
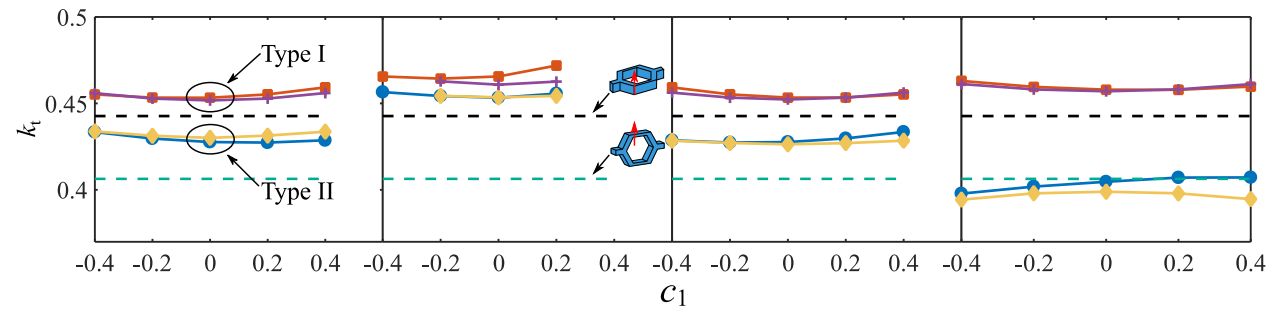
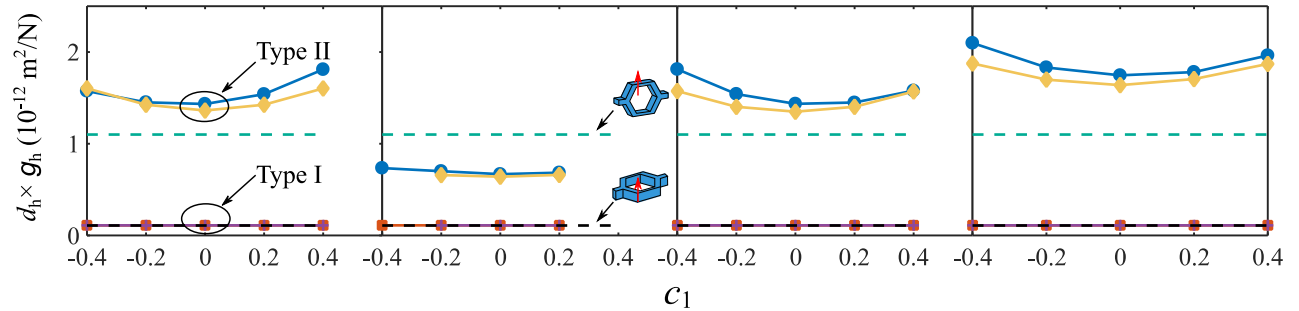
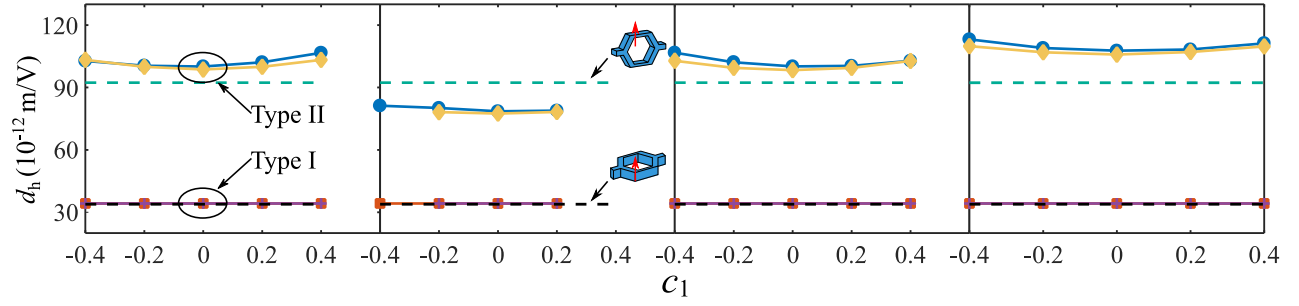


Figure 3.3 Variation of piezoelectric properties and figures of merit of type I and type II cellular metamaterial with solid volume fraction $f_v = 0.7$ and shape coefficient $c_2 = -0.2$. (Reprinted with permission from ref [188], copyright 2019 Elsevier)

3.2.2 Influence of shape parameters and polarization direction on effective thermal and pyroelectric properties for Type I/II metamaterials

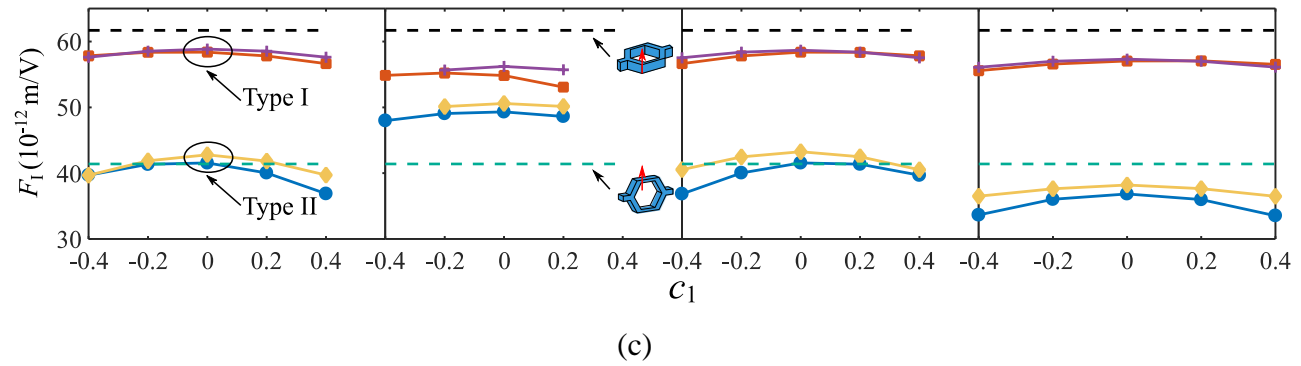
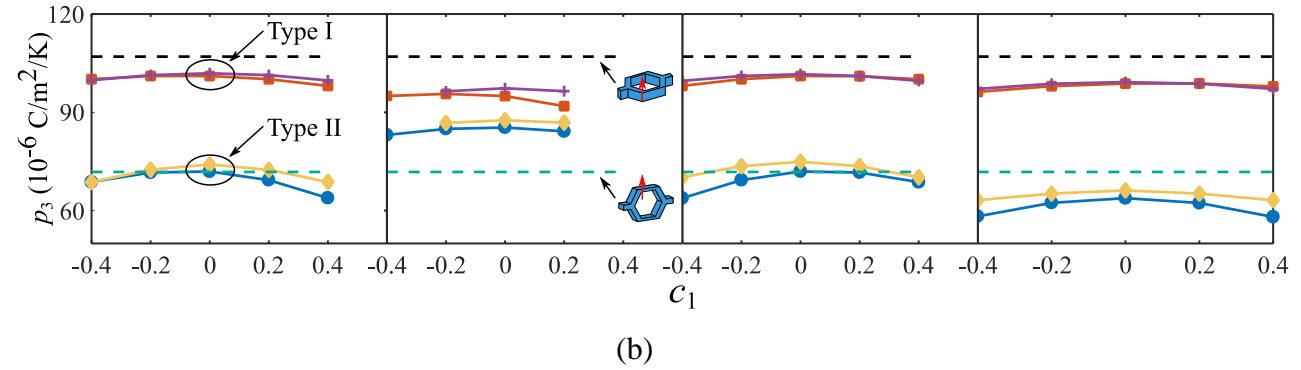
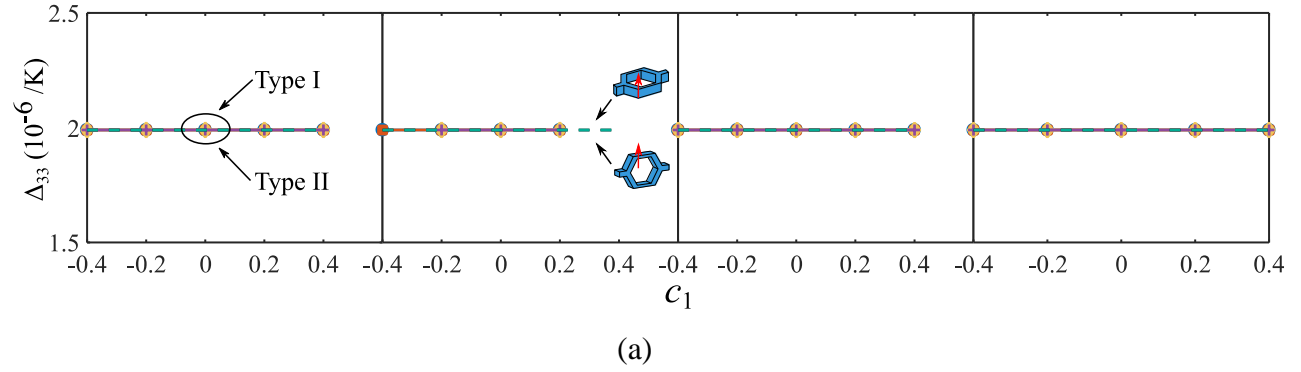
Figure 3.4 illustrates the influence of pore shape parameters on effective thermal conductive and pyroelectric properties of type I and type II metamaterials. Overall, with the exception of Δ_{33} and K_{33} , all other four properties are sensitive to pore shapes. In addition, type I and type II metamaterials share the same Δ_{33} even with different shape parameters. Detailed observations are made as follows:

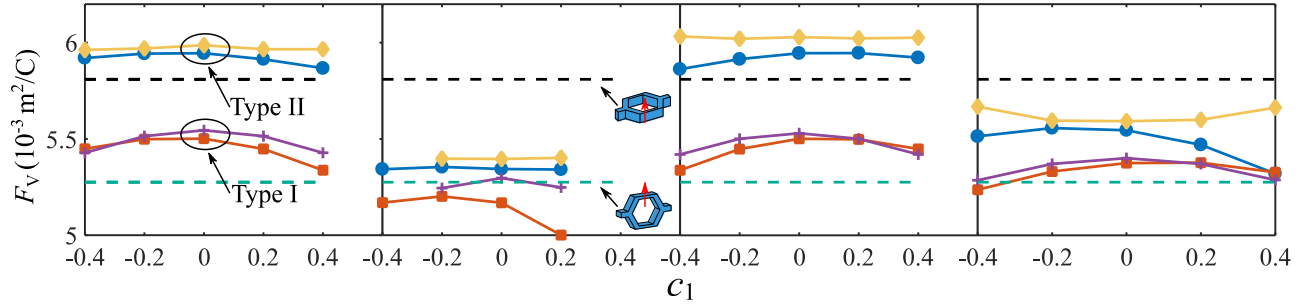
(i) No matter how the pore shape changes for type I and type II cellular ferroelectric metamaterials, thermal expansion, Δ_{33} (Figure 3.4a), always remains the same value as that of BaTiO_3 .

(ii) Different to piezoelectric properties, in Figure 3.4b-e, p_3 , F_I , F_V and F'_E of type I metamaterial show obvious dependence on pore shapes. More specially, p_3 and F_I share the exact same pattern due to constant solid volume fraction and heat capacity. Similar to fundamental piezoelectric properties along 3 direction of type II metamaterials (e.g., Figure 3.4b), p_3 and F_I are smaller than that of type I metamaterials and scaling the pore shapes of type II metamaterials decreases this difference. The same trend also occurs for F'_E (see Figure 3.4e). However, in Figure 3.4d, due to the decrease of κ_{33}^σ of type II metamaterials, F_V of type II metamaterial is higher than that of type I metamaterials. In addition, F_V of type II honeycomb is smaller than that of type I honeycomb, the decrease of κ_{33}^σ of type II metamaterials cannot compensate the smaller value of p_3 .

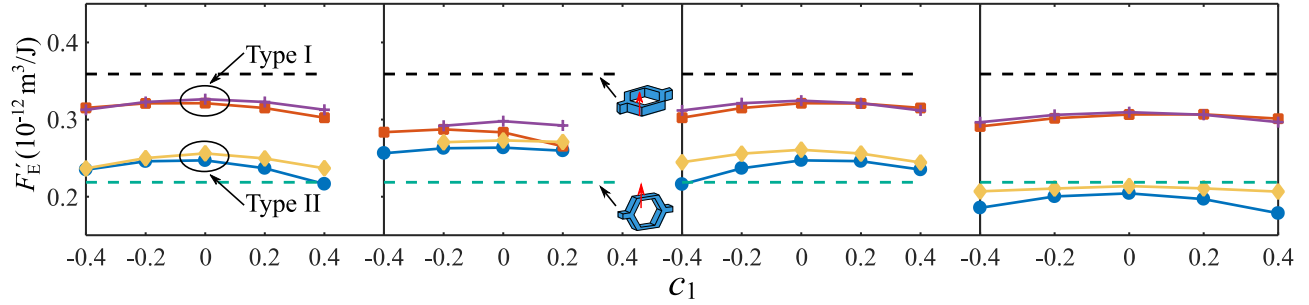
(iii) In Figure 3.4f, K_{33} of type I metamaterials is insensitive to pore shapes and are higher than that of type II metamaterials. In addition, scaling the pore shape (B category) will also increase this value of type II metamaterials.

(A) $\omega_r = 0$ and $s = 1$ (B) $\omega_r = 0$ and $s = 0.5$ (C) $\omega_r = 45^\circ$ and $s = 1$ (D) $\omega_r = 45^\circ$ and $s = 0.5$

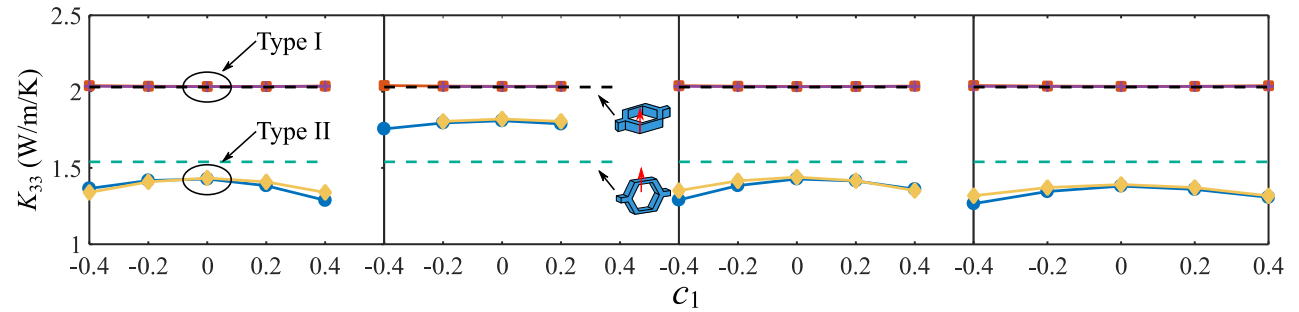




(d)



(e)



(f)

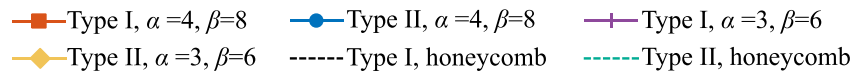
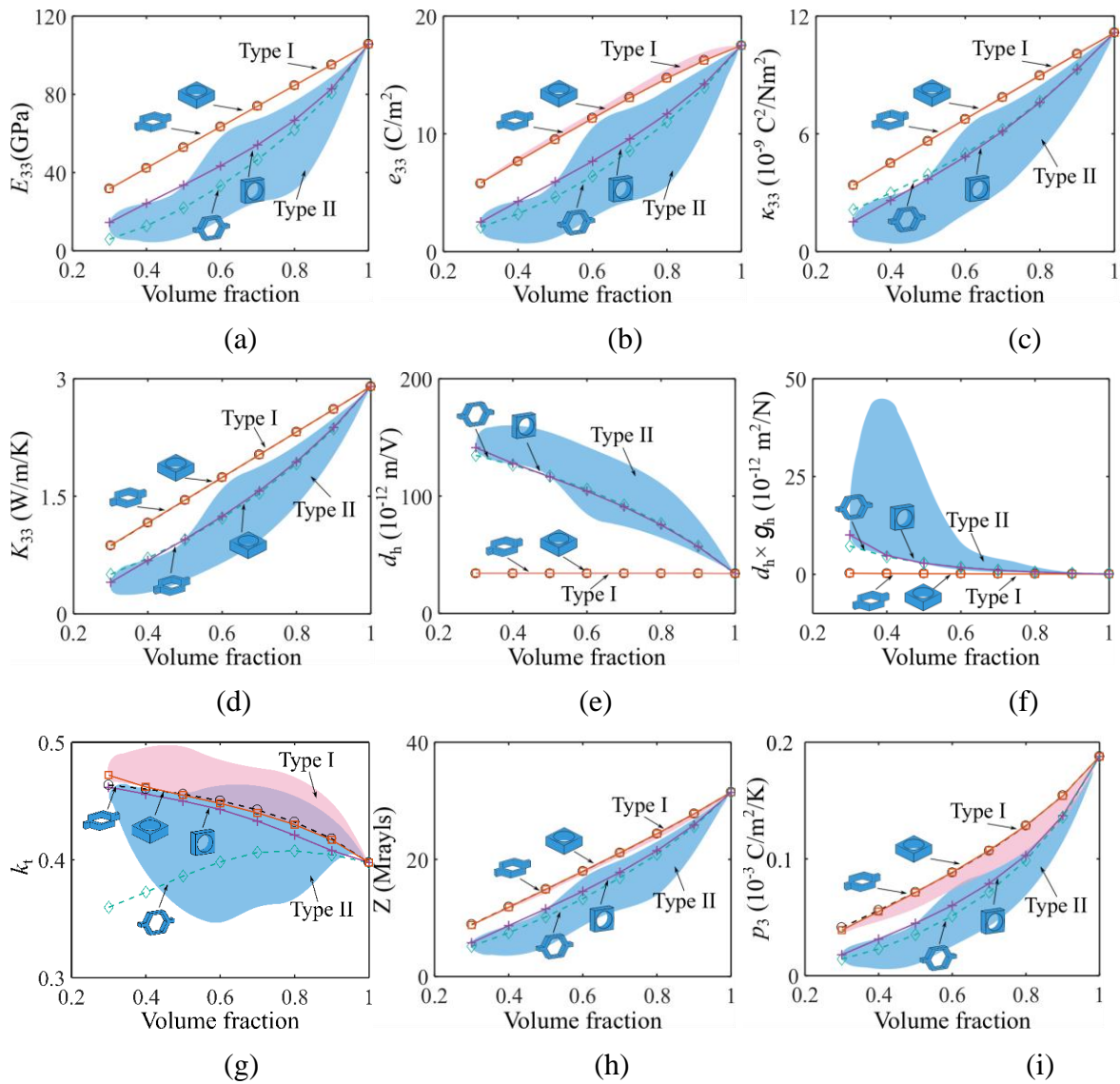


Figure 3.4 Variation of the thermal-related properties and associated figure of merits of type I and type II cellular metamaterials with a solid volume fraction $f_v = 0.7$ and shape coefficient $c_2 = -0.2$. (Reprinted with permission from ref [188], copyright 2019 Elsevier)

3.2.3 Relation between effective thermo-electro-mechanical properties and solid volume fraction

In order to understand the relationship between thermo-electro-mechanical properties and volume fraction of solid phase or porosity, Figure 3.5 presents seven piezoelectric-related

properties and five thermal-related properties for type I (red area) and type II metamaterials (blue area) with f_v varying from 0.3 to 1. For considered metamaterials, c_1 and c_2 are selected as -0.4, -0.2, 0, 0.2 or 0.4 while two groups of α and β , i.e., $\alpha = 4, \beta = 8$ and $\alpha = 3, \beta = 6$, are chosen for generating the microarchitectures. The pore shapes are further tailored by rotating and scaling the pores for the following four sets: $\omega_r = 0$ and $s = 1$ (original shape), $\omega_r = 0$ and $s = 0.5$ (scaled pore), $\omega_r = 45^\circ, s = 1$ (rotated pore) and $\omega_r = 45^\circ$ and $s = 0.5$ (rotated and scaled pore). Omitting inadmissible pore architectures, 1482 different cellular ferroelectric metamaterials are analyzed.



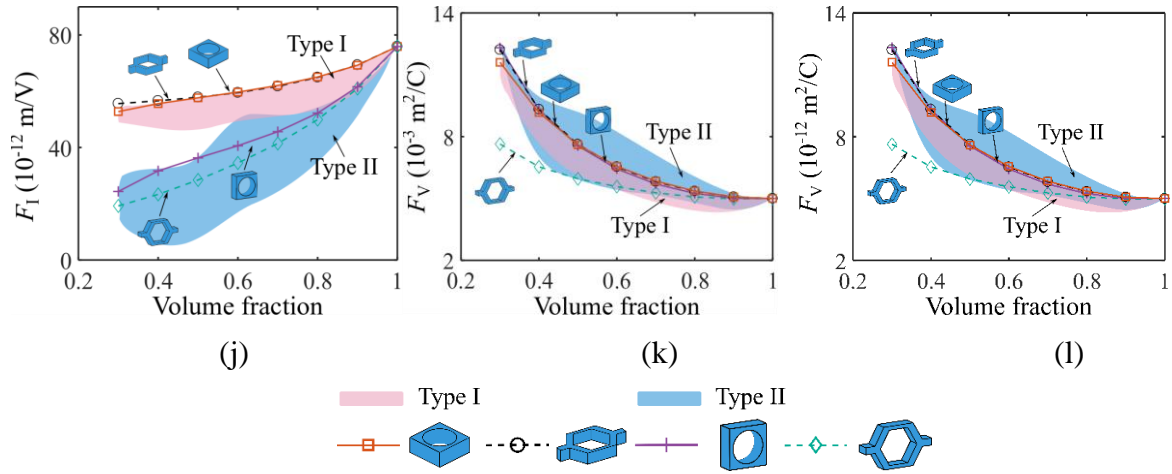


Figure 3.5 Property and figures of merit design charts for type I and type II cellular ferroelectric metamaterials with solid volume fraction f_v varying from 0.3 to 1. (Reprinted with permission from ref [188], copyright 2019 Elsevier)

As expected, apart from k_t (Figure 3.5g), p_3 (Figure 3.5i) and three pyroelectric figures of merit (Figure 3.5j–l), all other involved properties of type I metamaterials is linear with solid volume fraction, which is due to their insensitivity to pore shapes. In the meantime, type II metamaterials provide a wider range of material property selections for design. More specially,

(i) As found in Figures 3.3 and 3.4, fundamental piezoelectric properties and thermal conductivity along 3 direction, i.e., E_{33} , e_{33} , κ_{33} , and K_{33} , share similar variation trends with respect to shape parameters. Therefore, as shown in Figure 3.5a–d, E_{33} , e_{33} , κ_{33} , and K_{33} of both type I and type II metamaterials have the same property pattern where type I metamaterials have higher values while type II metamaterials provide more property selections, and increasing volume fraction will increase all these values for type I/II metamaterials.

(ii) As discussed in Chapter 3.2.1, type II metamaterials have much better performance on d_h and $d_h \times g_h$. In addition, in Figure 3.5e and f, d_h and $d_h \times g_h$ increase by decreasing the volume fraction and tailoring pore shapes is an effective method to further improve these two values. For

example, for type II metamaterials with $f_v = 0.6$, the maximum and minimum d_h are 142.39×10^{-12} m/V and 83.36×10^{-12} m/V, which are 320% and 146% higher than type I honeycomb with $f_v = 0.6$.

(iii) Except for type II honeycomb (green dashed line), piezoelectric coupling constant, k_t , of type I and type II cellular metamaterials with a circular pore and type I honeycomb show a decreasing trend with increasing volume fraction. In contrast to d_h and $d_h \times g_h$, type I metamaterials always show a maximum k_t value. For acoustic transducer applications, such as hydrophone, low Z is desired for better performance. Therefore, the decrease of the Z value with increasing porosity indicates that cellular ferroelectric metamaterials can improve the acoustic impedance of ferroelectric materials.

(vi) Similar as Figure 3.5b and c, it is easy to understand that p_3 (Figure 3.5i) and F_I (Figure 3.5j) share the same property pattern. In addition, increasing volume fraction will generally improve p_3 and F_I , and type I metamaterials always have higher p_3 and F_I than type II metamaterials. Therefore, introducing porosity and transverse polarization do not work for improving the pyroelectric coefficient and current responsivity.

(v) Different from p_3 and F_I , F_V (Figure 3.5k) has a decreasing trend with increasing solid volume fraction, and apart from the overlapping area, type II metamaterials provide higher F_V . Therefore, the combination of increasing porosity and tailoring pore shapes of type II metamaterials can enhance voltage responsivity. Decreasing volume fraction still can improve F'_E (Figure 3.5l) of type I metamaterial. However, it does not work for type II metamaterials. Furthermore, generally, type I metamaterials show higher F'_E than type II metamaterials. Therefore, porous type I metamaterials are good selections for pyroelectric energy harvesting applications.

3.2.4 Comparison between type I/II metamaterials and conventional honeycomb ferroelectric material

In order to provide a quantitative comparison between architected cellular ferroelectric metamaterials and conventional honeycomb ferroelectric materials, Figure 3.6 presents normalized optimum figures of merit shown in Figure 3.5, where maximum values of d_h , $d_h \times g_h$, k_t , F_v , and minimum values of Z , K_{33} at different volume fractions are normalized by type I honeycomb ferroelectric materials with same solid volume fraction. F_I and F'_E of cellular ferroelectric metamaterials are not presented here since their optimum values belong to honeycomb ferroelectric materials (Figure 3.5j and l). As shown in Figure 3.6a, the microarchitectures with optimum d_h and $d_h \times g_h$ change for different volume fractions. The improvement, however, decreases when the volume fraction increases. For example, when f_v is 0.4, d_h is increased by 375%, while 138% for $f_v = 0.9$. The achievable improvement for k_t is not considerable as shown in Figure 3.6b; the optimum normalized values of k_t only change in the range from 4.8% to 7.4% for different values of volume fraction and are all from type I metamaterials. However, type II metamaterials show the optimum normalized values for Z ; Z can be decreased by 70.44% compared to honeycomb ferroelectric counterparts when $f_v = 0.4$. It is worth mentioning that lower Z means better performance for an underwater acoustic transducer. In Figure 3.6c, it can be seen that there is a modest improvement for F_v (IR detection), increased by 3.4% ~ 26.5%, and a significant decrease for K_{33} by 23.18% ~ 77.24%, which is appropriate for thermal insulation applications.

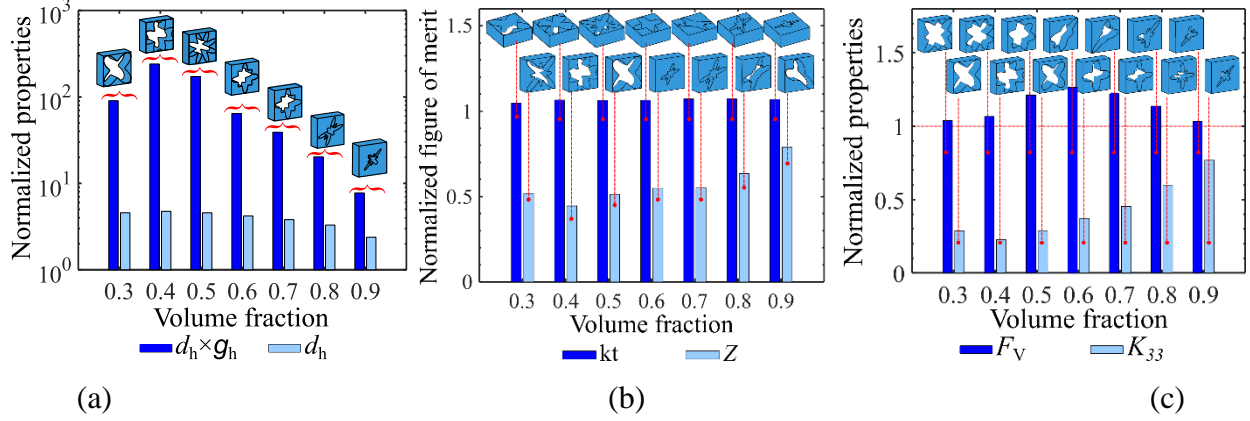


Figure 3.6 Normalized maximum figures of merit of Type I and Type II ferroelectric cellular metamaterials. (Reprinted with permission from ref [188], copyright 2019 Elsevier)

3.3 Porous ferroelectric metamaterials with bi-phase materials

Another two types of metamaterials, type III and type IV, are discussed in this section. Apart from pore shapes and polarization direction, the influence of pore and inclusion volume fraction on the effective properties is also considered.

3.3.1 Influence of inclusion and pore volume fraction on effective piezoelectric properties of type III/IV metamaterials

Figure 3.7 shows the relationship between nine piezoelectric properties and inclusion volume fraction, f_{vi} . Here, two pore volume fractions, $f_{pore} = 0.1$ and $f_{pore} = 0.3$ and two pore shapes with $\alpha = 4$, $\beta = 8$, $c_1 = 0$, $c_2 = 0$ (blue line) and $\alpha = 4$, $\beta = 8$, $c_1 = -0.4$, $c_2 = 0$ (red line), are considered. Due to the inadmissible geometry, inclusion volume fraction varies from 0.3 to 0.6 for $f_{pore} = 0.1$, while changes between 0.2 and 0.4 for $f_{pore} = 0.3$. In general, both inclusion and pore volume fraction are important factors in determining effective piezoelectric properties of type III and type IV metamaterials. However, apart from k_t , inclusion volume fraction has a more obvious influence on these properties. In addition, effective piezoelectric properties are greatly affected by the

polarization direction, while almost insensitive to pore shapes, except for four piezoelectric figures of merit of type IV metamaterials. Specifically,

(i) The three fundamental piezoelectric properties along polarization direction, i.e., E_{33} (Figure 3.7a), κ_{33} (Figure 3.7b), κ_{33}^{σ} (Figure 3.7c) of type III metamaterials show linear relationship with inclusion volume fraction, while nonlinear for type IV metamaterials. In addition, f_{pore} does not show significant influence on these three properties. For example, for type III metamaterials with $c_1 = 0$ and $c_2 = 0$, κ_{33} is $3.41 \times 10^{-9} \text{ C}^2/\text{Nm}^2$ when $f_{\text{pore}} = 0.3$ and $f_{\text{vi}}=0.3$, while the corresponding value for $f_{\text{pore}} = 0.1$ and $f_{\text{vi}}=0.3$ is $3.40 \times 10^{-9} \text{ C}^2/\text{Nm}^2$. It should be mentioned that κ_{33} and κ_{33}^{σ} share the same trend for type III and type IV metamaterials. Therefore, in the following analysis, only κ_{33} is discussed for type III and type IV metamaterials.

(ii) Although decreasing the inclusion volume fraction enhances both d_h (Figure 3.7g) and $d_h \times g_h$ (Figure 3.7g) for type III metamaterials, it is not the same case for considered type IV metamaterials. In addition, for d_h , different polarization directions result in a great difference between type III and type IV metamaterials. However, it is the inclusion volume fraction that determine $d_h \times g_h$ for both types of metamaterials. The reason is that in Figure 3.7d-f, although transverse polarization can significantly increase d_{31} (dash lines in Figure 3.7d) almost to zero, its d_{33} is also decreased to a small value, and correspondingly, the value of d_h for type IV metamaterials are still smaller than that of type III metamaterials, resulting in worse hydrophone performance. The great difference between κ_{33}^{σ} of type III and type IV metamaterials also compensates for the great difference between d_h and type IV metamaterials even higher $d_h \times g_h$. For example, when $c_1 = -0.4$, $c_2 = 0$, $f_{\text{pore}} = 0.3$, $f_{\text{vi}} = 0.4$, d_h of type IV metamaterials (i.e., $3.06 \times 10^{-13} \text{ m}^2/\text{N}$) is 41% higher than that of type III metamaterial (i.e., $2.17 \times 10^{-13} \text{ m}^2/\text{N}$).

(iii) Similar to d_h , k_t of longitudinally polarized type III metamaterials shows obvious superiority over that of type IV metamaterials. However, a lower inclusion volume fraction for both type III and type IV results in better acoustic impedance (smaller Z).

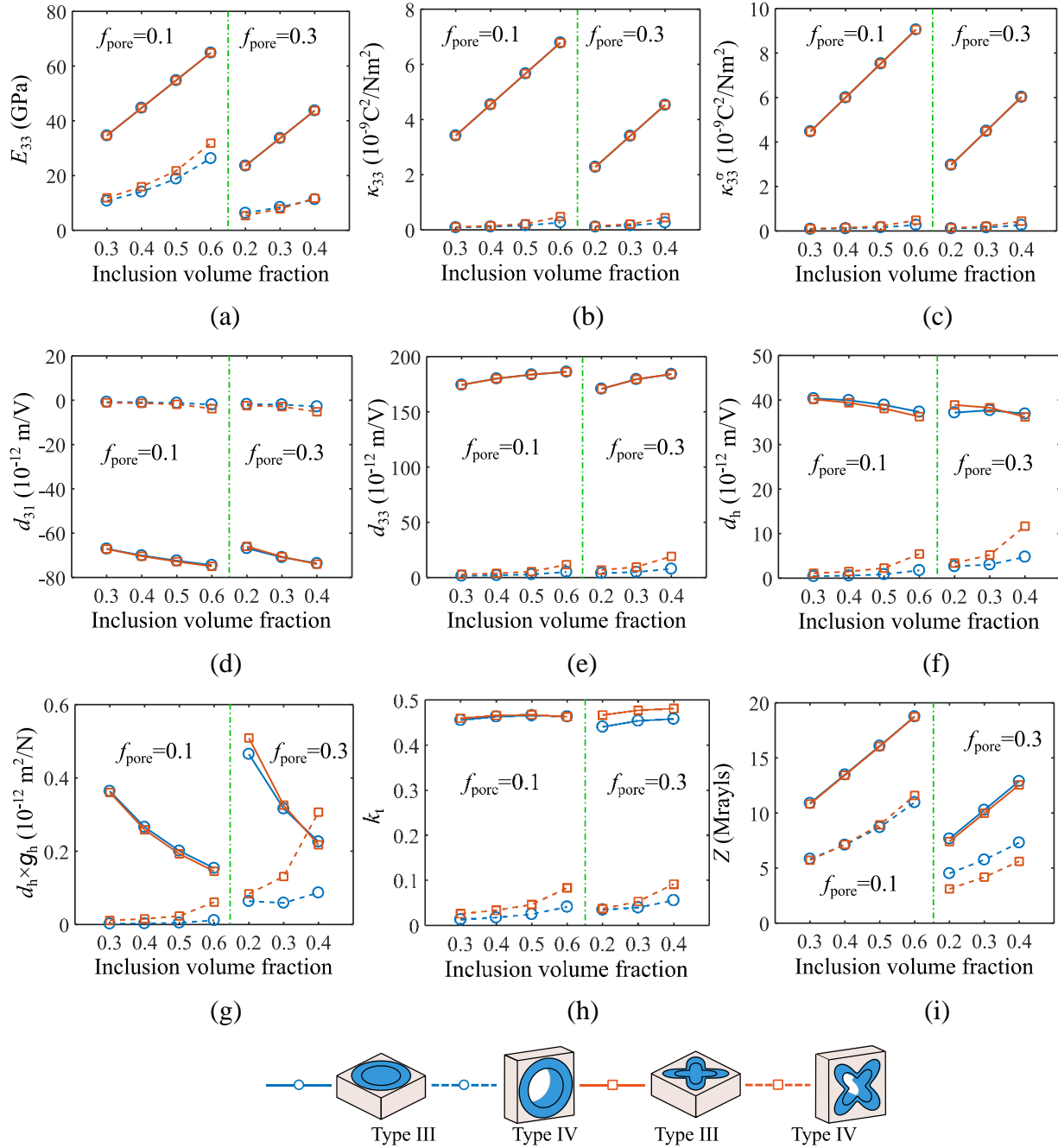


Figure 3.7 Influence of inclusion and pore volume fraction on piezoelectric properties of type III and type IV cellular ferroelectric metamaterials with pore volume fractions $f_{\text{pore}} = 0.1$ and 0.3 , $\alpha =$

4, $\beta = 8$, $c_1 = 0$ and $c_2 = 0$ (blue line), and $c_1 = -0.4$ and $c_2 = 0$ (red line). (Reprinted with permission from ref [188], copyright 2019 Elsevier)

3.3.2 Influence of inclusion and pore volume fraction on effective thermal and pyroelectric properties of type III/IV metamaterials

Figure 3.8 illustrates the variation of six thermal-related properties with respect to different inclusion and pore volume fractions for type III and type IV metamaterials. Overall, all six values of both type III and type IV metamaterials show dependence on inclusion and pore volume fraction. Besides, apart from F_v , polarization direction plays an important role in determining the effective thermal and pyroelectric properties of type III and IV metamaterials. More specifically,

(i) Δ_{33} (Figure 3.8a) of both types of metamaterials shows a decreasing trend with increasing inclusion volume fraction, where Δ_{33} of type III metamaterials is always smaller than that of type IV metamaterials. However, K_{33} (Figure 3.8b) shows a different trend, where K_{33} of four considered metamaterials almost linearly increases with increasing inclusion volume fraction.

(ii) With transverse polarization, p_3 (Figure 3.8c) of type III metamaterials is much higher than that of type IV metamaterials and linearly increases with inclusion volume fraction. In the meantime, increasing pore volume fraction will also improve p_3 of both types of metamaterials. It should be mentioned that since positive p_3 of type IV metamaterials almost decreases to zero for small inclusion volume fraction, with some specific pore shapes, negative p_3 can be found from type IV metamaterials, a similar behavior which has been reported previously for negative thermal expansion coefficient of bi-material lattices [198]. For example, for $c_1 = -0$, $c_2 = 0$, $f_{\text{pore}} = 0.2$, and $f_{\text{vi}} = 0.3$, $p_3 = -0.91 \times 10^{-6} \text{ C/m}^2/\text{K}$. As expected, p_3 and F_1 (Figure 3.8d) share the same trend with respect to inclusion and pore volume fraction.

(iii) Pore shapes, inclusion, and pore volume fraction are important factors in determining F_v for type III and type IV metamaterials (Figure 3.8e). When $f_{\text{pore}} = 0.1$, F_v can be slightly affected

by pore shapes and inclusion volume fraction. However, when $f_{\text{pore}} = 0.3$, properly selecting pore shapes and inclusion volume fraction can achieve a wider range for F_v , even with negative values. F'_E (Figure 3.8f) are greatly associated with polarization direction, where type III metamaterials are more suitable for pyroelectric energy harvesting. In addition, for higher pore volume fractions, tailoring pore shapes is also an efficient method to improve F'_E .

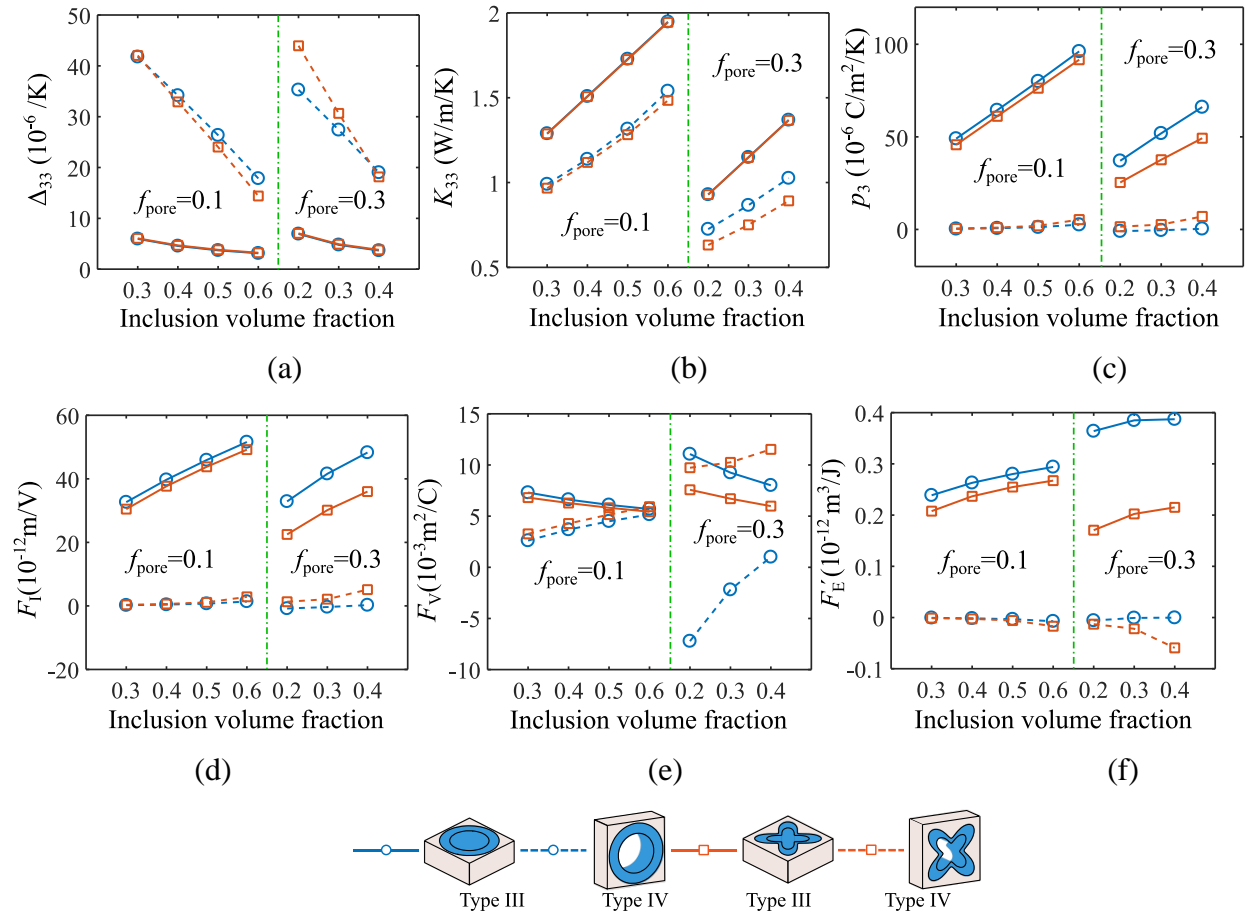


Figure 3.8 Influence of inclusion and pore volume fraction on the thermal related properties of type III and type IV cellular metamaterials with pore volume fractions $f_{\text{pore}} = 0.1$ and 0.3 , $\alpha = 4$, $\beta = 8$, $c_1 = 0$ and $c_2 = 0$ (blue line), $c_1 = -0.4$ and $c_2 = 0$ (red line). (Reprinted with permission from ref [188], copyright 2019 Elsevier)

3.3.3 Relation between effective thermo-electro-mechanical properties of type III/IV metamaterials and inclusion volume fraction

Figure 3.9 shows 12 piezoelectric and pyroelectric property areas for type III and type IV cellular ferroelectric metamaterials, where seven groups of $(f_{\text{pore}}, f_{\text{vi}})$ are selected for presentation: (0.1, 0.3), (0.1, 0.4), (0.1, 0.5), (0.1, 0.6), (0.3, 0.2), (0.3, 0.3) and (0.3, 0.4). The pore shapes considered in Figure 3.9 are determined by the same shape parameters mentioned in Figure 3.2. Therefore, there are 580 different admissible geometries for type III and type IV metamaterials. In addition, the commonly used type III (red solid line) and type IV (black dash line) metamaterials with solid circular inclusion ($c_1 = c_2 = f_{\text{pore}} = 0$) are given in Figure 3.9. Overall, type IV metamaterials are more sensitive to pore shapes and give more property selections. However, with longitudinal polarization, apart from $d_h \times g_h$ (Figure 3.9d), Δ_{33} (Figure 3.9g), F_v (Figure 3.9 k), and F'_E (Figure 3.9l), type III metamaterials always have higher values for all other involved properties. More specially,

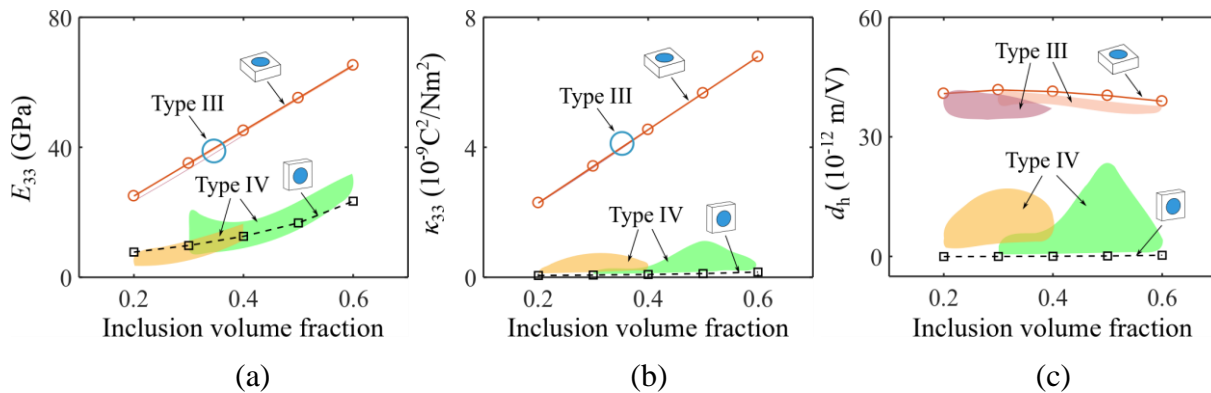
(i) E_{33} and κ_{33} of type III metamaterials are almost insensitive to pore shapes and increase linearly with increasing inclusion volume fraction. Although E_{33} of type IV metamaterials shows independence on inclusion volume fraction, κ_{33} of type IV metamaterials are more affected by pore shapes.

(ii) For type III metamaterials, changing inclusion and pore volume fraction can slightly improve d_h (Figure 3.9c). However, type III metamaterials with solid circular inclusion always have the highest d_h . On the contrary, by tailoring pore shapes, type IV metamaterials can achieve higher $d_h \times g_h$ (Figure 3.9d), where a large pore volume fraction (orange area) exhibits more potential for better hydrophone signal-to-noise performance.

(iii) Type III metamaterials almost remain the same k_t (Figure 3.9e) with different inclusion volume fractions. However, for both type III and type IV metamaterials, Z (Figure 3.9f) shows an obvious increase with increasing inclusion volume fraction. In addition, with a large pore volume fraction (orange area), type IV can achieve lower Z .

(iv) By tailoring pore shapes, type IV metamaterials can provide a wider selection for thermal expansion coefficient Δ_{33} . For example, based on different pore shapes and inclusion volume fractions, type IV metamaterials with $f_{\text{pore}} = 0.3$ (orange area in Figure 3.9g) provide Δ_{33} variation in the range of $21.2 \times 10^{-6} \text{ K}^{-1}$ and $68.5 \times 10^{-6} \text{ K}^{-1}$. In addition, type III metamaterials always give the smallest Δ_{33} . For both type III and type IV metamaterials, increasing inclusion volume fraction will increase K_{33} (Figure 3.9h), and tailoring pore shapes just has little influence.

(v) As expected, p_3 (Figure 3.9i) and F_1 (Figure 3.9j) share the same pattern and increasing inclusion volume fraction will enhance the pyroelectric effect and current responsivity of type III metamaterials. However, for F_V (Figure 3.9k) and F'_E (Figure 3.9l), tailoring the pore shapes is an effective method to obtain higher values to improve the performance of cellular ferroelectric metamaterials for IR detection and Pyroelectric energy harvesting. For example, compared to type III metamaterials with $\alpha = 4$, $\beta = 8$, $c_1 = c_2 = f_{\text{pore}} = 0$ and $f_{\text{vi}} = 0.3$ (solid red line), F_V and F'_E of type IV metamaterials are improved by 249.1% and 119.3 %, respectively.



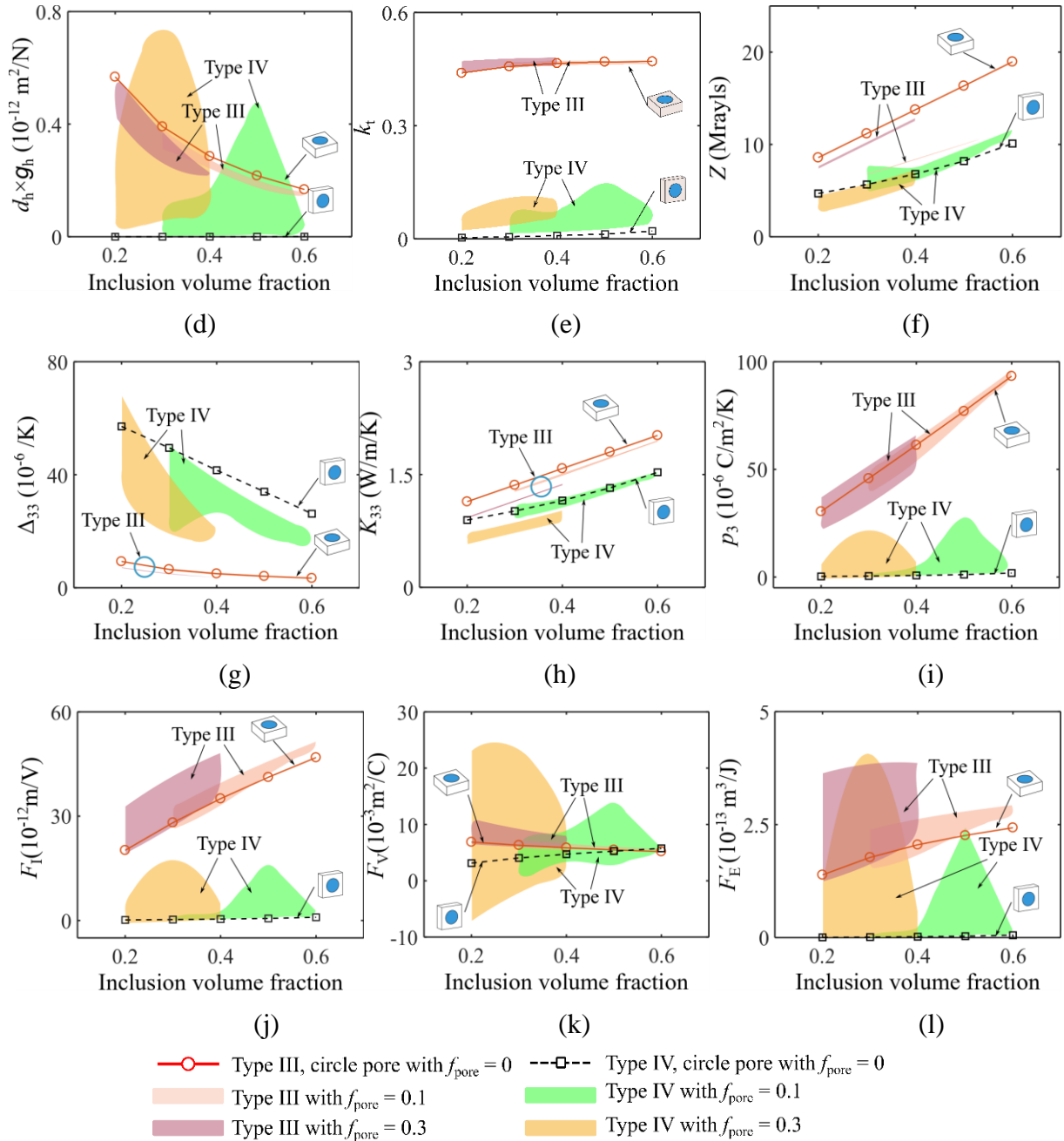


Figure 3.9 Design charts for thermo-electro-mechanical properties and figures of merit of type III and type IV cellular ferroelectric metamaterials for a wide range of inclusion solid volume fraction f_{vi} from 0.2 to 0.6. (Reprinted with permission from ref [188], copyright 2019 Elsevier)

3.4 Comparison between type I/II/III/IV metamaterials

A quantitative comparison between type I, type II, type III, and type IV cellular ferroelectric metamaterials are provided in Table 3.3, where all values are normalized by the corresponding

ones of type I honeycomb metamaterials. Both E_{33} and κ_{33} of type I and III metamaterials are higher than their counterparts of type II and type IV metamaterials. d_{31} , d_{32} , and d_{33} of type II, type III, and type IV metamaterials are all smaller than the corresponding properties of type I metamaterials. However, due to the different signs of d_{31} and d_{32} with d_{33} , type II and type III metamaterials have better hydrophone performance, while type IV metamaterials almost have zero d_h and $d_h \times g_h$. The improvement for k_t is limited, and the highest value is reported for type I metamaterials. Both type II and type IV metamaterials show smaller Z compared to type I and type III metamaterials. However, due to the poor performance on d_h , $d_h \times g_h$ and k_t of type IV metamaterials, type II metamaterials are more suitable for piezoelectric applications. For thermal-related properties, Δ_{33} can be greatly increased by type III and type IV metamaterials while remaining at the same value for type I and type II metamaterials. Both longitudinal polarization and adding matrix with higher K_{33} can be used to obtain higher effective thermal conductivity K_{33} . Therefore, type III metamaterials have the highest K_{33} , while type II metamaterials have the smallest one. Although type III metamaterials have the highest p_3 , for pyroelectric figures of merit of F_I , F_V and F'_E , type I metamaterials show better overall performance. It should be mentioned that since thermo-electro-mechanical properties of type IV metamaterials are strongly dependent on pore shapes, these properties for type IV metamaterials presented in Table 3.3 can be tuned arbitrarily.

Table 3.3. Comparison of properties of four types of cellular ferroelectric metamaterials with the solid volume fraction of 0.3. The considered type I and type II metamaterials are: regular honeycomb (left), $c_1 = 0$ and $c_2 = 0$ (middle) and $c_1 = -0.4$ and $c_2 = 0$ (right). From left to right, type III and type IV metamaterials include: $c_1 = 0$, $c_2 = 0$ and $f_{\text{pore}} = 0$ (first one), $c_1 = 0$, $c_2 = 0$ and $f_{\text{pore}} = 0.1$ (second one), $c_1 = 0$, $c_2 = 0$ and $f_{\text{pore}} = 0.3$ (third one), $c_1 = -0.4$, $c_2 = 0$ and $f_{\text{pore}} = 0.1$ (fourth one) and $c_1 = 0$, $c_2 = 0$ and $f_{\text{pore}} = 0.3$ (fifth one).

	Type I			Type II			Type III					Type IV				
																
E_{33}	1.00	1.00	1.00	0.18	0.46	0.25	1.11	1.09	1.06	1.09	1.06	0.31	0.34	0.27	0.38	0.25
κ_{33}	1.00	1.00	1.00	0.63	0.45	0.24	1.01	1.01	1.01	1.01	1.01	0.02	0.03	0.05	0.03	0.06
d_{31}	1.00	1.00	1.00	0.55	0.43	0.23	0.83	0.85	0.90	0.86	0.90	0.01	0.01	0.03	0.01	0.04
d_{32}	1.00	1.00	1.00	0.02	0.02	-0.01	0.83	0.85	0.90	0.86	0.90	0.00	0.00	0.00	0.01	0.02
d_{33}	1.00	1.00	1.00	0.94	0.93	0.90	0.90	0.91	0.94	0.91	0.94	0.00	0.01	0.03	0.02	0.05
d_h	1.00	1.01	1.01	3.97	4.17	4.57	1.23	1.19	1.11	1.18	1.13	0.00	0.01	0.09	0.03	0.15
$d_h \times g_h$	1.00	1.02	1.02	28.5	39.9	90.4	1.55	1.44	1.25	1.43	1.29	0.00	0.01	0.23	0.04	0.52
kt	1.00	1.02	1.05	0.78	1.00	1.00	0.98	0.98	0.98	0.99	1.03	0.01	0.03	0.09	0.06	0.11
Z	1.00	0.99	0.98	0.58	0.65	0.47	1.26	1.23	1.16	1.22	1.13	0.64	0.66	0.65	0.65	0.47
Δ_{33}	1.00	1.00	1.00	1.00	1.00	1.00	3.28	2.99	2.41	3.05	2.47	24.9	21.0	13.8	21.1	15.4
K_{33}	1.00	1.00	1.01	0.58	0.45	0.24	1.56	1.48	1.32	1.48	1.32	1.17	1.14	0.98	1.07	0.80
p_3	1.00	0.95	0.88	0.35	0.44	0.23	1.11	1.19	1.26	1.11	0.91	0.01	0.01	0.01	0.01	0.06
F_1	1.00	0.95	0.88	0.35	0.44	0.23	0.51	0.59	0.75	0.55	0.54	0.01	0.00	0.01	0.01	0.04
F_V	1.00	0.95	0.88	0.63	1.01	1.02	0.52	0.60	0.76	0.56	0.55	0.33	0.21	0.18	0.27	0.84
F_E	1.00	0.90	0.77	0.21	0.44	0.24	0.26	0.35	0.57	0.31	0.30	0.00	0.00	0.00	0.00	0.03

Figure 3.10 shows the lightweight and multifunctional potential for four types of metamaterials considered in this section. Here $\bar{\rho}$ is the relative density of metamaterial and $(\cdot)^s$ means solid BaTiO₃ property. It is clear that type II metamaterials have the best hydrophone sensitivity and hydrophone signal-to-noise ratio simultaneously (Figure 3.10a). In addition, type II metamaterials also hold this advantage for lightweight hydrophone design (Figure 3.10b). As shown in Figure 3.10c, type I metamaterials have a combination of large Z/Z^s and $k_t/(k_t)^s$ while type II metamaterials have a combination of the smallest Z/Z^s and reasonable $k_t/(k_t)^s$. However, for a given mass, type II metamaterials have the potential to design lightweight structures with the smallest acoustic impedance and highest energy coupling factor, similar to that of type I and type III metamaterials by tailoring pore shapes (Figure 3.10d). As for pyroelectric application, type I

metamaterials, especially type I honeycomb, are most suitable for designing devices/lightweight devices with the best current responsivity and pyroelectric energy harvesting performance (Figure 3.10e and f). However, in Figure 3.10g and h, type IV metamaterials provide the highest voltage responsivity, even with the lightest mass, while type I metamaterials still have the highest value for pyroelectric harvesting figure of merit.

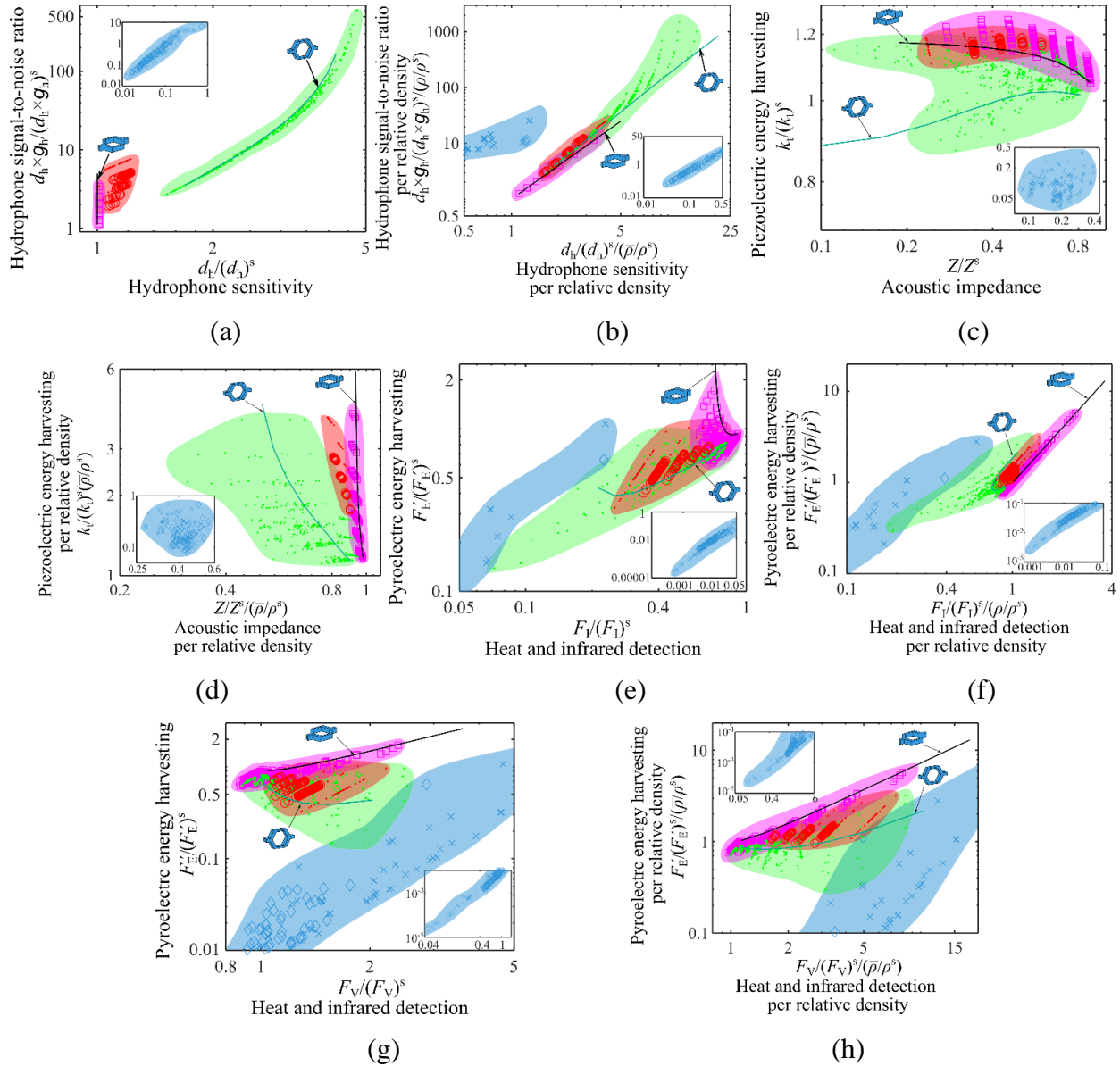


Figure 3.10 Comparison between piezoelectric and pyroelectric applications of four types of metamaterials. (Reprinted with permission from ref [188], copyright 2019 Elsevier)

3.5 Concluding remarks on 2D extruded cellular ferroelectric metamaterials

In this chapter, architected cellular ferroelectric metamaterials with periodic tunable microarchitectures are introduced as a new class of advanced multifunctional materials with optimized stiffness-to-weight ratio, thermal conductivity, and piezoelectric properties while reducing the consumption of environmentally-incompatible materials (e.g., lead-based ferroelectric materials) in smart structures. However, it has not been studied if the thermo-piezoelectric properties of smart materials with a 1-3 type of pores could be further optimized by tailoring the pore shape and introducing a non-ferroelectric matrix. The section conducts a strategic study on the role of pore microarchitecture and non-ferroelectric matrix on the effective thermo-electro-mechanical properties of 1-3 type of architected ferroelectric cellular metamaterials. The research leads to the following principal conclusions:

(1) E_{33} , e_{33} , κ_{33} , K_{33} , and four ferroelectric figures of merit of type I cellular ferroelectric metamaterials are insensitive to the pore architecture. However, p_3 and three pyroelectric figures of merit reveal great dependence on the pore architecture. In contrast, apart from thermal expansion and total pyroelectric constants, the other thermo-electro-mechanical properties of type II cellular ferroelectric metamaterials can be improved by optimizing the cell pore shape of smart metamaterials. For example, the $d_h \times g_h$ of an architected cellular ferroelectric metamaterial can be increased by 238% compared with a type II honeycomb cellular ferroelectric materials with the same volume fraction, which is appropriate for hydrophone devices.

(2) Δ_{33} and γ_3 of architected cellular metamaterials made of single ferroelectric materials are independent of the pore architecture, which has been proved mathematically.

(3) E_{33} , κ_{33} , d_h , k_t , Z , K_{33} , p_3 , and F_I of type III bi-phase metamaterials are always higher than that of type IV bi-phase metamaterials. In addition, for the given pore volume fraction of type III

metamaterials, decreasing the inclusion volume fraction is an effective method to improve $d_h \times g_h$ and Z for hydrophone devices. Furthermore, by tailoring the pore shapes, $d_h \times g_h$, F_V and F'_E of type IV metamaterials will exceed those of type III metamaterials. For example, maximum $d_h \times g_h$, F_V and F'_E of type IV metamaterials with inclusion volume fraction of 0.3 are 90.3%, 249.1%, and 119.3% higher than those of type III ferroelectric composite with solid circle ferroelectric inclusion.

(4) Among the four types of cellular ferroelectric metamaterials, type II metamaterials have the best performance on d_h , $d_h \times g_h$ and Z revealing their optimum performance for hydrophone devices, while E_{33} , κ_{33} , and K_{33} of type III metamaterials are higher than the others. The Δ_{33} of type IV metamaterials is always the largest, and d_h , $d_h \times g_h$, p_3 and three pyroelectric figures of merit of type IV metamaterials are strongly dependent on the pore shapes.

(5) Several factors contribute to the difference among the thermo-electro-mechanical properties of designed four types cellular ferroelectric metamaterials. For type I metamaterials, stretching deformation mode along the polarization direction results in larger E_{33} . However, for type II metamaterials, a lower bending dominant stiffness leads to larger deformation and higher hydrostatic charge constants. In some specific conditions, due to the porosity between two polarization faces or the existence of a non-ferroelectric matrix, smaller κ_{33} also contributes to a higher d_h and $d_h \times g_h$ for type II metamaterials and a higher $d_h \times g_h$, F_V , and F'_E for type IV metamaterials.

CHAPTER 4

3D Hierarchical lattice ferroelectric metamaterials

This chapter covers the effective ferroelectric properties of 3D hierarchical lattice ferroelectric metamaterials. The effect of hierarchical order, lattice topology, and relative density on piezoelectric and pyroelectric figures of merit as measures for assessing the performance of ferroelectric metamaterials as sensors and energy harvesters is explored. The chapter is divided into five main sections, including hierarchical lattice architectures, 1st-order lattice ferroelectric metamaterials, high-order hierarchical lattice ferroelectric metamaterials, comprehensive 2nd-order figures of merit, and a discussion on the scaling relationship.

4.1 3D hierarchical lattices

Figure 4.1 shows 3D lattice unit cells for constructing hierarchical lattice ferroelectric metamaterials examined in this study. The simple cube (SC), face-diagonal cube (FDC), face-centered cube (FCC), body-centered cube (BCC), octahedron, and octet truss are lattice topologies extensively studied here. The cuboctahedron, the only stretching-dominated Archimedean polyhedron, and tetrakaidecahedron, a bending-dominated polyhedron that minimizes the surface-

to-volume ratio, are also studied to evaluate their ferroelectric performance ([194]). Apart from the regular lattice unit cells (ratio of height and length, or aspect ratio, as 1) in Figure 4.1b, scaled-up and down counterparts along polarization direction (direction 3) with aspect ratios of 4 and 0.25, where the architectural features are retained, are also considered (Figure 4.1 a). Therefore, aspect ratio (AR), beam thickness (t), and unit cell length (L) determine these lattice architectures.

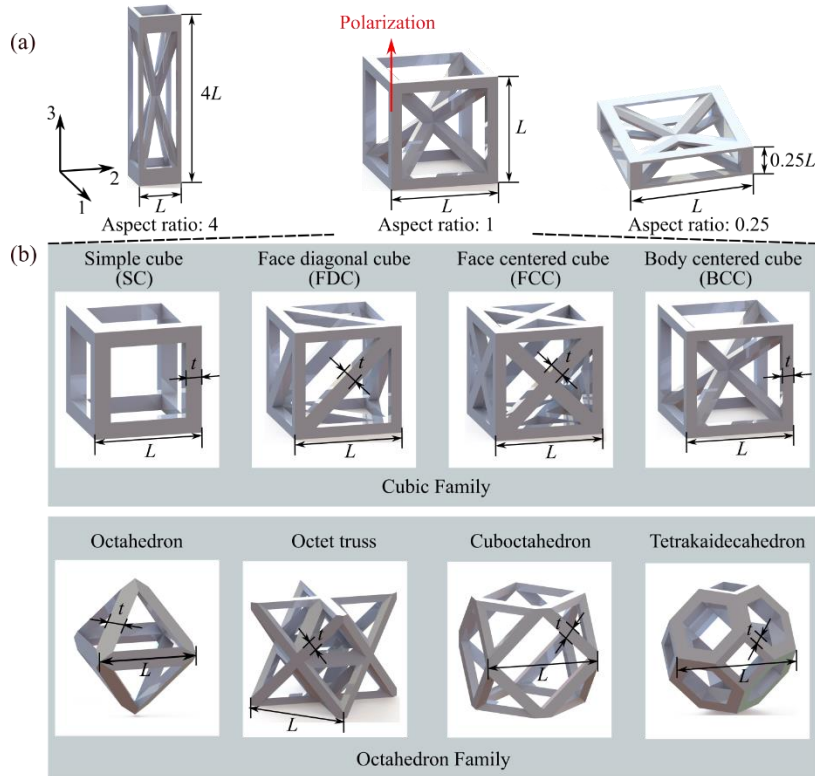


Figure 4.1 Topology of eight lattice architectures considered in this research: (a) Lattice architectures with three different aspect ratios and (b) Cubic and octahedron families with aspect ratio of 1. (Reprinted with permission from ref [192], copyright 2020 Elsevier)

Depending on the architecture of ferroelectric metamaterials, the lattice unit cells can be divided into two microarchitectural categories, i.e., cubic and octahedron families of unit cells (see Figure 4.1b). Another important criterion to classify lattice materials is their deformation mechanism which includes two categories, i.e., stretching-dominated and bending-dominated lattice materials. The former generates axial forces in the lattice struts upon external loading and is more

mechanically efficient (with a higher stiffness-to-weight ratio) than its bending-dominated counterpart, whose constituent beams mainly deform by bending. As shown in the spherical plot of the power law relationship between Young's modulus and relative density (see Figure 4.2), apart from the simple cube (Figure 4.2b) and tetrakaidekahedron (Figure 4.2i), all other lattice materials are stretching-dominated in all directions, even in directions not aligned with the symmetry axes of the architectures, showing the value of scaling power approaching 1. However, for the face-diagonal cube (Figure 4.2c), due to the asymmetry of cell architecture, its value of scaling power is slightly higher than 1, i.e., around 1.13, in the yellow area, leading to a mixed mode deformation. The simple cube (Figure 4.2b) is bending-dominated in all directions except in three directions aligned with the struts. In opposite, the tetrakaidekahedron (Figure 4.2i) is bending-dominated in all directions. Generally, the mechanical behavior of 3D lattice materials can be predicted by their connectivity (Z_n), which indicates the average number of struts connected at a node. Based on Maxwell's rule, the *necessary* and *sufficient* condition for 3D stretching-dominated lattice materials is $Z_n \geq 12$, e.g., $Z_n = 12$ for octet truss. In addition, the *necessary* condition for 3D stretching-dominated lattice materials is $Z_n \geq 6$, e.g., body-centered cube ($Z_n = 11$) and cuboctahedron ($Z_n = 8$) [199]. Compared with octet truss, although topologies with lower connectivities still can be stretching-dominated, they are more sensitive to imperfections and easy to activate bending deformation. The connectivity of tetrakaidekahedron is $Z_n = 4$, which does not satisfy the necessary condition for stretching-dominated lattice materials.

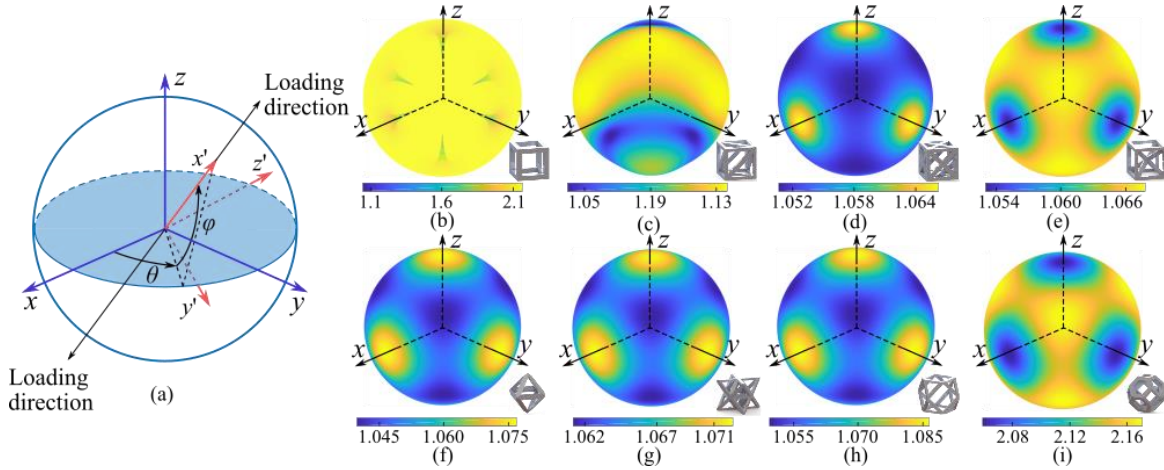


Figure 4.2 (a) Coordinate transformation. Power law relationship along different directions for (b) SC, (c) FDC, (d) FCC, (e) BCC, (f) Octahedron, (g) Octet truss, (h) Cuboctahedron and (i) Tetrakaidecahedron. (Reprinted with permission from ref [192], copyright 2020 Elsevier)

Since relative density, or volume fraction, does not change by scaling-up and scaling-down operation, the relative density (ρ) is only a function of t/L , and their relationship is given in Figure 4.3. Apart from octet truss and cuboctahedron, the least-square polynomial fitting method with cubic polynomial is used to express these relationships. In order to retain its architectural features, the maximum achievable relative density for tetrakaidecahedron is 0.5, which is the smallest value among the lattice architectures considered in this research.

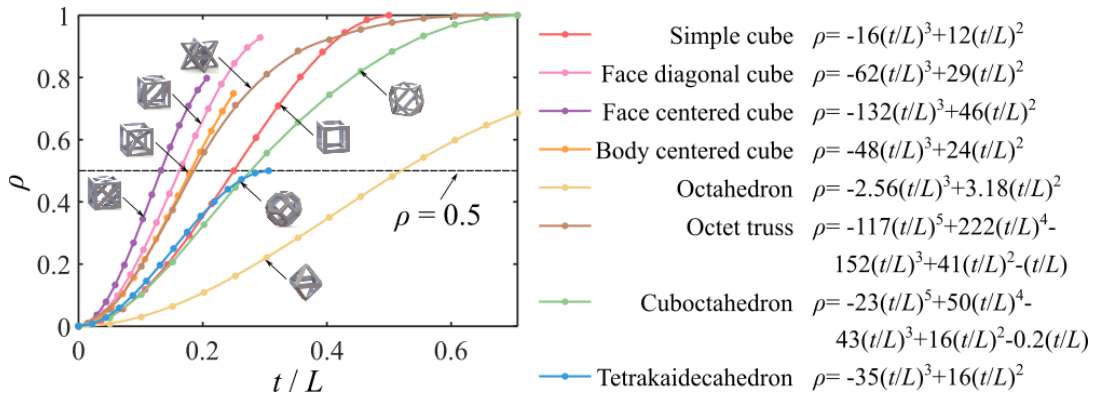


Figure 4.3 Relationship between relative density and architectural parameters for ferroelectric lattice metamaterials. (Reprinted with permission from ref [192], copyright 2020 Elsevier)

Based on the two families of lattices introduced in Figure 4.1, three families of hierarchical lattice ferroelectric metamaterials, i.e., cubic, octahedron, and hybrid families of hierarchical lattice ferroelectric metamaterials, are developed. Figure 4.4a illustrates the process of designing a 3rd-order hierarchical lattice metamaterial. For example, a 0th-order repeating unit, i.e., a square cross-section beam, is arranged into a 1st-order body-centered cube (BCC) architecture; it becomes the repeating unit cell for a 2nd-order H-BCC (H stands for hierarchical), which can be then arranged to create a 3rd-order H-BCC. This process can be repeated arbitrarily until a desired hierarchical order of H-BCC is achieved. It should be mentioned that this recursive design method patterns the unit cell based on constitutive beams of a self-similar unit cell, resulting in a fractal-like geometry. For the hybrid family of hierarchical lattice ferroelectric metamaterials, the unit cells in consecutive orders can be dissimilar, and the arrangement of their hierarchical orders can also be different. As shown in Figure 4.4b, cubic family hierarchical lattice ferroelectric metamaterials include four types of hierarchical lattice architectures: hierarchical simple-cube (H-SC), hierarchical face-diagonal cube (H-FDC), hierarchical face-centered cube (H-FCC), and hierarchical body-centered cube (H-BCC). Similarly, the octahedron family of hierarchical lattice ferroelectric metamaterials (Figure 4.4c) consists of the hierarchical octahedron (H-Octahedron), hierarchical octet truss (H-Octet truss), hierarchical cuboctahedron (H-Cuboctahedron), and hierarchical tetrakaidecahedron (H-Tetrakaidecahedron). Each hierarchical lattice ferroelectric metamaterial of the hybrid family contains at least two kinds of lattice architectures, e.g., 2nd-order H-BCC/Octet truss and H-Octet truss/BCC (Figure 4.4d).

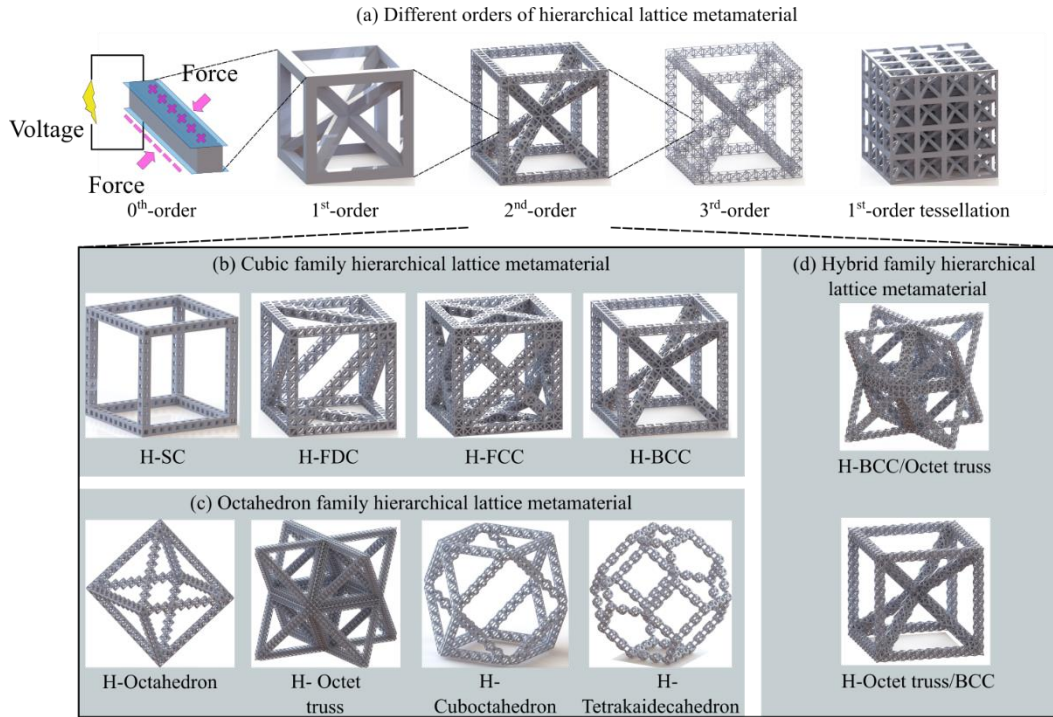


Figure 4.4 Hierarchical configurations: (a) Pattern mechanism, (b) Cubic family, (c) Octahedron family, and (d) Hybrid family. (Reprinted with permission from ref [192], copyright 2020 Elsevier)

In the following Sections, I conduct a computational approach based on previous proposed multiscale asymptotic homogenization (MAH) to theoretically predict the effect of hierarchical orders, unit cell topologies, and aspect ratio on the thermo-electro-mechanical properties of hierarchical lattice ferroelectric metamaterials. The solid material is BaTiO₃, an ecofriendly and biocompatible ferroelectric material, whose ferroelectric properties are provided in Tables 3.1 and 3.2.

4.2 1st-order lattice ferroelectric metamaterials

The 1st-order lattice ferroelectric metamaterials with different cell topologies are studied first to evaluate their piezoelectric and pyroelectric application. Figure 4.5 presents the influence of lattice topology, aspect ratio, and relative density on the eight figures of merit of ferroelectric metamaterials. Herein, three aspect ratios (AR), i.e., 0.25, 1, and 4, are considered, and the relative

density is selected between $0 \sim 0.5$, in accordance with the maximum achievable relative density for the 1st-order tetrakaidecahedron which is 0.5. All these figures of merit in this section are normalized by the corresponding value of the solid material. Apart from current responsivity, F_I , tailoring the microarchitecture of 1st-order ferroelectric metamaterials can significantly improve their piezoelectric and pyroelectric figures of merit. Detailed observations are made as follows:

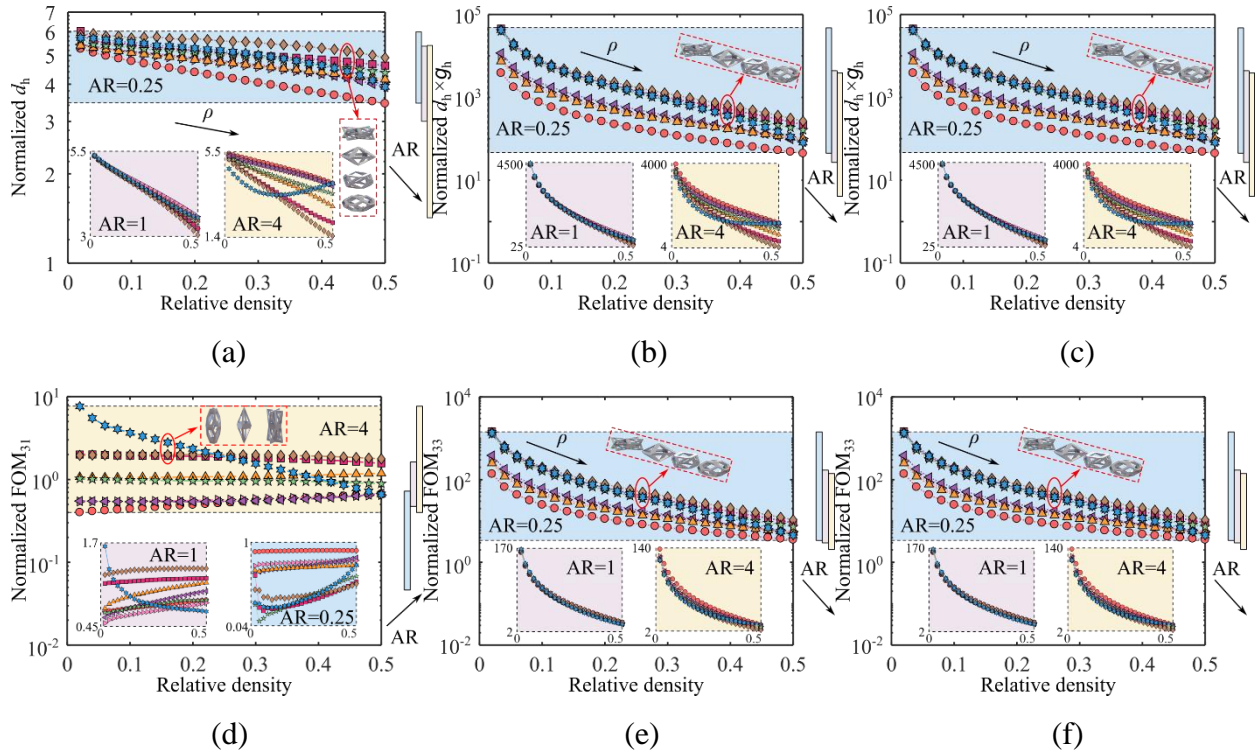
(i) Normalized hydrostatic charge coefficient (d_h) and hydrostatic figure of merit ($d_h \times g_h$) are always larger than 1, while acoustic impedance (Z) is smaller than 1 for all considered cases (see Figure 4.5a-c), which means the performance of hydrophone devices made out of lightweight 1st-order ferroelectric metamaterials is better than the one made of a solid ferroelectric material. In addition, for ferroelectric metamaterials with aspect ratios (AR) as 0.25, their d_h and $d_h \times g_h$ are the largest while Z is the smallest, suggesting that scaling down the ferroelectric lattice metamaterials can further improve the hydrophone device performance. Furthermore, the octahedron family, especially the 1st-order octet truss, shows a better performance for hydrophone application than the cubic family. For example, when $AR = 0.25$ and $\rho = 0.2$, the smallest normalized d_h for the octahedron family is 5.12 (1st-order cuboctahedron), while the largest one for a cubic family is 4.91 (1st-order face diagonal cube). It should be mentioned that except 1st-order tetrakaidecahedron with $AR = 4$, normalized hydrostatic charge coefficient (d_h) and hydrostatic figure of merit ($d_h \times g_h$) of all other ferroelectric metamaterials show a descending trend by increasing the relative density; however, an increase in relative density results in the increase of normalized acoustic impedance (Z).

(ii) In contrast to Figure 4.5a-c, only a few 1st-order ferroelectric metamaterials can improve the figure of merit (FOM_{31}) of bending mode piezoelectric energy harvesters (Figure 4.5d). In addition, scaling up the lattice architecture to aspect ratios (AR) of 4 can further increase the

improvement. More specifically, when $AR = 4$, all lattice metamaterials, apart from the 1st-order tetrakaidecahedron, are almost insensitive to relative density. For example, normalized FOM_{31} of 1st-order simple cube with $AR = 4$ varies from 1.96 to 1.98 when relative density changes from 0.02 to 0.3. Octahedron family, especially 1st-order tetrakaidecahedron, 1st-order octahedron, and 1st-order octet truss, demonstrates a higher FOM_{31} than that of the cubic family for $AR = 4$ and 1. As shown in Figure 4.5e, the trend for direct mode piezoelectric energy harvester figure of merit (FOM_{33}) is similar to that of hydrostatic charge coefficient (d_h) and hydrostatic figure of merit ($d_h \times g_h$), where higher FOM_{33} can be obtained by scaling downing the octahedron family lattice metamaterials and decreasing the relative density.

(iii) In Figure 4.5f, the normalized current responsivity (F_I) of all ferroelectric metamaterials is smaller than 1, and an increase in the relative density increases the normalized F_I . This suggests that ferroelectric lattice metamaterials are not suitable for infrared devices, which require high values of F_I . However, for designing lightweight heat and infrared devices, Figure 4.5f suggests that scaling up ($AR = 4$) the architecture of lattice metamaterials generates more current for a given temperature difference. As shown in Figure 4.5g, normalized voltage responsivity (F_V) is insensitive to the aspect ratio, while it changes from 30.07 to 1.11 when relative density varies between 0.02 and 0.5. Moreover, the normalized F_V of all ferroelectric metamaterials is larger than 1, which indicates their potential applications for heat and infrared devices, which requires high F_V . As opposed to Figure 4.5a-f, the cubic family shows a higher normalized voltage responsivity (F_V) than that of the octahedron family. For example, when $AR = 0.25$ and relative density is 0.1, the smallest normalized F_V for the cubic family is 6.0 (1st-order body-centered cube), while the largest one for the octahedron family is 5.0 (1st-order tetrakaidecahedron).

(iv) Similar to FOM_{31} and F_I , scaling up the architecture of ferroelectric metamaterials (AR = 4) can increase the normalized pyroelectric energy harvesting figure of merit (F_E^I) (see Figure 4.5h). In addition, apart from 1st-order octahedron, 1st-order octet truss, and 1st-order cuboctahedron with aspect ratios (AR) of 0.25, decreasing relative density can remarkably increase normalized F_E^I . For example, the normalized F_E^I of 1st-order octet truss with AR = 4 decreases from 10.58 to 0.86 by increasing relative density from 0.02 to 0.4. Furthermore, when aspect ratio is 4, the octahedron family shows a better pyroelectric energy harvesting performance compared with that of the cubic family; when the aspect ratio is 0.25 and 1, the cubic family is desired for thermal energy harvesting applications with a higher F_E^I .



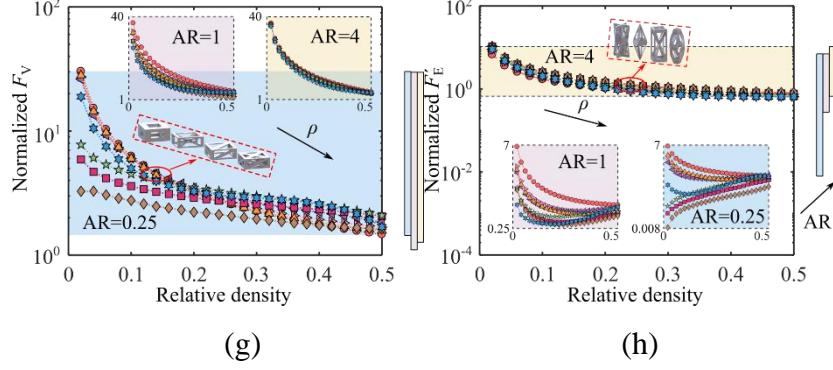


Figure 4.5 Normalized piezoelectric and pyroelectric figures of merit of 1st-order lattice ferroelectric metamaterials with different aspect ratios and relative densities. (Reprinted with permission from ref [192], copyright 2020 Elsevier)

4.3 High-order hierarchical lattice ferroelectric metamaterials

When designing high order ($n \geq 2$) hierarchical lattice metamaterials, three factors, i.e., hierarchical order, lattice topology, and relative density, should be considered. Herein, the influence of these three factors is studied to optimize the performance of hierarchical lattice metamaterials for piezoelectric and pyroelectric applications.

4.3.1 Influence of order of hierarchy on the improvement of figures of merit

Three hierarchical orders, i.e., $n = 2, 3$, and 4, are considered for hierarchical body-centered cube (H-BCC) and hierarchical octet truss (H-Octet truss) with an aspect ratio (AR) of 1 in Figure 4.6. The overall relative densities for these hierarchical lattice metamaterials are all kept at 0.05. The figures of merit for H-BCC and H-Octet truss are compared with those of 1st-order BCC and 1st-order octet truss with the same relative density, respectively, to determine the possible improvement achievable by higher orders of hierarchical metamaterials (see Figure 4.6a). Although hydrostatic charge coefficient (d_h) is almost insensitive to hierarchical orders, compared with the 1st-order metamaterials, the hydrostatic figure of merit ($d_h \times g_h$), piezoelectric (FOM₃₁ and FOM₃₃), and pyroelectric (F'_E) energy harvesting figures of merit, and voltage responsivity (F_V)

are all significantly increased, and acoustic impedance (Z) is remarkably decreased, which is suitable for hydrophone applications requiring low Z values. In addition, increasing hierarchical orders can further optimize the figures of merit, as indicated by the ellipses in Figure 4.6a. For example, for H-BCC, the improvement of the hydrostatic figure of merit ($d_h \times g_h$) increases from 48.7% to 162.1% by increasing the order of hierarchy from 2 to 4. However, for current responsivity (F_I), 2nd-order, 3rd-order, and 4th-order H-Octet truss almost have the same improvement (around 30%). Meanwhile, although 2nd-order H-BCC shows slight improvement for F_I , further increasing the hierarchical order decreases this value from 7.4% (2nd-order H-BCC) to -16.9% (4th-order H-BCC). One important reason for the improvement of $d_h \times g_h$, FOM_{31} , FOM_{33} , F_V , and F'_E is the decrease of κ_{33}^σ (dielectric constant under constant stress) of lattice material. Based on asymptotic homogenization, the effective κ_{33}^σ can be seen as the average D_3 (charge density along direction 3) over the unit cell with periodic boundary conditions and a uniform E_3 (electric field along direction 3). Figure 4.6b shows the distribution of D_3 within the solid material, 1st-order octet truss, and 1st-order BCC normalized by the uniform D_3 of solid material, whose average value can be seen as effective κ_{33}^σ . Most trusses of the 1st-order octet truss and 1st-order BCC show normalized D_3 smaller than 1, especially for those perpendicular to direction 3. Similar to stress concentration due to geometric discontinuities, there are also charge density concentrations on truss connection areas, resulting in large charge density (D_3) in small local areas. Therefore, replacing more solid ferroelectrics with lattice architectures and increasing the order of hierarchy results in smaller effective κ_{33}^σ . In Figure 4.6c, the left figure depicts the voltage distribution of a ferroelectric unimorph cantilever beam under unit point force at its tip. All voltage is normalized by the maximum value of unimorph cantilever beam with solid ferroelectric material. The right figure shows that increasing the hierarchical orders enhances the output voltage of

ferroelectric unimorph cantilever beams by increasing g_{33} (piezoelectric voltage constant along direction 3, given by $d_{33}/\kappa_{33}^\sigma$).

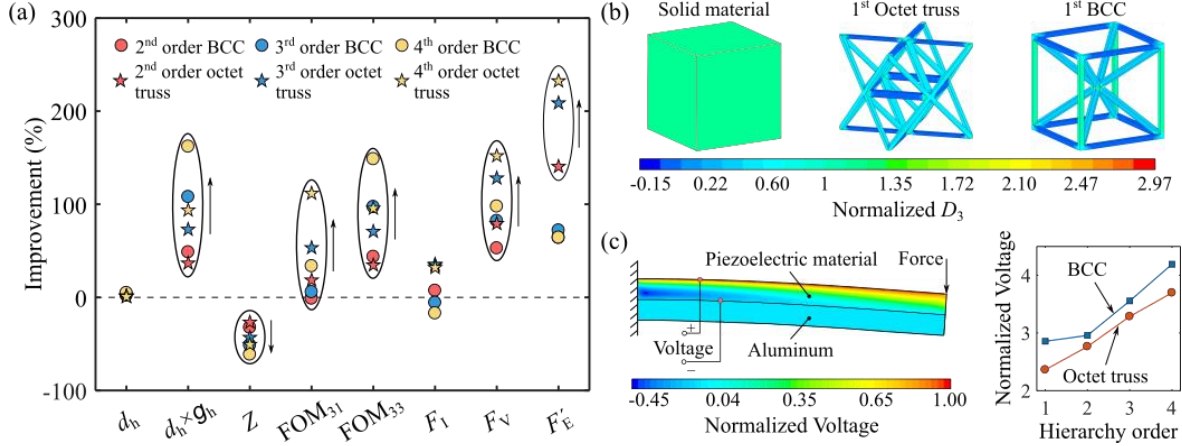


Figure 4.6 (a) Influence of hierarchical order on the improvement of figures of merit. The overall relative densities for these hierarchical lattice metamaterials are kept at 0.05. More specifically, when $n = 2$, the relative densities for 1st-order and 2nd-order are 0.1 and 0.5, respectively; when $n = 3$, the relative densities for the 1st -order, 2nd-order, and 3rd-order are 0.2, 0.5, and 0.5, respectively; when $n = 4$, the relative densities for 1st-order, 2nd-order, 3rd-order and 4th-order are 0.4, 0.5, 0.5 and 0.5, respectively; (b) Normalized D_3 of solid material, 1st-order octet-truss, and 1st-order BCC; (c) Influence of hierarchical order on the output voltage of ferroelectric unimorph cantilever beam. (Reprinted with permission from ref [192], copyright 2020 Elsevier)

4.3.2 Influence of lattice architecture on the improvement of figures of merit of 2nd-order hierarchical ferroelectric metamaterials

Figure 4.7 illustrates the improvement of figures of merit for 2nd-order hierarchical body-centered cube (H-BCC), H-BCC/Octet truss, H-Octet truss/BCC, and H-Octet truss with respect to the 1st-order BCC of the same relative density, where the overall relative density of these four metamaterials is 0.05. As expected, lattice topology is an important factor in determining the improvement of figures of merit. For example, the improvement of pyroelectric energy harvesting figure of merit (F'_E) for 2nd-order H-BCC is 64.1%, while it is 14.4% for 2nd-order H-Octet truss. Although the mindset is that the properties of hybrid metamaterials should be between those of

their constituents, hybrid hierarchical lattice ferroelectric metamaterials can reveal piezoelectric and pyroelectric properties not achievable by fractal-like metamaterials. Figure 4.7 reveals that hybrid hierarchical lattice ferroelectric metamaterials show the maximum improvement for the hydrostatic charge coefficient (d_h), hydrostatic figure of merit ($d_h \times g_h$), piezoelectric (direct mode FOM₃₃), and pyroelectric (F'_E) energy harvesting figures of merit and the minimum one for the acoustic impedance (Z). For example, the improvement of FOM₃₃ of 2nd-order H-Octet truss/BCC is 50.7%, which is higher than that of both 2nd-order H-BCC (43.8%) and H-Octet truss (43.2%). In contrast, the 2nd-order fractal-like H-Octet truss shows the maximum improvement for FOM₃₁, while the maximum improvement for F_V (voltage responsivity) and F'_E belong to the 2nd-order H-BCC.

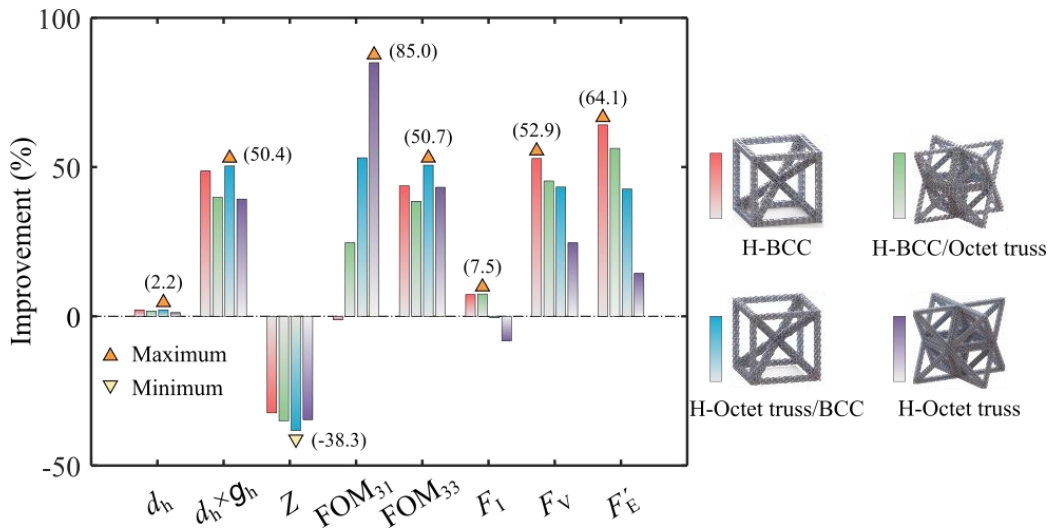


Figure 4.7 Influence of lattice topology on figures of merit. The overall relative densities for these hierarchical lattice metamaterials are 0.05. More specifically, the relative densities for the 1st-order and the 2nd-order are 0.1 and 0.5, respectively. (Reprinted with permission from ref [192], copyright 2020 Elsevier)

4.3.3 Influence of relative density

Figure 4.8 presents the relationship between the 1st-order relative density, ρ_1 , and the improvement of figures of merit of the 2nd-order hierarchical octet truss (H-Octet truss) compared

to the 1st-order octet truss of the same relative density, where the overall relative density is fixed as 0.05. As shown in Figure 4.8, when ρ_1 decreases to 0.05 or increases to 1, there is no improvement for all normalized figures of merit, indicating that the 2nd-order H-Octet truss degrades to the 1st-order octet truss. Moreover, the improvement of all figures of merit varies considerably for different ρ_1 . For example, the improvement of FOM₃₃ (direct mode piezoelectric energy harvesting figures of merit) reaches the maximum value (57.5%) for ρ_1 as 0.2, while the improvement decreases to 21.5% when ρ_1 increases to 0.6. In general, when ρ_1 is around 0.2, the 2nd-order H-Octet truss with the overall relative density of 0.05 demonstrates the best piezoelectric and pyroelectric performance. This optimized relative density can vary for different overall relative densities of hierarchical ferroelectric metamaterials, a phenomenon that requires a detailed optimization study to determine the optimized relative density combination for hierarchical metamaterials.

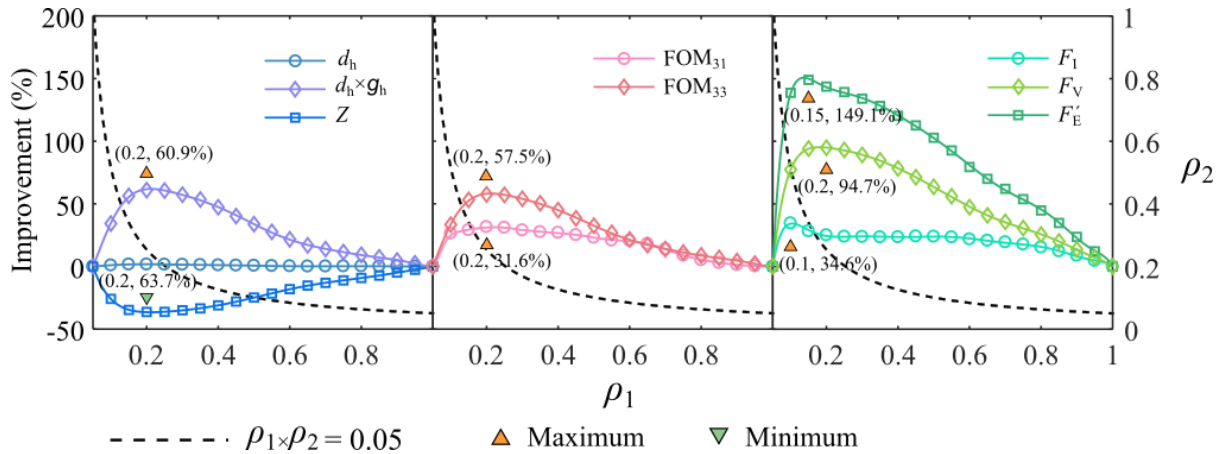


Figure 4.8 Influence of the 1st-order relative density of the 2nd-order H-Octet truss ferroelectric metamaterials with the overall relative density as 0.05 on the improvement of figures of merit. (Reprinted with permission from ref [192], copyright 2020 Elsevier)

4.4 Comprehensive 2nd-order figures of merit

Figure 4.9 shows a comprehensive analysis of the 2nd-order hierarchical lattice ferroelectric metamaterials, considering two architectural parameters discussed in Chapter 4.3, i.e., lattice architecture and relative density. More specifically, four cubic families, four octahedron families, and two hybrid families of metamaterials (2nd-order H-BCC/Octet truss and H-Octet truss/BCC) are included (see Figure 4.4). In order to cover a wide range of metamaterials, the relative densities of each hierarchical order cover the whole ranges of achievable relative density by the corresponding unit cells (see Figure 4.3). In addition, for each type of hierarchical metamaterials with specific overall relative density, only the maximum improvement of figures of merit (except for acoustic impedance, Z , in which the minimum improvement is selected) compared with that of the 1st-order counterpart with the same overall relative density, is plotted in Figure 4.9. Some specific hierarchical metamaterials are displayed by the solid line and dash line, where solid line means its value is maximum (or minimum for normalized Z) among all metamaterials. In general, although 1st-order ferroelectric metamaterials have already remarkably improved the piezoelectric and pyroelectric properties for different applications, 2nd-order hierarchical lattice ferroelectric metamaterials can further modify their figures of merit. In specific:

(i) As found in Chapter 4.3, hydrostatic charge coefficient (d_h) exhibits a slight improvement (below 10%) with 2nd-order hierarchical lattice metamaterial (see Figure 4.9a). In contrast, the hydrostatic figure of merit ($d_h \times g_h$) and acoustic impedance (Z) show obvious modification (maximum change is 89.8% for $d_h \times g_h$ and minimum change is -46.0% for Z), and this improvement is reduced with increasing relative density. However, it should be mentioned that for some types of metamaterials with specific overall relative density, hierarchical lattice metamaterials are unbeneficial for hydrophone application, indicated by the dots below the black dashed line for

hydrostatic charge coefficient (d_h) and hydrostatic figure of merit ($d_h \times g_h$) and dots above the black dashed line for normalized acoustic impedance (Z). For example, when $\rho = 0.5$, the normalized d_h of 2nd-order H-Octet truss decreases by 0.62% compared with that of 1st-order octet truss with the same relative density while decreases by 1.5% for normalized $d_h \times g_h$ when $\rho = 0.5$. Moreover, although the improvement of hydrostatic charge coefficient (d_h) for 2nd-order H-FDC is not the maximum, its normalized d_h is maximum for relative density smaller than 0.5 (indicated by the pink solid line in Figure 4.9a). A similar phenomenon can also be found in Figure 4.9b and c. Furthermore, since all the solid lines are above the black dashed line in Figure 4.9 (a)-(b) and below the black dashed line in Figure 4.9c, 2nd-order hierarchical lattice metamaterials extend the properties selection areas for hydrophone application that can be achieved by 1st-order lattice metamaterials. For example, when $\rho = 0.5$, the maximum normalized hydrostatic figure of merit ($d_h \times g_h$) for 2nd-order hierarchical lattice metamaterials is 46.5 (2nd-order H-FDC), while just 40.9 (2nd-order FDC) for 1st-order lattice metamaterials.

(ii) Both the improvement and normalized value of FOM₃₁ (bending mode piezoelectric energy harvester figure of merit) are highly dependent on lattice architectures (see Figure 4.9d). For example, the FOM₃₁ of the 2nd-order H-tetraikadecahedron decreases by 51.0% ~ 63.5% compared with that of the 1st-order counterpart of the same relative density while all 2nd-order H-BCC/Octet truss are above the baseline with the maximum improvement of 61.4%. In addition, the maximum values of normalized FOM₃₁, belonging to the 2nd-order H-Octet truss metamaterials, are accompanied by obvious improvement when relative density is smaller than 0.5, indicating the achievable FOM₃₁ is expanded by the 2nd-order hierarchical lattice ferroelectric metamaterials. In contrast, as shown in Figure 4.9e, for normalized FOM₃₃ (direct mode piezoelectric energy harvester figure of merit), hierarchical architecture is beneficial for most metamaterials with the

exception of a few types of architectures with specific relative densities. Moreover, as indicated by the dot color, normalized FOM_{33} mainly depends on relative density, and the cubic family shows better performance for direct mode piezoelectric energy harvesting with maximum value from H-FDC ($\rho \leq 0.65$) and H-SC ($\rho \geq 0.7$).

(iii) Most 2nd-order hierarchical lattice metamaterials have obvious improvement for both current responsivity (F_I) and voltage responsivity (F_V), with maximum improvement of 118.3% for F_I and 222.2% for F_V (see Figure 4.9f-g). However, although normalized F_I of the 1st-order simple cube metamaterials is the maximum among all the 1st-order metamaterials with an aspect ratio (AR) of 1 (see Figure 4.5f), 2nd-order H-Octet truss (solid blue line) have maximum normalized F_I (when $\rho \geq 0.5$) among 2nd-order metamaterials due to its high improvement. In addition, in spite of the maximum normalized current responsivity (F_I) being smaller than 1, the 2nd-order hierarchical lattice ferroelectric metamaterials offer a better solution for designing lightweight heat and infrared devices than the 1st-order metamaterials. In Figure 4.9g, with higher improvement of voltage responsivity (F_V), the 2nd-order H-FCC shows the maximum normalized values when the relative density is smaller than 0.6. Moreover, since all improvements of F_V are positive, hierarchical architecture is an effective approach in ferroelectric lattice metamaterials for improving their performance in IR devices.

(iv) Similar to voltage responsivity (F_V) in Figure 4.9g, the pyroelectric energy harvesting figure of merit (F'_E) is improved with 2nd-order hierarchical metamaterials, especially for low relative density with maximum improvement of 603.5% achieved by 2nd-order H-tetrapentacahedron. It should be mentioned that not all improvement of F'_E is larger than 1. Therefore, in order to achieve F'_E higher than that of solid bulk material, hierarchical lattice metamaterials with small relative densities ($\rho \leq 0.2$) can be developed.

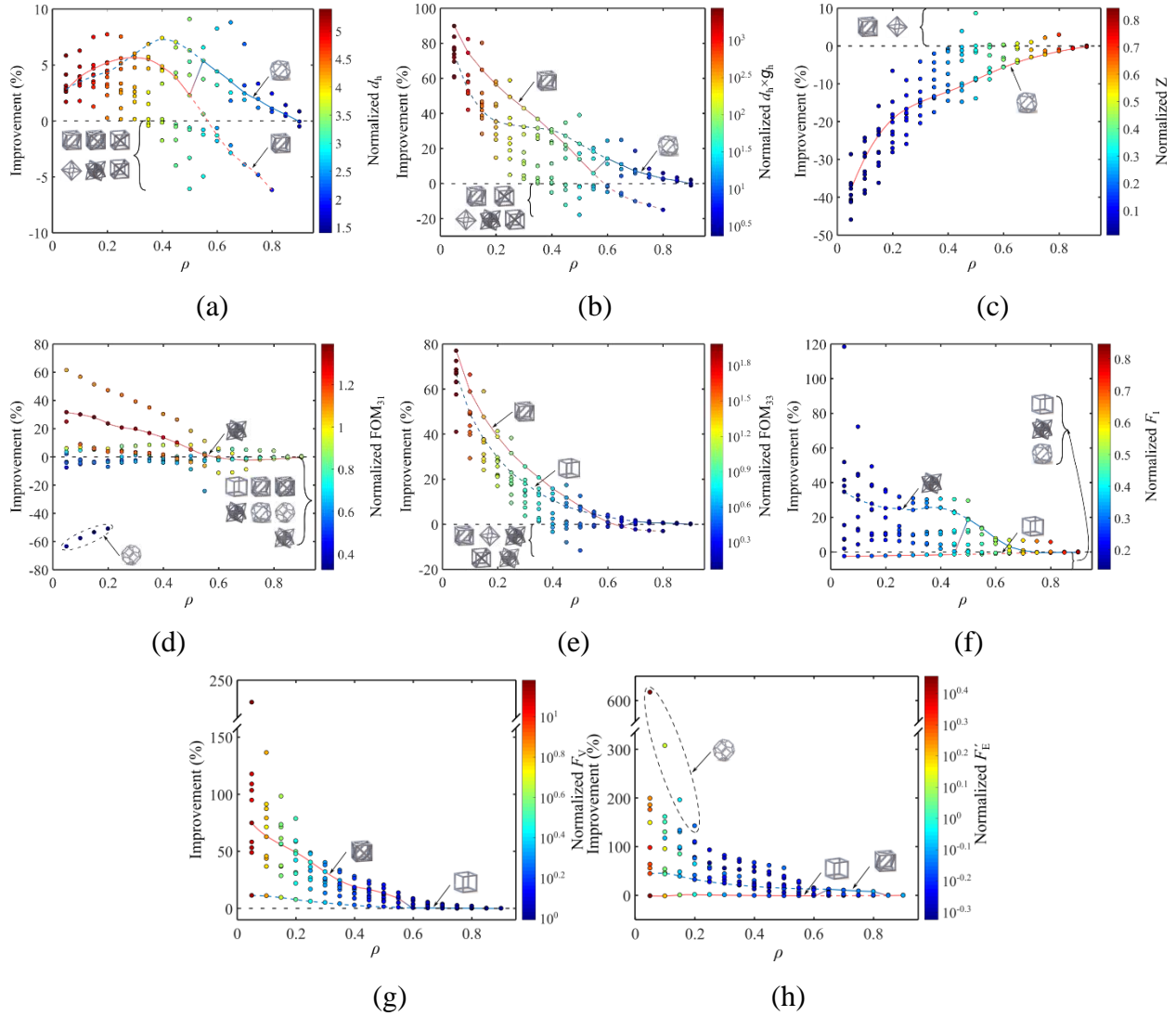


Figure 4.9 Maximum improvement and normalized figures of merit for the 2nd-order hierarchical lattice ferroelectric metamaterials with aspect ratio as 1. (Reprinted with permission from ref [192], copyright 2020 Elsevier)

For aspect ratios (ARs) of 2.5 and 4, the maximum improvement of the 2nd-order hierarchical lattice ferroelectric metamaterials compared with that of 1st-order counterpart is provided in Table 4.1, where overall relative density is selected as 0.05, and the bold numbers highlight the value of figures of merit with maximum normalized values (or minimum for normalized acoustic impedance, Z). In general, similar to Figure 4.9, hierarchical architectures can effectively improve the figures of merit for most lattice metamaterials, with the exception of hydrostatic charge

coefficient (d_h). More specifically, as mentioned in Chapter 4.3.2, hybrid family metamaterials, i.e., 2nd-order H-BCC/Octet truss, can achieve higher normalized d_h not achievable by fractal-like counterparts. When the aspect ratio (AR) is 0.25, not only the normalized hydrostatic figure of merit ($d_h \times g_h$) of the 1st-order metamaterials is higher than that of its counterpart with AR = 4, but also the improvement is higher than that of the 2nd-order hierarchical metamaterials. A similar phenomenon can be found for the normalized Z and FOM_{33} . On the contrary, the 2nd-order H-Octet truss with AR = 4 shows the maximum normalized FOM_{31} (bending mode piezoelectric energy harvesting figure of merit), F_I (current responsivity), and F'_E (pyroelectric energy harvesting figure of merit), which is attributed to the high improvement of FOM_{31} and the high normalized values for F_I and F'_E of the 1st-order ferroelectric metamaterials (see Figure 4.5f and g). Although the octahedron family has higher improvement for normalized F_v (voltage responsivity), the maximum normalized value belongs to the 2nd-order H-FCC with an aspect ratio of 0.25.

Table 4.1 Maximum improvement of figures of merit for the 2nd-order hierarchical lattice ferroelectric metamaterials with an overall relative density of 0.05 and aspect ratio of 4 and 0.25. The bold number highlights the maximum normalized figures of merit.

Family	Lattice	AR	Maximum improvement of figures of merit compared to 1 st -order counterparts (%)							
			d_h	$d_h \times g_h$	Z	FOM ₃₁	FOM ₃₃	F_I	F_V	F'_E
Cubic		0.25	2.8	104.3	-30.1	-9.8	90.8	-7.5	4.4	-4.4
		4	2.4	50.8	-26.8	-1.5	43.0	-1.3	17.9	8.5
		0.25	2.0	191.0	-54.8	-18.2	174.0	-9.6	36.2	-7.6
		4	3.4	49.7	-33.3	3.6	38.9	-1.7	27.9	21.7
		0.25	0.9	159.9	-61.2	-21.4	149.0	-13.6	49.6	24.2
		4	3.8	48.8	-31.3	3.4	36.8	-4.5	26.1	15.3
	0.25	2.1	182.9	-50.6	-44.5	166.5	-36.3	25.8	-27.9	
	4	2.0	30.4	-27.4	16.8	26.3	7.7	27.9	34.0	
Octa-hedron		0.25	-0.1	53.2	-31.6	11.3	52.6	109.4	189.1	439.8
		4	-0.3	-0.1	-25.3	84.6	15.87	16.6	27.0	45.3
		0.25	2.5	72.6	-36.0	3.3	71.6	78.3	162.8	368.6
		4	-0.7	16.4	-27.8	53.5	23.7	9.4	27.4	36.8
		0.25	3.7	71.3	-30.8	-10.0	70.3	46.1	114.3	209.2
		4	3.4	42.2	-31.7	-3.7	33.0	-0.4	29.2	25.4
	0.25	3.1	56.3	-29.8	-19.4	55.3	27.8	91.8	145.2	
	4	24.9	101.1	-30.2	-48.3	28.3	7.8	38.5	49.3	
Hybrid		0.25	-0.4	48.3	-37.5	50.1	47.7	901.2	379.9	415.7
		4	6.0	35.7	-25.7	17.3	25.4	5.9	22.1	28.8
		0.25	10.0	555.2	-93.1	-59.2	505.4	-46.9	56.7	-16.8
		4	-3.2	6.0	-25.2	119.8	16.3	16.4	29.1	48.5

4.5 Discussion on the scaling relationship of ferroelectric properties

To date, a considerable amount of theoretical and experimental research has been dedicated to designing 2D and 3D lattices and evaluating their mechanical properties [190,194,199–203]). One common analytical model for determining the mechanical properties of these lattice structures is based on the classical beam theory, in which the effective Young's modulus, E , and relative density, ρ , of lattices satisfy the following power relationship [202]:

$$E/E_s = B_1 \rho^{m_1} , \quad (4.1)$$

where the subscript ‘s’ stands for the corresponding value of solid base materials; the proportionality constant B_1 and scaling coefficients m_1 depend on the lattice architecture. More specifically, for rigid lattices, or stretch-dominated lattices, $m_1 = 1$, while $m_1 = 2$ for bending-dominated lattices [190,201]. However, this analytical model is limited to low relative density, where constructing trusses of lattices is modelled by Euler-Bernoulli or Timoshenko beams [190].

In contrast to mechanical properties, analytical models for describing the relationship between fundamental piezoelectric and pyroelectric properties, such as d_{31} (piezoelectric charge constant), κ_{33}^σ (dielectric constant under constant stress), and p_3 (pyroelectric constant), and relative density of different lattice topologies is yet to be established to analytically predict the figures of merit of lattices made of ferroelectric materials. Inspired by Eq. (4.1), we assume that κ_{33}^σ , d_{31} , and d_{33} also follow similar scaling relationships with respect to the relative density of lattices, namely

$$\begin{aligned} \kappa_{33}^\sigma / \kappa_{33,s}^\sigma &= B_2 \rho^{m_2}, \\ d_{31} / d_{31,s} &= B_3 \rho^{m_3}, \\ d_{33} / d_{33,s} &= B_4 \rho^{m_4}, \end{aligned} \quad (4.2)$$

where B_2 , B_3 , and B_4 are the proportionality constants of κ_{33}^σ , d_{31} and d_{33} , respectively, and m_2 , m_3 and m_4 are the corresponding scaling coefficients.

In order to obtain the constants given in Eq. (4.1) and Eq. (4.2), Figure 4.10 presents the curves of normalized E_{33} (Young’s modulus along polarization direction), κ_{33}^σ , d_{31} , and d_{33} versus relative density of 1st-order octet truss and tetrakaidecahedron with an aspect ratio (AR) of 1. Since the curves are plotted on a logarithmic scale, the slopes of each curve are the values of corresponding m_i ($i = 1, 2, 3, 4$). As expected, for low relative density ($\rho \leq 10\%$), m_1 of 1st-order octet truss (stretching-dominated lattice) is around 1 ($m_1 = 1.06$), while 2.05 for tetrakaidecahedron (bending-dominated lattice). For $\rho > 10\%$, m_1 of 1st-order octet truss changes to 2.01, and for tetrakaidecahedron, this value changes to 2.53. A similar phenomenon can also be found in

normalized κ_{33}^σ (dielectric constant under constant stress) and d_{31} (piezoelectric charge constant). Therefore, we can use a piecewise function with two sub-function to describe these curves, where B_2 , B_3 , m_2 and m_3 are also functions of ρ , i.e., $B_2 = B_2(\rho)$, $B_3 = B_3(\rho)$, $m_2 = m_2(\rho)$, and $m_3 = m_3(\rho)$. However, as for normalized d_{33} (piezoelectric charge constant), the horizontally distributed data indicates its independence on relative density, remaining the same value as that of solid material ($m_4 = 0$ and $B_4 = 1$). In addition, B_i ($i = 1, 2, 3, 4$) can be obtained from the intersection of these curves with the vertical axis. It should be mentioned that the critical relative density, ρ_{cr} , separating the sub-functions of normalized E_{33} , κ_{33}^σ and d_{31} are similar for the same lattice topology, with 0.1 for octet truss and 0.05 for tetrakaidecahedron. Therefore, in order to cover the whole range of relative densities from an ultralow value to the maximum achievable one, Eq. (4.1) and Eq. (4.2) should be rewritten as:

$$\begin{aligned}
 E(\rho)/E_s &= B_1(\rho)\rho^{m_1(\rho)} = \begin{cases} B_{11}\rho^{m_{11}}, & \rho \leq \rho_{cr} \\ B_{12}\rho^{m_{12}}, & \rho > \rho_{cr} \end{cases}, \\
 \kappa_{33}^\sigma(\rho)/\kappa_{33,s}^\sigma &= B_2(\rho)\rho^{m_2(\rho)} = \begin{cases} B_{21}\rho^{m_{21}}, & \rho \leq \rho_{cr} \\ B_{22}\rho^{m_{22}}, & \rho > \rho_{cr} \end{cases}, \\
 d_{31}(\rho)/d_{31,s} &= B_3(\rho)\rho^{m_3(\rho)} = \begin{cases} B_{31}\rho^{m_{31}}, & \rho \leq \rho_{cr} \\ B_{32}\rho^{m_{32}}, & \rho > \rho_{cr} \end{cases}, \\
 d_{33}(\rho)/d_{33,s} &= 1.
 \end{aligned} \tag{4.3}$$

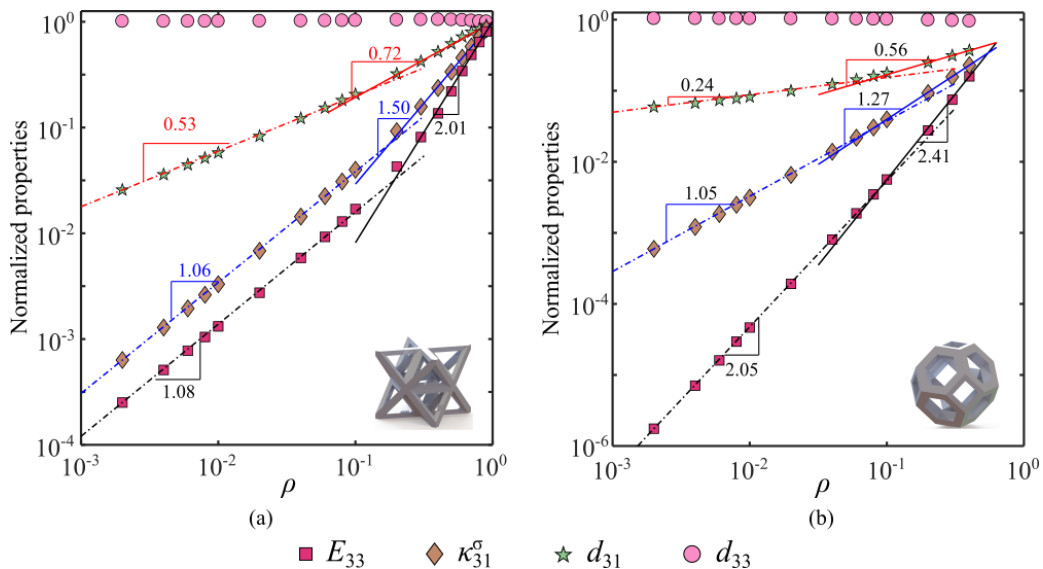


Figure 4.10 Normalized properties of 1st-order octet truss and tetrakaidecahedron with AR = 1 and ρ ranging from 0.001 to 1. (Reprinted with permission from ref [192], copyright 2020 Elsevier)

As mentioned in Chapter 3, we can obtain the hydrostatic charge coefficient (d_h), hydrostatic figure of merit ($d_h \times g_h$), and direct mode piezoelectric energy harvesting figure of merit (FOM₃₃) from κ_{33}^σ , d_{31} , and d_{33} . Therefore, based on Eq. (4.3), for the 1st-order lattice metamaterials, the relationship between normalized d_h , $d_h \times g_h$, and FOM₃₃ versus ρ can be expressed as:

$$\begin{aligned} d_h^{(1)}(\rho)/d_{h,s} &= (d_{33,s} + 2d_{31,s}B_3(\rho)\rho^{m_3(\rho)})/(d_{33,s} + 2d_{31,s}), \\ d_h^{(1)}(\rho) \times g_h^{(1)}(\rho)/(d_{h,s} \times g_{h,s}) &= \left[d_h^{(1)}(\rho)/d_{h,s} \right]^2 \kappa_{33,s}^\sigma / (B_2(\rho)\rho^{m_2(\rho)}), \\ \text{FOM}_{33}^{(1)}(\rho)/(FOM_{33,s}) &= 1 / (\kappa_{33,s}^\sigma B_2(\rho)\rho^{m_2(\rho)}), \end{aligned} \quad (4.4)$$

where the superscript means the hierarchical order.

For the 2nd-order hierarchical lattice ferroelectric metamaterials with ρ_1 as the relative density of the 1st-order architecture and ρ_2 as the relative density of the 2nd-order, by iterative operation, Eq. (4.3) can be rewritten as:

$$\begin{aligned} E^{(2)}(\rho_1 \times \rho_2)/E_s &= B_1(\rho_1)B_1(\rho_2)\rho_1^{m_1(\rho_1)}\rho_2^{m_1(\rho_2)}, \\ \kappa_{33}^{(2),\sigma}(\rho_1 \times \rho_2)/\kappa_{33,s}^\sigma &= B_2(\rho_1)B_2(\rho_2)\rho_1^{m_2(\rho_1)}\rho_2^{m_2(\rho_2)}, \\ d_{31}^{(2)}(\rho_1 \times \rho_2)/d_{31,s} &= B_3(\rho_1)B_3(\rho_2)\rho_1^{m_3(\rho_1)}\rho_2^{m_3(\rho_2)}, \\ d_{33}^{(2)}(\rho_1 \times \rho_2)/d_{33,s} &= 1. \end{aligned} \quad (4.5)$$

More specifically, the first three piecewise functions in Eq. (4.5) have four sub-functions. For example, $d_{31}^{(2)}(\rho_1 \times \rho_2)/d_{31,s}$ can be expanded as:

$$d_{31}^{(2)}(\rho_1 \times \rho_2)/d_{31,s} = \begin{cases} B_{31}^2(\rho_1 \times \rho_2)^{m_{31}}, & \rho_1, \rho_2 \leq \rho_{cr} \\ B_{31}B_{32}\rho_1^{m_{31}}\rho_2^{m_{32}}, & \rho_1 \leq \rho_{cr} \text{ and } \rho_2 > \rho_{cr} \\ B_{31}B_{32}\rho_1^{m_{32}}\rho_2^{m_{31}}, & \rho_1 > \rho_{cr} \text{ and } \rho_2 \leq \rho_{cr} \\ B_{32}^2(\rho_1 \times \rho_2)^{m_{32}}, & \rho_1, \rho_2 > \rho_{cr} \end{cases}. \quad (4.6)$$

For a given overall relative density, if both ρ_1 and ρ_2 are larger than ρ_{cr} , the normalized d_{31} of the 2nd-order lattice ferroelectric metamaterials are all the same. It should be mentioned that both

Eqs. (4.5) and (4.6) are limited to fractal-like hierarchical metamaterials. For hybrid hierarchical metamaterials, B_i and m_i ($i = 1, 2, 3, 4$) also depend on the geometry of unit cells. Interestingly, by selecting a proper selection of ρ_1 and ρ_2 with a fixed overall relative density, optimized proportionality constants and scaling coefficients can be obtained, which result in unprecedented properties of hybrid hierarchical lattice metamaterials not-achievable by their fractal-like counterparts (examples can be found in Chapter 4.3.2).

Similarly, the normalized d_h (hydrostatic charge coefficient), $d_h \times g_h$ (hydrostatic figure of merit), and FOM_{33} (direct mode piezoelectric energy harvesting figure of merit) of the 2nd-order lattice ferroelectric metamaterials can be expressed as:

$$\begin{aligned} d_h^{(2)}(\rho_1 \rho_2) / d_{h,s} &= d_h^{(1)}(\rho) (d_{33,s} + 2d_{31,s} B_3(\rho) \rho^{m_3(\rho)}) / (d_{33,s} + 2d_{31,s} B_3(\rho) \rho^{m_3(\rho)}), \\ d_h^{(2)}(\rho_1 \rho_2) \times g_h^{(2)}(\rho_1 \rho_2) / (d_{h,s} \times g_{h,s}) &= \left[d_h^{(2)}(\rho_1 \rho_2) / d_{h,s} \right]^2 / \kappa_{33}^{(2),\sigma}(\rho_1 \rho_2), \\ FOM_{33}^{(2)}(\rho_1 \rho_2) / (FOM_{33,s}) &= 1 / \kappa_{33}^{(2),\sigma}(\rho_1 \rho_2). \end{aligned} \quad (4.7)$$

In order to examine the accuracy of Eq. (4.7), the predicted normalized d_h , $d_h \times g_h$, and FOM_{33} of the 2nd-order H-Octet truss by the scaling relationships are compared with those calculated by multiscale asymptotic homogenization (MAH), and they are plotted in Figure 4.11. The overlapping red and blue dots indicate that Eq. (4.7) offers a reliable method for predicting the effective figures of merit of hierarchical ferroelectric metamaterials (the maximum error is 5.7% for normalized d_h , 9.7% for normalized $d_h \times g_h$, and 10.2% for normalized FOM_{33}).

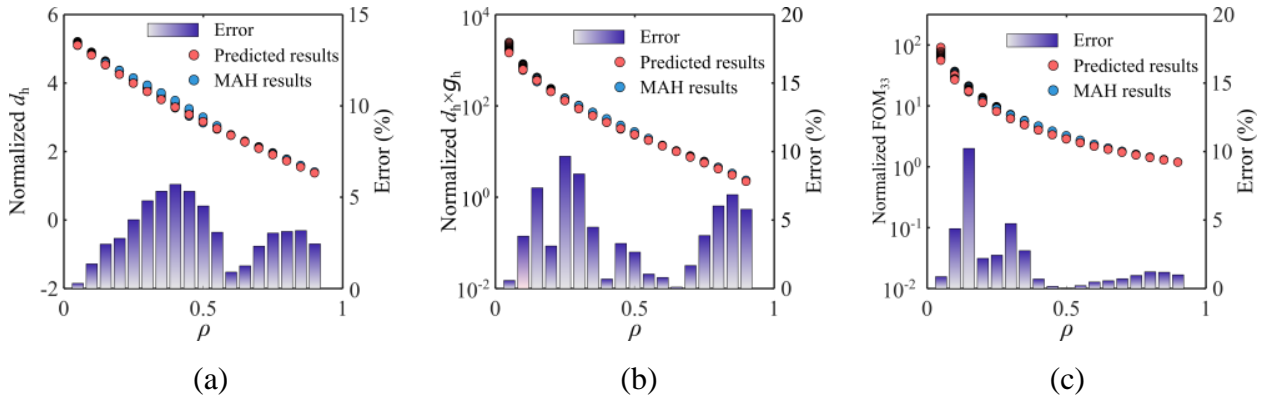


Figure 4.11 Comparison between the predicted results of developed scaling relationships and MAH of the 2nd-order H-Octet truss. (Reprinted with permission from ref [192], copyright 2020 Elsevier)

Besides the effective properties of 1st-order and 2nd-order hierarchical ferroelectric metamaterials, the effective piezoelectric properties provided in Eqs. (4.3) and (4.5) can also be generalized metamaterials with higher orders of hierarchy, namely $n \geq 3$, as follows:

$$\begin{aligned}
 E^{(n)}(\rho_1 \rho_2 \cdots \rho_n) / E_s &= B_1(\rho_1) B_1(\rho_2) \cdots B_1(\rho_n) \rho_1^{m_1(\rho_1)} \rho_2^{m_1(\rho_2)} \cdots \rho_n^{m_1(\rho_n)}, \\
 \kappa_{33}^{(n),\sigma}(\rho_1 \rho_2 \cdots \rho_n) / \kappa_{33,s}^\sigma &= B_2(\rho_1) B_2(\rho_2) \cdots B_2(\rho_n) \rho_1^{m_2(\rho_1)} \rho_2^{m_2(\rho_2)} \cdots \rho_n^{m_2(\rho_n)}, \\
 d_{31}^{(n)}(\rho_1 \rho_2 \cdots \rho_n) / d_{31,s} &= B_3(\rho_1) B_3(\rho_2) \cdots B_3(\rho_n) \rho_1^{m_3(\rho_1)} \rho_2^{m_3(\rho_2)} \cdots \rho_n^{m_3(\rho_n)}, \\
 d_{33}^{(n)}(\rho_1 \rho_2 \cdots \rho_n) / d_{33,s} &= 1.
 \end{aligned} \tag{4.8}$$

The scaling relationship is also suitable for other thermo-electro-mechanical properties of ferroelectric metamaterials, such as thermal conductivity and pyroelectric coefficient, for a wide range of lattice topologies. As a result, we can also use the iterative method to derive analytical expressions for normalized acoustic impedance (Z), piezoelectric (bending mode FOM₃₁), and pyroelectric (F_E^I) energy harvesting figures of merit, current responsivity (F_I), and voltage responsivity (F_V).

It should be mentioned that the abovementioned multiscale asymptotic homogenization (MAH) and scaling law assume the fully poling of ferroelectric metamaterials. However, due to the different permittivity of ferroelectric materials and air (e.g., the relative permittivity of unpoled BaTiO₃ is 1566 while 1 for air [82], it is very difficult to fully polarize ferroelectric lattice materials. During the poling process, the high electric field always concentrates in the air region, and the high permittivity region shows a smaller electric field, resulting in incomplete poling [79,80,82]. One possible method to facilitate polarization is immersing the ferroelectric lattice metamaterials

into an oil bath with similar permittivity as that of ferroelectric materials, possibly by mixing high permittivity particles in the oil [90].

It is worth mentioning that hierarchical design can possibly result in a detriment to the material strength of high relative density hierarchical lattice metamaterials, which is due to the recursive effect of stress concentration occurring at each hierarchical order [194]. However, hierarchical designs with ultralow relative densities have recently shown significant advantages for increasing strength and resilience [202,203]. The recently developed Large Area Projection Microstereolithography (LAP μ SL) has offered a promising solution to 3D print hierarchical lattice metamaterials with ultralow relative density (below 0.1%) in multiple length scales spanning from nanometer to centimeter sizes [203]. It has been experimentally proved that at ultralow relative densities (below 1%), the optimized hierarchical metamaterials can exhibit a near linear scaling relationship between material strength and relative density while the scaling power for the strength of 1st-order microlattice is more than 2.5 [202,203]; the material strength of 3rd-order hierarchical metamaterials has also shown to be two orders of magnitude higher than 1st-order microlattice, resulting from its tuned failure mode, i.e., nanoscale hollow tube wall buckling and struts buckling, by varying structural parameters [203]. The nanoscale size effect could also attribute to the enhanced mechanical strength of these nanoarchitected hierarchical metamaterials [204]. In addition, 3D printed hierarchical metamaterials have exhibited high resilience that stems from the bending deformation of intact struts [202,203]. Therefore, ultralight hierarchical metamaterials featuring nanoarchitectures have exhibited improved material strength even at the risk of introducing higher stress concentrations. Due to the high poling voltage of ferroelectric materials, e.g., around 30 kV/cm for PZT in [96], the size of most 3D ferroelectric materials, especially in poling direction, is limited to centimeter or millimeter, which can be printed by the

abovementioned LAP μ SL technology. Recently, piezoelectric zinc oxides have been printed on nanoscale [205]. This high precision fabrication method ensures the manufacture of our designed hierarchical lattice ferroelectric metamaterials. Further research can focus on exploring more shell-like TPMS shellulars.

4.6 Concluding remarks on 3D hierarchical lattice ferroelectric metamaterials

In summary, we have introduced a new class of architected cellular ferroelectric metamaterials with 3D hierarchical lattices repeated periodically in each hierarchical order. These so-called *3D hierarchical lattice ferroelectric metamaterials* can optimize the piezoelectric and pyroelectric properties of lightweight smart structures while reducing the consumption of environmentally-incompatible materials (e.g., lead-based ferroelectric material) in these intelligent metamaterials. This paper conducts a systematic study to explore the potential applications of hierarchical lattice ferroelectric metamaterials and offers design motifs for optimizing their multifunctional performance. The research leads to the following principal findings:

(1) Except for current responsivity (F_I), the 1st-order lattice ferroelectric metamaterials can remarkably improve the piezoelectric and pyroelectric figures of merit, especially with an aspect ratio (AR) of 0.25 for the hydrostatic charge coefficient (d_h), hydrostatic figure of merit ($d_h \times g_h$), acoustic impedance (Z), and direct mode piezoelectric energy harvesting figure of merit (FOM₃₃) and aspect ratio (AR) of 4 for bending mode piezoelectric energy harvesting figure of merit (FOM₃₁), voltage responsivity (F_V) and pyroelectric energy harvesting figure of merit (F'_E). For example, when $\rho = 0.1$, the maximum normalized $d_h \times g_h$ and FOM₃₃ are around 2300 and 78 times higher than the corresponding values for solid bulk ferroelectric materials. In general, the

octahedron family of ferroelectric lattice metamaterials outperforms the cubic family for most figures of merit.

(2) Ferroelectric metamaterials will take more advantage of 3D lattice structures by increasing hierarchical orders, e.g., 48.7% improvement of $d_h \times g_h$ (hydrostatic figure of merit) for 2nd-order hierarchical body-centered cube (H-BCC) and 162.1% for 4th-order H-BCC. In addition, lattice topology and relative density at each hierarchical order also significantly affect the figures of merit of ferroelectric metamaterials. Interestingly, hybrid hierarchical metamaterials can exhibit better piezoelectric and pyroelectric performance not achieved by their fractal-like counterparts. For example, FOM₃₃ of the 2nd-order H-Octet truss/BCC is 15.8% and 17.4% higher than that of 2nd-order H-BCC and 2nd-order H-Octet truss ($\rho_1 = 0.1, \rho_2 = 0.5, AR = 1$), respectively.

(3) 2nd-order hierarchical metamaterials improve most piezoelectric and pyroelectric figures of merit compared with those of 1st-order counterparts over all reachable relative densities, especially at low ones. For example, the maximum improvement for $d_h \times g_h$ (hydrostatic figure of merit), F_I (current responsivity), F_V (voltage responsivity), and F'_E (pyroelectric energy harvesting figure of merit), or minimum improvement for Z (acoustic impedance), are 89.8%, 118.3%, 222.2%, 603.5%, and -46.0%, respectively, which is obtained when $\rho = 0.05$. However, all these values are almost zero when $\rho = 0.90$. It should be mentioned that increasing hierarchical orders might have adverse effects on ferroelectric lattice metamaterials. For example, the FOM₃₁ of 1st-order tetrakaidcahedron decreases by 51.0% ~ 63.5% when hierarchical order increases to 2.

(4) Inspired by the analytical modelling for the mechanical behavior of 3D lattices, a generalized scaling relationship is proposed for the first time for evaluating the piezoelectric and pyroelectric properties of ferroelectric lattice metamaterials. Adopting these scaling relationships and iterative approaches, the figures of merit of hierarchical ferroelectric metamaterials can be

predicted with an acceptable discrepancy to provide reliable design routes for developing lightweight and multifunctional ferroelectric metamaterials.

CHAPTER 5

Hierarchical cubic cellular ferroelectric metamaterials

This chapter involves the investigation of ferroelectric properties of hierarchical cellular ferroelectric metamaterials constructed by six commonly used primitive unit cells of the cubic family. Apart from asymptotic homogenization, the scaling relationship is proposed to describe the effective multiphysical properties of the designed cellular ferroelectric metamaterials. In addition, different trends for the effective properties of hybrid hierarchical ferroelectric metamaterials are analyzed. Electric field distribution during poling and stress concentration factors are also presented.

5.1 Hierarchical cubic cellular metamaterials

As shown in Figure 5.1, apart from the commonly used 3-0, 3-1, and 3-3 cellular ferroelectric metamaterials, a new type of ferroelectrics, i.e., 3-2, is introduced here where the pores only connect in two directions (Figure 5.1 d and e). Since all these cellular metamaterials are derived from a cubic solid, we can call them 3D cubic cellular ferroelectric metamaterials. In addition, considering the polarization direction of the constitutive ferroelectric materials, four types of

ferroelectric metamaterials (i.e., 3-0, 3-1, 3-2, and 3-3) are further classified as 3-0 (Figure 5.1 a), L3-1 (Figure 5.1 b), T3-1 (Figure 5.1 c), LT3-2 (Figure 5.1 d), T3-2 (Figure 5.1 e), and 3-3 (Figure 5.1 f), where ‘L’ represents the polarization direction (axis 3) is parallel (longitudinal) to the pore direction, while ‘T’ indicates the polarization direction is perpendicular (transverse) to the pore direction.

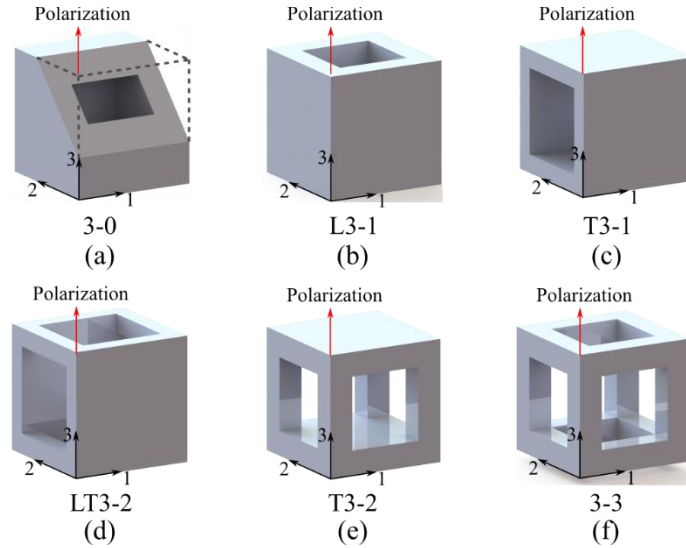


Figure 5.1 Six types of 3D cubic cellular ferroelectric metamaterials. (Reprinted with permission from ref [206], copyright 2020 Elsevier)

Figure 5.2 shows the process of constructing a 3rd-order cubic hierarchical cellular ferroelectric metamaterial. A 0th-order repeating unit, i.e., a beam with a square cross-section made of ferroelectric materials, is firstly assembled to form a 1st-order 3-3 cellular ferroelectric unit cell; it is then used as a building block for constructing the 2nd-order 3-3 cellular architecture, which is finally arranged to construct a 3rd-order 3-3 cellular ferroelectric metamaterial. Higher orders of hierarchical metamaterials can be achieved by repeating this process for desired times. This iterative design method forms the hierarchical unit cells based on the constitutive beams of a *self-similar* unit cell, resulting in a fractal-like architecture. However, the building blocks in

consecutive orders can be dissimilar, and their arrangement of them among different orders can also be different, which forms *hybrid* hierarchical ferroelectric metamaterials.

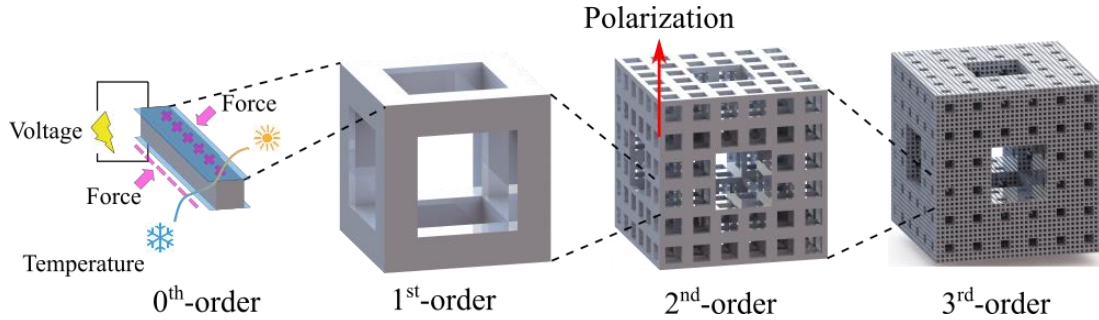


Figure 5.2 Successive hierarchical orders in 3D hierarchical cubic cellular ferroelectric metamaterials. (Reprinted with permission from ref [206], copyright 2020 Elsevier)

Based on the six types of cellular architectures introduced in Figure 5.1, we can develop 36 types of 2nd-order hierarchical cellular ferroelectric metamaterials. As shown in Figure 5.3, the 1st-order building block (highlighted in the red color) is assembled into the 2nd-order building block (highlighted in the blue color) to form the 2nd-order hierarchical unit cell. Based on the similarity of cellular architectures in the two orders of structural hierarchy, we have 6 different self-similar 2nd-order hierarchical metamaterials, i.e., 2nd-order 3-0/3-0, L3-1/L3-1, T3-1/T3-1, LT3-2/LT3-2, T3-2/T3-2, and 3-0/3-0 as well as 30 different types of hybrid 2nd-order hierarchical metamaterials, e.g., 2nd-order 3-0/L3-1 and T3-1/T3-2. The architectural features of hybrid hierarchical metamaterials can provide an opportunity to achieve desired unprecedented ferroelectric properties from the same constitutive ferroelectric material. In order to clearly distinguish alternative hierarchical metamaterials, hereafter, the hierarchical unit cells are written from left to right, with lower hierarchical orders denoted in left and are separated by ‘/’. For example, a 3rd-order hierarchical ferroelectric metamaterial 3-0/L3-1/T3-2 represents a hierarchical metamaterial with 3-0 cellular architecture as the 1st-order building block, L3-1 cellular architecture as the 2nd-order building block, and T3-2 as the 3rd-order building block.

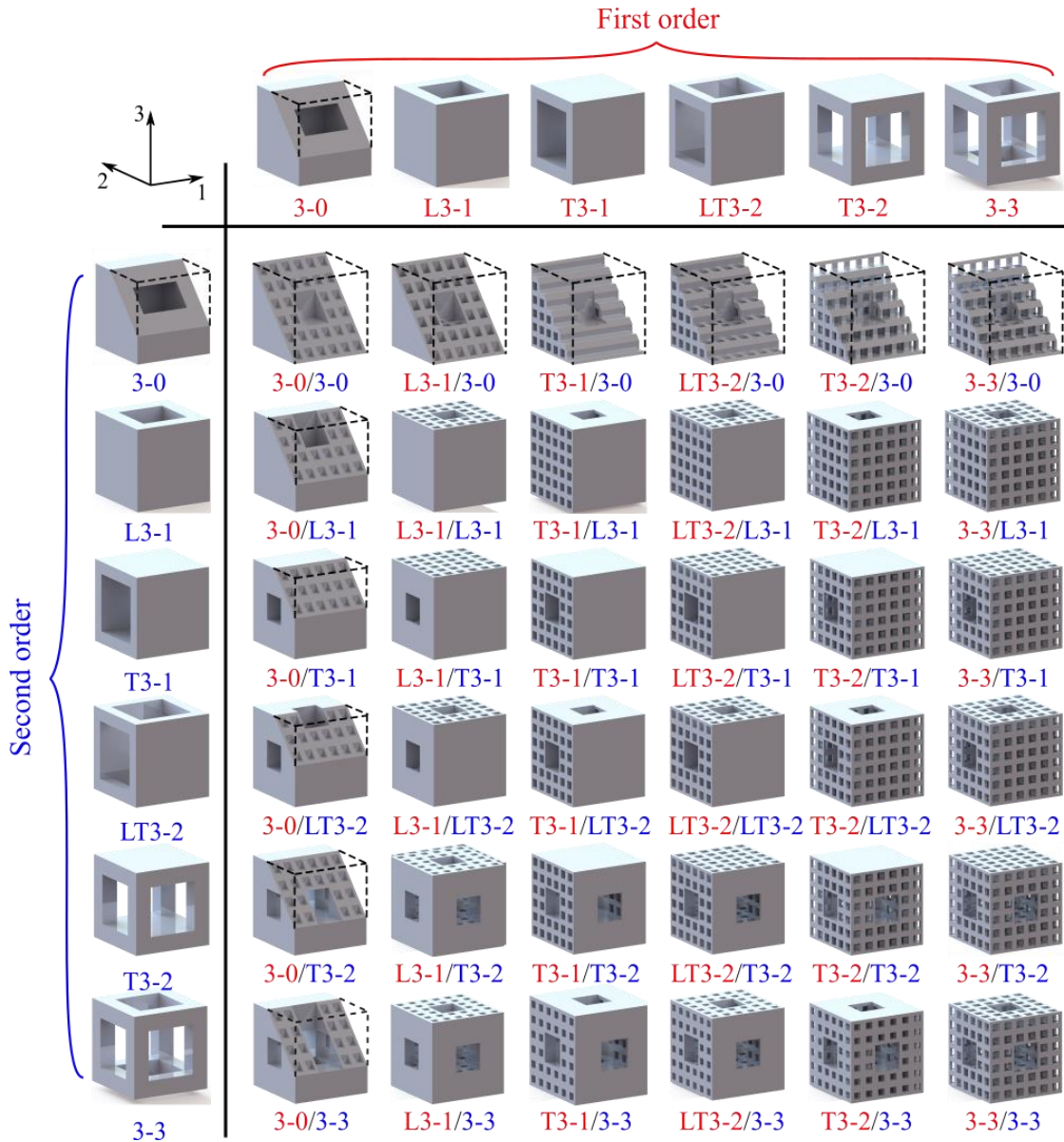


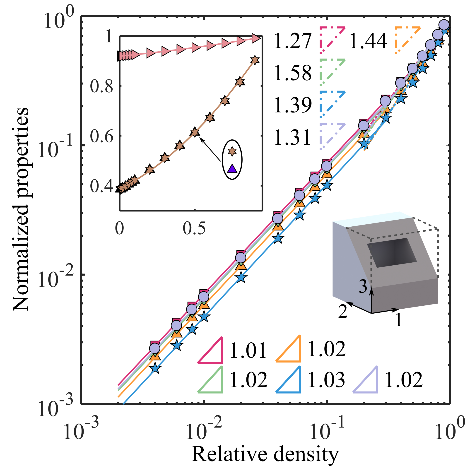
Figure 5.3 36 types of 2nd-order hierarchical cubic cellular ferroelectric metamaterials. (Reprinted with permission from ref [206], copyright 2020 Elsevier)

In the following section, the previously proposed MAH and scaling relationship are adopted to predict the unprecedented piezoelectric and pyroelectric properties of hierarchical cellular ferroelectric metamaterials. BaTiO₃, a lead-free ecofriendly, and biocompatible ferroelectric material is selected as a constitutive material of ferroelectric metamaterial. Its properties are provided in Tables 3.1 and 3.2. In addition, the influence of hierarchical order, relative density,

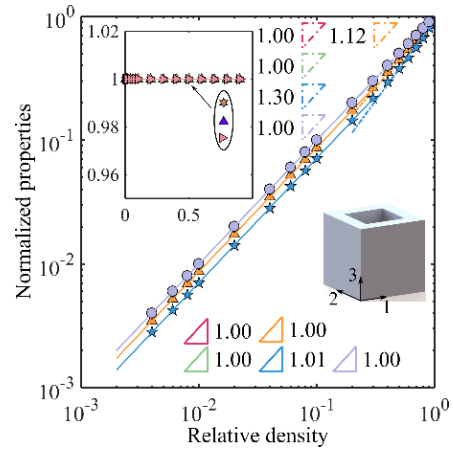
and cell topology on the effective thermo-electro-mechanical properties and figures of merit is explored. Apart from ferroelectric properties, stress concentration and electric field distribution during polarization of the hierarchical metamaterials are also investigated.

5.2 1st-order cellular ferroelectric metamaterials

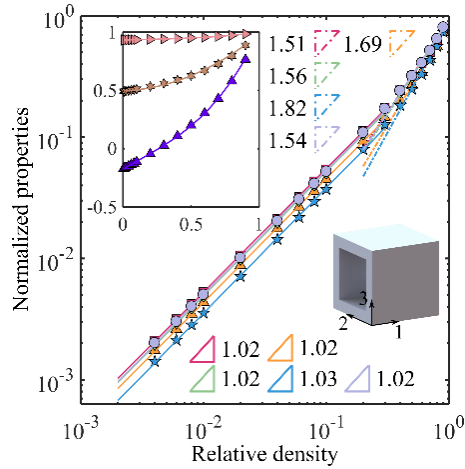
Figure 5.4 shows the relationship between the normalized E_{33} (Young's modulus along direction 3), C_{33}^D , κ_{33}^σ , p_3 , K_{33} (thermal conductivity along direction 3), d_{31} , d_{32} , d_{33} , and relative density for six considered 1st-order cellular ferroelectric metamaterials in a logarithmic scale, which is normalized by the corresponding value of the solid BaTiO₃. Generally, apart from d_{33} , d_{31} , and d_{32} , all other ferroelectric properties exhibit an increasing trend with the increase of relative density; all d_{33} values, especially for L3-1, T3-1, LT3-2, and 3-3, remain almost the same value as that of the solid counterpart. For example, for L3-1, the normalized κ_{33}^σ increases from 0.01 ($\rho = 0.01$) to 0.23 ($\rho = 0.23$), while normalized d_{33} remains stable as 1. As aforementioned, the scaling relationship of mechanical property is applicable for small relative density due to the effect of joint points [190]. Therefore, we divide the relative density into two parts with a critical value, ρ_{cr} , as 0.3, which distinguishes the range of relative density satisfying the scaling relationship of E_{33} . As shown in Figure 5.4, 1st-order 3-0, L3-1, T3-1, LT3-2, and 3-3 metamaterials show stretching-dominant deformation mode with a slope around 1 when $\rho < \rho_{cr}$; 1st-order T3-2 is the only bending-dominant structure with a slope around 2. Interestingly, when $\rho > \rho_{cr}$, we can use another straight line with different a slope as a fitting curve to show the relationship between E_{33} and relative density. More specifically, when $\rho > \rho_{cr}$, the slopes of E_{33} in Figure 5.4 a-f are 1.17, 1.00, 1.32, 1.06, 2.10, and 1.49, respectively. Therefore, we can use a piecewise function with two sub-function to describe these curves.



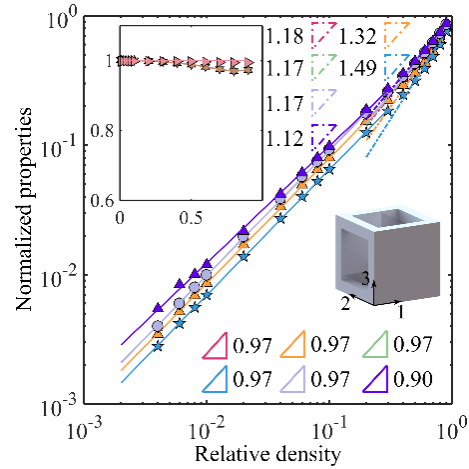
(a)



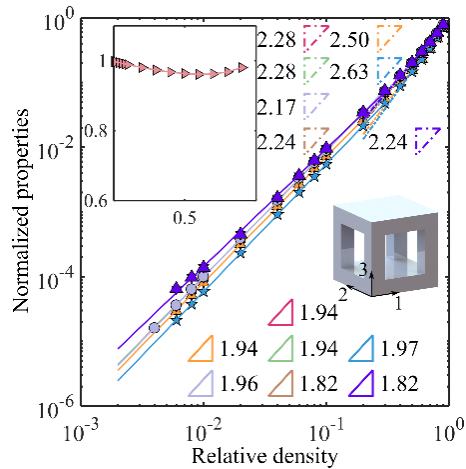
(b)



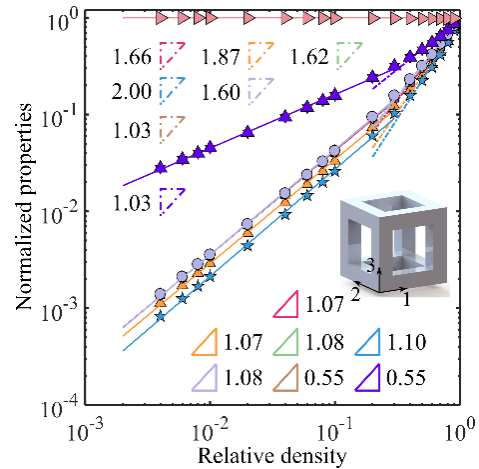
(c)



(d)



(e)



(f)

Figure 5.4 Ashby charts where the normalized ferroelectric properties versus relative density for six types of 1st-order cellular ferroelectric metamaterials are plotted. (Reprinted with permission from ref [206], copyright 2020 Elsevier)

Similar to Chapter 4, the relationship between ferroelectric properties and relative density can be presented by a straight line on a logarithmic scale. For example, in Figure 5.4 a, when $\rho < \rho_{cr}$, the slope of C_{33}^D , κ_{33}^σ , p_3 , and K_{33} are 1.01, 1.01, 1.01, and 1.00, respectively, while these values are 1.27, 1.22, 1.39, and 1.21, respectively when $\rho > \rho_{cr}$. Furthermore, apart from the 1st-order T3-2, all slopes of C_{33}^D , κ_{33}^σ , p_3 , and K_{33} are around 1 when $\rho < \rho_{cr}$. It should be mentioned that in Figure 5.4 a and c, d_{31} , and d_{32} do not exhibit the scaling relationship with relative density in logarithmic scale and, as a result, are plotted in the inset with a linear scale. However, we can still use polynomial to fit these curves. The ferroelectric properties, which satisfy the scaling relationship, can be described by the following equations:

$$\begin{aligned}
 E_{33}^{(1)}(\rho) &= \begin{cases} E_{33,s} B_{11} \rho^{n_{11}}, & \rho \ll \rho_{cr} \\ E_{33,s} B_{12} \rho^{n_{12}}, & \rho > \rho_{cr} \end{cases}, \quad C_{33}^{(1),D}(\rho) = \begin{cases} C_{33,s}^D B_{21} \rho^{n_{21}}, & \rho \ll \rho_{cr} \\ C_{33,s}^D B_{22} \rho^{n_{22}}, & \rho > \rho_{cr} \end{cases}, \quad \kappa_{33}^{(1),\sigma}(\rho) = \begin{cases} \kappa_{33,s}^{(1),\sigma} B_{31} \rho^{n_{31}}, & \rho \ll \rho_{cr} \\ \kappa_{33,s}^{(1),\sigma} B_{32} \rho^{n_{32}}, & \rho > \rho_{cr} \end{cases}, \\
 p_3^{(1)}(\rho) &= \begin{cases} p_{3,s} B_{41} \rho^{n_{41}}, & \rho \ll \rho_{cr} \\ p_{3,s} B_{42} \rho^{n_{42}}, & \rho > \rho_{cr} \end{cases}, \quad K_{33}^{(1),D}(\rho) = \begin{cases} K_{33,s} B_{51} \rho^{n_{51}}, & \rho \ll \rho_{cr} \\ K_{33,s} B_{52} \rho^{n_{52}}, & \rho > \rho_{cr} \end{cases}, \quad d_{31}^{(1)}(\rho) = \begin{cases} d_{31,s} B_{61} \rho^{n_{61}}, & \rho \ll \rho_{cr} \\ d_{31,s} B_{62} \rho^{n_{62}}, & \rho > \rho_{cr} \end{cases}, \\
 d_{32}^{(1)}(\rho) &= \begin{cases} d_{32,s} B_{71} \rho^{n_{71}}, & \rho \ll \rho_{cr} \\ d_{32,s} B_{72} \rho^{n_{72}}, & \rho > \rho_{cr} \end{cases}, \quad d_{33}(\rho) = d_{33,s}
 \end{aligned} \tag{5.1}$$

where the superscript (\cdot) means the hierarchical order; the subscript ‘s’ means the corresponding ferroelectric properties of solid material; B_{ij} and n_{ij} ($i = 1, 2, \dots, 6$ and $j = 1, 2$) are proportionality and scaling constants respectively, which are provided in Table 5.1. The d_{31} and d_{32} in the insets of Figure 5.4 a and c are specially denoted by the following polynomials:

$$\text{For 3 - 0 : } d_{31}^{(1)}(\rho) = d_{32}^{(1)}(\rho) = d_{31,s}(0.302\rho^2 + 0.302\rho + 0.386)$$

$$\text{For T3-1 : } d_{31}^{(1)}(\rho) = d_{31,s}(0.451\rho^2 + 0.032\rho + 0.497)$$

$$d_{32}^{(1)}(\rho) = d_{32,s}(0.784\rho^3 - 0.323\rho^2 + 0.709\rho - 0.177) \quad (5.2)$$

Table 5.1. Proportionality and scaling constants of six 1st-order cellular ferroelectric metamaterials for the normalized E_{33} , C_{33}^D , κ_{33}^σ , p_3 , K_{33} , d_{31} , and d_{32} ($i = 1, 2$).

1 st -order metamaterial	Relative density	$E_{33}^{(1)}$		$C_{33}^{(1),D}$		$\kappa_{33}^{(1),\sigma}$		$p_3^{(1)}$		$K_{33}^{(1)}$		$d_{31}^{(1)}$		$d_{32}^{(1)}$	
		B_{1i}	n_{1i}	B_{2i}	n_{2i}	B_{3i}	n_{3i}	B_{4i}	n_{4i}	B_{5i}	n_{5i}	B_{6i}	n_{6i}	B_{7i}	n_{7i}
	$\rho < \rho_{cr}$	0.75	1.01	0.62	1.02	0.70	1.02	0.53	1.03	0.72	1.02	/			
	$\rho > \rho_{cr}$	0.95	1.27	0.92	1.44	0.96	1.33	0.92	1.58	0.97	1.31				
	$\rho < \rho_{cr}$	1.00	1.00	0.88	1.00	1.00	1.00	0.72	1.01	1.00	1.00	1	0	1	0
	$\rho > \rho_{cr}$	1.00	1.00	0.97	1.12	1.00	1.00	0.93	1.30	1.00	1.00	1	0	1	0
	$\rho < \rho_{cr}$	0.58	1.02	0.48	1.02	0.55	1.02	0.41	1.03	0.56	1.02	/			
	$\rho > \rho_{cr}$	0.91	1.51	0.87	1.69	0.93	1.56	0.89	1.82	0.94	1.54				
	$\rho < \rho_{cr}$	0.85	0.97	0.73	0.97	0.85	0.97	0.61	0.97	0.85	0.97	1	0	0.79	0.90
	$\rho > \rho_{cr}$	0.95	1.18	0.91	1.32	0.96	1.17	0.89	1.49	0.96	1.17	1	0	0.97	1.12
	$\rho < \rho_{cr}$	0.77	1.94	0.62	1.94	0.77	1.94	0.52	1.97	0.81	1.96	0.63	1.82	0.63	1.82
	$\rho > \rho_{cr}$	0.93	2.28	0.88	2.50	0.96	2.28	0.92	2.63	0.93	2.17	0.97	2.24	0.97	2.24
	$\rho < \rho_{cr}$	0.50	1.07	0.40	1.07	0.52	1.08	0.35	1.10	0.53	1.08	0.58	0.55	0.58	0.55
	$\rho > \rho_{cr}$	0.95	1.66	0.91	1.87	0.96	1.62	0.91	2.00	0.97	1.60	0.96	1.03	0.96	1.03

Based on the classical beam theory, the in-plane and out-of-plane mechanical properties of hexagonal cellular solids were first analyzed by Ashby [55]. The slopes of Young's modulus versus relative density curves are also related to stretching/bending-dominated deformation modes. As shown in Eq. (5.1), when the power (n_{11}) is 1, the topology is stretching dominated, which is more mechanically efficient; the non-rigid topology is governed by bending of beams with the power as 2. However, an analytical model for explaining the slopes of ferroelectric properties versus relative density curves (Figure 5.4) is yet to be developed. In Table 5.1, the mechanism behind the relationship between relative density and effective properties of 3-3 unit cells is revealed based on a simple micromechanics method.

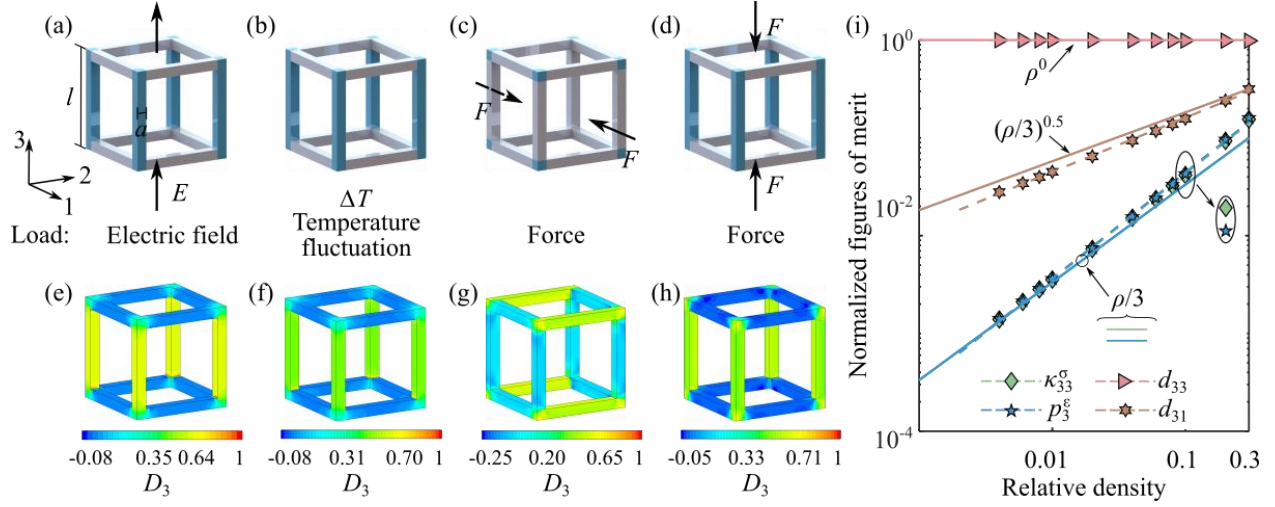


Figure 5.5 Loading conditions and effective volumes used to obtain the effective (a) κ_{33} , (b) p_3^ϵ , (c) d_{31} , and (d) d_{33} ; the corresponding electric displacement along direction 3 for (e) κ_{33} , (f) p_3^ϵ , (g) d_{31} , and (h) d_{33} ; (i) comparison of effective pyroelectric properties obtained by MAH and proposed analytical method, solid line: analytical results, dashed line with markers: MAH results. (Reprinted with permission from ref [206], copyright 2020 Elsevier)

Figure 5.5 shows the loading conditions (Figure 5.5a-d) and corresponding electric displacement, D_3 , (Figure 5.5e-h) for obtaining the effective dielectric coefficient under constant stress, κ_{33}^σ (Figure 5.5 a and e), effective primary pyroelectric coefficient, p_3^ϵ (Figure 5.5 b and (f)), effective d_{31} (Figure 5.5 c and g), and effective d_{33} (Figure 5.5 d and h) of 1st-order 3-3 cellular metamaterial. In Figure 5.5 a, a unit uniform electric field along direction 3 is applied; the average D_3 over the unit cell is seen as the effective κ_{33}^σ . The columns parallel to direction 3 (denoted by blue color) make the great contribution to κ_{33}^σ ; the other volumes contribute little to the effective dielectric properties as they are connected by low-dielectric air, which is indicated in Figure 5.5 e. Therefore, the effective κ_{33}^σ can be expressed as:

$$\kappa_{33}^{(1),\sigma} = 4(a/l)^2 \kappa_{33,s}^\sigma \quad (5.3)$$

For small relative density ($\rho < \rho_{cr}$), the relationship between the effective κ_{33}^σ and relative density can be obtained:

$$\kappa_{33}^{(1),\sigma} = \rho/3 \kappa_{33,s}^\sigma \quad (5.4)$$

which explains the slope of 1.08 for κ_{33}^σ in Figure 5f. In Figure 5.5 b, a unit temperature fluctuation is considered and the average D_3 over the unit cell is seen as the effective p_3^ε . Similar as Figure 5.5 a, only columns parallel to direction 3 determine p_3^ε (see Figure 5.5 f). Therefore, we can also express p_3^ε as

$$p_3^{(1),\varepsilon} = \rho/3 p_{3,s}^\varepsilon \quad (5.5)$$

which means the linear relationship between p_3^ε and relative density. Therefore, based on Eq. (5.5), the slope of p_3 in Figure 5.4 (f) is around 1. In Figure 5.5c, a unit force along direction 1 is applied, and the average D_3 is considered as effective d_{31} . Although the columns parallel to direction 1 exhibit the maximum D_3 (see Figure 5.5g), only the eight cubes (marked by blue color) in Figure 5.5c contribute to d_{31} since the rest of these columns parallel to direction 3 is series in the 3-direction with air. Therefore, we can express the effective d_{31} as:

$$d_{31}^{(1)} = 8(a/l)^3 d_{31,s} / [4(a/l)^2] = 2(a/l) d_{31,s} \sim \rho^{0.5} / \sqrt{3} d_{31,s} \quad (5.6)$$

which corresponds to the slope of 0.55 in Figure 5.4f. In Figure 5.5d, a unit force along direction 3 is applied and the average D_3 is seen as the effective d_{33} . Similarly, the columns marked by blue color contribute to d_{33} , and its effective value can be expressed as:

$$d_{33}^{(1)} = 4(a/l)^2 d_{33,s} / [4(a/l)^2] = d_{33,s} \quad (5.7)$$

which shows the independence of the effective d_{33} on relative density. Figure 5.5i illustrates the comparison between MAH and Eq. (5.1). The excellent agreement between these two results indicates the accuracy of the proposed analytical method.

To examine the effects of 1st-order cellular metamaterials on the improvement of ferroelectric properties, Figure 5.6 shows the variation of normalized piezoelectric and pyroelectric figures of merit of six 1st-order cellular metamaterials with respect to relative density. In general, apart from F_1 (Figure 5.6f), 1st-order cellular metamaterials can effectively improve the performance of piezoelectric and pyroelectric devices made of ferroelectric materials. More specifically, the following findings are made:

(i) Apart from the normalized d_h of 1st-order L3-1 cellular metamaterials, decreasing relative density can markedly improve the hydrophone performance made of ferroelectric material, i.e., increasing normalized d_h (Figure 5.6a), and $d_h \times g_h$ (Figure 5.6b), and decreasing normalized Z (Figure 5.6c). For example, the normalized d_h of 1st-order 3-3 cellular metamaterials increases from 3.49 to 5.14 when relative density decreases from 0.5 to 0.05, while decreases from 0.35 to 0.03 for normalized Z . In addition, 1st-order T3-2 cellular metamaterial shows the best performance for hydrophone application with maximum normalized value for d_h (5.58) and $d_h \times g_h$ (13300), and minimum normalized value for Z (0.01).

(ii) In contrast to Figure 5.6a-c, 1st-order T3-2 cellular metamaterials exhibit the smallest normalized FOM_{31} , and decreasing its relative density reduces this normalized value, declining from 0.21 to 0.003 when relative density changes from 0.5 to 0.05 (Figure 5.6d). Interestingly, 1st-order LT3-2, L3-1, T3-1, and 3-0 cellular metamaterials significantly improve the normalized FOM_{31} with a maximum normalized value of 20.72 when $\rho = 0.05$. Similar to Figure 5.6a-c, the maximum normalized FOM_{33} is obtained by 1st-order T3-2, and decreasing relative density enhances its piezoelectric energy harvesting performance under direct excitement mode (Figure 5.6e).

(iii) In Figure 5.6f, the normalized F_I of all ferroelectric metamaterials is smaller than 1, and an increase in the relative density increases the normalized F_I . This suggests that cellular ferroelectric metamaterials are not suitable for IR devices, which require high values of F_I . However, for designing lightweight IR devices, Figure 5.6f suggests that 1st-order L3-1 cellular metamaterials generate more current for a given temperature difference. As shown in Figure 5.6g, normalized F_V is insensitive to cellular topologies, and this value shows a decreasing trend with increasing relative density.

(iv) Similar to Figure 5.6f, 1st-order L3-1 cellular metamaterials show the maximum normalized F'_E (Figure 5.6h). Furthermore, except 1st-order T3-2 cellular metamaterials, for small relative density, decreasing ρ will result in higher normalized F'_E . It should be mentioned that when relative density exceeds specific relative density, 1st-order cellular metamaterials are unbeneficial for pyroelectric energy harvesting. For example, the normalized F'_E of 1st-order L3-1 cellular metamaterial is 3.41 when $\rho = 0.15$, while smaller than 1 when $\rho \geq 0.6$.

Apart from the MAH method, we can also use the scaling relationship to express the effective figures of merit as:

$$\begin{aligned}
d_h^{(1)}(\rho) &= d_{31}^{(1)}(\rho) + d_{32}^{(1)}(\rho) + d_{33,s}; & d_h^{(1)}(\rho) \times g_h^{(1)}(\rho) &= [d_h^{(1)}(\rho)]^2 / \kappa_{33}^{(1),\sigma}(\rho); \\
Z^{(1)}(\rho) &= [\rho C_{33}^{(1),D}(\rho)]^{0.5}; & \text{FOM}_{31}^{(1)}(\rho) &= [d_{31}^{(1)}(\rho)]^2 / \kappa_{33}^{(1),\sigma}(\rho); \\
\text{FOM}_{33}^{(1)}(\rho) &= [d_{33,s}^2(\rho)]^2 / \kappa_{33}^{(1),\sigma}(\rho); & F_I^{(1)}(\rho) &= p_3^{(1)}(\rho) / (\rho c_p); \\
F_V^{(1)}(\rho) &= p_3^{(1)}(\rho) / (\rho c_p \kappa_{33}^\sigma(\rho)); & F_E^{(1),\prime}(\rho) &= [p_3^{(1)}(\rho)]^2 / (c_E^2 \kappa_{33}^\sigma(\rho))
\end{aligned} \tag{5.8}$$

where $d_{31}(\rho)$, $d_{33}(\rho)$, $C_{33}^D(\rho)$, $\kappa_{33}^\sigma(\rho)$, and $p_3(\rho)$ are obtained from Eq. (5.1) and (5.2). In order to verify the accuracy of Eq. (5.8), the error bar in Figure 5.6 shows the difference between effective figures of merit of 3-0 cellular metamaterials obtained by MAH and the scaling relationship. The

maximum difference for normalized d_h , $d_h \times g_h$, Z , FOM₃₁, FOM₃₃, F_I , F_V , and F_E^I are 3.4%, 8.6%, 3.0%, 3.5%, 4.8%, 7.3%, 3.1%, and 9.9%, respectively, which indicates the reliability of the proposed prediction method.

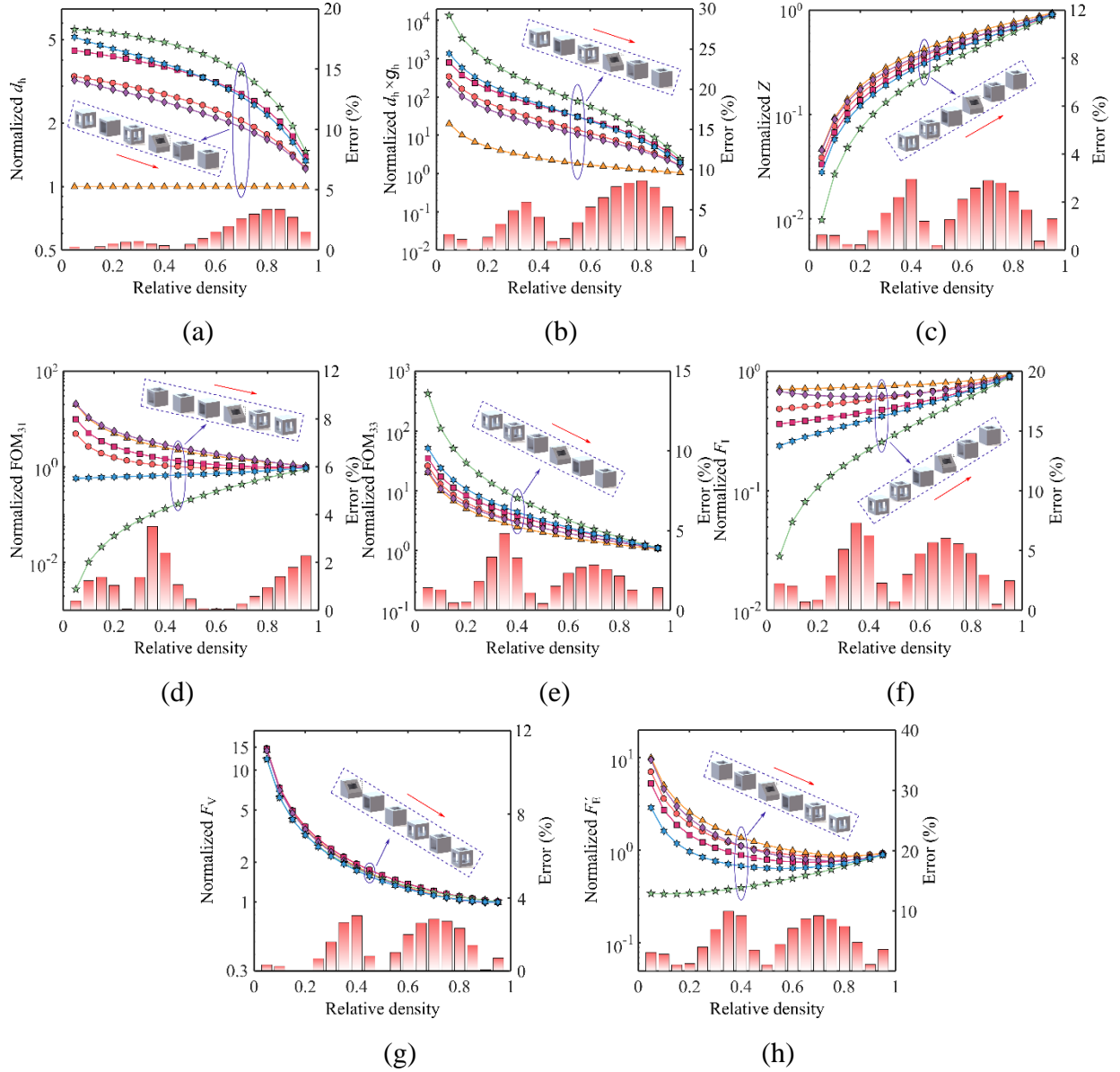
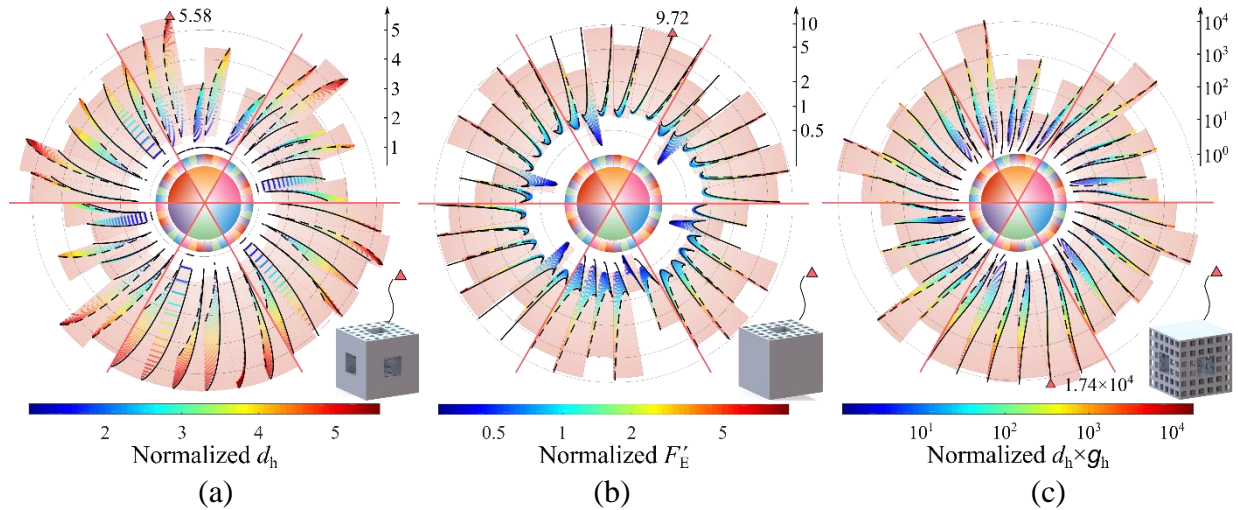


Figure 5.6 Piezoelectric and pyroelectric figures of merit of 1st-order cellular ferroelectric metamaterials. The error bar shows the difference between the figures of merit of 1st-order 3-0 cellular metamaterial obtained by MAH and the scaling relationship. (Reprinted with permission from ref [206], copyright 2020 Elsevier)

5.3 2nd-order hierarchical cellular ferroelectric metamaterials

In order to evaluate the improvement of hierarchical architectures on the multifunctional properties of ferroelectric materials, the rose charts in Figure 5.7 present normalized ferroelectric figures of merit of 36 types of 2nd-order hierarchical cellular metamaterials (see Figure 5.3) with overall relative density, ρ , varying from 0.05 to 0.95 (increasing linearly in a counterclockwise direction in each subsection). Since there are different combinations of 1st-order relative density, ρ_1 , and 2nd-order relative density, ρ_2 , for a given overall relative density ($\rho = \rho_1 \times \rho_2$), we can obtain the property area for each kind of 2nd-order hierarchical cellular metamaterial, consisting of 6156 scattered dots in Figure 5.7. In addition, the solid black and dashed black lines denote the corresponding normalized figures of merit of 1st-order and 2nd-order unit cells for the same overall relative density, respectively. The shaded pink area covers the achievable figures of merit of each kind of the 2nd-order hierarchical metamaterials.



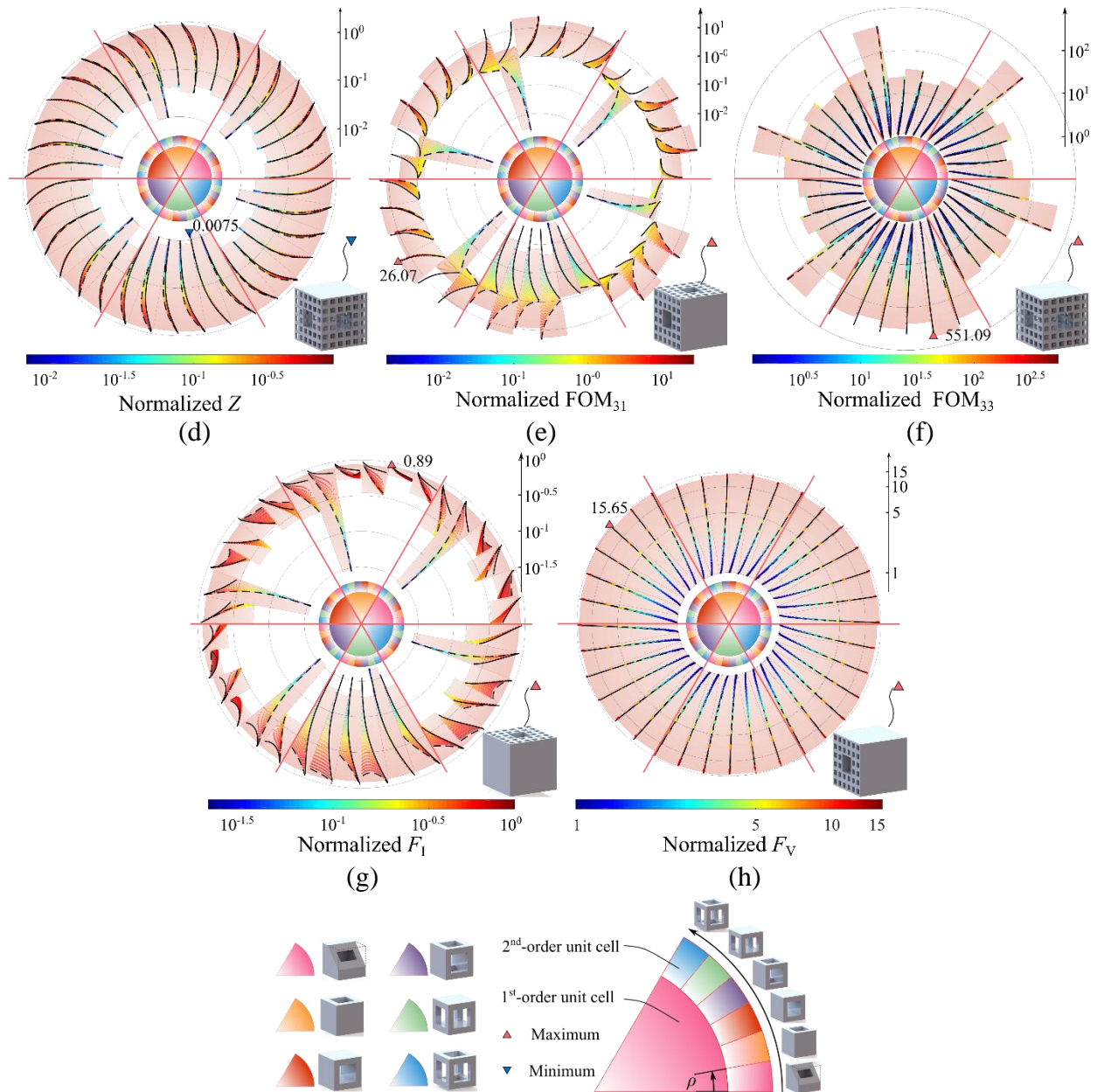


Figure 5.7 Ferroelectric figures of merit of 36 types of 2nd-order hierarchical cellular metamaterials with overall relative densities varying from 0.05 to 0.95. The relative density within each subsection increases linearly in a counterclockwise direction; the color shown in the inner circle denotes the 1st-order unit cell, and the color shown in the outer circle indicates the 2nd-order unit cell; the solid black and dashed black lines show the figures of merit of 1st-order unit cell and 2nd-order unit cell, respectively. (Reprinted with permission from ref [206], copyright 2020 Elsevier)

As expected, the most effective properties of 2nd-order hierarchical metamaterials compromise between those of 1st-order and 2nd-order unit cells, where the scattered dots are enclosed by the solid black and dashed black lines. In addition, increasing the overall relative density of ferroelectric metamaterials decreases the sensitivity of these values to ρ_1 or ρ_2 , indicated by the reduced area for higher relative densities. Apart from normalized F_I , the effective properties of the 2nd-order hierarchical metamaterials highly depend on the topologies of the 1st-order and 2nd-order unit cells. More specifically:

(i) In general, similar to Figure 5.6a-c, normalized d_h (Figure 5.7a) and $d_h \times g_h$ (Figure 5.7b) show a decreasing trend with increasing overall relative density while increasing trend for normalized Z (Figure 5.7c). Since 1st-order T3-2 obtains the maximum normalized d_h (Figure 5.6a) and $d_h \times g_h$ (Figure 5.6b), and minimum normalized Z (Figure 5.6c), 2nd-order hierarchical metamaterials with T3-2 as 1st-order unit cell, especially 2nd-order T3-2/3-0, T3-2/L3-1, T3-2/T3-1, T3-2/LT3-2, and T3-2/3-3, exhibit considerable improvement on these three values compared with their 2nd-order unit cell with the same relative density. In addition, the 2nd-order T3-2/T3-2 shows the maximum normalized $d_h \times g_h$ (1.74×10^4) and minimum normalized Z (0.0075). However, the maximum normalized d_h is obtained from the 2nd-order L3-1/T3-2 (5.58), which means hybrid hierarchical cellular metamaterials can reveal ferroelectric properties not achievable by self-similar metamaterials.

(ii) Different from d_h , $d_h \times g_h$, and Z , replacing the solid beam/plate of the 2nd-order unit cell with T3-2 results in a drastic reduction of FOM_{31} (Figure 5.7d). For example, the normalized FOM_{31} of 1st-order L3-1 ($\rho = 0.05$) decreases from 19.95 to 0.10 exhibited by the 2nd-order T3-2/L3-1 ($\rho_1 = 0.2, \rho_2 = 0.25$). On the contrary, adopting LT3-2 as the 1st-order unit cell provides a reliable method to design hierarchical metamaterials with improved FOM_{31} . As for the normalized FOM_{33} , the 2nd-

order hierarchical metamaterials without the T3-2 as the 1st-order or 2nd-order unit cell share similar property areas (Figure 5.7e), with maximum achievable values around 39.81. However, involving T3-2 in designing hierarchical metamaterials greatly improves the normalized FOM₃₃. For example, the normalized FOM₃₃ of 2nd-order T3-2/L3-1 ($\rho_1 = 0.2, \rho_2 = 0.25$) is 117.49, higher than 19.95 from the 1st-order L3-1 ($\rho = 0.05$).

(iii) Similar to FOM₃₁, T3-2 is not beneficial for high-performance hierarchical metamaterials used for heat and infrared detection with high F_I (Figure 5.7f), indicated by its property areas distributed over the inner scope. L3-1, instead, enhances the normalized F_I of hierarchical metamaterials, especially for 2nd-order L3-1/T3-1, L3-1/T3-2, and L3-1/3-3, and the maximum value (0.89) is also exhibited by 2nd-order L3-1/L3-1. It should be mentioned that the normalized F_I of hierarchical metamaterials sometimes is even smaller than that of its 1st-order and 2nd-order unit cells with the pink area below the solid and dashed black line. For example, the normalized F_I of 2nd-order T3-1/3-0 ($\rho_1 = 0.2, \rho_2 = 0.25$) is 0.26 while 0.36 for T3-1 and 0.48 for 3-0 ($\rho = 0.05$). In Figure 5.7g, all kinds of 2nd-order hierarchical ferroelectric metamaterials share similar property areas with their maximum values around 15. Moreover, due to the marginal difference amongst the six 1st-order unit cells, the normalized F_V of the 2nd-order hierarchical metamaterials is almost insensitive to ρ_1 and ρ_2 . Therefore, decreasing overall relative density is the most effective method to improve the voltage responsivity of ferroelectric metamaterials.

(iv) In Figure 5.7h, both maximum and minimum achievable normalized F'_E for each kind of 2nd-order hierarchical metamaterials depend on the topology of the 1st-order and 2nd-order unit cells. For example, the achievable range for 2nd-order 3-0/3-3 is between 0.63 and 3.79 while between 0.22 and 1.66 for 2nd-order T3-1/T3-2. However, the minimum normalized d_h , $d_h \times g_h$, FOM₃₃, and F_V , and maximum Z , FOM₃₁, and F_I are close to the same value as that of solid material.

To further explain the influence of ρ_1 and ρ_2 on the effective properties of 2nd-order hierarchical metamaterials and the observed phenomena in Figure 5.7, Figure 5.8 presents six representative trends of 2nd-order hierarchical metamaterials with varying ρ_1 and fixed overall relative density ($\rho = 0.05$), i.e., decreasing, increasing, concave, convex, summit, and valley trends. Here, the ratio shows the comparison between the effective properties of 2nd-order hierarchical metamaterials and that of 2nd-order unit cells with $\rho = 0.05$. When $\rho_1 = 1$ and $\rho_2 = 0.05$, the 2nd-order hierarchical metamaterials degrade to 2nd-order unit cells, and when $\rho_1 = 0.05$ and $\rho_2 = 1$, it becomes tessellated 1st-order unit cells, indicated by the topology variation in the bottom of Figure 5.8. Therefore, it is easy to understand the decreasing (Figure 5.8a) and increasing (Figure 5.8b) trend for hybrid hierarchical metamaterials, where effective properties vary monotonically by increasing ρ_1 . This also explains that most pink areas in Figure 5.7 are surrounded by solid black and dashed black lines. However, for self-similar hierarchical metamaterials, due to the same properties of 1st-order and 2nd-order unit cells, the ratio should achieve the maximum (concave, Figure 5.8c) or minimum (convex, Figure 5.8d) value at optimum ρ_1 before decreasing or increasing to 1, uncovering why the properties of self-similar hierarchical metamaterials are always higher or smaller than that of basic unit cells. As for hybrid hierarchical metamaterials, apart from monotonically decreasing and increasing trend, they can also reveal maximum (summit, Figure 5.8e) or minimum (valley, Figure 5.8f) effective properties beyond the bounds of that of their constitutive 1st-order and 2nd-order unit cells. For example, in Figure 5.7a, hybrid 2nd-order L3-1/T3-2 achieving the maximum normalized d_h demonstrates the summit trend.

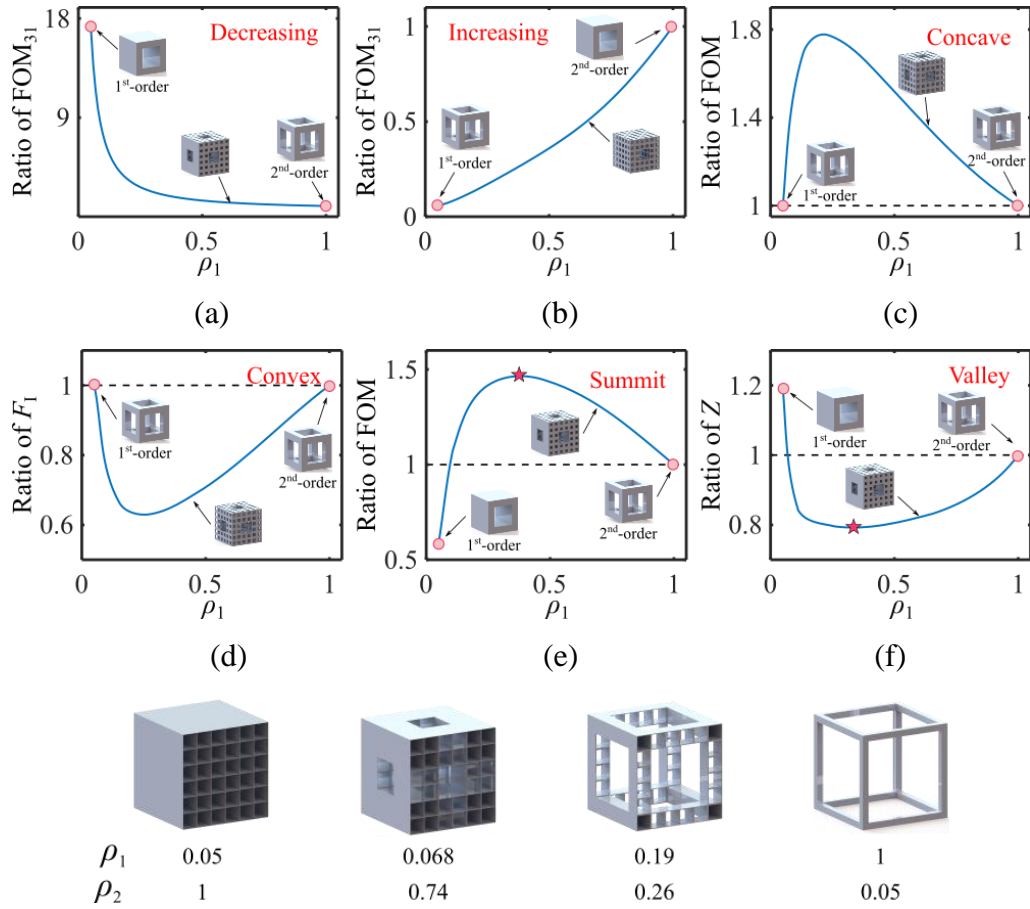


Figure 5.8 Six different trends for effective properties of the 2nd-order hierarchical cellular ferroelectric metamaterials with varying ρ_1 . The overall relative density of this 2nd-order hierarchical metamaterial is 0.05. (Reprinted with permission from ref [206], copyright 2020 Elsevier)

5.4 High order hierarchical cellular ferroelectric metamaterials

In this section, the influence of hierarchical order, i.e., $n = 2, 3,$ and 4 , on the effective properties of hierarchical metamaterials is discussed. Although MAH has remarkably reduced the computational time, designing optimized hierarchical architectures with $n \geq 2$ is still a cumbersome task. For example, for 2nd-order hierarchical metamaterials, there are 6156 different cases considered in Figure 5.7, and more than 300000 cases are needed for 3rd-order hierarchical metamaterials. Based on the scaling relationship, we can quickly predict the effective properties

with acceptable discrepancies even for hierarchical orders higher than 3. Based on Eq. (5.8), the effective κ_{33}^σ of the 2nd-order hierarchical ferroelectric metamaterials can be expressed as:

$$\kappa_{33}^{(2),\sigma}(\rho_1, \rho_2) = \begin{cases} \kappa_{33,s}^\sigma B_{31}^2 (\rho_1 \times \rho_2)^{m_{31}}, & \rho_1, \rho_2 \ll \rho_{cr} \\ \kappa_{33,s}^\sigma B_{31} B_{32} \rho_1^{m_{31}} \rho_2^{m_{32}}, & \rho_1 \ll \rho_{cr}, \rho_2 > \rho_{cr} \\ \kappa_{33,s}^\sigma B_{31} B_{32} \rho_1^{m_{32}} \rho_2^{m_{31}}, & \rho_1 > \rho_{cr}, \rho_2 \ll \rho_{cr} \\ \kappa_{33,s}^\sigma B_{32}^2 (\rho_1 \times \rho_2)^{m_{32}}, & \rho_1, \rho_2 > \rho_{cr} \end{cases} \quad (5.9)$$

Similarly, we can also obtain $C_{33}^{(2),D}$, $p_3^{(2)}$, $K_{33}^{(2)}$, $d_{31}^{(2)}$, $d_{32}^{(2)}$, and $d_{33}^{(2)}$. It should be mentioned that Eq. (5.9) is only suitable for self-similar hierarchical metamaterials; for hybrid types, B_{31} and B_{32} are also functions of cell topologies. After obtaining the effective 2nd-order ferroelectric properties, the figures of merit of self-similar 2nd-order hierarchical ferroelectric metamaterials can be expressed as:

$$\begin{aligned} d_h^{(2)}(\rho_1, \rho_2) &= d_{33,s}^{(2)} + d_{31}^{(2)}(\rho_1, \rho_2) + d_{32}^{(2)}(\rho_1, \rho_2) \\ d_h^{(2)}(\rho_1, \rho_2) \times g_h^{(2)}(\rho_1, \rho_2) &= [d_h^{(2)}(\rho_1, \rho_2)]^2 / \kappa_{33}^{(2),\sigma}(\rho_1, \rho_2) \\ Z^{(2)}(\rho_1, \rho_2) &= (\rho_2 C_{33}^{(2),D}(\rho_1))^{0.5} \\ FOM_{31}^{(2)}(\rho_1, \rho_2) &= [d_{31}^{(2)}(\rho_1, \rho_2)]^2 / \kappa_{33}^{(2),\sigma}(\rho_1, \rho_2) \\ FOM_{33}^{(2)}(\rho_1, \rho_2) &= d_{33,s}^{(2)} / \kappa_{33}^{(2),\sigma}(\rho_1, \rho_2) \\ F_1^{(2)}(\rho_1, \rho_2) &= p_3^2(\rho_1, \rho_2) / (\rho_1 \rho_2 c_p) \\ F_V^{(2)}(\rho_1, \rho_2) &= p_3^2(\rho_1, \rho_2) / (\rho_1 \rho_2 c_p \kappa_{33}^{(2),\sigma}(\rho_1, \rho_2)) \\ F_E^{(2),'}(\rho_1, \rho_2) &= [p_3^2(\rho_1, \rho_2)]^2 / (\rho_1^2 \rho_2^2 c_p^2 \kappa_{33}^{(2),\sigma}(\rho_1, \rho_2)) \end{aligned} \quad (5.10)$$

with which the FEM simulations in Chapter 5.3 can be avoided. Iteratively, when $n > 2$, the effective κ_{33}^σ of this n^{th} -order hierarchical ferroelectric metamaterials can be obtained by

$$\kappa_{33}^{(n),\sigma}(\rho_1, \rho_2, \dots, \rho_n) = \begin{cases} \kappa_{33}^{(n-1),\sigma}(\rho_1, \rho_2, \dots, \rho_{n-1}) B_{31} \rho_n^{n_{31}}, & \rho < \rho_{cr} \\ \kappa_{33}^{(n-1),\sigma}(\rho_1, \rho_2, \dots, \rho_{n-1}) B_{32} \rho_n^{n_{32}}, & \rho > \rho_{cr} \end{cases} \quad (5.11)$$

where $\kappa_{33}^{(n-1),\sigma}$ is the effective κ_{33}^σ of $(n-1)^{\text{th}}$ -order hierarchical metamaterials, and obtained from the ferroelectric metamaterials of lower orders of hierarchy. Similar equations can also be derived for $C_{33}^{(n),D}$, $p_3^{(n)}$, $K_{33}^{(n)}$, $d_{31}^{(n)}$, $d_{32}^{(n)}$, and $d_{33}^{(n)}$. The corresponding figures of merit of the n^{th} -order hierarchical metamaterials are:

$$\begin{aligned}
d_h^{(n)}(\rho_1, \rho_2, \dots, \rho_n) &= d_{33,s} + d_{31}^{(n)}(\rho_1, \rho_2, \dots, \rho_n) + d_{32}^{(n)}(\rho_1, \rho_2, \dots, \rho_n) \\
d_h^{(n)}(\rho_1, \rho_2, \dots, \rho_n) \times g_h^{(n)}(\rho_1, \rho_2, \dots, \rho_n) &= \left[d_h^{(n)}(\rho_1, \rho_2, \dots, \rho_n) \right]^2 / \kappa_{33}^{(n),\sigma}(\rho_1, \rho_2, \dots, \rho_n) \\
Z^{(n)}(\rho_1, \rho_2, \dots, \rho_n) &= \left(\rho_n C_{33}^{(n-1),D}(\rho_1, \rho_2, \dots, \rho_{n-1}) \right)^{0.5} \\
\text{FOM}_{31}^{(n)}(\rho_1, \rho_2, \dots, \rho_n) &= \left[d_{31}^{(n)}(\rho_1, \rho_2, \dots, \rho_n) \right]^2 / \kappa_{33}^{(n),\sigma}(\rho_1, \rho_2, \dots, \rho_n) \quad (5.12) \\
\text{FOM}_{33}^{(n)}(\rho_1, \rho_2, \dots, \rho_n) &= d_{33,s}^2 / \kappa_{33}^{(n),\sigma}(\rho_1, \rho_2, \dots, \rho_n) \\
F_I^{(n)}(\rho_1, \rho_2, \dots, \rho_n) &= p_3^{(n)}(\rho_1, \rho_2, \dots, \rho_n) / (\rho_1 \rho_2 \dots \rho_n c_p) \\
F_V^{(n)}(\rho_1, \rho_2, \dots, \rho_n) &= p_3^{(n)}(\rho_1, \rho_2, \dots, \rho_n) / \left(\rho_1 \rho_2 \dots \rho_n c_p \kappa_{33}^{(n),\sigma}(\rho_1, \rho_2, \dots, \rho_n) \right) \\
F_E^{(n),'}(\rho_1, \rho_2, \dots, \rho_n) &= \left[p_3^{(n)}(\rho_1, \rho_2, \dots, \rho_n) \right]^2 / \left(\rho_1^2 \rho_2^2 \dots \rho_n^2 c_p^2 \kappa_{33}^{(n),\sigma}(\rho_1, \rho_2, \dots, \rho_n) \right)
\end{aligned}$$

The effective properties of high order hierarchical metamaterials with overall relative density as 0.05 are shown in Figure 5.9, where 2nd-order ($\rho_1 = 0.1$, $\rho_2 = 0.5$), 3rd-order ($\rho_1 = 0.2$, $\rho_2 = 0.5$, $\rho_3 = 0.5$) and 4th-order ($\rho_1 = 0.4$, $\rho_2 = 0.5$, $\rho_3 = 0.5$, $\rho_4 = 0.5$) hierarchical metamaterials are considered. MAH is used to obtain the effective properties of these six metamaterials, which are compared with that of 1st-order T3-2. For hybrid hierarchical metamaterials (denoted by circle), increasing hierarchical order will further improve $d_h \times g_h$, Z , FOM_{33} , and F_V ; for involved self-similar hierarchical metamaterials (denoted by pentagram), FOM_{31} , F_I , and F_E' , instead, show an increasing trend with higher hierarchical order. Therefore, increasing hierarchical orders can further optimize figures of merit. For example, for considered hybrid hierarchical metamaterials,

the improvement of FOM_{33} , evaluating the piezoelectric energy harvesting performance, is enhanced from 15.84% (2nd-order) to 70.32% (4th-order) with 39.2% for 3rd-order. However, it should be mentioned that adopting hierarchical architectures may have an adverse effect on some effective properties, e.g., d_h of the self-similar hierarchical metamaterial.

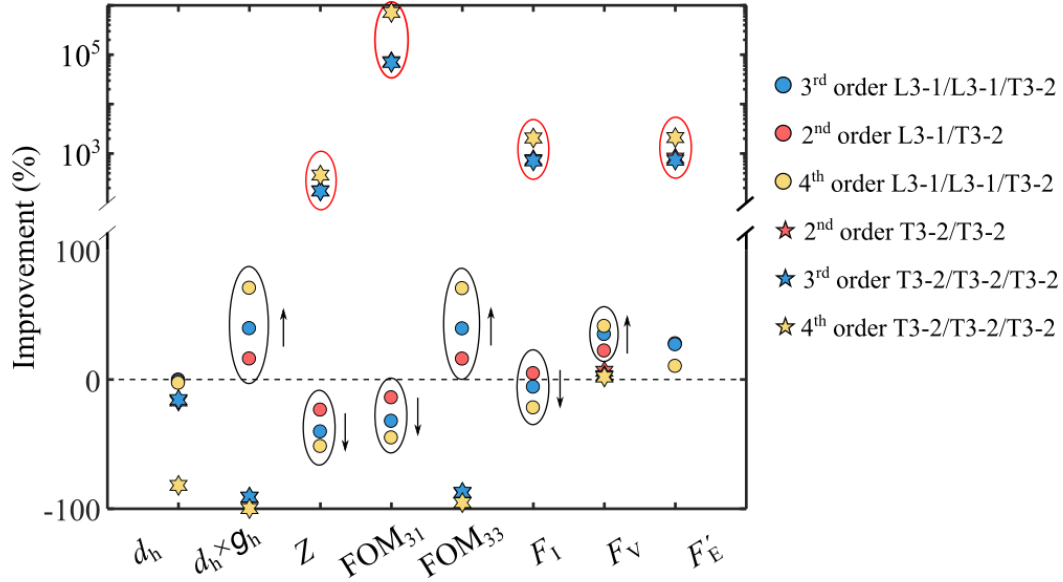


Figure 5.9 Influence of hierarchical order on the improvement of figures of merit. The overall relative density is 0.05. In specific, $\rho_1 = 0.1, \rho_2 = 0.5$ for 2nd-order; $\rho_1 = 0.2, \rho_2 = 0.5, \rho_3 = 0.5$ for 3rd-order; $\rho_1 = 0.4, \rho_2 = 0.5, \rho_3 = 0.5, \rho_4 = 0.5$ for 4th-order. (Reprinted with permission from ref [206], copyright 2020 Elsevier)

In order to determine the effective application scopes of hierarchical metamaterials, Figure 5.10 a-h illustrates the maximum improvement of 3rd-order hierarchical metamaterials (1st-order and 2nd-order share the same unit cell) compared with that of 3rd-order unit cell with $\rho = 0.05$. In general, d_h (Figure 5.10a), $d_h \times g_h$ (Figure 5.10b), and Z (Figure 5.10c) are always beneficial from hierarchical metamaterials. More specifically, the d_h and $d_h \times g_h$ of L3-1 show the most obvious improvement by replacing the solid plate with finer cellular structures; T3-2, however, contributes to the modification of $d_h \times g_h$ and Z when used as 1st-order and 2nd-order unit cells, respectively. As for FOM_{31} (Figure 5.10d), F_I (Figure 5.10f), and F'_E (Figure 5.10h), T3-2 is greatly enhanced by

hierarchical architectures with a maximum improvement of 8928 for FOM_{31} , 16.8 for F_I , and 15 for F'_E . On the contrary, in Figure 5.10e, T3-2 is inappropriate to be used as 3rd-order unit cell while beneficial for improving FOM_{33} when considered as 1st-order and 2nd-order unit cell. F_V (Figure 5.10g), however, exhibits no improvement or even suffers from hierarchical metamaterials. Similar behaviors observed in Figure 5.10a-h can also be found in Figure 5.8.

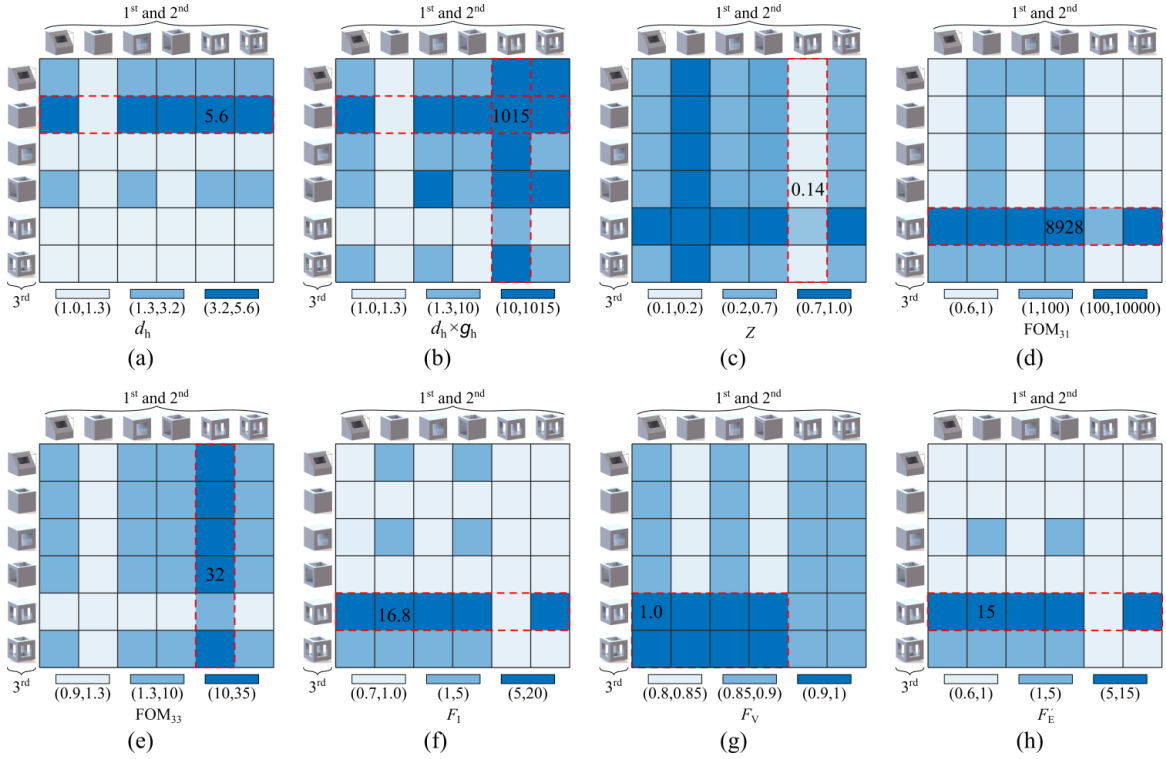


Figure 5.10 Maximum improvement of figures of merit of 3rd-order hierarchical metamaterials compared with that of 3rd-order unit cell with $\rho = 0.05$. 1st-order and 2nd-order share the same unit cell. (Reprinted with permission from ref [206], copyright 2020 Elsevier)

Figure 5.11 shows the application of hierarchical cellular ferroelectric metamaterials on the generated voltage within piezoelectric cymbal transducer (PCT), which is widely used in vibration controllers [56] actuator of microstructure [57], and mechanical energy harvesters [58]. As shown in Figure 5.11a, the PCT is composed of a piezoelectric disc ($D_3 = 20$ mm and $t_p = 2$ mm) sandwiched between two copper caps ($D_1 = 6$ mm, $D_2 = 12$ mm, $t_c = 0.6$ mm, and $h = 2$ mm),

Figure 5.11 Piezoelectric cymbal transducer (PCT) with hierarchical cellular ferroelectric metamaterials: (a) Geometric information of PCT, (b) Generated voltage in piezoelectric disc, (c) Effect of hierarchical orders on the output voltage of PCT with 1st-order 3-0 and 3-3 ($\rho_1 = 0.05$), 2nd-order 3-0/3-0 and 3-3/3-3 ($\rho_1 = 0.1, \rho_2 = 0.5$), 3rd-order 3-0/3-0/3-0 and 3-3/3-3/3-3 ($\rho_1 = 0.2, \rho_2 = 0.5, \rho_3 = 0.5$), 4th-order 3-0/3-0/3-0/3-0 and 3-3/3-3/3-3/3-3 ($\rho_1 = 0.4, \rho_2 = 0.5, \rho_3 = 0.5, \rho_4 = 0.5$). (Reprinted with permission from ref [206], copyright 2020 Elsevier)

5.5 Discussion on the electric field distribution and stress concentration

5.5.1 Electric field distribution during poling

Ferroelectric materials exhibit no (or negligible) piezoelectric and pyroelectric effects without polarization where a large static electric field is applied across the materials. In specific, when the local electric field, E_l , is larger than the coercive field, E_c , the ferroelectric material in this area will become poled in the direction of the applied field [80,81]. In Chapter 5.4, both MAH and scaling relationship assume fully-poled ferroelectric metamaterials. However, during the poling process of cellular materials, a high electric field concentrates in low permittivity air ($\epsilon_r = 1$) while a low electric field is observed in high permittivity ferroelectric ceramics ($\epsilon_r = 1187.5$ for BaTiO₃), leading to incomplete poling in these areas. This phenomenon is easy to understand by Gauss' law [80]:

$$E_l = q / (A \cdot \epsilon_r \cdot \epsilon_0) \quad (5.13)$$

where q is charge, A is area, and ϵ_0 is the permittivity of the free space. The complete poling of ferroelectric materials cannot be simply implemented by increasing the poling electric field, which leads to the dielectric breakdown within the air. To increase the allowable poling electric field, cellular ferroelectric materials are often poled via corona poling with a silicon oil bath [96], where silicon oil obtains higher dielectric strength than air, and the absence of conducting electrode further protects the materials from short-circuiting. Another possible method for realizing fully

polarization is to add high permittivity particles into the silicon oil, which increases the effective dielectric permittivity of the silicon oil and diminishes the permittivity difference between the ferroelectric materials and its surrounding medium.

Apart from the poling electric field, the topologies of cellular metamaterials also affect the poling performance. Figure 5.12 simulates the electric field distribution of six kinds of self-similar hierarchical metamaterials ($\rho_1 = 0.6$, $\rho_2 = 0.5$, and $\rho_3 = 0.4$) during the poling process with a silicon oil bath. The dielectric permittivity of the unpoled BaTiO₃ before poling is seen as an average value ($\epsilon_r = 1187.5$) of poled BaTiO₃ in 1- and 3- directions. Since the relative permittivity of the overall cellular structure is mainly determined by the relative density instead of the amount of poled materials [80], the MAH is used to obtain the effective dielectric properties of these hierarchical metamaterials. The normalized poling electric field applied on the topmost order of these hierarchical metamaterials is 1.2 while the normalized coercive field of BaTiO₃ is 1, sharing the same ratio with Reference [80] (poling electric field is 0.6 MV/m and coercive electric field is 0.5 MV/m). As shown in the first column of the plots in Figure 5.12, the yellow color indicates this region is occupied by silicon oil ($\epsilon_r = 2.56$). Since the single pore in the 3-0 unit cell is enclosed by the ferroelectric material, the blue color means the air fills up this void space ($\epsilon_r = 1$). In the second column of the plots in Figure 5.12, an electric potential difference is applied in the two surfaces along 3 direction such that an overall electric field of 1.2 is realized. If the local electric field component along 3 direction is larger than 1, this ferroelectric region is successfully poled, denoted by the red color in the inset; otherwise green color for unpoled material ($E_l < 1$). The normalized electric field versus fraction curves illustrates the relationship between the responsive electric field within the unit cell and the percentage of corresponding element volumes over the whole volume of ferroelectric elements. After that, the proportion of poled materials, V_f , is

obtained, and the average electric field over these poled elements is applied at the 2nd-order unit cell (third column of the plots in Figure 5.12). This step is repeated for 1st-order unit cell and plotted in the fourth column of Figure 5.12. The dielectric properties of ferroelectric materials constituting the high order unit cell are obtained by conducting asymptotic homogenization in low order unit cell while the dielectric permittivities of air/silicon oil keep constant.

In Figure 5.12, apart from L3-1, all other unit cells cannot be fully poled. The proportion of overall poled materials of the hierarchical metamaterials is simply the product of the percentage of poled materials at each order. In Specific, the percentage of overall poled materials for self-similar hierarchical metamaterials made of 3-0, L3-1, T3-1, LT3-2, T3-2, and 3-3 are 30%, 100%, 12%, 47%, 1%, and 6%, respectively, which reveals the importance of unit cell topologies on the poling result. In general, the amount of ferroelectric materials continuously distributed along the 3 direction determines the percentage of poled materials, indicated by the red regions in insets. For example, all ferroelectric materials in the L3-1 unit cell are concentrated in the four plates parallel to the poling direction, which results in the uniform distribution of the electric field and leads to full polarization of these materials. In contrast, for T3-2 unit cell, only a small amount of ferroelectric materials are poled, corresponding to the small percentage of ferroelectric materials distributed in the four columns parallel to the poling direction. Furthermore, apart from 3rd-order LT3-2/LT3-2/LT3-2 hierarchical metamaterials, more ferroelectric materials are poled in lower order unit cells e.g., 31% for 3rd-order 3-3 unit cell, 38% for 2nd-order 3-3 unit cell, and 48% for 1st-order 3-3 unit cell. Since the piezoelectric charge constants are greatly affected by the amount of poled ferroelectric materials [80], the hydrophone and piezoelectric energy harvesting (with high FOM₃₃) performance of T3-2 unit cell will be a tradeoff between the relative density and

polarization. However, due to the full polarization of the L3-1 unit cell, it is still a good choice for pyroelectric energy harvesting and IR detection device.

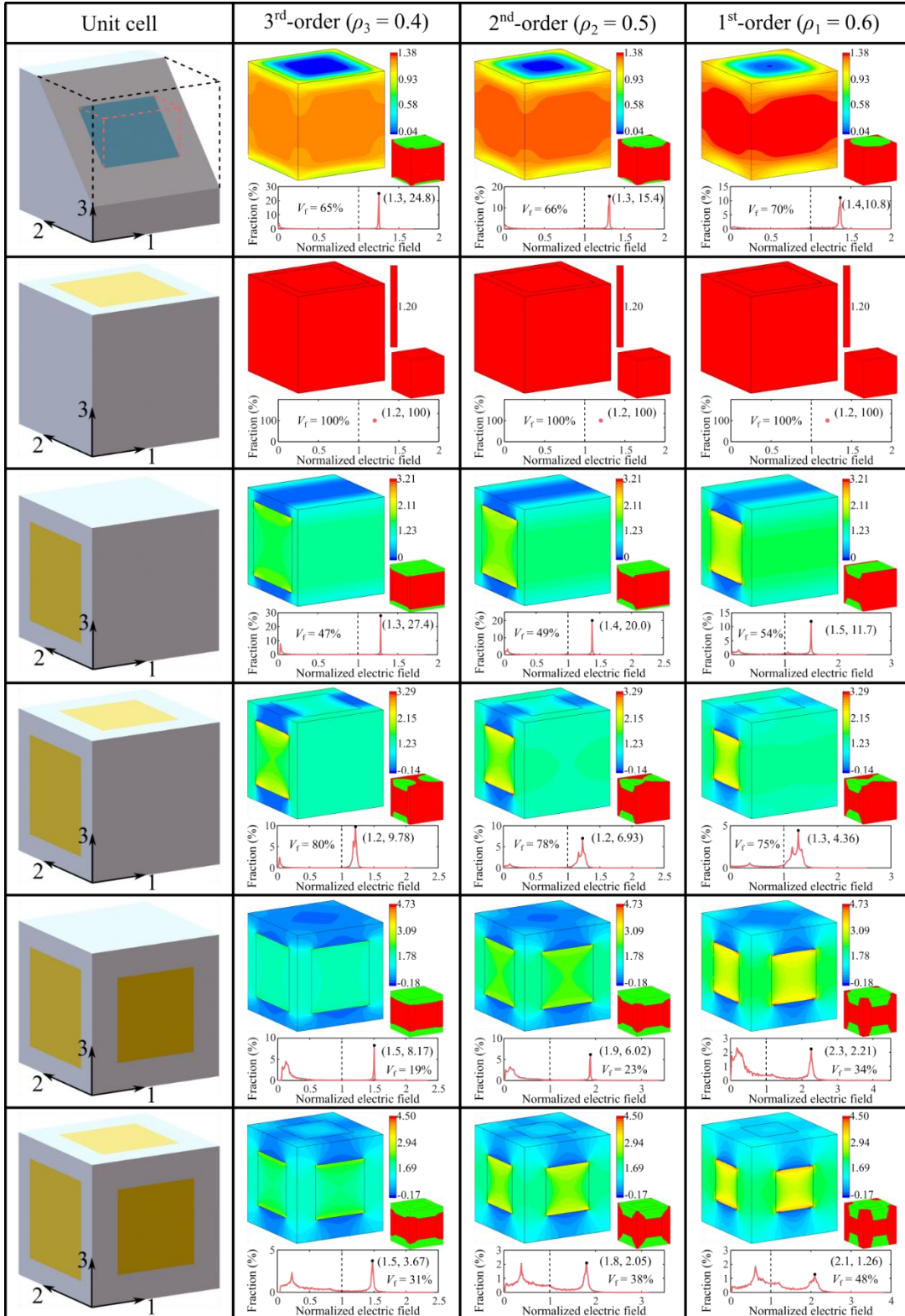


Figure 5.12 Electric field distribution at each level of 3rd-order hierarchical cubic ferroelectric metamaterials with $\rho_3 = 0.4$, $\rho_2 = 0.5$, and $\rho_1 = 0.6$ during polarization. The left large contour figures indicate the normalized electric field; the right small contour presents the poled regions (red color) and unpoled regions (green color). The normalized electric field versus fraction curve indicates the distribution of electric field over population of ferroelectric material elements. (Reprinted with permission from ref [206], copyright 2020 Elsevier)

5.5.2 Stress concentration factor

Apart from piezoelectric and pyroelectric properties, mechanical strength is also of great importance on the application since it describes the ability of ferroelectric metamaterials to withstand an applied load without failure. To evaluate the mechanical strength of a hierarchical cellular ferroelectric metamaterials, the magnitude and location of local stress concentration should be first determined. For brittle ferroelectric metamaterials, the failure stress can be approximated by dividing the constitutive material strength with the stress concentration factor. Figure 5.13 shows the stress distribution and concentration factor in response to a uniaxial macroscopic compressive strain calculated by ANSYS 19.2. In specific, six kinds of self-similar hierarchical metamaterials with $\rho_1 = 0.6$, $\rho_2 = 0.5$, and $\rho_3 = 0.4$ are considered. As shown in the second column of the plots in Figure 5.13, a uniaxial compression strain of 0.01 along direction 3 is firstly applied at the 3rd-order unit cell. After that, the element with the highest von Misses stress is identified, and the component of its strain is used as load and applied at the 2nd-order unit cell (third column of the plots in Figure 5.13). A similar procedure is also repeated for 1st-order unit cell and plotted in the fourth column of Figure 5.13. It should be mentioned that the material properties of the high order unit cells are from the effective values of corresponding lower-order instead of that of the solid constitutive material. For example, the material properties of 3rd-order 3-0/3-0/3-0 are same as the effective properties of 2nd-order 3-0/3-0. In order to obtain the macroscopic compression stress, $\bar{\sigma}$, the lattice is considered as a homogeneous equivalent material,

and $\bar{\sigma}$ is calculated by dividing the reaction forces applied on the outer surface of the cube bearing the external compressive pressure with its corresponding loading surface areas. The stress concentration factor, presented by SC, is then defined by the ratio of the maximal stress to the topmost order macroscopic stress. However, due to the possible distortion of some elements, the stress field singularities often occur in ANSYS, and the maximum stress is also not straightforward, which increases with finer mesh. Therefore, it is not reliable to obtain the maximum stress from a single element. Statistical analysis is more accurate; in this section, the maximum stress, σ_m , is defined as the average value of the top 1% population of the elements possessing the highest von Mises stress [207]. Consequently, the corresponding strain is also seen as the mean value of these elements, which will be applied in lower order.

In Figure 5.13, all the values are normalized by the corresponding values of effective macroscopic homogeneous solids with the same deformation. In Specific, the 3rd-order T3-2/T3-2/T3-2 hierarchical metamaterials exhibit the maximum normalized SC of 628.9 while the minimum value of 8.33 is from 3rd-order L3-1/L3-1/L3-1. The SC of 3rd-order 3-0/3-0/3-0, T3-1/T3-1/T3-1, LT3-2/LT3-2/LT3-2, and 3-3/3-3/3-3 are 28.88, 58.22, 41.53, and 140.6, respectively. In addition, within a hierarchical metamaterial, lower-order unit cell always has higher SC. For example, for 3rd-order 3-0/3-0/3-0, the SC of 3rd-order unit cell is 3.81, and this value increases to 11.6 at 2nd-order unit cell. The normalized von Mises stress versus fraction curve below each contour figure presents the distribution of stress over the population of elements. Apart from 3rd-order L3-1/L3-1/L3-1, all the curves of the remaining metamaterials show two peak values, which correspond to two distinct regions in the relating contour figure. For example, for the 3rd-order unit cell of 3-0/3-0/3-0, the first peak with normalized stress of 0.04 corresponds to the blue area in its contour figure (perpendicular to the loading direction), while the second peak

value with normalized stress of 3.5 is from the green region (parallel to the loading direction). Since the stress concentration factor is always higher than that at the second peak value, a smaller fraction of the regions parallel to the loading direction results in a higher stress concentration factor, which is validated by the comparison between SC of 3rd-order T3-2 and 3-3 unit cells.

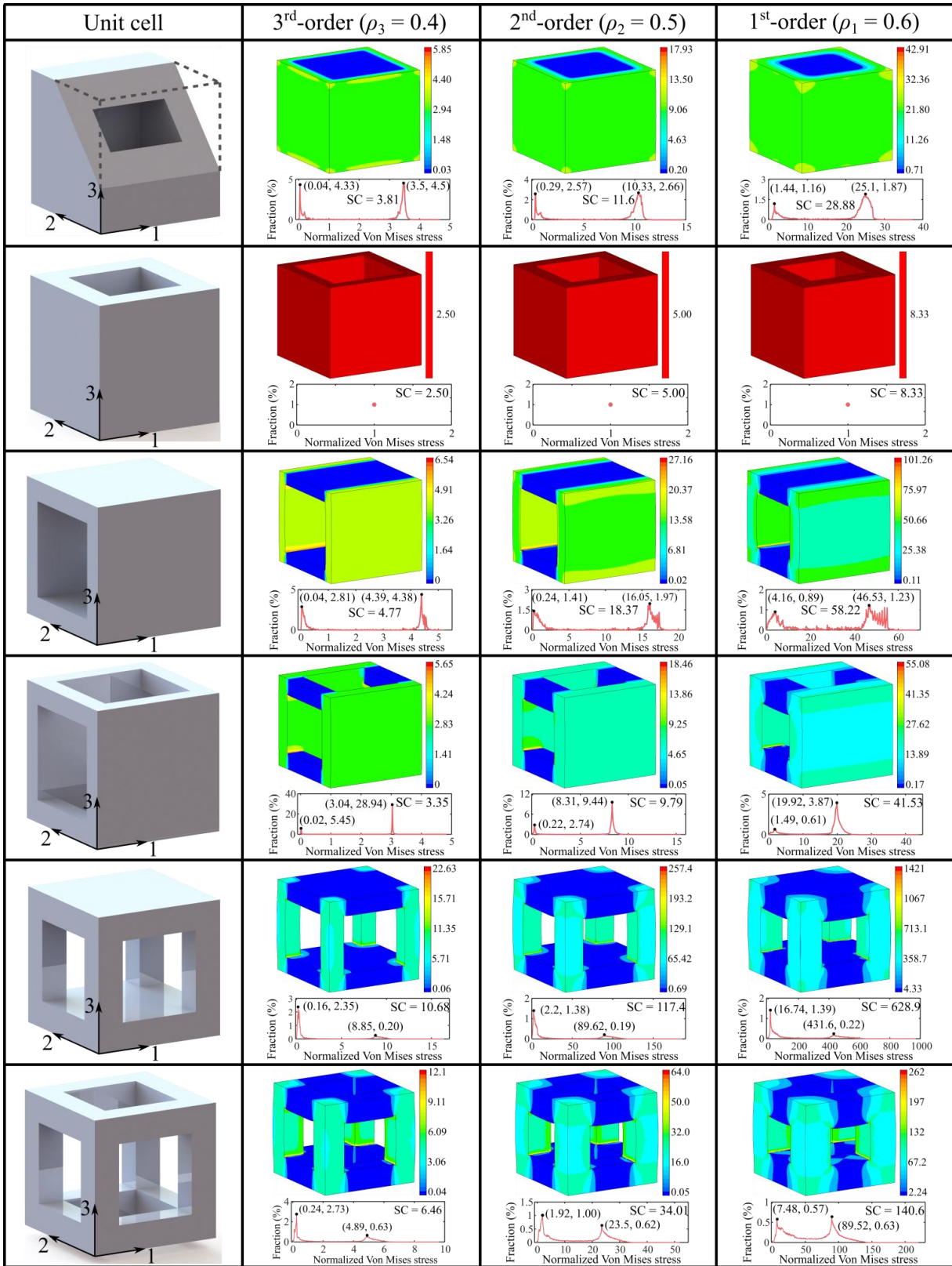


Figure 5.13 Stress distribution and concentration at each level of 3rd-order hierarchical cubic ferroelectric metamaterials with $\rho_3 = 0.4$, $\rho_2 = 0.5$, and $\rho_1 = 0.6$. Colors indicate the normalized von Miss stress. The normalized von Mises stress versus fraction curve indicates the distribution of stress over population of elements. (Reprinted with permission from ref [206], copyright 2020 Elsevier)

5.6 Conclusion remarks on hierarchical cubic cellular ferroelectric metamaterials

In this section, hierarchical cellular ferroelectric metamaterials are introduced as a new class of architected smart metamaterials. A design motif is introduced to develop alternative classes of self-similar or hybrid hierarchical ferroelectric metamaterials. In order to observe their advantages over the base solid materials, the effective piezoelectric and pyroelectric properties of these ferroelectric metamaterials are obtained by multiscale asymptotic homogenization and are compared with that of the constitutive solid materials. A systematic study is conducted to explore the effect of relative density, cell topology, and structural hierarchy on the potential applications of ferroelectric metamaterials, including applications as piezoelectric and pyroelectric energy harvesters. The research leads to the following principal findings:

- (1) Similar to mechanical properties, the scaling relationship is also applicable for ferroelectric properties, described by piecewise functions with two sub-functions, which shows a good agreement with the MAH result. It is shown that the scaling relationship can serve as an efficient alternative method for predicting the effective properties of hierarchical ferroelectric metamaterials (Figure 5.6 and 5.11).
- (2) For small relative density, the simple micromechanics model provides a visualized method to obtain the effective ferroelectric properties and explain the scaling relationship found in the 1st-order unit cell (Figure 5.7).

(3) Cellular ferroelectric metamaterials with hierarchical microarchitectures can significantly enhance the ferroelectric figures of merit. They can provide ultralight design solutions for fabricating advanced smart materials and intelligent structures with exceptional multifunctional properties (Figure 5.8, 5.9 and 5.12).

(4) For 1st-order ferroelectric metamaterials, T3-2 exhibits the best performance for hydrophone (highest d_h , $d_h \times g_h$, and smallest Z) and piezoelectric energy harvesting (FOM₃₃) applications. Instead, L3-1 with high values of F_1 is the most suitable design for infrared detection devices and pyroelectric energy harvesters; LT3-2 presents the highest FOM₃₁ while there is a negligible difference between the F_V of six types of cellular ferroelectric metamaterials (Figure 5.6).

(5) Apart from F_V , some 2nd-order hierarchical cellular ferroelectric metamaterials exhibit remarkable improvement compared to that of their corresponding 2nd-order unit cells with the same overall relative density. For example, the normalized FOM₃₃ of hybrid 2nd-order T3-2/L3-1 ($\rho_1 = 0.2$, $\rho_2 = 0.25$) is 117.49, while it is 19.95 for 1st-order L3-1 with a relative density of $\rho = 0.05$. In addition, the hybrid hierarchical cellular metamaterials can reveal ferroelectric properties not achievable by fractal-like metamaterials. For example, the maximum normalized d_h is obtained from 2nd-order L3-1/T3-2. The observed phenomena for the figures of merit of the 2nd-order hierarchical metamaterials have been elucidated by six representative trends (Figure 5.9 and 5.10).

(6) Increasing structural hierarchical order can further improve the effective properties of hierarchical cellular ferroelectric metamaterials. For example, compared with the 1st-order T3-2 ($\rho = 0.05$), the normalized FOM₃₃ is enhanced from 15.84% for the 2nd-order L3-1/T3-2 ($\rho_1 = 0.1$, $\rho_2 = 0.5$) to 70.32% for the 4th-order L3-1/ L3-1/L3-1/T3-2 ($\rho_1 = 0.4$, $\rho_2 = \rho_3 = \rho_4 = 0.5$). However, adopting hierarchical architectures may result in adverse effects on some effective ferroelectric

properties (Figure 5.12 and 5.13), uneven electric field distribution during polarization (Figure 5.12), and lead to higher stress concentration factors (Figure 5.13) which ultimately can reduce the fracture strength of ferroelectric metamaterials unless for nanoscale metamaterials or for nanoarchitected metamaterials with ultrathin constitutive struts where elastic buckling makes the hierarchical metamaterial structurally resilient [202][200].

CHAPTER 6

Machine learning-assisted design of ferroelectric spinodoids

This chapter includes the machine learning-assisted design of ferroelectric spinodoids. The effect of spinodoid geometrical parameters on the effective piezoelectric properties of spinodoids is studied, and optimally selected spinodoids are identified with the assistance of machine learning. The chapter is divided into five sections, including spinodoid modelling, finite element homogenization, machine learning implementation, piezoelectric properties of spinodoids, and experimental tests.

6.1 Parametric spinodoid metamaterials

The parametric spinodoid metamaterials are derived from spinodal topologies, which are close to stochastic bicontinuous microstructures and originated from a spinodal decomposition of two homogeneous phases [208,209]. Spinodal decomposition is a near-instantaneous diffusion-driven phase transformation that converts a single-phase material into a two-phase material (one possibly being a void space), with the two phases arranged in a bi-continuous topology and separated by a surface with nearly uniform negative Gaussian curvature and nearly zero mean curvature [210].

As shown in Figure 6.1a, the homogeneous parent phase grows in time until two separate phases are formed [211]. This phenomenon can be found in a variety of physical processes, e.g., the dealloying of an Au/Ag solid solution or the heating/cooling of an emulsion gel. For example, based on the electrochemical dealloying of $\text{Ag}_{93}\text{Au}_7$ master alloy in 0.01M H_2SO_4 aqueous electrolyte, spinodal and hierarchical nested-network nanoporous structures have been fabricated, which exhibit enhanced strength and stiffness at a given solid fraction (Figure 6.1b) [212].

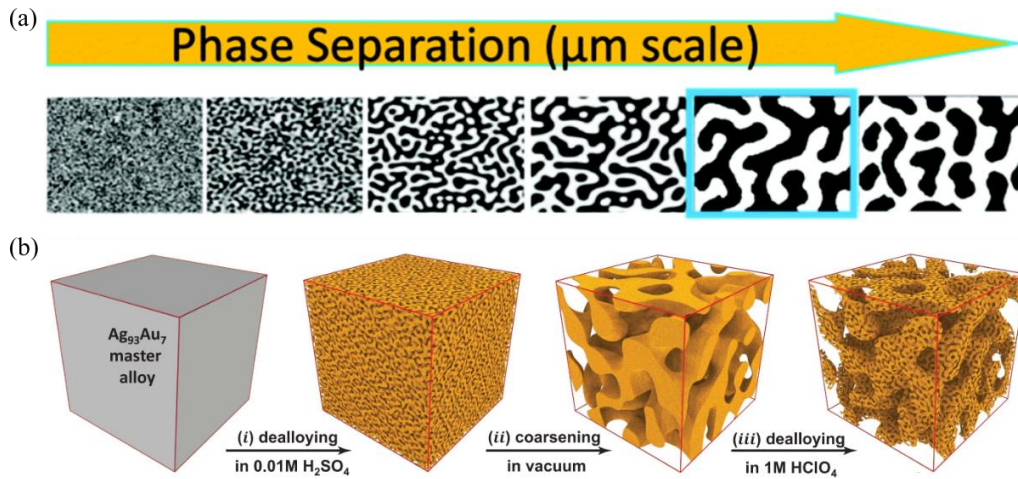


Figure 6.1 (a) The phase separation process to generate porous spinodal material (black: solid, white: air). (b) Electrochemical dealloying of $\text{Ag}_{93}\text{Au}_7$ master alloy (yellow) in 0.01M H_2SO_4 aqueous electrolyte (white) leading to a hierarchical spinodal nanoscale. (Figure 6.1a adapted from ref [211] under the terms of the CC BY 4.0 license; Figure 6.1b reprinted with permission from ref [212]. Copyright 2021 AAAS)

Mathematically, spinodal decomposition process can be described with a phase field approach and by using the following Cahn-Hilliard equation [208]:

$$\frac{\partial \varphi}{\partial t} = \Delta \left[\frac{df(\varphi)}{d\varphi} - \theta^2 \Delta \varphi \right] \quad (6.1)$$

where φ is the concentration difference between the materials (in the case of porous spinodoids, one of the materials/phases is the constitutive solid while the other one is void/air) that varies between -1 and 1 ($\varphi = 1$ presents a fully solid material and $\varphi = -1$ denotes a complete void); f is a

double-well free-energy function chosen as $f(\varphi) = (\varphi^2 - 1)^2/4$; θ is the width of the interface between the two phases (i.e., solid and void in the case of a porous spinodoid) and t is time, describing the coarsening process and temporal evolution of the spinodal topologies; Δ is the Laplacian operator. However, it takes hours on a modern computer to solve the time-dependent phase separation process equation. To overcome this limitation, one alternative method is to use a superposition of a large number $N \gg 1$ of standing sinusoidal waves with a constant wavenumber $\beta > 0$ to denote the early stages of spinodal decomposition, represented by a truncated Fourier series or a Gaussian random field (GRF) as following [213]:

$$\varphi(\mathbf{x}) = \sqrt{\frac{2}{N}} \sum_{i=1}^N \cos(\beta \mathbf{n}_i \cdot \mathbf{x} + \gamma_i), \quad \gamma_i \sim [0, 2\pi] \quad (6.2)$$

where \mathbf{x} is the position vector; \mathbf{n}_i and γ_i denote, respectively, the direction vector and phase angle of the i^{th} unit wave vector, which is randomly selected from the three-dimensional space; $N = 5000$ different wave vectors are used to calculate the GRF and the constant wavenumber is $\beta = 12\pi$ [209,214,215]. From Eq. (6.2), we can generate a bicontinuous topology by computing level sets of the phase field. Here, a binary indicator function, $G(\mathbf{x})$, is defined to determine the material or void at position \mathbf{x} :

$$G(\mathbf{x}) = \begin{cases} 1 & \text{if } \varphi(\mathbf{x}) \leq \varphi_0 \quad (\text{Solid material}) \\ 0 & \text{if } \varphi(\mathbf{x}) > \varphi_0 \quad (\text{Void/air}) \end{cases} \quad (6.3)$$

where $G(\mathbf{x}) = 0$ indicates void and 1 is used solid material; φ_0 is the level cut value and can be calculated by exploiting the Gaussian properties of the random field as:

$$\varphi_0 = \sqrt{2} \operatorname{inverf}(2\rho - 1) \quad (6.4)$$

where $\operatorname{inverf}(\dots)$ represents the inverse error function and ρ is relative density.

It should be noted that since the wave vector is randomly sampled from the whole three-dimensional space, the generated spinodal topologies are isotropic. In order to extend the spinodal architectures and achieve anisotropic properties, the wave vector directions can be limited to be selected within specific regions, favoring some directions and neglecting others. As shown in Figure 6.2a, three angles (θ_1 , θ_2 , and $\theta_3 < \pi/2$) are used to denote the available regions related to axis x , y , and z in a Cartesian coordinate system. For example, $\theta_1 = \theta_2 = 0$, and nonzero θ_3 leads to a cone sampling area with respect to axis z (purple cone in Figure 6.2a). The generated topologies are then voxelized and exported to ANSYS 2020R2 for computational homogenization to obtain their effective ferroelectric properties (Figure 6.2b). Since the resulting topologies approximate the products of spinodal decomposition, *spinodoid* topologies are used to name these derivatives, which can be simply described by four parameters, i.e., θ_1 , θ_2 , θ_3 , and ρ . Three types of spinodoid architectures are shown in Figure 6.2c (lamellar), Figure 6.2d (columnar), and Figure 6.2e (cubic), with geometry parameters (θ_1 , θ_2 , θ_3 , ρ) as $(0^\circ, 0^\circ, 30^\circ, 0.5)$, $(30^\circ, 30^\circ, 0^\circ, 0.5)$, and $(60^\circ, 60^\circ, 60^\circ, 0.5)$, respectively.

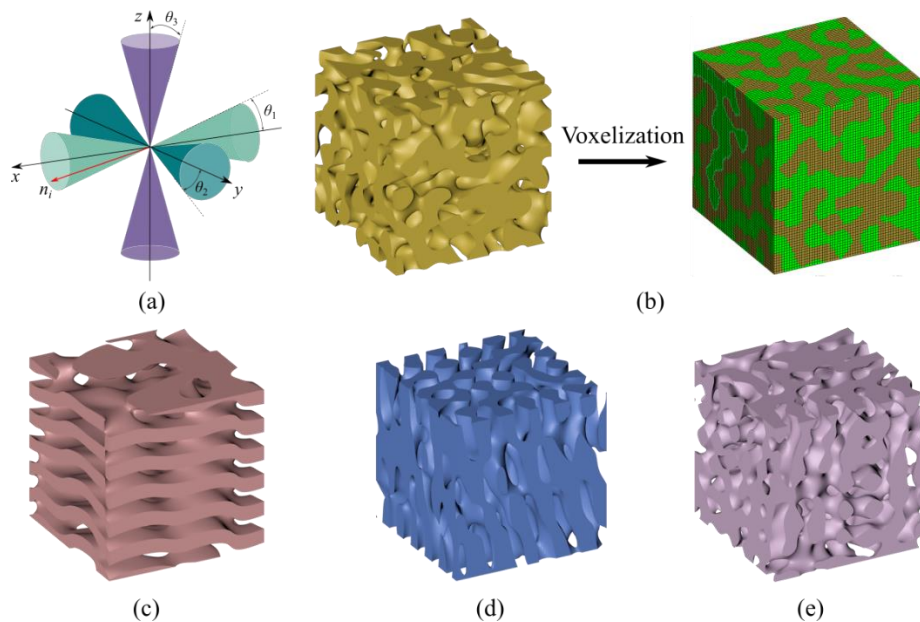


Figure 6.2. (a) Schematic of the design parameters: $\theta_1, \theta_2, \theta_3$. (b) Discretization/voxelization of the spinodoid (elements in green refers to air, and elements in brown present the solid material). (c) Lamellar, (d) Columnar, and (e) Cubic spinodoids.

6.2 Finite element homogenization

Before conducting homogenization analysis, poling process is firstly simulated to determine the local polarization direction of the spinodoid unit cells. As shown in Figure 6.3a, an electric field is applied to the unpoled spinodoid unit cells by applying an electric potential difference between the upper and lower surfaces. The local polarization direction is then aligned with the simulated poling electric field.

Due to the lack of periodicity of the spinodoid structures, the previously derived AH method, which requires periodic boundary conditions, cannot be used to predict the effective ferroelectric properties of the spinodoid metamaterial. In this section, a finite element homogenization is proposed to determine their effective thermo-electro-mechanical properties. As shown in Figure 6.3b, six boundaries are considered for spinodoid structures: $A^- (x = 0)$, $A^+ (x = L)$, $B^- (y = 0)$, $B^+ (y = W)$, $C^- (z = 0)$, $C^+ (z = H)$, where L, W , and H are the structure sizes along the three directions.

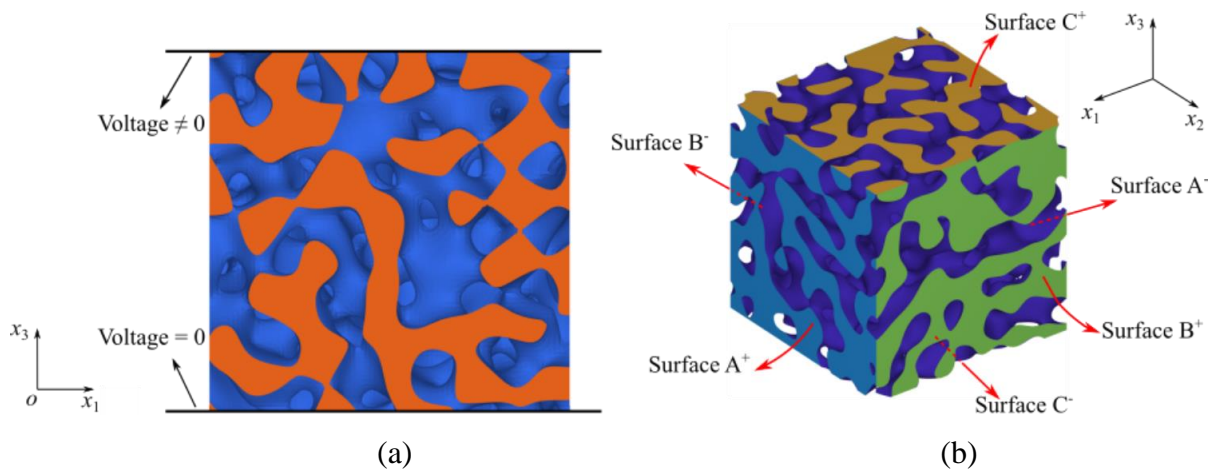


Figure 6.3 (a) Poling simulation. (b) Six boundary surfaces.

The average strains and electric fields can be applied on the unit cell by setting the displacements, u_i , and voltage, ϕ , at boundaries through:

$$u_i^{K^+} - u_i^{K^-} = \overline{C}_{ij} (x_j^{K^+} - x_j^{K^-}) \quad (6.5a)$$

$$\phi^{K^+} - \phi^{K^-} = \overline{\kappa}_i (x_i^{K^+} - x_i^{K^-}), \quad i, j = 1, 2, 3 \quad (6.5b)$$

where the index ‘K⁺’ refers to the surface along the positive x_j direction and ‘K⁻’ refers to the surface along the negative x_j direction (surfaces A⁻/A⁺, B⁻/B⁺ and C⁻/C⁺ in Figure 6.3b); \overline{C}_{ij} and $\overline{\kappa}_i$ are the effective stiffness and dielectric constant of the unit cell, respectively. It is assumed that the average mechanical and electric properties of a unit cell are equal to the average properties of the whole architected structure. The resulting average strains $\overline{\varepsilon}_{ij}$, stresses $\overline{\sigma}_{ij}$, electric fields \overline{E}_i , and electric displacements \overline{D}_i , of the unit cell are obtained as:

$$\overline{\varepsilon}_{ij} = \frac{1}{V} \int_V \varepsilon_{ij} dV \quad \text{and} \quad \overline{\sigma}_{ij} = \frac{1}{V} \int_V \sigma_{ij} dV \quad \text{with } i, j = 1, 2, 3 \quad (6.6a)$$

$$\overline{E}_i = \frac{1}{V} \int_V E_i dV \quad \text{and} \quad \overline{D}_i = \frac{1}{V} \int_V D_i dV \quad \text{with } i = 1, 2, 3 \quad (6.6b)$$

In this research, ANSYS is used to conduct the finite element homogenization, and the average quantities in Eq. (6.6) are calculated by a summation over averaged element values multiplied by the corresponding element volume divided by the overall volume of the unit cell, i.e.,

$$\overline{\varepsilon}_{ij} = \frac{\sum_{e=1}^N \varepsilon_{ij}^{(e)} V^{(e)}}{\sum_{e=1}^N V^{(e)}}, \quad \text{and} \quad \overline{\sigma}_{ij} = \frac{\sum_{e=1}^N \sigma_{ij}^{(e)} V^{(e)}}{\sum_{e=1}^N V^{(e)}} \quad \text{with } i, j = 1, 2, 3 \quad (6.7a)$$

$$\overline{E}_i = \frac{\sum_{e=1}^N E_i^{(e)} V^{(e)}}{\sum_{e=1}^N V^{(e)}}, \quad \text{and} \quad \overline{D}_i = \frac{\sum_{e=1}^N D_i^{(e)} V^{(e)}}{\sum_{e=1}^N V^{(e)}} \quad \text{with } i = 1, 2, 3 \quad (6.7b)$$

where $V^{(e)}$, $\varepsilon_{ij}^{(e)}$, $\sigma_{ij}^{(e)}$, $E_i^{(e)}$, and $D_i^{(e)}$ are the volume, strain, stress, electric field, and electric displacement of the element e ; N is the total number of elements used to discretize the unit cell.

To find the effective properties coefficients, special mechanical and electric loads with suitable boundary conditions should be applied in such a way that for a particular load case, only one value in the strain/electric field vector is non-zero, and all the others are zero. Table 6.1 lists the nine boundary conditions required to obtain the effective multiphysical properties of ferroelectric spinodoids, in which q is an arbitrary quantity.

Table 6.1 Boundary conditions (displacement/electric potential) and equations to calculate the effective properties of spinodoid unit cell. $i = 1, 2, 3$ and $j = 1, 2, 3, 4, 5, 6$.

Loading	A ⁺ /A ⁻	B ⁺ /B ⁻	C ⁺ /C ⁻	Effective properties
1	$u_1^{A^-} = 0, u_1^{A^+} = q$	$u_2^{B^-} = u_2^{B^+} = 0$	$u_3^{C^-} = u_3^{C^+} = 0$ $\phi^{C^-} = \phi^{C^+} = 0$	$\overline{C}_{i1} = \overline{\sigma}_{i1}/\overline{\varepsilon}_1,$ $\overline{e}_{i1} = \overline{D}_i/\overline{\varepsilon}_1$
2	$u_1^{A^-} = u_1^{A^+} = 0$	$u_2^{B^-} = 0, u_2^{B^+} = q$	$u_3^{C^-} = u_3^{C^+} = 0$ $\phi^{C^-} = \phi^{C^+} = 0$	$\overline{C}_{i2} = \overline{\sigma}_{i2}/\overline{\varepsilon}_2,$ $\overline{e}_{i2} = \overline{D}_i/\overline{\varepsilon}_2$
3	$u_1^{A^-} = u_1^{A^+} = 0$	$u_2^{B^-} = u_2^{B^+} = 0$	$u_3^{C^-} = 0, u_3^{C^+} = q$ $\phi^{C^-} = \phi^{C^+} = 0$	$\overline{C}_{i3} = \overline{\sigma}_{i3}/\overline{\varepsilon}_3,$ $\overline{e}_{i3} = \overline{D}_i/\overline{\varepsilon}_3$
4	$u_1^{A^-} = 0$	$u_3^{B^-} = 0, u_3^{B^+} = q$ $\phi^{B^-} = \phi^{B^+} = 0$	$u_2^{C^-} = 0, u_2^{C^+} = q$	$\overline{C}_{i4} = \overline{\sigma}_{i4}/\overline{\varepsilon}_4,$ $\overline{e}_{i4} = \overline{D}_i/\overline{\varepsilon}_4$
5	$u_3^{A^-} = 0, u_3^{A^+} = q$ $\phi^{A^-} = \phi^{A^+} = 0$	$u_2^{B^-} = 0$	$u_1^{C^-} = 0, u_1^{C^+} = q$	$\overline{C}_{i5} = \overline{\sigma}_{i5}/\overline{\varepsilon}_5,$ $\overline{e}_{i5} = \overline{D}_i/\overline{\varepsilon}_5$
6	$u_2^{A^-} = 0, u_2^{A^+} = q$	$u_1^{B^-} = 0, u_1^{B^+} = q,$	$u_3^{C^-} = \phi^{C^+} = 0$	$\overline{C}_{i6} = \overline{\sigma}_{i6}/\overline{\varepsilon}_6,$ $\overline{e}_{i6} = \overline{D}_i/\overline{\varepsilon}_6$
7	$u_3^{A^-} = u_3^{A^+} = 0,$ $\phi^{A^-} = 0, \phi^{A^+} = q$	$u_2^{B^-} = 0$	$u_1^{C^-} = u_1^{C^+} = 0$	$\overline{e}_{j1} = \overline{D}_i/\overline{E}_1$ $\overline{\kappa}_{i1} = \overline{D}_i/\overline{E}_1$
8	$u_1^{A^-} = 0$	$u_3^{B^-} = u_3^{B^+} = 0$ $\phi^{B^-} = 0, \phi^{B^+} = q$	$u_2^{C^-} = u_2^{C^+} = 0$	$\overline{e}_{j2} = \overline{D}_i/\overline{E}_2$ $\overline{\kappa}_{i2} = \overline{D}_i/\overline{E}_2$
9	$u_1^{A^-} = u_1^{A^+} = 0$	$u_2^{B^-} = u_2^{B^+} = 0$	$u_3^{C^-} = u_3^{C^+} = 0$ $\phi^{C^-} = 0, \phi^{C^+} = q$	$\overline{e}_{j3} = \overline{D}_i/\overline{E}_3$ $\overline{\kappa}_{i3} = \overline{D}_i/\overline{E}_3$

It is noted that since the average strain/electric field in Eq. (6.7) is approximated by applying uniform displacement/voltage on the corresponding two opposite surfaces, the periodic boundary conditions, which are not applicable for the designed spinodoid metamaterials, are thus avoided.

The accuracy of the developed methodology is verified in Figure 6.4. The calculated results are compared with those based on the AH method. In order to apply periodic boundary conditions,

octet truss unit cells with different relative densities are considered. BaTiO₃, whose properties are provided in Table 3.1, is selected as the solid ferroelectric material. It can be seen that there is no difference between the results of these two methods with mean absolute error (MAE) of 2×10^{-4} GPa in Figure 6.4a and 1×10^{-12} C²/Nm² in Figure 6.4b, and the proposed finite element homogenization is reliable in predicting the effective multiphysical properties of spinodoids.

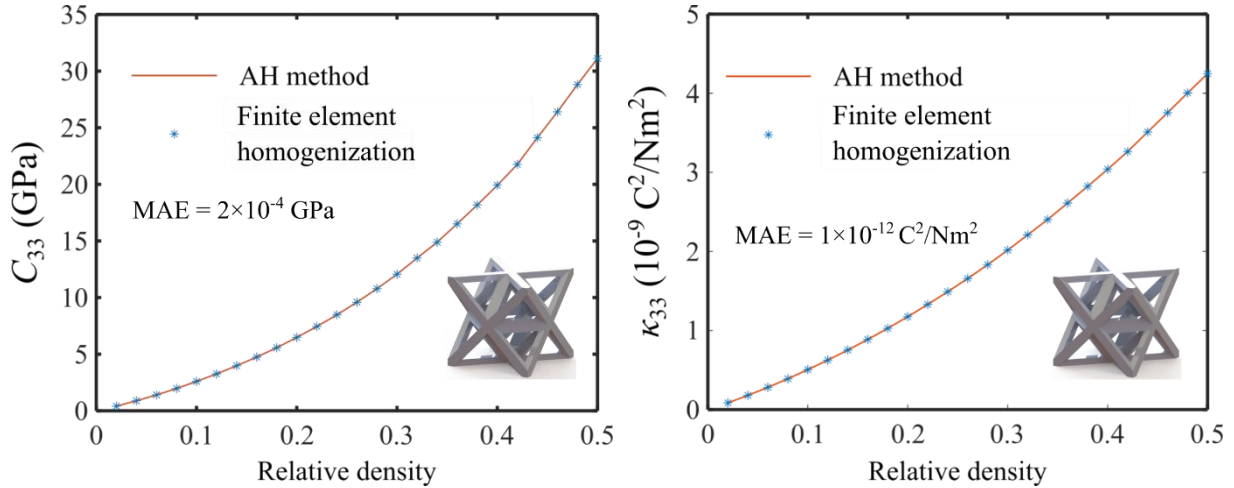


Figure 6.4 Comparison of the effective stiffness (C_{33}) (a) and dielectric constant (k_{33}) (b) of ferroelectric octet truss metamaterials calculated by AH method and finite element homogenization.

Although the proposed finite element homogenization provides an efficient way to predict the effective properties of spinodoid metamaterials, it is still impossible to account for all the different spinodoid topologies. In the following section, we use a well-trained machine learning network to predict the effective properties of more cases.

6.3 Machine learning implementation

6.3.1 Multilayer perceptron (MLP)

The artificial neural network is a set of interconnected nodes used for understanding and solving modeling problems that have complex relationships between causal factors and responses.

Multilayer Perceptron Neural Network (MLP) is one of the most effective artificial neural network techniques, and thus it has been used as the benchmark model by many researchers [216]. In this study, MLP is employed to analyze and predict the ferroelectric coefficients.

As illustrated in Figure 6.4, MLP is a multilayer feedforward network trained by an error back propagation algorithm. In this feedforward MLP network, the input layer contains input information $(x_1, x_2, x_3, x_4) = (\rho, \theta_1, \theta_2, \theta_3)$, which is necessary to describe a spinodoid structure; the hidden layer, h_i , consists of m_i neuron nodes, and the output layer includes a target output \mathbf{y} , i.e., the effective multiphysical properties obtained by previously proposed finite element homogenization. To obtain the network output, we need to compute the output of each node in each layer. When an input information \mathbf{x} is transferred into a neuron node j in the hidden layer h_i , the output h_i^j of this neuron is computed by [217]:

$$h_i^j = f \sum_{k=1}^{m_{i-1}} (w_{k,j}^{i-1} h_{i-1}^k + b_{k,j}^{i-1}), \quad i = 1, 2, \dots, N \quad (6.8)$$

where $w_{k,j}^i$ and $b_{k,j}^i$ are the weight and bias between the neuron k in the hidden layer i and the neuron j in the hidden layer $i+1$, respectively; f is the nonlinear activation function that is continuous and differentiable. Eq. (6.8) can also be used to calculate the output \mathbf{y} . Therefore, the learning process for the MLP is to adapt the connections weights and biases in order to obtain a minimal difference between the network output (predicted result) and finite element homogenization result (true result).

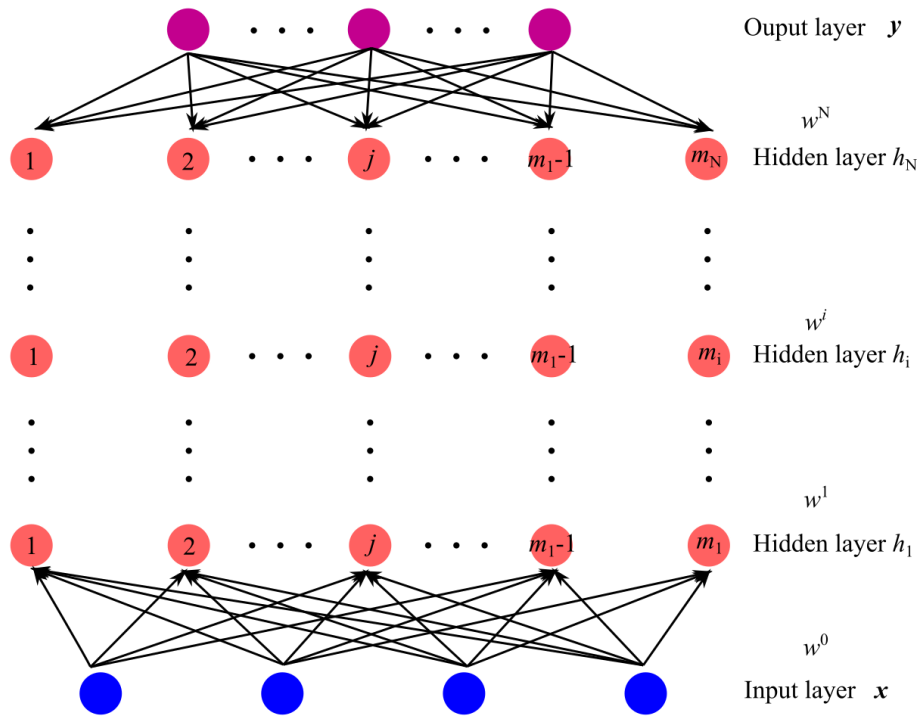


Figure 6.5. Feedforward MLP network structure. The blue circles mean the input, purple circles mean the output, and the red ones mean hidden layer neurons.

To estimate the performance of the neural network, a cost function should be defined to measure the discrepancy between the network output and the desired output. The cost function takes the outputs of the last layer and the ground-truth label as input and returns a scalar value as an error to be minimized. To adjust the MLP parameters properly, the back propagation algorithm computes the gradient of the cost function with respect to each weight and bias, indicating how much the error would increase or decrease if the parameter is increased by a tiny amount. Then each parameter is adjusted in the opposite direction to its gradient.

In this study, MLP is carried out on an Intel (R) Core (TM) i7 - 9700 8 Cores 3.00 GHz CPU with 64 GB DDR4 RAM, and all the programs are implemented in Matlab 2022a Deep Learning Toolbox. In specific, ReLu is selected as the activation function, Adam solver is used as the optimization solver, L2-regularization coefficient is selected as 0.0002 as default, the learning rate

is 0.0001, and dropout is not used. Hidden layer dimensions, batch size, and number of epochs, are determined in the following section.

6.3.2 Dataset generation

Three thousand spinodoid structures are considered for developing the MLP model. In specific, the relative density is randomly sampled in the range of 0.3 to 0.7. In order to represent the anisotropic design space, 40%, 30%, and 30% of the samples in the dataset are generated with one, two, and three non-zero angles $(\theta_1, \theta_2, \theta_3)$, respectively. Each non-zero angle is sampled in a range between 30° and 90° based on:

$$\theta_i = 30^\circ + 60^\circ(1 - \cos(\frac{\pi c}{2})), \quad \text{where } c \in [0, 1], \quad i = 1, 2, 3. \quad (6.9)$$

Smaller angles are deliberately biased in Eq. (6.9), since larger angles lead to close-to-isotropic topologies.

To eliminate overfitting, the dataset is split into a training set and a test set. The test set is kept fully hidden while the model is trained. To assess the performance of the trained MLP model, the unseen data (or test set) is used. Here, 20% of the data is randomly selected and kept hidden from the model as a test set, and the remaining 80% of data in the dataset is used as a training set.

6.3.3 Model performance assessment

Once the model is successfully built, the performance of the model is assessed using the Root-Mean-Square Error (RMSE), the Mean Absolute Error (MAE), and the coefficient of determination, or R-Squared (R^2), which can be calculated as follows [218]:

$$\text{RMSE} = \sqrt{\frac{\sum_{i=1}^n (y_i - t_i)^2}{n}} \quad (6.10a)$$

$$\text{MAE} = \frac{1}{n} \sum_{i=1}^n |y_i - t_i| \quad (6.10b)$$

$$R^2=1-\frac{\sum_{i=1}^n (y_i - t_i)^2}{\sum_{i=1}^n (t_i - \bar{y})^2} \quad (6.10c)$$

where y_i and \bar{y} are the predicted values of the i sample and the predicted mean value of the samples from the obtained models, respectively; t_i is the simulated value of the i sample from finite element homogenization; n is the total number of samples. The lower the RMSE and MAE, the higher the performance of the model. The R^2 ranges between $-\infty$ and 1. The larger the R^2 is, the better prediction is made by the MLP model.

6.4 Ferroelectric properties of spinodoid metamaterials

6.4.1 MLP model parameters

The MLP model is built firstly, whose number of the epoch, batch size, and hidden layer dimensions are determined to achieve a minimum difference between the prediction and finite element homogenization results. Here, we use the effective dielectric constant along the poling direction, κ_{33} , to train the MLP model. Figure 6.6 shows the convergence of RMSE with respect to the number of epochs and batch size. The six hidden layers are used, and their number of neurons is 128, 128, 64, 64, 32, and 32, respectively [214]. The relationship between the RMSE and the number of epoch are given Figure 6.6a, where the batch size is fixed as 100. It can be seen that the RMSE decreases fast when the number of epochs increases to 20 (from 4.99 to 0.08). After that, small fluctuation is observed by increasing the number of epochs, and this value is almost constant when the number of epoch is more than 50. Therefore, 100 epochs are used in this work to train the MLP model. Figure 6.6b shows the influence of batch size on RMSE, in which the number of the epoch is 100. Generally, apart from some fluctuations, RMSE exhibits an increasing trend with increasing batch size. In this MLP model, the batch size is selected as 50, which results in the smallest RMSE of 0.0148.

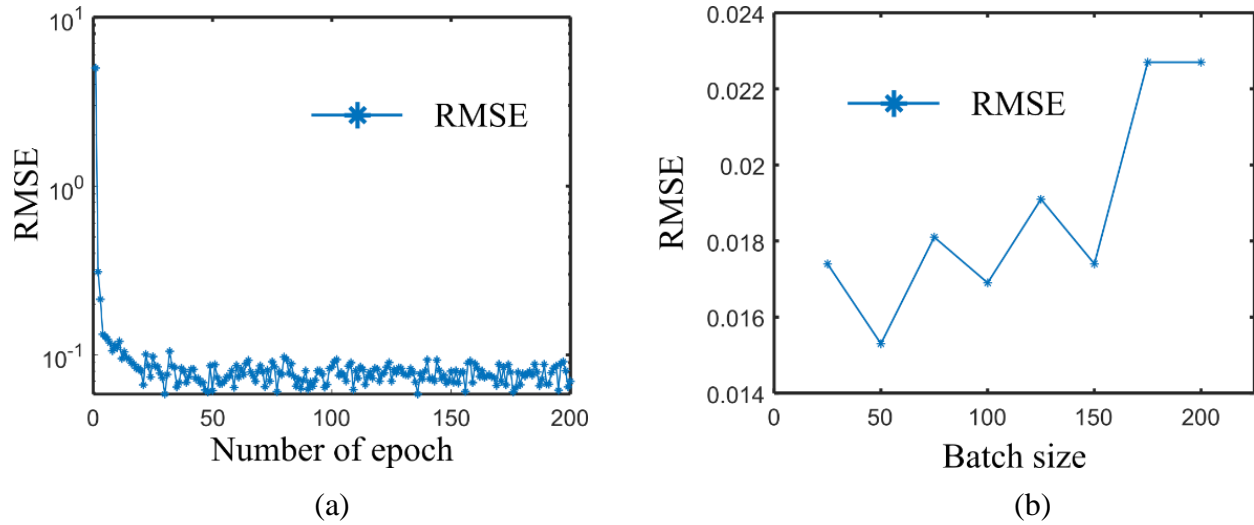


Figure 6.6. Influence of the number of (a) epoch and (b) batch size on the convergence of RMSE.

In order to determine the hidden layer dimension, Table 6.2 shows the influence of the hidden layer dimension on the RMSE, MAE, and R^2 . Here, six layers are considered for the MLP model, and the different number of neurons in each layer are optimized, which is selected from six configurations. All these three metric values (i.e., RMSE, MAE, and R^2) improve with increasing the number of neurons in each hidden layer, from 0.0188, 0.1940, and 0.994 to 0.0088, 0.1329, and 0.998, respectively. However, more neurons lead to a longer computation time. Therefore, No.5 configuration is used in this MLP model, whose metric values are closed to those of No.6 configuration while requiring fewer computation resources.

Table 6.2 Influence of hidden layer dimension on the RMSE, MAE, and R^2 .

No.	Hidden layer dimension	RMSE	MAE	R^2
1	(64, 64, 32, 32, 16,16)	0.0188	0.1940	0.994
2	(128, 128, 64, 64, 32, 32)	0.0148	0.1722	0.996
3	(256, 256, 128, 128, 64, 64)	0.0131	0.1619	0.996
4	(512, 512, 256, 256, 128, 128)	0.0110	0.1484	0.997
5	(1024, 1024, 512, 512, 256, 256)	0.0094	0.1374	0.997
6	(2048, 2048, 1024, 1024, 512, 512)	0.0088	0.1329	0.998

6.4.2 Performance of MLP model

In order to show the accuracy of the MLP model for predicting the multiphysical properties of the spinodoid ferroelectric metamaterials, Figure 6.7 shows the comparison between the effective mechanical properties obtained by finite element homogenization (true result) and MLP prediction (predicted result) in the test dataset. All results lie close to the diagonal line, i.e., $y = x$, which confirms that the true and predicted results share similar values. The high R^2 values (≥ 0.994) of these nine independent mechanical properties also indicate that our well-trained MLP model can provide reliable and accurate predicted mechanical properties. It can be seen that the spinodoid topology has a great influence on effective mechanical properties. For the considered test dataset, the C_{11} , C_{22} , and C_{33} can be tuned between 0 and 80 GPa, and 0 and 30 GPa for C_{12} , C_{13} , C_{23} , C_{44} , C_{55} , and C_{66} .

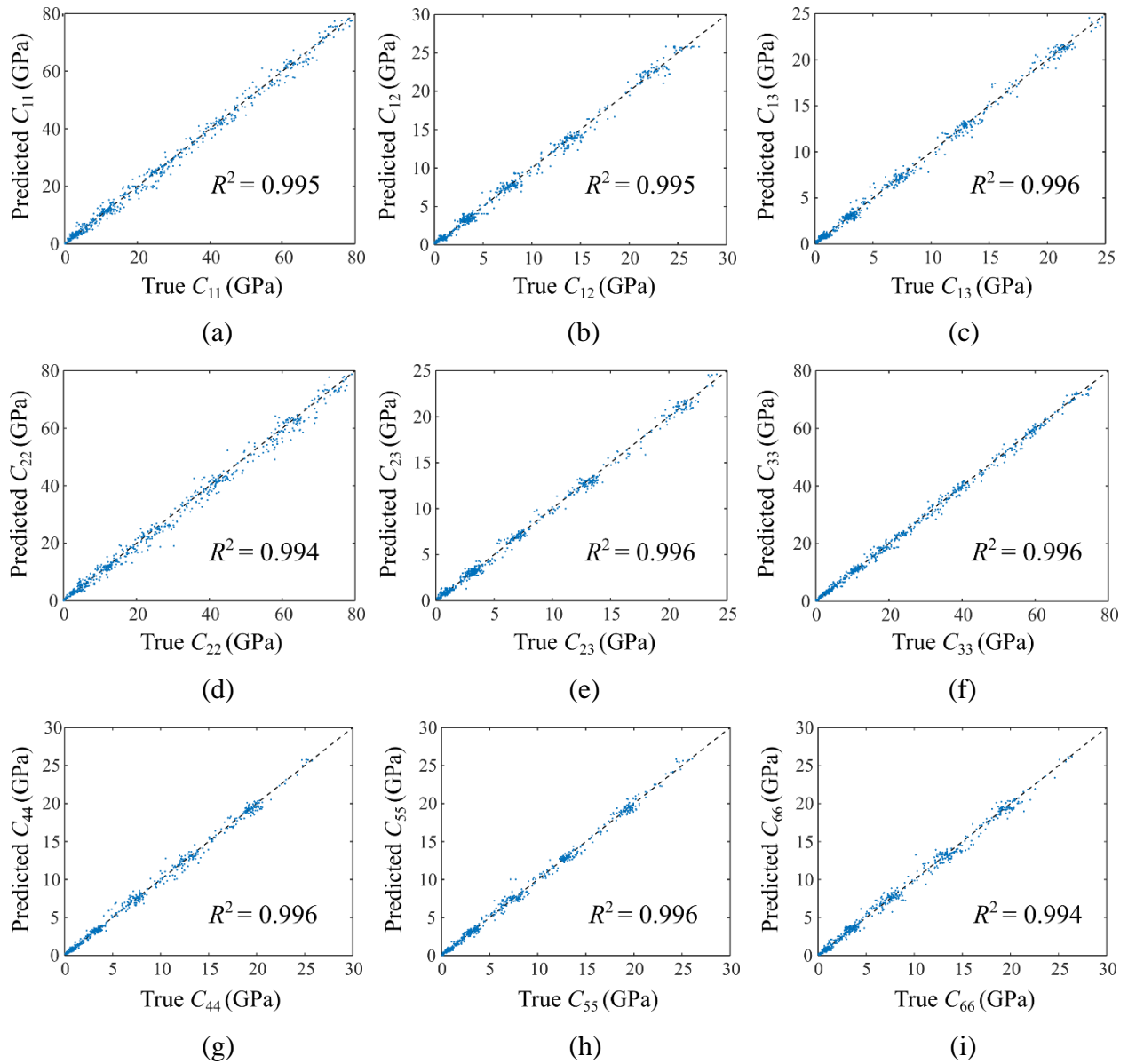


Figure 6.7 Comparison between the true and predicted effective mechanical properties of spinodoid ferroelectric metamaterials.

The comparison between the true and predicted effective piezoelectric properties is shown in Figure 6.8. Both e_{31} and e_{32} share the same R^2 of 0.969, while the R^2 value of e_{33} , e_{42} , and e_{51} is around 0.996; d_{33} , which is calculated based on C_{ij} and e_{ij} , exhibits a relatively smaller R^2 of 0.946. Compared to e_{33} , e_{42} , and e_{51} , e_{31} and e_{32} are more sensitive to the spinodoid topology, whose values include both positive and negative values. On the other hand, d_{33} only varies a little in the

test dataset, from 0.14×10^{-9} to 0.19×10^{-9} m/V. For high d_{33} values ($> 0.17 \times 10^{-9}$ m/V), both true and predicted values are close to each other; for smaller d_{33} ($< 0.17 \times 10^{-9}$ m/V), the difference between these two types of values slightly increases, leading to a smaller R^2 . However, the small difference between the true and predicted d_{33} (maximum difference of 15%) still proves the reliability of the developed MLP model. It is noted that although the relative density of these test structures varies between 0.3 and 0.7, their d_{33} still can achieve the same value as that of solid material, i.e., 0.19×10^{-9} m/V.

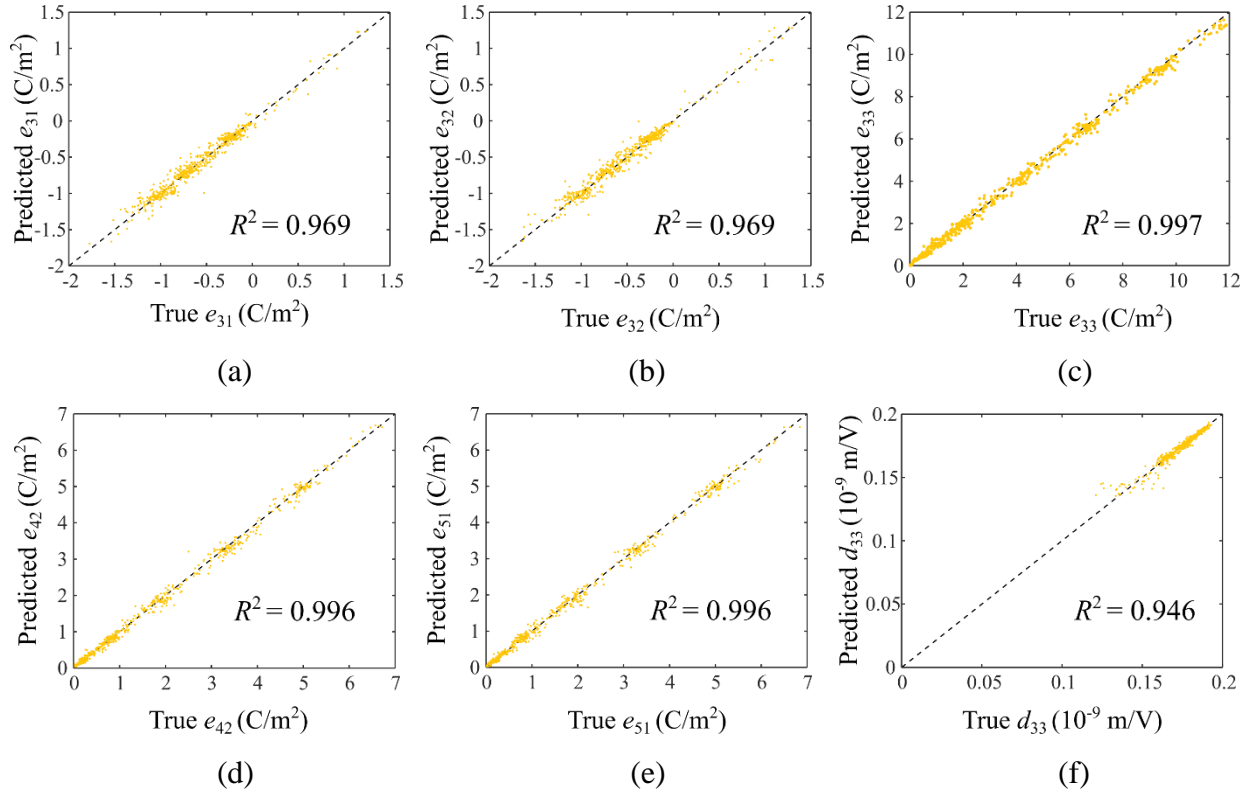


Figure 6.8. Comparison between the true and predicted effective piezoelectric properties of spinodoid ferroelectric metamaterials.

Figure 6.9 shows the performance of the MLP model for predicting the effective dielectric constant of the test dataset. Similar to Figure 6.8, the predicted results are close to the true ones, with R^2 values of 0.994, 0.994, and 0.998 for κ_{11} , κ_{22} , and κ_{33} , respectively. In addition, for the

considered test dataset, the effective dielectric constants vary significantly, from 0 to 10^{-8} C²/Nm². Although traditional fabricated porous ferroelectric materials also exhibit decreased dielectric constant, their values are proportional to the relative density [81], inhibiting to achievement of ultralow values observed in Figure 6.9 for relative density ranging from 0.3 to 0.7.

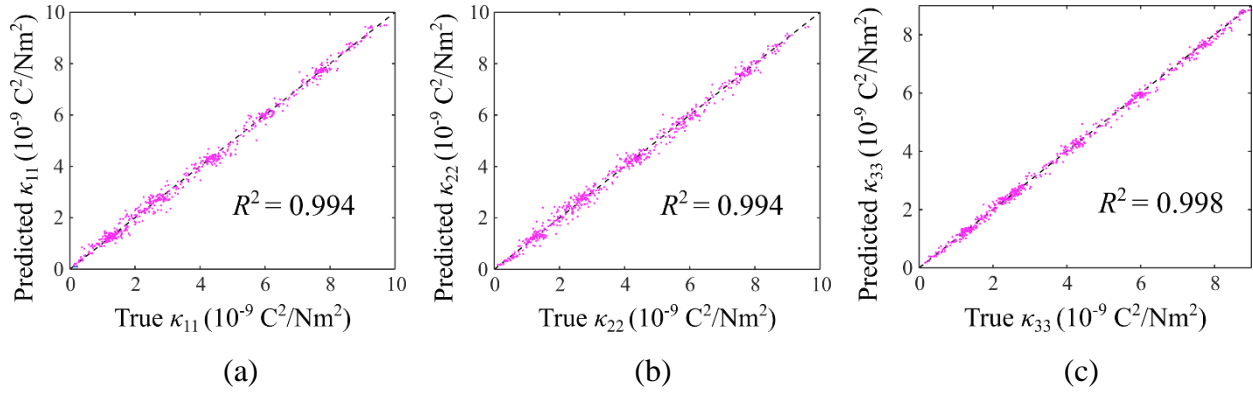


Figure 6.9. Comparison between the true and predicted effective dielectric constants of spinodoid ferroelectric metamaterials.

6.4.3 Prediction of ferroelectric properties of spinodoid ferroelectric metamaterials using MLP model

In this section, the trained MLP model is used to predict the effective piezoelectric properties of the spinodoid ferroelectric metamaterials. In order to select the geometry parameters of spinodoids with superior performance, the brute-force search method is used to conduct an exhaustive investigation of the performance of alternative spinodoid architectures, a study that is feasible with an efficient machine learning method instead of using computationally demanding homogenization technique. In specific, 50 different relative densities, uniformly varying from 0.3 to 0.7, is utilized, and 22 different angles, including 0° , and uniform distributed degrees between 30° and 90° , are used to construct all the possible spinodoid metamaterials. More than 530,000 architectures are considered here to extract the geometrical parameters with desired and optimized piezoelectric properties.

Figure 6.10 shows the relationship between relative density and predicted piezoelectric properties through the trained MLP model. Four metric values, i.e., d_{33} , κ_{33} , g_{33} , and FOM_{33} , are analyzed here, which assess the sensing (d_{33}), actuating (g_{33}), and energy harvesting (FOM_{33}) performance of the ferroelectric materials. Compared to relative density, structural topology has a more significant influence on the effective d_{33} (Figure 6.10a). For example, the d_{33} value varies from 0.140×10^{-9} m/V to 0.187×10^{-9} m/V at relative density of 0.4, while from 0.143×10^{-9} m/V to 0.192×10^{-9} m/V at relative density of 0.6. It is noted that compared with solid materials (red dashed line, $d_{33} = 0.19 \times 10^{-9}$ m/V), introducing porosity does not necessarily lead to decreased d_{33} , which is commonly observed in porous ferroelectric foam fabricated by traditional methods [79,81]. For example, for structure type B ($30^\circ, 30^\circ, 0^\circ$), when the relative density is between 0.5 and 0.7, its d_{33} is even slightly higher than 0.19×10^{-9} m/V. On the other hand, structure type A ($30^\circ, 30^\circ, 0^\circ$) exhibits the smallest d_{33} , whose values are always smaller than the solid counterpart. The isotropic spinodoids (type B, marked by circles) lie between type A and C, and show an increasing trend (from 0.165×10^{-9} m/V to 0.186×10^{-9} m/V) with the increase in relative density.

As shown in Figure 6.10b, the effective dielectric constant κ_{33} , increases by increasing relative density. For example, the κ_{33} increases from 0.12×10^{-9} , 2.80×10^{-9} , and 1.26×10^{-9} C²/Nm² to 4.18×10^{-9} , 8.93×10^{-9} , and 7.76×10^{-9} C²/Nm² for types A, B, and C, respectively. Similar behavior also can be found in conventional ferroelectric foams, where the dielectric constant is proportional to the relative density [81]. In addition, architectural topology plays an important role in determining effective κ_{33} . Similar to d_{33} , the smallest κ_{33} is found for type A spinodoid architecture, while the highest one is for type B. With a relative density of 0.5, the κ_{33} of type B (6.00×10^{-9} C²/Nm²) is 6.84 times higher than type A (0.88×10^{-9} C²/Nm²), which are 45% and

6.6% of the associated values for the solid counterpart, respectively. The ultralow value of κ_{33} imparts the spinodoid metamaterial with an excellent piezoelectric figure of merit.

Figures 6.10c and d show that both g_{33} and FOM_{33} share the same relationship with relative density. As opposed to d_{33} and κ_{33} , the type A structure exhibits the highest values in Figure 6.10c and d, while the type B structures feature the smallest values. For example, for a relative density of 0.3, the g_{33} of type A (1.14 Vm/N) is 19 times higher than type B (0.06 Vm/N). A similar comparison also happens for FOM_{33} , in which the value for type B ($10 \times 10^{-12} \text{ m}^2/\text{N}$) is only 6.3% of type A ($160 \times 10^{-12} \text{ m}^2/\text{N}$). The reason is although the d_{33} value of type A structures is smaller than that of type B, the maximum difference between them is 30% at a relative density of 0.5. However, the minimum κ_{33} difference between these two types of structures is 55% when the relative density is 0.6. As mentioned in Chapter 2.1, $g_{33} = d_{33}/\kappa_{33}$ and $\text{FOM}_{33} = d_{33} \cdot g_{33} = d_{33}^2/\kappa_{33}$, the smallest κ_{33} of type A leads to the highest g_{33} and FOM_{33} . It is noted that compared to the solid material (g_{33} of 0.014 Vm/N and FOM_{33} of $2.7 \times 10^{-12} \text{ m}^2/\text{N}$), all of these three types of structures exhibit improvement even at a relative density of 0.7, i.e., g_{33} of 0.038, 0.022, and 0.024 Vm/N and FOM_{33} of 6.2×10^{-12} , 4.2×10^{-12} , and $4.5 \times 10^{-12} \text{ m}^2/\text{N}$ for types A, B, and C structures, respectively. In the following section, a 3D printing technology is developed to fabricate the spinodoid ferroelectric metamaterials to experimentally validate their high performance.

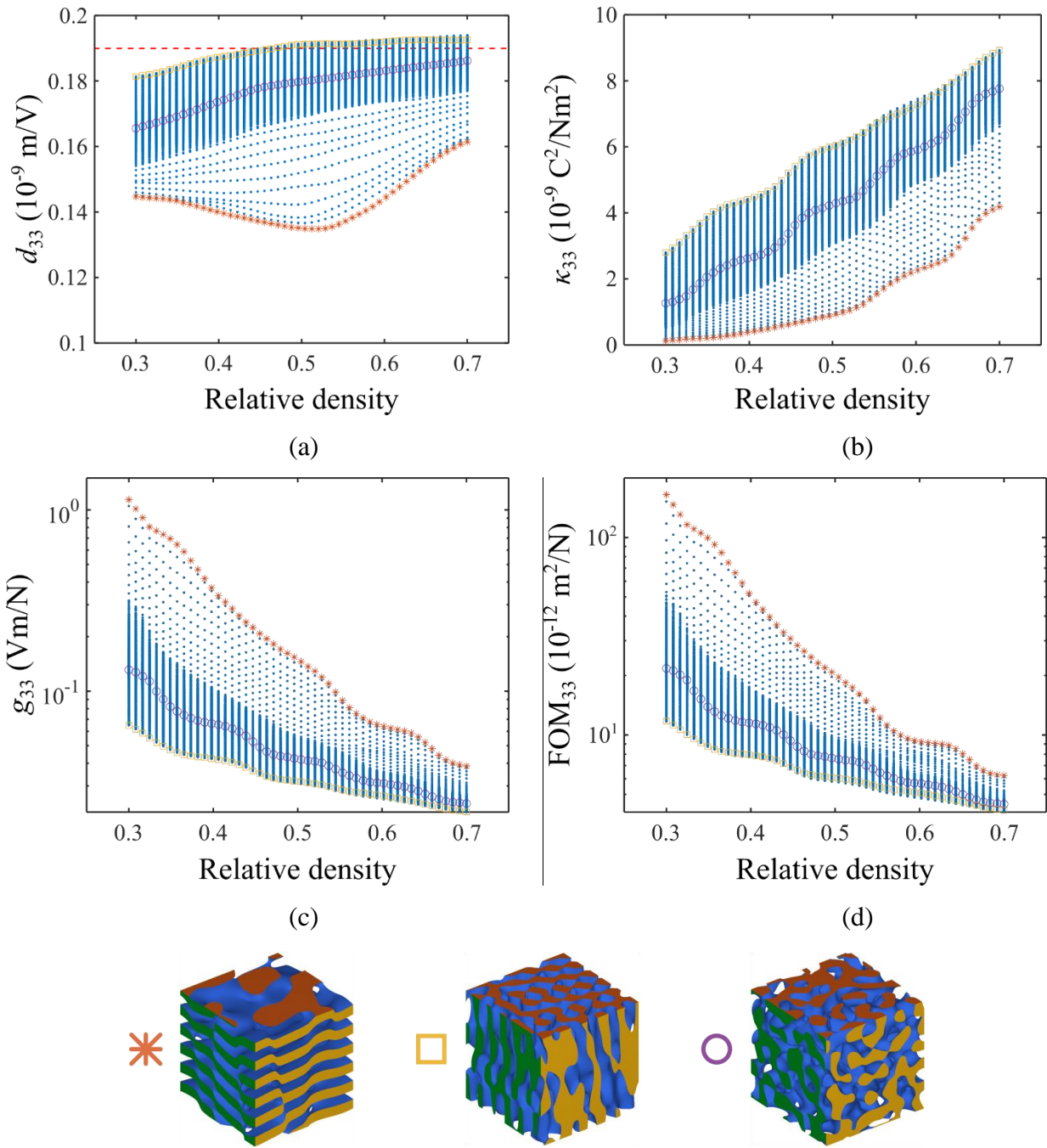


Figure 6.10. The predicted piezoelectric properties of spinodoid ferroelectric metamaterials based on the trained MLP model: (a) d_{33} , (b) κ_{33} , (c) g_{33} , and (d) FOM_{33} . Three representative structures are marked in these figures, where ‘*’, ‘□’, and ‘○’ stand for spinodoid structure types A, B, and C with geometrical parameters as (0°, 0°, 30°), (30°, 30°, 0°), and (60°, 60°, 60°), respectively.

6.5 Experiment

6.5.1 DLP 3D printing of ferroelectric ceramic

The ferroelectric materials produced by traditional methods are usually limited to simple shapes, such as plates, discs, and rings. However, the abovementioned spinodoid ferroelectric metamaterials have complex underlying structures that are impossible to be developed by conventional manufacturing techniques; as a result, new fabrication methods are needed for developing freeform ferroelectric materials. The most promising method is additive manufacturing or 3D printing, which provides an effective way to produce complicated structures. Among the different 3D printing technologies, digital light processing (DLP) based on photopolymerization of liquid resin is used in this research due to its high resolution and easy feedstock preparation.

The commercial DLP 3D printer B9C Core 530 is used for additive manufacturing. The lead-free BaTiO₃ powders with a mean particle size smaller than 3 μm are selected as the ferroelectric material and the polyethylene glycol (250) diacrylate (PEG(250)DA) is chosen as the photopolymer. Diphenyl(2, 4, 6-trimethylbenzoyl)phosphine oxide (TPO, Aladdin, Shanghai, China) is used as a photoinitiator with an absorption peak range from 350 to 410 nm. All these materials are purchased from Sigma-Aldrich and used as received.

Figure 6.11 shows the DLP process. The DLP printer has a 405 nm wavelength light source, which can be absorbed well by the photoinitiator TPO. Prepared CAD models of ferroelectric metamaterials are sliced into 2D images for printing. The cured photopolymer is then solidified into a desired pattern due to the cross-linked polymer. After the completion of the current layer printing, the build platform moves upwards, and new resin will flow into the curing area. This process is repeated until the whole structure is 3D printed.

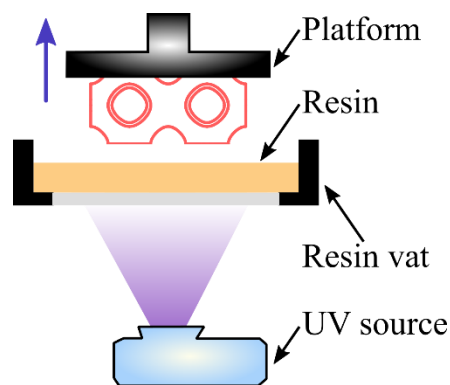


Figure 6.11. Schematic of DLP 3D printing process.

The 3D printed samples, or green bodies, exhibit small piezoelectric properties. A sintering process is needed to convert these ferroelectric composites into dense ceramics. In order to keep the precise geometry of the designed spinodoid during sintering, the photosensitive slurry should contain a high volume fraction of ceramic particles. However, the viscosity of the resin is significantly increased with high particle loading, and the flowability of the prepared slurry is affected adversely, which impedes the self-leveling of the slurry during the printing process [143]. In this research, BYK (BYK Chemie, Germany) is selected as a dispersant to chemically modify the ceramic particles [219]. Different amount of BYK is firstly added to ethanol and ultrasonically dispersed for 10 min. The ceramic powders are then added to the ethanol solution and ultrasonically dispersed for 20 min to first deagglomerate ceramic powders. The solution is further magnetically stirred overnight to enhance the absorption of dispersant on the particle surfaces. The treated ceramic particles are separated from the solvent through centrifugation at the speed of 6000 rpm for 5 min, followed by drying at 80 °C. Finally, the printable homogeneous slurry is prepared by mixing the modified ceramic powders with PEG(250)DA and photoinitiator by ultrasonic dispersion for 1 hour. In order to optimize the dispersant concentration, Figure 6.12 shows the viscosity of the suspensions with dispersant concentrations ranging from 0.5 wt% to 5 wt% (based on the weight of BaTiO₃ particles) at a shear rate of 50 s⁻¹. It is obvious that for the lowest viscosity

of the resin, the optimal amount of BYK dispersant for modifying BaTiO₃ ceramic particles is 1 wt%. Below that value, the ceramic resin is not sufficiently stabilized and has a considerably high viscosity value. With the increase of dispersant concentration beyond the optimal amount, the viscosity shows an upward trend with a slight rise, which indicates that the rheological behavior of the suspensions deteriorates. In this research, 1 wt% BYK dispersant is used to modify the surface of the ceramic particles. The 80 wt% (42 vol%) ceramic suspensions with 2 wt% TPO (based on the weight of PEG(250)DA) are prepared for 3D printing. The layer thickness is 30 μm, and the expose energy is 13 mJ.

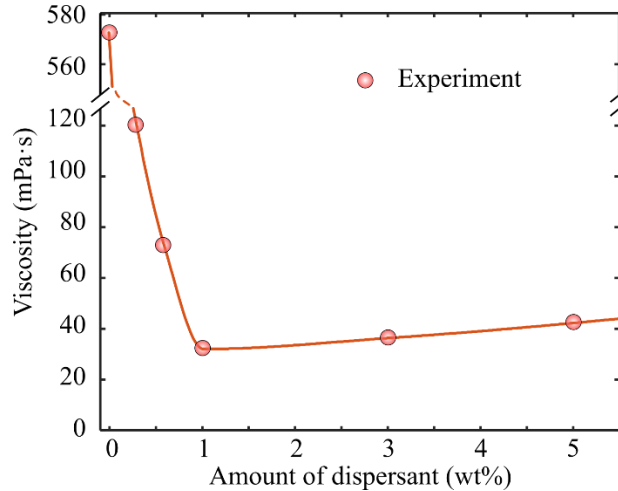


Figure 6.12. The relationship between the viscosity of the ceramic slurry and dispersant concentration at a 50 s⁻¹ shear rate.

Debinding and sintering are essential to achieve dense ceramics after 3D printing green bodies [143,219]. In order to determine the debinding temperature profile in the post processing stage for the manufacturing of defect-free architected ferroelectric metamaterials, thermogravimetric analysis (TGA) of the printed green body is carried out with a TGA Q500 (TA Instruments, USA). A heating rate of 5 °C / min is used with temperatures varying from 20 °C to 700 °C in a nitrogen atmosphere, and three replicates are tested to ensure the reliability of the obtained results. Figure

6.13 shows the thermal decomposition curves of the green body with 80 wt% of ceramic particles. The green body does not have an obvious change for temperatures lower than 300 °C since the samples have been dried before the TGA test; only one main mass loss is detected at temperature ranges between 300 and 550 °C, involving 19.6% binder elimination. In specific, the exothermic peak shows the fastest mass loss occurs at 402 °C. No further weight change is recorded once the temperature exceeds 550 °C, indicating the complete removal of the PEGDA.

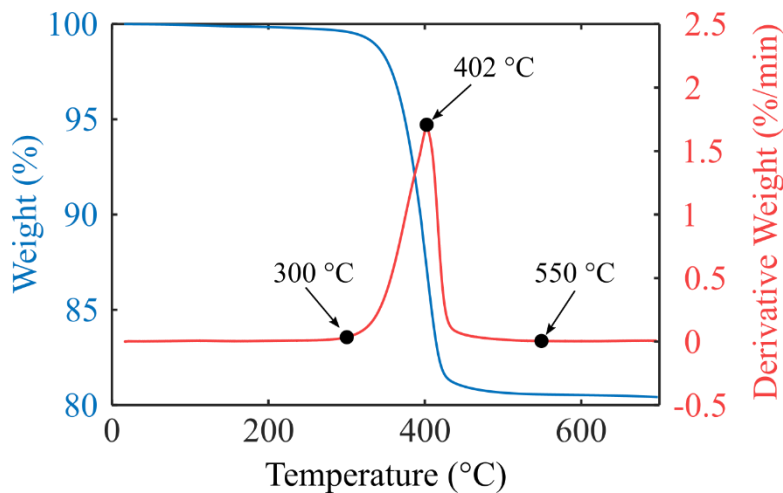


Figure 6.13. TGA curves for the thermal decomposition of the PEGDA in the printed green body.

To avoid the crack formation or deformation of samples during the sintering process, the fabricated green body is debinded in a vacuum tube furnace. Based on the TGA analysis, the debinding temperature profile of the 3D printed green bodies is designed and shown in Figure 6.14a. The temperature is raised from room temperature to 200 °C at a rate of 1 °C/min and is kept at this temperature for one hour; the temperature is then increased from 200 °C to 600 °C at a rate of 0.33 °C/min and is held for one hour at 300 °C, 400 °C, 500 °C, and 600 °C, respectively, to ensure the complete elimination of binders during the debinding process (Figure 6.14a). In Figure 6.14b, the debinded samples are sintered by heating from 20 °C to 600 °C at a rate of 1.5 °C/min; temperature is kept at 600 °C for two hours and is then gradually increased to 1340 °C at a rate of

3 °C/min; the sample is kept at this temperature for four hours. The sintered bodies are then cooled down to room temperature with furnace cooling.

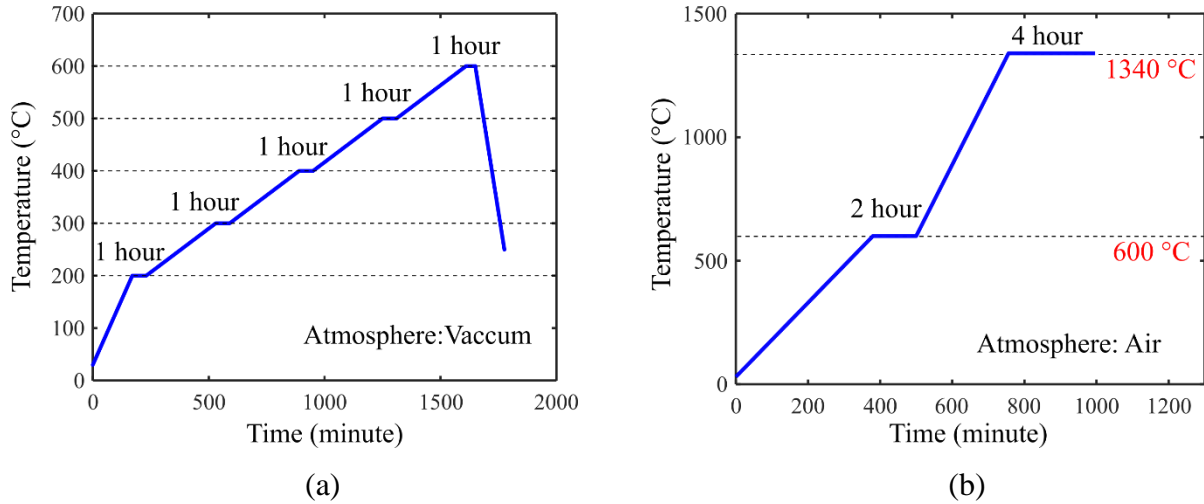


Figure 6.14. (a) Debinding and (b) sintering temperature profiles of the 3D printed green bodies.

Figure 6.15 shows the as-design 3D models and as-built 3D printed samples of the three abovementioned designed spinodoid ferroelectric architectures. The sample size after sintering is $6 \times 6 \times 6$ mm, with a size shrink of around 23% compared with the green body. It can be seen that our printed samples maintain the same architectural features as the designed 3D models, validating the high precision of our developed 3D printing technology that can offer a reliable method to realize high-performance spinodoid ferroelectric metamaterials.

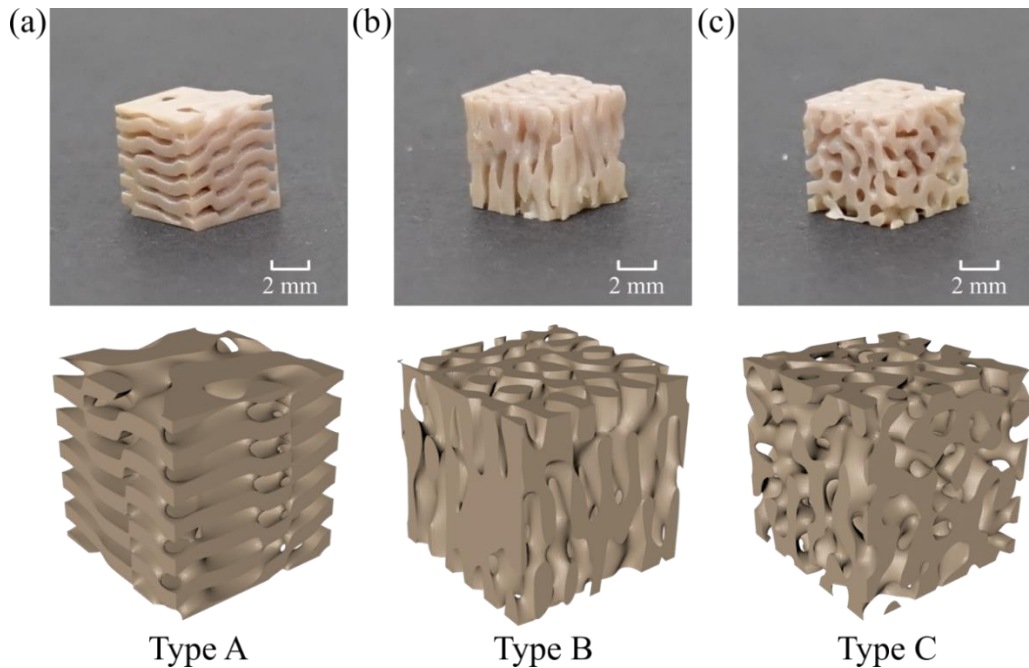


Figure 6.15. 3D printed along with the 3D models of (a) Type A, (b) Type B, and (c) Type C samples.

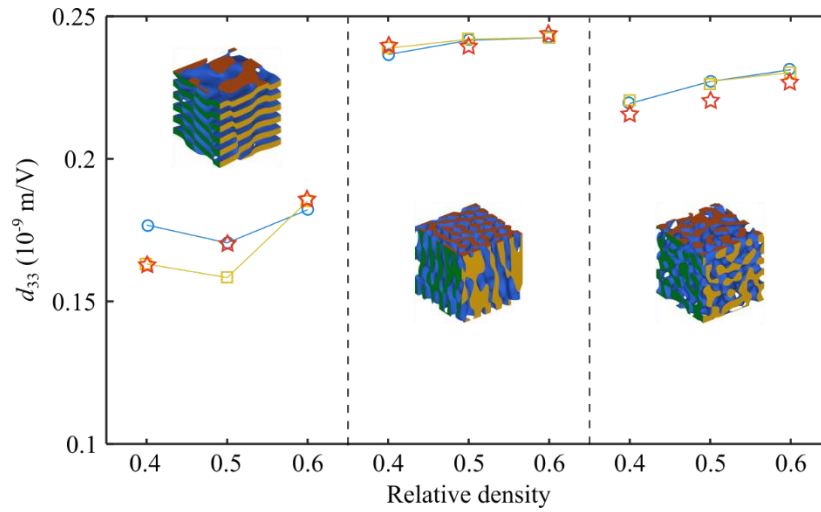
6.5.2 Ferroelectric properties of printed spinodoid metamaterials

In order to demonstrate the high-performance piezoelectric properties of our designed spinodoid ferroelectric metamaterials, the abovementioned three types of spinodoids with a relative density of 0.4, 0.5, and 0.6 are 3D printed and experimentally tested. The size of all the samples after sintering is $6 \times 6 \times 6$ mm, and each design is printed with three replicates. The as-fabricated ferroelectric ceramic is poled in a silicone oil bath using an electric field of 3 kV/mm at room temperature. The d_{33} value is measured by a piezoelectric meter (PolyK PKD3-2000), and the dielectric constant is measured by a Stanford Research Systems SR715 LCR meter at a frequency of 1 kHz. The d_{33} and dielectric constants of the solid material are first determined through conducting the experimental test on the bulk structure of $6 \times 6 \times 3$ mm at 240 m/V and 19.04×10^{-9} C²/Nm², respectively. Therefore, the results of MLP prediction and finite element

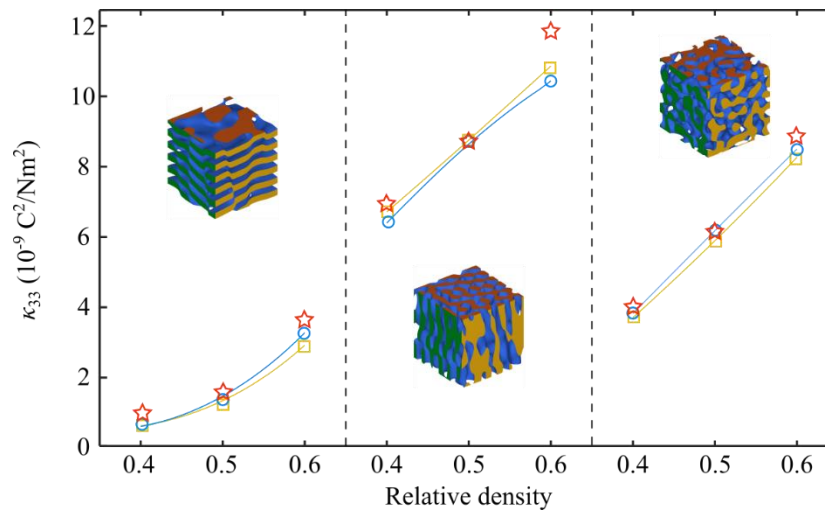
homogenization are scaled based on the ratio between the measured d_{33} and κ_{33} and those properties given in Table 3.1.

Figure 6.16 shows the comparison of the effective piezoelectric properties of the three types of spinodoids determined by experimental tests, MLP predictions, and finite element homogenization. As shown in Figure 6.16a, good agreement is achieved among the three methods, especially for type B and C architectures, corroborating the reliability of our developed homogenization and trained MLP network. The maximum difference among the values determined by the three methods for type A is 7% at a relative density of 0.4, which might be due to the small shape distortion of the 3D printed samples during the sintering process. The experimental results validate the trend observed in Figure 6.16a, in which the type B design exhibits a constant value of d_{33} at different relative densities and around that of the solid counterpart (240 m/V); the type A architecture shows the minimum d_{33} among the three different designs. All these three methods share similar values for the effective dielectric constant (Figure 6.16b), and the experimental results are slightly higher than that of the other two methods. For example, the experiment result of type B at the relative density of 0.6 is $11.80 \times 10^{-9} \text{ C}^2/\text{Nm}^2$, while it is $10.85 \times 10^{-9} \text{ C}^2/\text{Nm}^2$ and $10.44 \times 10^{-9} \text{ C}^2/\text{Nm}^2$ based on finite element homogenization and MLP prediction, respectively. Generally, decreasing relative density leads to a decreased κ_{33} ; adopting the type A structure can further decrease this value. For example, the maximum experimental κ_{33} of type A is $3.76 \times 10^{-9} \text{ C}^2/\text{Nm}^2$ for the relative density of 0.6, which is still smaller than the minimum value of type C ($3.9 \times 10^{-9} \text{ C}^2/\text{Nm}^2$ at a relative density of 0.4). Therefore, both g_{33} (Figure 6.16c), and FOM_{33} (Figure 6.16d) show a reverse trend with respect to a relative density where both quantities decrease by increasing relative density and type A structures exhibit the best performance. For example, the experimental results for g_{33} (Figure 6.16c) of type A are 0.177 Vm/N, 0.117 Vm/N, and 0.051

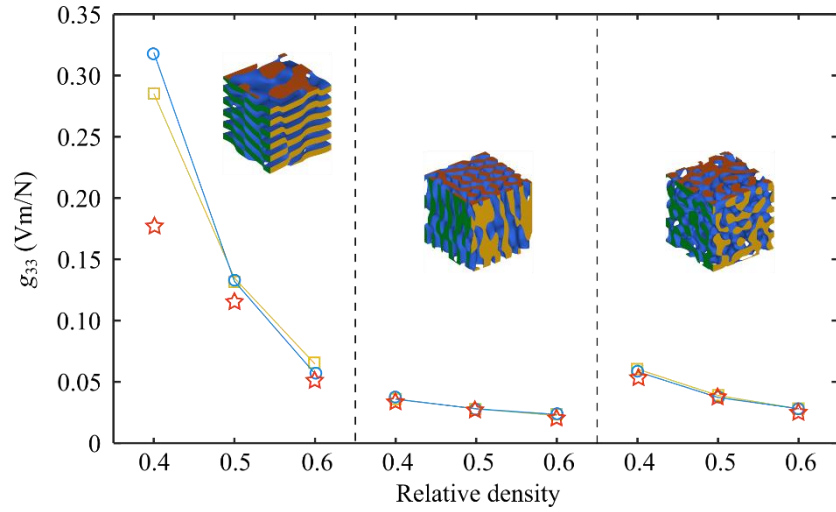
V_m/N for relative densities of 0.4, 0.5, and 0.6, respectively, while the experimental results for FOM_{33} (Figure 6.16d) of type A are $29.1 \times 10^{-12} \text{ m}^2/N$, $19.4 \times 10^{-12} \text{ m}^2/N$, and $9.6 \times 10^{-12} \text{ m}^2/N$ respectively; the corresponding values of solid counterparts for g_{33} and FOM_{33} are 0.013 Vm/N and $3.03 \times 10^{-12} \text{ m}^2/N$ respectively. It is noted that the difference between the results of the three aforementioned methods for type A structure at a relative density of 0.4 is due to the small difference between the three dielectric constants ($0.90 \times 10^{-9} \text{ C}^2/N\text{m}^2$ in the experiment and $0.54 \times 10^{-9} \text{ C}^2/N\text{m}^2$ for homogenization and MLP prediction).



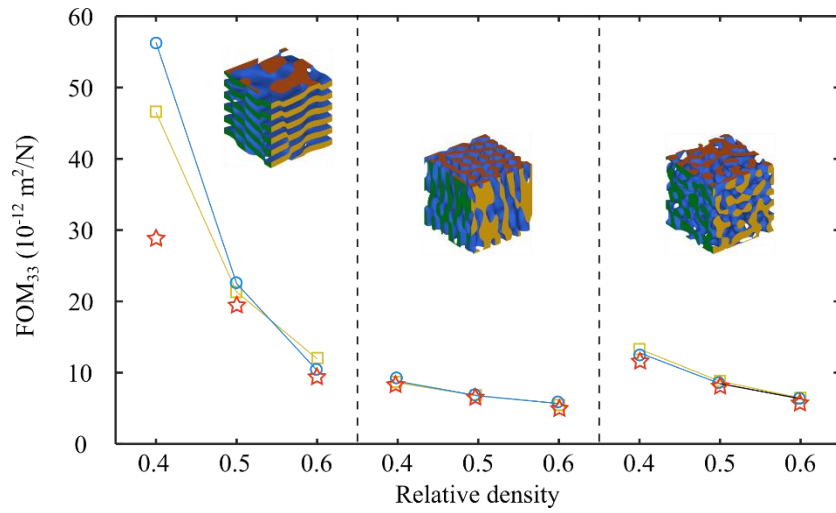
(a)



(b)



(c)



(d)

data are then used to train the MLP machine learning method. The multiphysical results predicted by the well-trained MLP show good agreement with that of finite element homogenization, with R^2 value reaching 0.998. The highly efficient MLP method makes it possible to investigate the influence of geometrical parameters on the effective piezoelectric properties of spinodoid through investigating the properties of massive cases of different spinodoid, enabled by the utilization of machine learning. It is found that by tailoring the spinodoid topologies, we can realize unconventional multiphysical properties unachievable by conventional fabricated porous ferroelectric materials. For example, the d_{33} value of columnar spinodoids maintains a constant value as that of solid material even with decreased relative density. The effective dielectric constant not only depends on the relative density but also on the underlying architecture of ferroelectric metamaterials. For example, the dielectric constant of lamellar (type A) spinodoid can be as small as 6.6% of that of solid counterpart for a relative density of 0.5. The low dielectric constant contributes to improved piezoelectric figures of merit, i.e., g_{33} and FOM_{33} . In addition, a 3D printing technology has been adopted for fabricating ferroelectric ceramics into the shape of our delicately selected spinodoid topologies. The experimental results corroborate the developed homogenization and MLP methods and validate the feasibility of realizing high-performance spinodoid metamaterials with enhanced piezoelectric figures of merit. This work highlights the potential of spinodoid ferroelectric metamaterial as the next generation of sensors and energy harvesters.

CHAPTER 7

Programmable Multistable Perforated Shellular

This chapter includes the development of programmable multistable perforated shellular metamaterials; the ferroelectric materials introduced in the previous chapter can be integrated into mechanical metamaterials in future studies to develop deployable and shape-reconfigurable intelligent metastructures. Two design strategies, i.e., elliptical perforations and multilayer staggered perforations, are used to realize the bistable and multistable perforated shellulars. The chapter is divided into two main sections, including bistable shellulars with elliptical holes and multistable shellular with multilayer staggered perforations.

7.1 Bistable shellular with elliptical holes

The unit cells of bistable perforated shellular metamaterials are designed by adding perforations through P shellulars. Mathematically, the P shellular surface is defined by $\cos(x) + \cos(y) + \cos(z) = f$, where f is level set constant that varies from 0 to 1 [220]. The proposed bistable mechanism in this study finds inspiration from the bistability of a spherical cap, similar to the shell surface eversion of an umbrella in a strong gust of wind or a contact lens when being inside out. The unit

cells of designed perforated P shellular metamaterials, as a family of thin shells and inclined beams, can exhibit a bistable behavior with symmetrically deformed perforated segments under compression applied on their top surface (marked by orange color); fixed boundary conditions are assigned to the four side surfaces (indicated by red color) (Figure 7.1a). Negative incremental stiffness is observed in the compressive stress-strain curves for both intact (Figure 7.1b) and perforated (Figure 7.1c) half-cells when a compressive force reaches F_{\max} . However, upon unloading, the intact shellular part returns to its original stable state (state i in Figure 7.1b) and merely presents a positive noninitial minimum force $F_{\min}>0$, demonstrating a *monostable* snap-through behavior. In Figure 7.1c, the half-cell of perforated shellular, in contrast, restores state iii and holds two stable states (states i and iii) and exhibits *bistable* behavior. In the following analyses, we use the ratio of E_{out} , due to the second stable configuration, and E_{in} , the energy required for material instability in the unloading and loading, respectively, to assess the structural bistability of perforated shellular unit cells and to evaluate their potentials for absorbing and trapping energy.

Figure 7.1d shows our perforated shellular unit cell, where a solid frame is used to fix the displacement of shell sides, and the two cylindrical bars at the top and bottom limit the local shell deformation. The elliptical holes are located in the center of eight evenly divided shellular segments at the top and bottom sides along the cylindrical bars. To evaluate the relationship between geometrical parameters and structural bistability, three samples with three replicates and alternative level set constants (f), and surface thickness (t) are 3D printed by Selective Laser Sintering (SLS) out of thermoplastic polyurethane (TPU). The unit cell size is $5\text{cm} \times 5\text{cm} \times 5\text{cm}$ with frame length L , as 5cm, shellular size $2S$, as 3cm, and cylinder bar height d , as 1cm. The mechanical properties of the TPU are determined by the uniaxial compression of a cylinder based

on ASTM D575. Mooney-Rivlin model, the form of strain energy density with 5 parameters, is used to describe the mechanical behavior of TPU as follows [221]:

$$W = C_{10}(\bar{I}_1 - 1) + C_{01}(\bar{I}_2 - 1) + C_{20}(\bar{I}_1 - 1)^2 + C_{11}(\bar{I}_1 - 1)(\bar{I}_2 - 1) + C_{02}(\bar{I}_2 - 1)^2 + \frac{1}{d}(J - 1)^2 \quad (7.1)$$

where W is strain energy density; \bar{I}_1 and \bar{I}_2 are the first and second deviatoric strain invariants; J is square root of third deviatoric strain invariants; C_{10} , C_{01} , C_{11} , C_{20} , and C_{02} are material constants; and d represents the material incompressibility determined by:

$$d = (1 - 2\mu)/(C_{10} + C_{01}) \quad (7.2)$$

where μ is Poisson's ratio. In this research, the material is modeled as nearly incompressible, featured by $\mu = 0.49$. The corresponding material constants, i.e., C_{10} , C_{01} , C_{20} , C_{11} , and C_{02} , are calculated as 20.95 MPa, -17.16 MPa, 14.71 MPa, -8.68 MPa, and 2.04 MPa, respectively.

While the viscoelasticity of TPU causes energy dissipation through the rate dependent deformation and the rate independent snap-back behavior, the bi/multistability of our rationally-designed perforated shellulars is not affected by the viscoelastic energy dissipation of the parent material, since the stable states are defined based on the quasi-static response of the designed architectures, requiring sufficient resting time for the base material to reach a steady state equilibrium.

The influence of level set constant f and relative thickness t/S on the response of perforated shellular unit cells under uniaxial compression is also investigated by finite element (FE) simulation under a quasi-static condition. As reflected in Figure 7.1e, snap-through and bistable behaviors of the half-cells of the designed metamaterials highly depend on the assessed architectural parameters. In specific, increasing the level set constant f or decreasing relative thickness t/S , leads to stronger bistability, indicated by a phase transition boundary (solid black

line) and a high $E_{\text{out}}/E_{\text{in}}$ (darker blue areas). For example, for a small level set constant and a high relative thickness ($f = 0$, $t/S = 2/15$), both numerical and experimental results approve the monostable snap-through behavior for sample I, while samples II ($f = 0.4$, $t/S = 1/15$) and III ($f = 0.8$, $t/S = 1/15$) present bistable behavior with energy trapping capabilities. Although we have observed a bistable domain for the half-cell of intact P shellulars (enclosed by dashed red lines in Figure 7.1e), introducing perforations on the P shellular remarkably expands the bistable region, offering bistability for a wide range of f from 0 to 0.8. The smaller bistability region for the intact shellular might be due to the relatively higher circumferential stiffness of the intact shellular; the constrained circumferential expansion under compression can lead to shell wrinkling that prevents symmetrical deformation and results in a global buckling of the shellular.

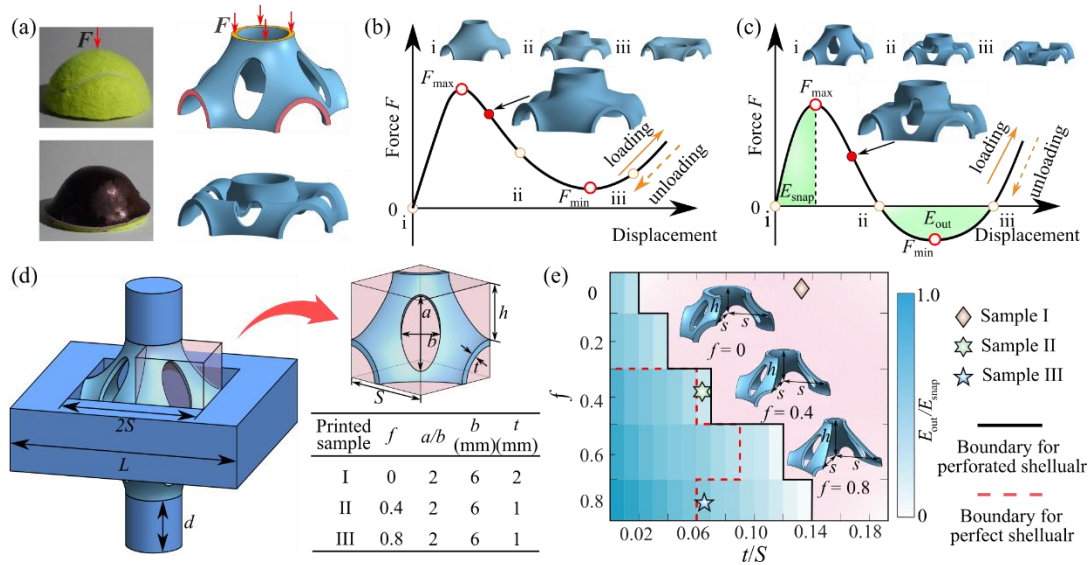


Figure 7.1. Overview of bistable P shellulars motif. (a) The designed half-cell of perforated P shellular metamaterial can exhibit two stable states when four sides (marked by red color) are fixed, and the pressure is applied on the top surface (highlighted by orange color). (b, c) Force-displacement curve of a half-cell of intact P shellular with $f = 0$ shows snap-through behavior while the perforated counterpart can present mechanical bistability, indicated by the sign of their reaction force F . (d) Geometrical parameters of the designed perforated P shellular unit cells. Three samples with different level set constants f and thickness t are 3D printed by SLS. (e) Effect of

level set f and shell thickness t/S on the bistability of perforated and intact shellulars, investigated by FE simulation. (Reprinted with permission from ref [222], copyright 2021 Wiley-VCH GmbH)

Figure 7.2a and b show the stress-strain curve and deformation mode of the 3D printed samples I and III through experimentation and FE simulation. Two noninitial positive local minima for stress during loading indicate the monostable snap-through behavior of sample I. Meanwhile, sample III demonstrates snap-through and tristable response with three stable states at $\varepsilon = 0, 0.24,$ and 0.42 . As shown in Figure 7.1e, increasing h/S or f and decreasing t facilitate the bistability of perforated shellulars. The agreement between numerical and experimental results corroborates the accuracy of the FE simulations carried out for preparing Figure 7.1e.

Although samples I and III in Figure 7.2a and b deform in a layer-by-layer manner, due to the uniformity of topological features of the two layers (top and bottom shells), the deformation sequence is uncertain and is mainly governed by the geometrical imperfections of the 3D printed samples and the boundary conditions imposed by the testing machine's fixture. A heterogeneous design of perforated shellulars, in which the architectural parameters of neighboring motifs are distinct, can prevail the indeterminacy of the deformation sequence of metamaterials made by tessellation of unstable unit cells to offer designing mechanical metamaterials with controllable configurations. For controlling deformation sequence, perforated shellular samples containing $2 \times 2 \times 2$ cells (three replicates for each design) are designed, and 3D printed based on samples II and III (introduced in Figure 7.1d), and the experimental test results are presented in Figure 7.2c. Based on the magnitude of maximum snapping force/stress, the deformation sequence of the perforated shellular metamaterial starts from sample III and then is propagated to sample II with snapping stresses at approximately 10 kPa and 13 kPa, respectively.

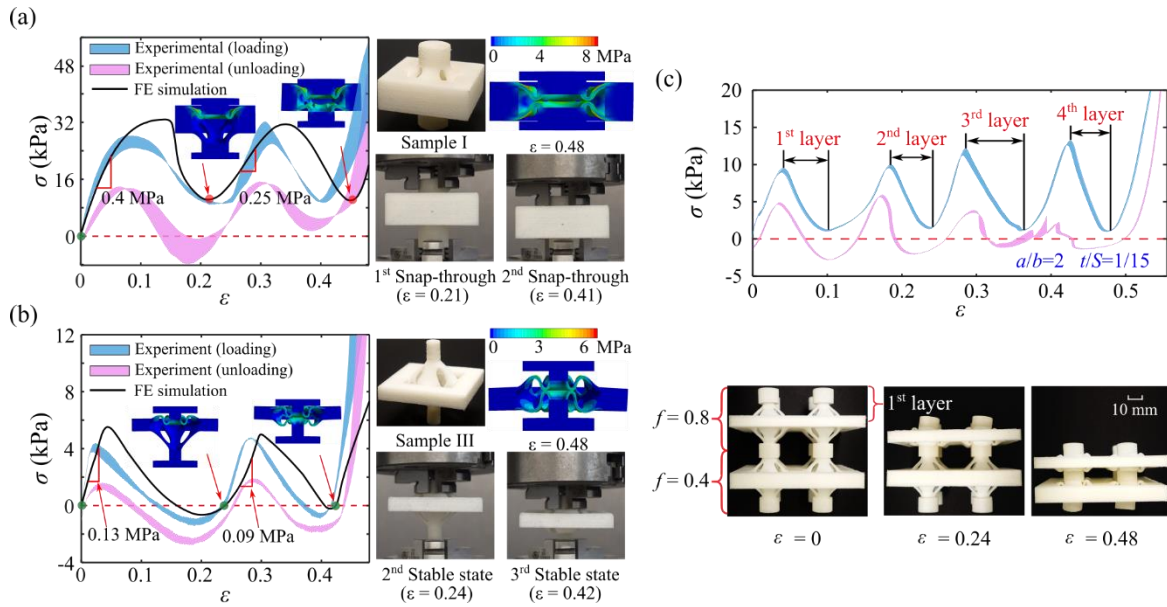


Figure 7.2. Programmability of bistable perforated P shellulars. (a, b) Experimental (blue and pink area) and FE simulation (solid black line) stress-strain curves of samples I and III. (c) Experimental results of 3D printed graded perforated shellulars with the same thickness. (Reprinted with permission from ref [222], copyright 2021 Wiley-VCH GmbH)

7.2 Multistable shellular with multilayer staggered perforations

To realize multistable perforated shellulars, we create staggered multilayer rectangular perforations on the shellular surface. Figure 7.3a shows perforation patterns on one-eighth of P shellular surface with f as 0.8, where the brown area represents a single staggered layer, characterized by projected layer height (δh), projected layer distance (δc), the projected height (t') of the circumferential beam (purple part in top right inset), and radial beam (orange part in the top right inset) spacing angle α . Different from the previous compression–bending bistable mechanism in single perforated shellulars (Figure 7.1a), the induced bistability of each staggered layer arises mainly from the counteraction between bending and torsion force of the flexible circumferential beam of the staggered perforation pattern. Due to the high rigidity of rings connecting the neighboring staggered layers, the generated torsion and bending cannot be transferred to the

adjacent layers, and structural instability is localized in one specific staggered layer at a time, leading to a layer-by-layer multistable behavior when multiple staggered perforation is created on the shellular surface. Since the bistability of each staggered layer is decoupled from the rest of the layers, creating n -layer staggered perforations on the surface of P shellular motif can result in a maximum of 2^{n-1} stable states during loading and unloading. Owing to the narrow flexible regions in staggered perforations, P shellular surfaces with small level set constants are not preferred for multistable design. In this research, different combinations of t' and α , which determine the bending and torsion stiffness of the flexible circumferential beam, are analyzed through numerical simulation and experimentation on 3D printed samples. In this research, different combinations of t' and α , which determine the bending and torsion stiffness of the flexible circumferential beam, are analyzed through numerical simulation and experimentation on 3D printed samples. In specific, five different structures, i.e., $t' = 0.05$ mm and $\alpha = 6^\circ$ (Sample M-I), $t' = 0.05$ mm and $\alpha = 18^\circ$ (sample M-II), $t' = 0.1$ mm and $\alpha = 10^\circ$ (sample M-III), $t' = 0.15$ mm and $\alpha = 6^\circ$ (sample M-IV), and $t' = 0.15$ mm and $\alpha = 18^\circ$ (sample M-V) are involved and each of them is 3D printed with three replicates. All these five samples include three perforation layers and share the same level set constant ($f = 0.8$), P shellular size ($2S = 50$ mm), shell thickness ($t = 1$ mm), layer height ($\delta h = 3$ mm), and layer distance ($\delta c = 4.5$ mm). Similar to the bistable shellular with single perforations in Figure 7.1d, a solid frame with a width of 10 mm and two solid cylinder bars with a height of 10 mm is used to constrain four sides, and the top and bottom surfaces of the staggered perforation motif, respectively.

As presented in Figure 7.3b, apart from the initial state, the half shellular with a three-layer staggered perforation would exhibit at most another three stable states, caused by the bending and torsional deformation of the flexible circumferential beams. In addition, snap-back behavior is

observed from the loading and unloading stress-strain curves, indicated by dashed lines. Figure 7.3c shows the deformation of 3D printed sample M-II. Four stable configurations corresponding to the stable strain of 0, 0.25, 0.57, and 0.3, respectively, are observed, which proves our design concept.

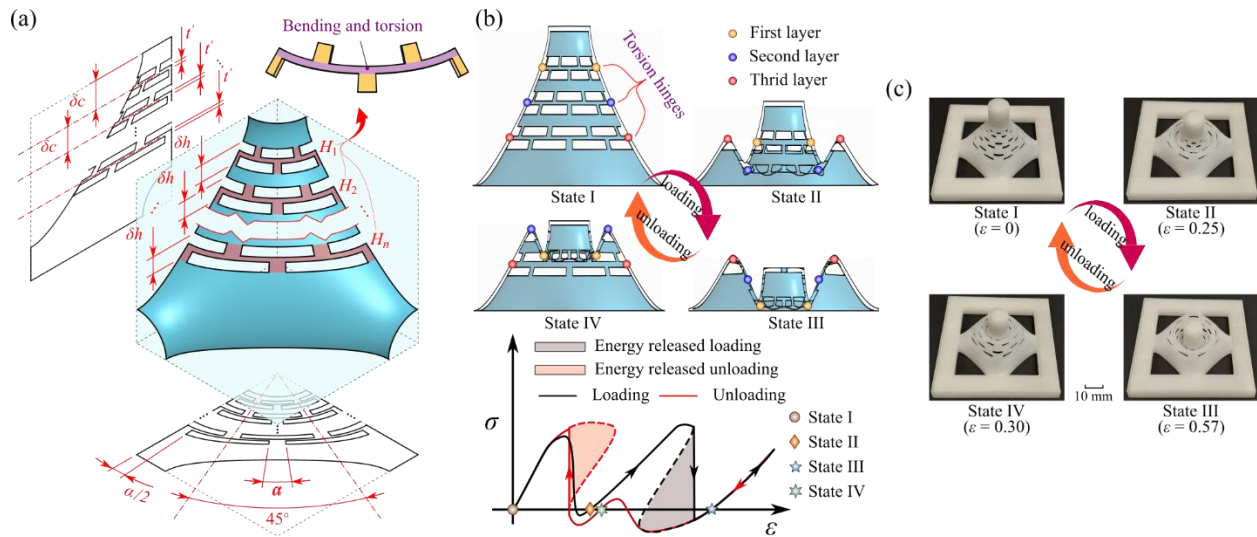


Figure 7.3. Multistable behavior of staggered perforated P shellulars. (a) Schematic view showing the staggered perforated P shellular. (b) Representative deformation pattern and stress-strain curve of the designed multistable metamaterial during the loading and unloading. (c) Four stable states of 3D printed sample II during loading and unloading. (Reprinted with permission from ref [222], copyright 2021 Wiley-VCH GmbH)

To have a better understanding of the influence of geometrical parameters on the structural multistability, Figure 7.4a presents the number of stable configurations of the five 3D printed staggered perforated P shellular motifs. Increasing the circumferential angle α and decreasing the flexible beam height t' lead to the maximum number of stability, i.e., 4 stable configurations found in sample M-II. In specific, sample M-I misses the stable state II in Figure 7.3b, while sample M-II exhibits all the four representative stable states.

A comprehensive parametric study on the multistable behavior of staggered perforated shellulars by FE simulation is conducted, and the number of stable states (blue contour), maximum snap-back induced energy dissipation (green contour) during loading and unloading, and total snap-back induced energy dissipation during cyclic loading (hysteresis) (red contour), are presented in Figure 7.4b. It is noted that apart from sample M-IV, experimental observations on the number of stable configurations presented in Figure 7.4a for four 3D printed samples are in agreement with FE simulation predictions. The discrepancy between the number of stable states observed from experimental (3 stable states), and numerical anticipation (1 stable state) in M-IV sample is because the frictional forces arising from the self-contact of the deformed shellular provide extra forces that hold the shellular at unanticipated stable states. However, the self-contact is not observed in the FE simulation, which might be due to the difference between the as-designed and SLS 3D printed as-built samples. To assess the snap-back induced energy dissipation, the maximum and total energy dissipations presented in Figure 7.4b are normalized by the corresponding values of a motif with $\alpha = 18^\circ$ and $t' = 0.1$ mm.

The shape morphing of the multidirectional multistable perforated shellular unit cell, with possible applications as a building block for developing soft and load-bearable robotic muscles or constructing impact energy absorbers, is presented in Figure 7.4c. The perforated motifs of this unit cell along the three orthogonal directions can be independently transformed into up to four stable configurations during tension and compression. The 3D printed shellular in Figure 7.4c presents about 75% reduction in the volume of the unit cell when it is morphed from the initial stable state to the most compact stable state.

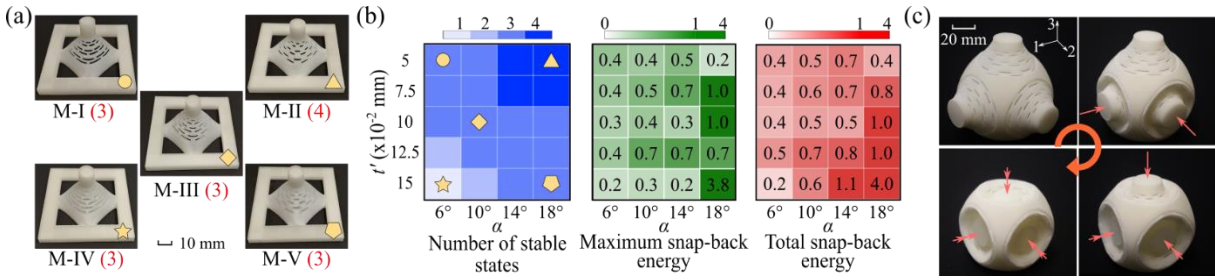


Figure 7.4. Analysis of geometrical parameters' effect on the snapping behavior of the designed multidirectional multistable perforated shellular metamaterials. (a) Five 3D printed motifs. Red numbers in parenthesis indicate the number of stable states, including the initial configuration. (b) Contour associated with the number of stable states (left blue color), maximum snap-back induced energy dissipation (middle green color), and total snap-back induced energy dissipation during a cyclic load (right red color) with respect to the circumferential angle α and flexible beam height t' , determined by FE simulation. (c) 3D deployment of multidirectional multistable unit cell. (Reprinted with permission from ref [222], copyright 2021 Wiley-VCH GmbH)

7.3 Conclusion remarks on multistable perforated shellular

We have developed a novel class of P shellular metamaterial, which can be one/two/three-directional multistable, deployable, programmable, and reusable under both tension and compression, enabled by a delicate and systematic design of the perforation patterns. Two perforation design strategies are introduced, and the associated mechanical and stability properties of the perforated shellulars are analyzed by FE simulations and mechanical testing on SLS 3D printed samples. The first strategy realizes bistable shellular motifs by introducing elliptical holes where the bistability arises from the balance between compression-induced buckling and bending of flexible parts. The mechanical responses of these perforated shellular structures can be controlled by tuning the geometrical parameters of the underlying shell and their perforation. In the second strategy, a multistable shellular motif is developed via multilayer staggered perforations. The bending-torsional hinges, imparted by staggered perforations in each layer, contribute to the overall multistability of perforated shellular metamaterials. With n -layer staggered perforations (n

hinges), maximum 2^{n-1} stable states can be achieved in each shellular motif, offering a new paradigm for the realization of the desired number of stable configurations in shell-like mechanical metamaterials. Compared to the existing bistable metamaterials, our developed and prototyped multistable meta-materials are based on multistable perforated shellular motifs (rather than bistable truss motifs), and damp energy through a combined snap-back and self-contact induced energy dissipation mechanisms. We deem the designed perforated shellular metamaterials capable of serving as the next generation of multifunctional metamaterials with versatile applications, spanning from reusable energy absorbers/dampers and programmable wave filters to reconfigurable and intelligent robotic arms and multipurpose energy harvesters. In addition, if the multistable shellulars are made of ferroelectric material, we can achieve reconfigurable smart materials by 3D printing ferroelectric composites or embedding the ferroelectric microarchitectures into the perforated shellulars.

CHAPTER 8

General Conclusions

By tailoring their periodically repeated microarchitectures, cellular materials have delivered many exotic properties, including those yet to be found in natural materials or chemically synthesized substances. Porous structures evolved in nature have inspired the design of lightweight, stiff, and strong materials, such as honeycombs and truss-like structures used in aerospace and wave absorbers. Nonetheless, most of the current research studies mainly concentrate on exploring their mechanical properties. Responsive to thermal, electric, and mechanical stimuli, cellular ferroelectric materials exhibit unique features in environments and working conditions with accessible multiple physical fields. However, due to the limitation of conventional fabrication methods, only simple 2D architecture or 3D random porous structures have been designed and fabricated. In this dissertation, we not only proposed the theoretical methods to predict the effective properties of cellular ferroelectric metamaterials but also rationally design and fabricate complex 3D cellular materials made of ferroelectric ceramics, corroborating the potential of optimized cell topologies for improving the ferroelectric properties.

The multiphysical multiscale asymptotic homogenization method has been developed to calculate the effective ferroelectric properties of designed cellular smart materials. Compared to

time-consuming full-scale numerical simulations, the proposed homogenization method only involves a single unit cell with periodic boundary conditions. Apart from the homogenization technique, more efficient analytical solutions and scaling law relationships have been presented to further decipher the relationship among the thermo-electro-mechanical properties and architectures of hierarchical lattices. In order to select the optimized structures through analysis of massive alternatives of spinodoids, a machine learning method is trained to predict the properties of arbitrary spinodoid topologies. In addition, a DLP 3D printing technology is adopted to fabricate the ferroelectric metamaterials with designed complex architectures. The good agreement between the homogenization method, machine learning prediction, and experimental tests approves the possibility of the realization of high-performance optimized ferroelectric spinodoid metamaterials. Furthermore, we have designed a programmable multistable perforated shellular by adding delicate perforations on the shellular surface, which can be employed in the future for developing reconfigurable intelligent structures made out of ferroelectric materials.

Generally, our results show that engineering the microarchitectures of cellular materials is an effective method to tune and program the multiphysical response of lightweight smart metamaterials. By tailoring the underlying structure of cellular materials, we can improve their piezoelectric and pyroelectric figures of merit, including piezoelectric coupling constant, acoustic impedance, hydrostatic charge constant, hydrostatic figure of merit, pyroelectric voltage responsivity, pyroelectric current responsivity, and pyroelectric energy harvesting, and the multistability of reconfigurable metamaterials. The following statements can be used for designing smart cellular metamaterials:

(1) The longitudinally polarized 2D extruded cellular materials are almost insensitive to pore topologies, while the transversely poled ones provide an opportunity to enhance the ferroelectric properties by tailoring the pore shapes.

(2) The 1st-order ferroelectric metamaterials remarkably improve the figures of merit compared to the fully-solid ferroelectrics; increasing hierarchical order can magnify the improvements.

(3) There are six different trends for the hybrid hierarchical ferroelectric metamaterials, which offer the opportunity to obtain auxiliary improvements for ferroelectric properties not achievable by fractal-like metamaterials.

(4) Based on limited training cases, machine learning can accurately predict the effective properties of a large number of spinodoid ferroelectric metamaterials and metastructures in much less time.

(5) Lamellar spinodoid with low relative density features higher piezoelectric figures of merit, and columnar spinodoid maintains the constant piezoelectric charge constant even with decreased relative density.

(6) Adding elliptical perforations to the shellular surface leads to bistability, while introducing multilayer staggered perforations along three directions results in multidirectional multistability.

Depending on the applications of the smart cellular metamaterials, the above-mentioned conclusions can be used as a guideline for developing a suitable underlying microarchitecture for multifunctional metamaterials. The following examples present the benefit of our findings for industrial applications:

Sensor: The piezoelectric sensors, such as accelerometers, force sensors, and ultrasonic transducers, convert an external force to an electric signal. If we replace the bulk piezoelectric

materials with the cellular ones, the piezoelectric figures of merit, such as the piezoelectric voltage constant, can be improved, resulting in the enhancement of the sensor sensitivity. Similarly, our research is beneficial in pyroelectric infrared sensors.

Construction: With the advantage of additive manufacturing, we can design high-performance ferroelectric cellular materials that could be embedded into intelligent infrastructures to deliver multiple functionalities, such as self-monitoring, location mapping, and energy harvesting, without a need for additional sensing components and power supply.

Energy: The ferroelectric materials can harvest external mechanical and thermal energy through piezoelectric and pyroelectric effects, respectively. Compared to bulk materials, the cellular ferroelectric metamaterials exhibit improved piezoelectric/pyroelectric energy harvesting figures of merit. Therefore, our structure design strategy can be used to achieve highly efficient energy harvesters. In addition, our designed multistable perforated shellular can also store external mechanical energy in the form of elastic strain energy.

8.1 Future directions

Architected cellular metamaterials exhibit many unprecedented and unusual multifunctional properties, such as negative refractive index, negative effective density, negative incremental stiffness, and negative Poisson's ratio. This dissertation concentrates on the development of smart cellular metamaterials, including cellular ferroelectric metamaterials and multistable mechanical materials; however, more research in related fields remains to be explored. The following statement list suggested topics for further investigations on smart cellular metamaterials:

8.1.1 Ferroelectric ceramic aspect

In addition to the cellular ferroelectric ceramics considered in this research, more studies can focus on the following subjects:

- Designing high-performance metamaterials with improved d_{33} even higher than solid materials and ultrahigh d_{42} or d_{51} , relating the shear force to the electric signal.
- Deriving closed-form equations to describe the relationship between microarchitectures and multiphysical properties in ferroelectric metamaterials, and propose the design strategy to realize ultrahigh piezoelectric constants.
- Analyzing the influence of perforation patterns on the effective ferroelectric properties inspired by multistable perforated shellular metamaterials.

8.1.2 Ferroelectric composite aspect

Although ferroelectric ceramics show high piezoelectric and pyroelectric effects, they are brittle and are difficult to be used in wearable, flexible devices. Ferroelectric composites encapsulating the ferroelectric ceramic into a flexible polymer can be an interesting topic for expanding the applications of ferroelectric materials. The following aspects can be considered for further studies on ferroelectric composites:

- Proposing versatile and efficient surface modification methods to enable a good connection between ferroelectric particles and polymer matrix.
- Investigating the mechanical and ferroelectric properties of ferroelectric composites consisting of architected ferroelectric polymers.
- Developing multistable metamaterials featuring piezoelectric and pyroelectric properties based on the flexibility of ferroelectric composites.

Bibliography

- [1] L.J. Gibson, M.F. Ashby, B.A. Harley, Cellular materials in nature and medicine LK, Cambridge University Press, Cambridge, 2010.
- [2] T.A. Schaedler, W.B. Carter, Architected Cellular Materials, *Annu. Rev. Mater. Res.* 46 (2016) 187–210.
- [3] R. Donate, M. Monzón, M.E. Alemán-Domínguez, Additive manufacturing of PLA-based scaffolds intended for bone regeneration and strategies to improve their biological properties, *E-Polymers*. 20 (2020) 571–599.
- [4] M.P. Ansell, 1 - Wood microstructure – A cellular composite, in: M.P.B.T.-W.C. Ansell (Ed.), Woodhead Publishing, 2015: 3–26.
- [5] U.G.K. Wegst, H. Bai, E. Saiz, A.P. Tomsia, R.O. Ritchie, Bioinspired structural materials, *Nat. Mater.* 14 (2015) 23–36.
- [6] V.M. Shalaev, W. Cai, U.K. Chettiar, H.-K. Yuan, A.K. Sarychev, V.P. Drachev, A. V Kildishev, Negative index of refraction in optical metamaterials, *Opt. Lett.* 30 (2005) 3356–3358.
- [7] V.M. Shalaev, Optical negative-index metamaterials, *Nat. Photonics*. 1 (2007) 41–48.
- [8] J. Li, C.T. Chan, Double-negative acoustic metamaterial, *Phys. Rev. E*. 70 (2004) 55602.
- [9] H. Chen, C.T. Chan, Acoustic cloaking in three dimensions using acoustic metamaterials, *Appl. Phys. Lett.* 91 (2007) 183518.
- [10] A. Rafsanjani, A. Akbarzadeh, D. Pasini, Snapping Mechanical Metamaterials under Tension, *Adv. Mater.* 27 (2015) 5931–5935.

- [11] J.T.B. Overvelde, K. Bertoldi, Relating pore shape to the non-linear response of periodic elastomeric structures, *J. Mech. Phys. Solids*. 64 (2014) 351–366.
- [12] S. Babaei, J. Shim, J.C. Weaver, E.R. Chen, N. Patel, K. Bertoldi, 3D Soft Metamaterials with Negative Poisson's Ratio, *Adv. Mater.* 25 (2013) 5044–5049.
- [13] J.T.B. Overvelde, T.A. de Jong, Y. Shevchenko, S.A. Becerra, G.M. Whitesides, J.C. Weaver, C. Hoberman, K. Bertoldi, A three-dimensional actuated origami-inspired transformable metamaterial with multiple degrees of freedom, *Nat. Commun.* 7 (2016) 10929.
- [14] M.G. Lee, J.W. Lee, S.C. Han, K. Kang, Mechanical analyses of “Shellular”, an ultralow-density material, *Acta Mater.* 103 (2016) 595–607.
- [15] S.T. A., J.A. J., T. A., S.A. E., L. J., G.J. R., V. L., C.W. B., Ultralight Metallic Microlattices, *Science*. 334 (2011) 962–965.
- [16] M. Maldovan, Sound and heat revolutions in phononics, *Nature*. 503 (2013) 209–217.
- [17] S. Narayana, Y. Sato, Heat Flux Manipulation with Engineered Thermal Materials, *Phys. Rev. Lett.* 108 (2012) 214303.
- [18] W.E. Lee, Cellular solids, structure and properties, *Mater. Sci. Technol.* 16 (2000) 233.
- [19] L.E. Murr, S.M. Gaytan, F. Medina, E. Martinez, J.L. Martinez, D.H. Hernandez, B.I. Machado, D.A. Ramirez, R.B. Wicker, Characterization of Ti–6Al–4V open cellular foams fabricated by additive manufacturing using electron beam melting, *Mater. Sci. Eng. A*. 527 (2010) 1861–1868.
- [20] J.J. Andrew, J. Ubaid, F. Hafeez, A. Schiffer, S. Kumar, Impact performance enhancement of honeycombs through additive manufacturing-enabled geometrical tailoring, *Int. J. Impact Eng.* 134 (2019) 103360.
- [21] F.F. Safadi, M.F. Barbe, S.M. Abdelmagid, M.C. Rico, R.A. Aswad, J. Litvin, S.N. Popoff, Bone Structure, Development and Bone Biology BT - Bone Pathology, in: J.S. Khurana (Ed.), Humana Press, Totowa, NJ, 2009: pp. 1–50.
- [22] J. Rödel, J.-F. Li, Lead-free piezoceramics: Status and perspectives, *MRS Bull.* 43 (2018) 576–580.

- [23] N. Ma, Y. Yang, Enhanced self-powered UV photoresponse of ferroelectric BaTiO₃ materials by pyroelectric effect, *Nano Energy*. 40 (2017) 352–359.
- [24] F. Li, D. Lin, Z. Chen, Z. Cheng, J. Wang, C. Li, Z. Xu, Q. Huang, X. Liao, L.-Q. Chen, T.R. Shrout, S. Zhang, Ultrahigh piezoelectricity in ferroelectric ceramics by design, *Nat. Mater.* 17 (2018) 349–354.
- [25] S. Guerin, A. Stapleton, D. Chovan, R. Mouras, M. Gleeson, C. McKeown, M.R. Noor, C. Silien, F.M.F. Rhen, A.L. Kholkin, N. Liu, T. Soulimane, S.A.M. Tofail, D. Thompson, Control of piezoelectricity in amino acids by supramolecular packing, *Nat. Mater.* 17 (2018) 180–186.
- [26] S. Egusa, Z. Wang, N. Chocat, Z.M. Ruff, A.M. Stolyarov, D. Shemuly, F. Sorin, P.T. Rakich, J.D. Joannopoulos, Y. Fink, Multimaterial piezoelectric fibres, *Nat. Mater.* 9 (2010) 643–648.
- [27] X. Lu, H. Qu, M. Skorobogatiy, Piezoelectric Micro- and Nanostructured Fibers Fabricated from Thermoplastic Nanocomposites Using a Fiber Drawing Technique: Comparative Study and Potential Applications, *ACS Nano*. 11 (2017) 2103–2114.
- [28] M.S. C., K.R. B., D.V. Iwijn, B. Gustaaf, F.M. R., R.M. L., Multifunctional Nanomechanical Systems via Tunably Coupled Piezoelectric Actuation, *Science* (780-783). 317 (2007) 780–783.
- [29] W. Xuwen, H. Xuexia, Z. Hongfei, S. Linfeng, F. Wei, W. Xingli, H.L. Chee, W. Hong, Z. Qingsheng, Z. Wu, W. Jun, J. Zhong, S. Zexiang, L. Jie, Z. Ting, L. Zheng, Subatomic deformation driven by vertical piezoelectricity from CdS ultrathin films, *Sci. Adv.* 2 (2022) e1600209.
- [30] R. Ganeshkumar, C.W. Cheah, R. Xu, S.-G. Kim, R. Zhao, A high output voltage flexible piezoelectric nanogenerator using porous lead-free KNbO₃ nanofibers, *Appl. Phys. Lett.* 111 (2017) 13905.
- [31] G. Gafforelli, A. Corigliano, R. Xu, S.-G. Kim, Experimental verification of a bridge-shaped, nonlinear vibration energy harvester, *Appl. Phys. Lett.* 105 (2014) 203901.
- [32] C.R. Bowen, J. Taylor, E. Leboulbar, D. Zabek, A. Chauhan, R. Vaish, Pyroelectric materials and devices for energy harvesting applications, *Energy Environ. Sci.* (2014) 3836-

3856.

- [33] A. Safari, E.K. Akdoğan, Piezoelectric and acoustic materials for transducer applications, 2008.
- [34] W.R. McCall, K. Kim, C. Heath, G. La Pierre, D.J. Sirbully, Piezoelectric Nanoparticle–Polymer Composite Foams, *ACS Appl. Mater. Interfaces*. 6 (2014) 19504–19509.
- [35] S.-H. Lee, S.-H. Jun, H.-E. Kim, Y.-H. Koh, Fabrication of Porous PZT–PZN Piezoelectric Ceramics With High Hydrostatic Figure of Merits Using Camphene-Based Freeze Casting, *J. Am. Ceram. Soc.* 90 (2007) 2807–2813.
- [36] J.I. Roscow, Y. Zhang, M.J. Krašný, R.W.C. Lewis, J. Taylor, C.R. Bowen, Freeze cast porous barium titanate for enhanced piezoelectric energy harvesting, *J. Phys. D. Appl. Phys.* 51 (2018) 225301.
- [37] S. Yi, W. Zhang, G. Gao, H. Xu, D. Xu, Structural design and properties of fine scale 2-2-2 PZT/epoxy piezoelectric composites for high frequency application, *Ceram. Int.* 44 (2018) 10940–10944.
- [38] L. Wucherer, J.C. Nino, G. Subhash, Mechanical properties of BaTiO₃ open-porosity foams, *J. Eur. Ceram. Soc.* 29 (2009) 1987–1993.
- [39] W. Liu, N. Li, Y. Wang, H. Xu, J. Wang, J. Yang, Preparation and properties of 3–1 type PZT ceramics by a self-organization method, *J. Eur. Ceram. Soc.* 35 (2015) 3467–3474.
- [40] K. Bertoldi, M.C. Boyce, Mechanically triggered transformations of phononic band gaps in periodic elastomeric structures, *Phys. Rev. B*. 77 (2008) 52105.
- [41] P. Wang, F. Casadei, S. Shan, J.C. Weaver, K. Bertoldi, Harnessing Buckling to Design Tunable Locally Resonant Acoustic Metamaterials, *Phys. Rev. Lett.* 113 (2014) 14301.
- [42] N.I. Zheludev, E. Plum, Reconfigurable nanomechanical photonic metamaterials, *Nat. Nanotechnol.* 11 (2016) 16–22.
- [43] J.Y. Ou, E. Plum, L. Jiang, N.I. Zheludev, Reconfigurable Photonic Metamaterials, *Nano Lett.* 11 (2011) 2142–2144.
- [44] S. Shan, S.H. Kang, J.R. Raney, P. Wang, L. Fang, F. Candido, J.A. Lewis, K. Bertoldi, Multistable Architected Materials for Trapping Elastic Strain Energy, *Adv. Mater.* 27 (2015)

4296–4301.

- [45] J. Qiu, J.H. Lang, A.H. Slocum, A curved-beam bistable mechanism, *J. Microelectromechanical Syst.* 13 (2004) 137–146.
- [46] M. Alturki, R. Burgueño, Response characterization of multistable shallow domes with cosine-curved profile, *Thin-Walled Struct.* 140 (2019) 74–84.
- [47] J. Tichý, J. Erhart, E. Kittinger, J. Přívratská, Principles of Piezoelectricity BT - Fundamentals of Piezoelectric Sensorics: Mechanical, Dielectric, and Thermodynamical Properties of Piezoelectric Materials, in: J. Tichý, J. Erhart, E. Kittinger, J. Přívratská (Eds.), Springer Berlin Heidelberg, Berlin, Heidelberg, 2010: pp. 1–14.
- [48] S.B. Lang, Pyroelectricity: A 2300-year history, *Ferroelectrics.* 7 (1974) 231–234.
- [49] S.T. Liu, D. Long, Pyroelectric detectors and materials, *Proc. IEEE.* 66 (1978) 14–26.
- [50] K. Uchino, 1 - The development of piezoelectric materials and the new perspective, in: K.B.T.-A.P.M. Uchino (Ed.), Woodhead Publ. Ser. Electron. Opt. Mater., Woodhead Publishing, 2010: pp. 1–85.
- [51] C.R. Bowen, H.A. Kim, P.M. Weaver, S. Dunn, Piezoelectric and ferroelectric materials and structures for energy harvesting applications, *Energy Environ. Sci.* 7 (2014) 25–44.
- [52] J. Haines, O. Cambon, D.A. Keen, M.G. Tucker, M.T. Dove, Structural disorder and loss of piezoelectric properties in α -quartz at high temperature, *Appl. Phys. Lett.* 81 (2002) 2968–2970.
- [53] F. Jona 1922-, *Ferroelectric crystals* / by Franco Jona and G. Shirane, Pergamon Press, Oxford, 1962.
- [54] J.J. Wang, F.Y. Meng, X.Q. Ma, M.X. Xu, L.Q. Chen, Lattice, elastic, polarization, and electrostrictive properties of BaTiO₃ from first-principles, *J. Appl. Phys.* 108 (2010) 34107.
- [55] A.L. Kholkin, N.A. Pertsev, A. V Goltsev, Piezoelectricity and Crystal Symmetry BT - Piezoelectric and Acoustic Materials for Transducer Applications, in: A. Safari, E.K. Akdoğan (Eds.), Springer US, Boston, MA, 2008: pp. 17–38.
- [56] J.-C. Dubois, *Ferroelectric polymers: Chemistry, physics, and applications*. Edited by Hari Singh Nalwa, Marcel Dekker, New York 1995, XII, pp. 895.

- [57] C. Li, P. Wu, S. Lee, A. Gorton, M.J. Schulz, C.H. Ahn, Flexible Dome and Bump Shape Piezoelectric Tactile Sensors Using PVDF-TrFE Copolymer, *J. Microelectromechanical Syst.* 17 (2008) 334–341.
- [58] Z.-G. Ye, High-Performance Piezoelectric Single Crystals of Complex Perovskite Solid Solutions, *MRS Bull.* 34 (2009) 277–283.
- [59] S. Zhang, C.A. Randall, T.R. ShROUT, Recent developments in high Curie temperature perovskite single crystals, *IEEE Trans. Ultrason. Ferroelectr. Freq. Control.* 52 (2005) 564–569.
- [60] L.B. Kong, T.S. Zhang, J. Ma, F. Boey, Progress in synthesis of ferroelectric ceramic materials via high-energy mechanochemical technique, *Prog. Mater. Sci.* 53 (2008) 207–322.
- [61] X. Yang, Analysis of Mechanical and Electrical Damages in Piezoelectric Ceramics, in: G. Zeng (Ed.), *IntechOpen, Rijeka, 2010*: p. Ch. 5.
- [62] H. Kawai, The Piezoelectricity of Poly (vinylidene Fluoride), *Jpn. J. Appl. Phys.* 8 (1969) 975–976.
- [63] R.E. Newnham, D.P. Skinner, L.E. Cross, Connectivity and piezoelectric-pyroelectric composites, *Mater. Res. Bull.* 13 (1978) 525–536.
- [64] R. Kar-Gupta, C. Marcheselli, T.A. Venkatesh, Electromechanical response of 1–3 piezoelectric composites: Effect of fiber shape, *J. Appl. Phys.* 104 (2008) 24105.
- [65] R. Kar-Gupta, T.A. Venkatesh, Electromechanical response of piezoelectric composites: Effects of geometric connectivity and grain size, *Acta Mater.* 56 (2008) 3810–3823.
- [66] C. Marcheselli, T.A. Venkatesh, Electromechanical response of 1-3 piezoelectric composites with hollow fibers, *Appl. Phys. Lett.* 93 (2008) 22903.
- [67] S. Iyer, T.A. Venkatesh, Electromechanical response of (3–0,3–1) particulate, fibrous, and porous piezoelectric composites with anisotropic constituents: A model based on the homogenization method, *Int. J. Solids Struct.* 51 (2014) 1221–1234.
- [68] R. de Medeiros, R. Rodríguez-Ramos, R. Guinovart-Díaz, J. Bravo-Castillero, J.A. Otero, V. Tita, Numerical and analytical analyses for active fiber composite piezoelectric

- composite materials, *J. Intell. Mater. Syst. Struct.* 26 (2014) 101–118.
- [69] M.-L. Feng, C.-C. Wu, A study of three-dimensional four-step braided piezo-ceramic composites by the homogenization method, *Compos. Sci. Technol.* 61 (2001) 1889–1898.
- [70] S. Kari, H. Berger, U. Gabbert, Numerical evaluation of effective material properties of randomly distributed short cylindrical fibre composites, *Comput. Mater. Sci.* 39 (2007) 198–204.
- [71] R. Guinovart-Díaz, P. Yan, R. Rodríguez-Ramos, J.C. López-Realpozo, C.P. Jiang, J. Bravo-Castillero, F.J. Sabina, Effective properties of piezoelectric composites with parallelogram periodic cells, *Int. J. Eng. Sci.* 53 (2012) 58–66.
- [72] S.L. Vatanabe, G.H. Paulino, E.C.N. Silva, Design of functionally graded piezocomposites using topology optimization and homogenization – Toward effective energy harvesting materials, *Comput. Methods Appl. Mech. Eng.* 266 (2013) 205–218.
- [73] A. Deraemaeker, H. Nasser, Numerical evaluation of the equivalent properties of Macro Fiber Composite (MFC) transducers using periodic homogenization, *Int. J. Solids Struct.* 47 (2010) 3272–3285.
- [74] R. Haj-Ali, H. Zemer, R. El-Hajjar, J. Aboudi, Piezoresistive fiber-reinforced composites: A coupled nonlinear micromechanical–microelectrical modeling approach, *Int. J. Solids Struct.* 51 (2014) 491–503.
- [75] C.N. Della, D. Shu, The performance of 1–3 piezoelectric composites with a porous non-piezoelectric matrix, *Acta Mater.* 56 (2008) 754–761.
- [76] J. Bennett, G. Hayward, Design of 1-3 piezocomposite hydrophones using finite element analysis, *IEEE Trans. Ultrason. Ferroelectr. Freq. Control.* 44 (1997) 565–574.
- [77] C.R. Bowen, J. Taylor, E. Le Boulbar, D. Zabek, V.Y. Topolov, A modified figure of merit for pyroelectric energy harvesting, *Mater. Lett.* 138 (2015) 243–246.
- [78] S. Priya, Criterion for material selection in design of bulk piezoelectric energy harvesters, *IEEE Trans. Ultrason. Ferroelectr. Freq. Control.* 57 (2010) 2610–2612.
- [79] Y. Zhang, J. Roscow, R. Lewis, H. Khanbareh, V.Y. Topolov, M. Xie, C.R. Bowen, Understanding the effect of porosity on the polarisation-field response of ferroelectric

- materials, *Acta Mater.* 154 (2018) 100–112.
- [80] J.I. Roscow, R.W.C. Lewis, J. Taylor, C.R. Bowen, Modelling and fabrication of porous sandwich layer barium titanate with improved piezoelectric energy harvesting figures of merit, *Acta Mater.* 128 (2017) 207–217.
- [81] R.W.C. Lewis, A.C.E. Dent, R. Stevens, C.R. Bowen, Microstructural modelling of the polarization and properties of porous ferroelectrics, *Smart Mater. Struct.* 20 (2011) 85002.
- [82] G. Martínez-Ayuso, M.I. Friswell, H. Haddad Khodaparast, J.I. Roscow, C.R. Bowen, Electric field distribution in porous piezoelectric materials during polarization, *Acta Mater.* 173 (2019) 332–341.
- [83] E.W. Yap, J. Glaum, J. Oddershede, J.E. Daniels, Effect of porosity on the ferroelectric and piezoelectric properties of $(\text{Ba}_{0.85}\text{Ca}_{0.15})(\text{Zr}_{0.1}\text{Ti}_{0.9})\text{O}_3$ piezoelectric ceramics, *Scr. Mater.* 145 (2018) 122–125.
- [84] J. Bravo-Castillero, R. Rodríguez-Ramos, R. Guinovart-Díaz, F.J. Sabina, A.R. Aguiar, U.P. Silva, J.L. Gómez-Muñoz, Analytical formulae for electromechanical effective properties of 3–1 longitudinally porous piezoelectric materials, *Acta Mater.* 57 (2009) 795–803.
- [85] S. Iyer, T.A. Venkatesh, Electromechanical response of (3-0) porous piezoelectric materials: Effects of porosity shape, *J. Appl. Phys.* 110 (2011) 34109.
- [86] R. Kar-Gupta, T.A. Venkatesh, Electromechanical response of porous piezoelectric materials: Effects of porosity distribution, *Appl. Phys. Lett.* 91 (2007) 62904..
- [87] R. Kar-Gupta, T.A. Venkatesh, Electromechanical response of porous piezoelectric materials, *Acta Mater.* 54 (2006) 4063–4078.
- [88] S. Iyer, M. Alkhader, T.A. Venkatesh, Electromechanical behavior of auxetic piezoelectric cellular solids, *Scr. Mater.* 99 (2015) 65–68.
- [89] S. Iyer, M. Alkhader, T.A. Venkatesh, Electromechanical Response of Piezoelectric Honeycomb Foam Structures, *J. Am. Ceram. Soc.* 97 (2014) 826–834.
- [90] S. Iyer, M. Alkhader, T.A. Venkatesh, On the relationships between cellular structure, deformation modes and electromechanical properties of piezoelectric cellular solids, *Int. J. Solids Struct.* 80 (2016) 73–83.

- [91] K.S. Challagulla, T.A. Venkatesh, Electromechanical response of piezoelectric foams, *Acta Mater.* 60 (2012) 2111–2127.
- [92] P.W. Bosse, K.S. Challagulla, T.A. Venkatesh, Effects of foam shape and porosity aspect ratio on the electromechanical properties of 3-3 piezoelectric foams, *Acta Mater.* 60 (2012) 6464–6475.
- [93] K.A. Khan, M.A. Khan, 3-3 piezoelectric metamaterial with negative and zero Poisson's ratio for hydrophones applications, *Mater. Res. Bull.* 112 (2019) 194–204.
- [94] K.K. A., A.-M. S., K.S. Z., K.M. A., Piezoelectric Metamaterial with Negative and Zero Poisson's Ratios, *J. Eng. Mech.* 145 (2019) 4019101.
- [95] L. Shu, R. Liang, Y. Yu, T. Tian, Z. Rao, Y. Wang, Unique elastic, dielectric and piezoelectric properties of micro-architected metamaterials, *J. Mater. Chem. C.* 7 (2019) 2758–2765.
- [96] H. Cui, R. Hensleigh, D. Yao, D. Maurya, P. Kumar, M.G. Kang, S. Priya, X. (Rayne) Zheng, Three-dimensional printing of piezoelectric materials with designed anisotropy and directional response, *Nat. Mater.* 18 (2019) 234–241.
- [97] Y. Zhang, M. Xie, J. Roscow, Y. Bao, K. Zhou, D. Zhang, C.R. Bowen, Enhanced pyroelectric and piezoelectric properties of PZT with aligned porosity for energy harvesting applications, *J. Mater. Chem. A.* 5 (2017) 6569–6580.
- [98] A. Navid, C.S. Lynch, L. Pilon, Purified and porous poly(vinylidene fluoride-trifluoroethylene) thin films for pyroelectric infrared sensing and energy harvesting, *Smart Mater. Struct.* 19 (2010) 55006.
- [99] J.D. Eshelby, R.E. Peierls, The determination of the elastic field of an ellipsoidal inclusion, and related problems, *Proc. R. Soc. London. Ser. A. Math. Phys. Sci.* 241 (1957) 376–396.
- [100] W. Biao, Three-dimensional analysis of an ellipsoidal inclusion in a piezoelectric material, *Int. J. Solids Struct.* 29 (1992) 293–308.
- [101] M.L. Dunn, M. Taya, Micromechanics predictions of the effective electroelastic moduli of piezoelectric composites, *Int. J. Solids Struct.* 30 (1993) 161–175.
- [102] T. Chen, Piezoelectric properties of multiphase fibrous composites: Some theoretical results,

- J. Mech. Phys. Solids. 41 (1993) 1781–1794.
- [103] E.M. Hassan, A.L. Kalamkarov, A. V Georgiades, K.S. Challagulla, An asymptotic homogenization model for smart 3D grid-reinforced composite structures with generally orthotropic constituents, *Smart Mater. Struct.* 18 (2009) 75006.
- [104] A.L. Kalamkarov, I. V Andrianov, V. V Danishevs'kyi, Asymptotic Homogenization of Composite Materials and Structures, *Appl. Mech. Rev.* 62 (2009).
- [105] H. Berger, S. Kari, U. Gabbert, R. Rodriguez-Ramos, R. Guinovart, J.A. Otero, J. Bravo-Castillero, An analytical and numerical approach for calculating effective material coefficients of piezoelectric fiber composites, *Int. J. Solids Struct.* 42 (2005) 5692–5714.
- [106] D.P. Skinner, R.E. Newnham, L.E. Cross, Flexible composite transducers, *Mater. Res. Bull.* 13 (1978) 599–607.
- [107] R.E. Newnham, D.P. Skinner, K.A. Klicker, A.S. Bhalla, B. Hardiman, T.R. Gururaja, Ferroelectric ceramic-plastic composites for piezoelectric and pyroelectric applications, *Ferroelectrics.* 27 (1980) 49–55.
- [108] K. Rittenmyer, T. Shrout, W.A. Schulze, R.E. Newnham, Piezoelectric 3–3 composites, *Ferroelectrics.* 41 (1982) 189–195.
- [109] A. Yang, C.-A. Wang, R. Guo, Y. Huang, Microstructure and Electrical Properties of Porous PZT Ceramics Fabricated by Different Methods, *J. Am. Ceram. Soc.* 93 (2010) 1984–1990.
- [110] H. Kara, R. Ramesh, R. Stevens, C.R. Bowen, Porous PZT ceramics for receiving transducers, *IEEE Trans. Ultrason. Ferroelectr. Freq. Control.* 50 (2003) 289–296.
- [111] G. Zhang, P. Zhao, X. Zhang, K. Han, T. Zhao, Y. Zhang, C.K. Jeong, S. Jiang, S. Zhang, Q. Wang, Flexible three-dimensional interconnected piezoelectric ceramic foam based composites for highly efficient concurrent mechanical and thermal energy harvesting, *Energy Environ. Sci.* (2018).
- [112] M.J. Creedon, W.A. Schulze, Axially distorted 3–3 piezoelectric composites for hydrophone applications, *Ferroelectrics.* 153 (1994) 333–339.
- [113] V. Schmitt, F. Raether, Effect of cobalt doping on the sintering mechanisms of the lead-free

- piezoceramic (Bi_{0.5}Na_{0.5})TiO₃, *J. Eur. Ceram. Soc.* 34 (2014) 15–21.
- [114] L. Hu, C.-A. Wang, Y. Huang, C. Sun, S. Lu, Z. Hu, Control of pore channel size during freeze casting of porous YSZ ceramics with unidirectionally aligned channels using different freezing temperatures, *J. Eur. Ceram. Soc.* 30 (2010) 3389–3396.
- [115] T. Fukasawa, Z.-Y. Deng, M. Ando, T. Ohji, S. Kanzaki, Synthesis of Porous Silicon Nitride with Unidirectionally Aligned Channels Using Freeze-Drying Process, *J. Am. Ceram. Soc.* 85 (2002) 2151–2155.
- [116] T.D. Ngo, A. Kashani, G. Imbalzano, K.T.Q. Nguyen, D. Hui, Additive manufacturing (3D printing): A review of materials, methods, applications and challenges, *Compos. Part B Eng.* 143 (2018) 172–196.
- [117] S. Ahn, M. Montero, D. Odell, S. Roundy, P.K. Wright, Anisotropic material properties of fused deposition modeling ABS, *Rapid Prototyp. J.* 8 (2002) 248–257.
- [118] A. Bellini, S. Güçeri, Mechanical characterization of parts fabricated using fused deposition modeling, *Rapid Prototyp. J.* 9 (2003) 252–264.
- [119] D. Lin, S. Jin, F. Zhang, C. Wang, Y. Wang, C. Zhou, G.J. Cheng, 3D stereolithography printing of graphene oxide reinforced complex architectures, *Nanotechnology.* 26 (2015) 434003.
- [120] J.Z. Manapat, Q. Chen, P. Ye, R.C. Advincula, 3D Printing of Polymer Nanocomposites via Stereolithography, *Macromol. Mater. Eng.* 302 (2017) 1600553.
- [121] Q. Mu, L. Wang, C.K. Dunn, X. Kuang, F. Duan, Z. Zhang, H.J. Qi, T. Wang, Digital light processing 3D printing of conductive complex structures, *Addit. Manuf.* 18 (2017) 74–83.
- [122] K. Xiao, W. Jiangtao, C. Kaijuan, Z. Zeang, D. Zhen, H. Fengjingyang, F. Daining, Q.H. Jerry, Grayscale digital light processing 3D printing for highly functionally graded materials, *Sci. Adv.* 5 (2022) eaav5790.
- [123] C.B. Highley, C.B. Rodell, J.A. Burdick, Direct 3D Printing of Shear-Thinning Hydrogels into Self-Healing Hydrogels, *Adv. Mater.* 27 (2015) 5075–5079.
- [124] G.M. Gratson, M. Xu, J.A. Lewis, Direct writing of three-dimensional webs, *Nature.* 428 (2004) 386.

- [125] F. Fina, A. Goyanes, C.M. Madla, A. Awad, S.J. Trenfield, J.M. Kuek, P. Patel, S. Gaisford, A.W. Basit, 3D printing of drug-loaded gyroid lattices using selective laser sintering, *Int. J. Pharm.* 547 (2018) 44–52.
- [126] D.N. Silva, M. Gerhardt de Oliveira, E. Meurer, M.I. Meurer, J.V. Lopes da Silva, A. Santa-Bárbara, Dimensional error in selective laser sintering and 3D-printing of models for craniomaxillary anatomy reconstruction, *J. Cranio-Maxillofacial Surg.* 36 (2008) 443–449.
- [127] N.T. Aboulkhair, M. Simonelli, L. Parry, I. Ashcroft, C. Tuck, R. Hague, 3D printing of Aluminium alloys: Additive Manufacturing of Aluminium alloys using selective laser melting, *Prog. Mater. Sci.* 106 (2019) 100578.
- [128] C.Y. Yap, C.K. Chua, Z.L. Dong, Z.H. Liu, D.Q. Zhang, L.E. Loh, S.L. Sing, Review of selective laser melting: Materials and applications, *Appl. Phys. Rev.* 2 (2015) 41101.
- [129] E.R. Cholleti, A Review on 3D printing of piezoelectric materials, *IOP Conf. Ser. Mater. Sci. Eng.* 455 (2018) 12046.
- [130] C. Lee, J.A. Tarbuton, Electric Poling-assisted Additive Manufacturing Process for Lead-free Piezoelectric Device Fabrication, *Procedia Manuf.* 1 (2015) 320–326.
- [131] S. Bodkhe, G. Turcot, F.P. Gosselin, D. Therriault, One-Step Solvent Evaporation-Assisted 3D Printing of Piezoelectric PVDF Nanocomposite Structures, *ACS Appl. Mater. Interfaces.* 9 (2017) 20833–20842.
- [132] K. Kim, W. Zhu, X. Qu, C. Aaronson, W.R. McCall, S. Chen, D.J. Sirbuly, 3D Optical Printing of Piezoelectric Nanoparticle–Polymer Composite Materials, *ACS Nano.* 8 (2014) 9799–9806.
- [133] F. Qi, N. Chen, Q. Wang, Preparation of PA11/BaTiO₃ nanocomposite powders with improved processability, dielectric and piezoelectric properties for use in selective laser sintering, *Mater. Des.* 131 (2017) 135–143.
- [134] H. Kim, F. Torres, Y. Wu, D. Villagran, Y. Lin, T.-L. Tseng, Integrated 3D printing and corona poling process of PVDF piezoelectric films for pressure sensor application, *Smart Mater. Struct.* 26 (2017) 85027.
- [135] H. Kim, F. Torres, D. Villagran, C. Stewart, Y. Lin, T.-L.B. Tseng, 3D Printing of

- BaTiO₃/PVDF Composites with Electric In Situ Poling for Pressure Sensor Applications, *Macromol. Mater. Eng.* 302 (2017) 1700229.
- [136] E. Suaste-Gómez, G. Rodríguez-Roldán, H. Reyes-Cruz, O. Terán-Jiménez, Developing an Ear Prosthesis Fabricated in Polyvinylidene Fluoride by a 3D Printer with Sensory Intrinsic Properties of Pressure and Temperature, *Sensors*. 16 (2016) 332.
- [137] H. Kim, T. Fernando, M. Li, Y. Lin, T.-L.B. Tseng, Fabrication and characterization of 3D printed BaTiO₃/PVDF nanocomposites, *J. Compos. Mater.* 52 (2017) 197–206.
- [138] S. Bodkhe, P.S.M. Rajesh, F.P. Gosselin, D. Therriault, Simultaneous 3D Printing and Poling of PVDF and Its Nanocomposites, *ACS Appl. Energy Mater.* 1 (2018) 2474–2482.
- [139] J.E. Smay, J. Cesarano III, B.A. Tuttle, J.A. Lewis, Directed Colloidal Assembly of Linear and Annular Lead Zirconate Titanate Arrays, *J. Am. Ceram. Soc.* 87 (2004) 293–295.
- [140] R.L. Walton, M.A. Fanton, R.J. Meyer Jr., G.L. Messing, Dispersion and rheology for direct writing lead-based piezoelectric ceramic pastes with anisotropic template particles, *J. Am. Ceram. Soc.* 103 (2020) 6157–6168.
- [141] M. Gao, L. Li, W. Li, H. Zhou, Y. Song, Direct Writing of Patterned, Lead-Free Nanowire Aligned Flexible Piezoelectric Device, *Adv. Sci.* 3 (2016) 1600120.
- [142] D. Yao, H. Cui, R. Hensleigh, P. Smith, S. Alford, D. Bernero, S. Bush, K. Mann, H.F. Wu, M. Chin-Nieh, G. Youmans, X. (Rayne) Zheng, Achieving the Upper Bound of Piezoelectric Response in Tunable, Wearable 3D Printed Nanocomposites, *Adv. Funct. Mater.* 29 (2019) 1903866.
- [143] Z. Chen, X. Song, L. Lei, X. Chen, C. Fei, C.T. Chiu, X. Qian, T. Ma, Y. Yang, K. Shung, Y. Chen, Q. Zhou, 3D printing of piezoelectric element for energy focusing and ultrasonic sensing, *Nano Energy*. 27 (2016) 78–86.
- [144] B. Tiller, A. Reid, B. Zhu, J. Guerreiro, R. Domingo-Roca, J. Curt Jackson, J.F.C. Windmill, Piezoelectric microphone via a digital light processing 3D printing process, *Mater. Des.* 165 (2019) 107593.
- [145] C. Shuai, W. Huang, P. Feng, C. Gao, X. Shuai, T. Xiao, Y. Deng, S. Peng, P. Wu, Tailoring properties of porous Poly (vinylidene fluoride) scaffold through nano-sized 58s bioactive

- glass, *J. Biomater. Sci. Polym. Ed.* 27 (2016) 97–109.
- [146] F. Qi, N. Chen, Q. Wang, Dielectric and piezoelectric properties in selective laser sintered polyamide11/BaTiO₃/CNT ternary nanocomposites, *Mater. Des.* 143 (2018) 72–80.
- [147] E. Tarasova, I. Juravleva, I. Shishkovsky, R. Ruzhechko, Layering laser-assisted sintering of functional graded porous PZT ceramoplasts, *Phase Transitions.* 86 (2013) 1121–1129.
- [148] X.-Q. Sun, K.R. Farmer, W.N. Carr, A bistable microrelay based on two-segment multimorph cantilever actuators, in: *Proc. MEMS 98. IEEE. Elev. Annu. Int. Work. Micro Electro Mech. Syst. An Investig. Micro Struct. Sensors, Actuators, Mach. Syst. (Cat. No.98CH36176, 1998: pp. 154–159.*
- [149] Z. Zhang, X. Ni, W. Gao, H. Shen, M. Sun, G. Guo, H. Wu, S. Jiang, Pneumatically Controlled Reconfigurable Bistable Bionic Flower for Robotic Gripper, *Soft Robot.* (2021).
- [150] M. Sulfridge, T. Saif, N. Miller, K. O’Hara, Optical actuation of a bistable MEMS, *J. Microelectromechanical Syst.* 11 (2002) 574–583.
- [151] B.P. Mann, B.A. Owens, Investigations of a nonlinear energy harvester with a bistable potential well, *J. Sound Vib.* 329 (2010) 1215–1226.
- [152] P.M. Sobota, K.A. Seffen, Bistable polar-orthotropic shallow shells, *R. Soc. Open Sci.* 6 (2022) 190888.
- [153] J.R. Raney, N. Nadkarni, C. Daraio, D.M. Kochmann, J.A. Lewis, K. Bertoldi, Stable propagation of mechanical signals in soft media using stored elastic energy, *Proc. Natl. Acad. Sci.* 113 (2016) 9722 LP – 9727.
- [154] H. Yang, L. Ma, 1D to 3D multi-stable architected materials with zero Poisson’s ratio and controllable thermal expansion, *Mater. Des.* 188 (2020) 108430.
- [155] J. Hua, H. Lei, Z. Zhang, C. Gao, D. Fang, Multistable Cylindrical Mechanical Metastructures: Theoretical and Experimental Studies, *J. Appl. Mech.* 86 (2019) 071007.
- [156] J. Meaud, K. Che, Tuning elastic wave propagation in multistable architected materials, *Int. J. Solids Struct.* (2017) 69-80.
- [157] Y. Jiang, L.M. Korpas, J.R. Raney, Bifurcation-based embodied logic and autonomous actuation, *Nat. Commun.* 10 (2019) 128.

- [158] H.Y. Jeong, E. Lee, S. Ha, N. Kim, Y.C. Jun, Multistable Thermal Actuators Via Multimaterial 4D Printing, *Adv. Mater. Technol.* 4 (2019) 1800495.
- [159] F. Pan, Y. Li, Z. Li, J. Yang, B. Liu, Y. Chen, 3D Pixel Mechanical Metamaterials, *Adv. Mater.* 31 (2019) 1900548.
- [160] H. Fang, K.W. Wang, S. Li, Asymmetric energy barrier and mechanical diode effect from folding multi-stable stacked-origami, *Extrem. Mech. Lett.* 17 (2017) 7–15.
- [161] S. Zhu, X. Tan, B. Wang, S. Chen, J. Hu, L. Ma, L. Wu, Bio-inspired multistable metamaterials with reusable large deformation and ultra-high mechanical performance, *Extrem. Mech. Lett.* 32 (2019) 100548.
- [162] B. Haghpanah, L. Salari-Sharif, P. Pourrajab, J. Hopkins, L. Valdevit, Multistable Shape-Reconfigurable Architected Materials, *Adv. Mater.* 28 (2016) 7915–7920.
- [163] X. Tan, S. Chen, B. Wang, S. Zhu, L. Wu, Y. Sun, Design, fabrication, and characterization of multistable mechanical metamaterials for trapping energy, *Extrem. Mech. Lett.* 28 (2019) 8–21.
- [164] K. Fu, Z. Zhao, L. Jin, Programmable Granular Metamaterials for Reusable Energy Absorption, *Adv. Funct. Mater.* 29 (2019) 1901258.
- [165] M. Pezulla, N. Stoop, M.P. Steranka, A.J. Bade, D.P. Holmes, Curvature-Induced Instabilities of Shells, *Phys. Rev. Lett.* 120 (2018) 48002.
- [166] M. Taffetani, X. Jiang, D.P. Holmes, D. Vella, Static bistability of spherical caps, *Proc. R. Soc. A Math. Phys. Eng. Sci.* 474 (2018) 20170910.
- [167] Y. Forterre, J.M. Skotheim, J. Dumais, L. Mahadevan, How the Venus flytrap snaps, *Nature.* 433 (2005) 421–425.
- [168] H. Shao, S. Wei, X. Jiang, D.P. Holmes, T.K. Ghosh, Bioinspired Electrically Activated Soft Bistable Actuators, *Adv. Funct. Mater.* 28 (2018) 1802999.
- [169] A.D. Norman, K.A. Seffen, S.D. Guest, Multistable corrugated shells, *Proc. R. Soc. A Math. Phys. Eng. Sci.* 464 (2008) 1653–1672.
- [170] A. Iniguez-Rabago, Y. Li, J.T.B. Overvelde, Exploring multistability in prismatic metamaterials through local actuation, *Nat. Commun.* 10 (2019) 5577.

- [171] S.C. Han, J.W. Lee, K. Kang, A New Type of Low Density Material: Shellular, *Adv. Mater.* 27 (2015) 5506–5511.
- [172] S.C. Han, K. Kang, Another stretching-dominated micro-architected material, shellular, *Mater. Today*. 31 (2019) 31–38.
- [173] K. Hamzeh, I. Yoshikazu, H. Jiuhui, L. Pan, C. Mingwei, Extraordinary tensile strength and ductility of scalable nanoporous graphene, *Sci. Adv.* 5 (2022) eaat6951.
- [174] C.M. Portela, A. Vidyasagar, S. Krödel, T. Weissenbach, D.W. Yee, J.R. Greer, D.M. Kochmann, Extreme mechanical resilience of self-assembled nanolabyrinthine materials, *Proc. Natl. Acad. Sci.* 117 (2020) 5686 LP – 5693.
- [175] S. Hyde, B.W. Ninham, S. Andersson, K. Larsson, T. Landh, Z. Blum, S. Lidin, Chapter 1 - The Mathematics of Curvature, in: S. Hyde, B.W. Ninham, S. Andersson, K. Larsson, T. Landh, Z. Blum, S. Lidin (Eds.), Elsevier Science B.V., Amsterdam, 1997: pp. 1–42.
- [176] J. Shi, L. Zhu, L. Li, Z. Li, J. Yang, X. Wang, A TPMS-based method for modeling porous scaffolds for bionic bone tissue engineering, *Sci. Rep.* 8 (2018).
- [177] S. Tan, J. Gu, S.C. Han, D.-W. Lee, K. Kang, Design and fabrication of a non-clogging scaffold composed of semi-permeable membrane, *Mater. Des.* 142 (2018) 229–239.
- [178] M.S. Morey, A. Davidson, G.D. Stucky, Silica-Based, Cubic Mesostructures: Synthesis, Characterization and Relevance for Catalysis, *J. Porous Mater.* 5 (1998) 195–204.
- [179] T. Femmer, A.J.C. Kuehne, M. Wessling, Estimation of the structure dependent performance of 3-D rapid prototyped membranes, *Chem. Eng. J.* 273 (2015) 438–445.
- [180] N. Sreedhar, N. Thomas, O. Al-Ketan, R. Rowshan, H. Hernandez, R.K. Abu Al-Rub, H.A. Arafat, 3D printed feed spacers based on triply periodic minimal surfaces for flux enhancement and biofouling mitigation in RO and UF, *Desalination*. 425 (2018) 12–21.
- [181] J.G. Werner, G.G. Rodríguez-Calero, H.D. Abruña, U. Wiesner, Block copolymer derived 3-D interpenetrating multifunctional gyroidal nanohybrids for electrical energy storage, *Energy Environ. Sci.* 11 (2018) 1261–1270.
- [182] R. Sachse, A. Westermeier, M. Mylo, J. Nadasdi, M. Bischoff, T. Speck, S. Poppinga, Snapping mechanics of the Venus flytrap (*Dionaea muscipula*), *Proc. Natl. Acad. Sci. U. S.*

- A. (2020) 16035-16042.
- [183] M. Cho, J. Oh, Higher order zig-zag theory for fully coupled thermo-electric–mechanical smart composite plates, *Int. J. Solids Struct.* 41 (2004) 1331–1356.
- [184] M.C. Dökmeci, Vibrations of piezoelectric crystals, *Int. J. Eng. Sci.* 18 (1980) 431–448.
- [185] A.H. Akbarzadeh, D. Pasini, Multiphysics of multilayered and functionally graded cylinders under prescribed hygrothermomagneto electromechanical loading, *J. Appl. Mech. Trans. ASME.* 81 (2014).
- [186] M.L. Dunn, Micromechanics of coupled electroelastic composites: Effective thermal expansion and pyroelectric coefficients, *J. Appl. Phys.* 73 (1993) 5131–5140.
- [187] A.H. Akbarzadeh, M.H. Babaei, Z.T. Chen, Coupled thermopiezoelectric behaviour of a one-dimensional functionally graded piezoelectric medium based on C–T theory, *Proc. Inst. Mech. Eng. Part C J. Mech. Eng. Sci.* 225 (2011) 2537–2551.
- [188] J. Shi, A.H. Akbarzadeh, Architected cellular piezoelectric metamaterials: Thermo-electro-mechanical properties, *Acta Mater.* 163 (2019) 91–121.
- [189] Y. Koutsawa, F. Biscani, S. Belouettar, H. Nasser, E. Carrera, Multi-coating inhomogeneities approach for the effective thermo-electro-elastic properties of piezoelectric composite materials, *Compos. Struct.* 92 (2010) 964–972.
- [190] L.R. Meza, G.P. Philipot, C.M. Portela, A. Maggi, L.C. Montemayor, A. Comella, D.M. Kochmann, J.R. Greer, Reexamining the mechanical property space of three-dimensional lattice architectures, *Acta Mater.* 140 (2017) 424–432.
- [191] H.L.W. Chan, J. Unsworth, Simple model for piezoelectric ceramic/polymer 1-3 composites used in ultrasonic transducer applications, *IEEE Trans. Ultrason. Ferroelectr. Freq. Control.* 36 (1989) 434–441.
- [192] J. Shi, A.H. Akbarzadeh, 3D Hierarchical lattice ferroelectric metamaterials, *Int. J. Eng. Sci.* 149 (2020) 103247.
- [193] J.B. Castillero, J.A. Otero, R.R. Ramos, A. Bourgeat, Asymptotic homogenization of laminated piezocomposite materials, *Int. J. Solids Struct.* 35 (1998) 527–541.
- [194] A. Vigliotti, D. Pasini, Mechanical properties of hierarchical lattices, *Mech. Mater.* 62 (2013)

32–43.

- [195] J.T.B. Overvelde, S. Shan, K. Bertoldi, Compaction Through Buckling in 2D Periodic, Soft and Porous Structures: Effect of Pore Shape, *Adv. Mater.* 24 (2012) 2337–2342.
- [196] F. Fantoni, A. Bacigalupo, M. Paggi, Multi-field asymptotic homogenization of thermopiezoelectric materials with periodic microstructure, *Int. J. Solids Struct.* 120 (2017) 31–56.
- [197] Y. He, Heat capacity, thermal conductivity, and thermal expansion of barium titanate-based ceramics, *Thermochim. Acta.* 419 (2004) 135–141.
- [198] R. Lakes, Cellular solid structures with unbounded thermal expansion, *J. Mater. Sci. Lett.* 15 (1996) 475–477.
- [199] V.S. Deshpande, M.F. Ashby, N.A. Fleck, Foam topology: bending versus stretching dominated architectures, *Acta Mater.* 49 (2001) 1035–1040.
- [200] M.L. R., D. Satyajit, G.J. R., Strong, lightweight, and recoverable three-dimensional ceramic nanolattices, *Science.* 345 (2014) 1322–1326.
- [201] Z. Xiaoyu, L. Howon, W.T. H., S. Maxim, D. Joshua, D.E. B., K.J. D., B.M. M., G. Qi, J.J. A., K.S. O., F.N. X., S.C. M., Ultralight, ultrastiff mechanical metamaterials, *Science* (80-.). 344 (2014) 1373–1377.
- [202] M.L. R., Z.A. J., C. Nigel, M.A. J., K.D. M., G.J. R., Resilient 3D hierarchical architected metamaterials, *Proc. Natl. Acad. Sci.* 112 (2015) 11502–11507.
- [203] X. Zheng, W. Smith, J. Jackson, B. Moran, H. Cui, D. Chen, J. Ye, N. Fang, N. Rodriguez, T. Weisgraber, C.M. Spadaccini, Multiscale metallic metamaterials, *Nat. Mater.* 15 (2016) 1100–1106.
- [204] D. Jang, L.R. Meza, F. Greer, J.R. Greer, Fabrication and deformation of three-dimensional hollow ceramic nanostructures, *Nat. Mater.* 12 (2013) 893–898.
- [205] D.W. Yee, M.L. Lifson, B.W. Edwards, J.R. Greer, Additive Manufacturing of 3D-Architected Multifunctional Metal Oxides, *Adv. Mater.* 31 (2019) 1901345.
- [206] J. Shi, A.H. Akbarzadeh, Hierarchical cellular ferroelectric metamaterials: A design motif to enhance multifunctional figures of merit, *Compos. Struct.* 250 (2020) 112395.

- [207] P. Lohmuller, J. Favre, B. Piotrowski, S. Kenzari, P. Laheurte, Stress Concentration and Mechanical Strength of Cubic Lattice Architectures, *Mater.* 11 (2018) 1146.
- [208] M.-T. Hsieh, B. Endo, Y. Zhang, J. Bauer, L. Valdevit, The mechanical response of cellular materials with spinodal topologies, *J. Mech. Phys. Solids.* 125 (2019) 401–419.
- [209] C. Soyarslan, S. Bargmann, M. Pradas, J. Weissmüller, 3D stochastic bicontinuous microstructures: Generation, topology and elasticity, *Acta Mater.* 149 (2018) 326–340.
- [210] P.C. M., V. A., K. Sebastian, W. Tamara, Y.D. W., G.J. R., K.D. M., Extreme mechanical resilience of self-assembled nanolabyrinthine materials, *Proc. Natl. Acad. Sci.* 117 (2020) 5686–5693.
- [211] X. Lu, K. Nakanishi, Synthesis of Hierarchically Porous Metal Oxide Monoliths via Sol–Gel Process Accompanied by Phase Separation From Divalent Metal Salts: A Short Review , *Front. Chem. Eng.* 3 (2021) 787788.
- [212] S. Shan, L. Yong, N.-D. Bao-Nam, M. Jürgen, W. Jörg, Scaling behavior of stiffness and strength of hierarchical network nanomaterials, *Science.* 371 (2021) 1026–1033.
- [213] J.W. Cahn, Phase Separation by Spinodal Decomposition in Isotropic Systems, *J. Chem. Phys.* 42 (1965) 93–99.
- [214] S. Kumar, S. Tan, L. Zheng, D.M. Kochmann, Inverse-designed spinodoid metamaterials, *Npj Comput. Mater.* 6 (2020) 73.
- [215] L. Zheng, S. Kumar, D.M. Kochmann, Data-driven topology optimization of spinodoid metamaterials with seamlessly tunable anisotropy, *Comput. Methods Appl. Mech. Eng.* 383 (2021) 113894.
- [216] J.F. Durodola, Machine learning for design, phase transformation and mechanical properties of alloys, *Prog. Mater. Sci.* 123 (2022) 100797.
- [217] J. Tang, C. Deng, G. Huang, Extreme Learning Machine for Multilayer Perceptron, *IEEE Trans. Neural Networks Learn. Syst.* 27 (2016) 809–821.
- [218] P. Chopra, R.K. Sharma, M. Kumar, T. Chopra, Comparison of Machine Learning Techniques for the Prediction of Compressive Strength of Concrete, *Adv. Civ. Eng.* 2018 (2018) 5481705.

- [219] W. Wang, J. Sun, B. Guo, X. Chen, K.P. Ananth, J. Bai, Fabrication of piezoelectric nanoceramics via stereolithography of low viscous and non-aqueous suspensions, *J. Eur. Ceram. Soc.* 40 (2020) 682–688.
- [220] H.G. von Schnering, R. Nesper, Nodal surfaces of Fourier series: Fundamental invariants of structured matter, *Zeitschrift Für Phys. B Condens. Matter.* 83 (1991) 407–412.
- [221] C.P. Okeke, A.N. Thite, J.F. Durodola, M.T. Greenrod, Hyperelastic polymer material models for robust fatigue performance of automotive LED lamps, *Procedia Struct. Integr.* 5 (2017) 600–607.
- [222] J. Shi, H. Mofatteh, A. Mirabolghasemi, G. Desharnais, A. Akbarzadeh, Programmable Multistable Perforated Shellular, *Adv. Mater.* 33 (2021) 2102423.